Scuola Normale Superiore

Ph.D. Thesis

The First Black Holes in the Cosmic Dark Ages

Candidate:
Fabio Pacucci

Supervisor:
Prof. Andrea Ferrara

A Thesis submitted in partial fulfilment of the requirements for the degree of Doctor of Philosophy in Physics

A.A. 2015/2016

SCUOLA
NORMALE
SUPERIORE

Ai miei genitori, per aver sempre creduto in me.

"All I know is a door into the dark."

Seamus Heaney

Abstract

The main objective of the original work presented in this Thesis is to develop a theoretical framework to understand the growth, cosmological evolution and observational features of the first black holes, formed when the Universe was younger than $\sim 1\,\mathrm{Gyr}$.

In the first part a growth model is assembled, based on the developed radiation hydrodynamic code *GEMS* (Growth of Early Massive Seeds). We find that the accretion onto a Direct Collapse Black Hole (DCBH) of initial mass $M_0 = 10^5\,\mathrm{M}_\odot$ occurs at an average, super-Eddington, rate $\dot{M}_\bullet \simeq 1.35\,\dot{M}_{Edd} \simeq 0.1\,\mathrm{M}_\odot\,\mathrm{yr}^{-1}$, is intermittent (duty-cycle $\lesssim 50\%$) and lasts $\sim 100\,\mathrm{Myr}$, during which the black hole can accrete only up to $\sim 20\%$ of the available mass. Our model identifies a "feeding-dominated" accretion regime for massive DCBHs ($\gtrsim 10^{5-6}\,\mathrm{M}_\odot$) and a "feedback-limited" one for light ones ($\lesssim 10^{3-4}\,\mathrm{M}_\odot$), the latter being characterized by intermittent (duty cycles $\lesssim 0.5$) and inefficient growth, with recurring outflow episodes. We have also explored slim disk models, appropriate for super-Eddington accretion, in which outflows play a negligible role and a black hole can accrete $80\% - 100\%$ of the gas mass of the host halo in $\sim 10\,\mathrm{Myr}$. We find that the differential growth of light and massive DCBH seeds leads to a bimodal cosmological evolution in mass.

In the second part we investigate the observational properties of these sources. The time-evolving spectrum emerging from the host halo of a DCBH is analyzed: the emission occurs predominantly in the observed infrared-submm ($1 - 1000\,\mu\mathrm{m}$) and X-ray ($0.1 - 100\,\mathrm{keV}$) bands. Such signal should be easily detectable by the JWST at $\sim 1\,\mu\mathrm{m}$, and by ATHENA (between 0.1 and 10 keV). Deep X-ray surveys like the CDF-S could have already detected these systems. Based on this, we provide upper limits for the $z \gtrsim 6$ black hole mass density for both accretion models. A photometric method to identify DCBH candidates in deep multi-wavelength surveys is developed: these sources are characterized by a steep spectrum in the infrared ($1.6 - 4.5\,\mu\mathrm{m}$), i.e. by very red colors. The method selects the only 2 objects with a robust X-ray detection found in the CANDELS/GOODS-S survey with $z \gtrsim 6$. To date, the selected objects represent the most promising black hole seed candidates, possibly formed via the DCBH scenario, with predicted mass $> 10^5\,\mathrm{M}_\odot$. Finally, we note that the abrupt collapse of a massive and rotating object such as a DCBH is a powerful source of gravitational waves emission. We show that the predicted signal lies above the foreseen sensitivity of the DECIGO observatory in the frequency range $(0.8 - 300)\,\mathrm{mHz}$, with a peak amplitude $\Omega_{gw} = 1.1 \times 10^{-54}$ at $\nu_{max} = 0.9\,\mathrm{mHz}$ and a peak Signal-to-Noise Ratio ~ 22 at $\nu = 20\,\mathrm{mHz}$.

Contents

Abbreviations

AGN	**A**ctive **G**alactic **N**ucleus
CDF	**C**handra **D**eep **F**ield
DCBH	**D**irect **C**ollapse **B**lack **H**ole
GW	**G**ravitational **W**ave
GR	**G**eneral **R**elativity
HDP	**H**igh **D**ensity **P**rofile
HST	**H**ubble **S**pace **T**elescope
IGM	**I**nter **G**alactic **M**edium
IMBH	**I**ntermediate **M**ass **B**lack **H**ole
IMF	**I**nitial **M**ass **F**unction
ISCO	**I**nnermost **S**table **C**ircular **O**rbit
JWST	**J**ames **W**ebb **S**pace **T**elescope
LDP	**L**ow **D**ensity **P**rofile
LW	**L**yman **W**erner
MBH	**M**assive **B**lack **H**ole
NS	**N**eutron **S**tars
ODE	**O**rdinary **D**ifferential **E**quation
QSO	**Q**uasi **S**tellar **O**bject
SED	**S**pectral **E**nergy **D**istribution
SFR	**S**tar **F**ormation **R**ate
SMBH	**S**uper **M**assive **B**lack **H**ole
SMS	**S**uper **M**assive **S**tar
SNR	**S**ignal to **N**oise **R**atio
VLT	**V**ery **L**arge **T**elescope

Part I

General Introduction

Chapter 1

The Dark Ages

The word "darkness" usually implies something that is unknown, or not well understood. In fact, it is necessary to "shed some light" on a mystery in order to solve it. One of the most mysterious periods in the history of the Universe is strictly related to darkness: the so-called dark ages of the Universe.

In this case, the use of the word "dark" assumes a standard meaning, since it really suggests the absence of light. In fact, during the first $\sim 150 - 300\,\mathrm{Myr}$ of cosmic history, there was no visible light, due to the fact that the first stars were yet to be formed. The cosmic microwave background, in addition, did not fall in the visible part of the spectrum. The formation of the first metal-free (Pop III) stars, i.e. stars composed only by the primordial elements (hydrogen, helium and traces of lithium), is nowadays subject of intense studies. A deep understanding of the formation of the first stars is fundamental to obtain a clear picture of the primeval evolution of galaxies, the fundamental building blocks of the Universe. Currently, the most distant galaxy ever observed shines only $\sim 400\,\mathrm{Myr}$ after the Big Bang, posing an important time constraint on the duration of the Dark Ages.

With the formation of the first stars, also the formation of the first collapsed objects occurred. The first black holes exerted an important feedback effect on the evolution of their surrounding environment. Both the first stars and the first black holes were most likely different from the ones we observe in the local Universe. In fact, there are wide-spread theoretical indications that such objects were more massive than local ones, due to the particular environmental properties of the primordial Universe. In addition,

the observation of SMBHs already at $z \sim 7$, less than $\sim 800\,\mathrm{Myr}$ after the Big Bang, poses very stringent time constraints on the growth process of these objects. From all these elements, one of the crucial question related to the early Universe arises: how did these SMBHs emerged from the Dark Ages?

In this Ph.D. Thesis, the work personally developed in this field is presented. The general organization of this Thesis is as follows.

Chapter 1 presents a general introduction to Cosmology, with a summary of the currently accepted cosmological model, the main stages of primordial cosmic evolution and some remarks about the formation of the first structures.

Chapter 2 is focused on black holes. A general theory is presented, along with the problem of the formation of the first SMBHs. Moreover, the different formation scenarios for the first black hole seeds are presented, with particular emphasis given to the Direct Collapse Black Hole (DCBH) model.

After these two introductory chapters, the original work developed during the Ph.D. is described.

The first part is focused on theory.

Chapter 3 describes the accretion phase of a DCBH at high redshift ($z \sim 10$), which eventually forms an Intermediate-Mass Black Hole (IMBH). The time evolution of the collapse phase is investigated.

Chapter 4 describes the theoretical framework developed to investigate the growth efficiency of high-z black hole seeds.

The second part is focused on observations.

Chapter 5 presents our results on the study of the time-evolving spectrum emerging from the host halo of a high-z black hole seed.

Chapter 6 presents a novel photometric method to select DCBH candidates in deep multi-wavelength fields. Moreover, the detection of the first two DCBH candidates in the CANDELS/GOODS-S field is presented.

Chapter 7 presents the calculation of the gravitational signal emitted by the collapse of a DCBH at high redshifts, along with a study of its observability with future gravitational waves observatories.

The final Appendix presents additional works developed during the Ph.D., but not included in the present Thesis.

1.1 The Cosmological Model

Since its infancy, humanity has always questioned the Nature about its origins, its meaning and its end. The history of science portraits several heroic attempts to unveil the mysteries of the Universe, even with scarce or without any data to describe it. The first "cosmological models" were far from realistically describing the Universe as we now know it nowadays.

From the XX century we live in the remarkable situation of having plenty of data on our Universe. The Cosmology, from being a philosophic attempt to answer the most profound questions of human nature, has turned out to be a precision science.

In order to understand and eventually describe our Universe, we need a cosmological model, a theoretical framework to build our theories and predictions upon. Remarkably enough, the Universe described by the current cosmological model is extremely simple and based on three fundamental ingredients:

- A theory for the gravitational interaction: the *General Relativity*.
- A premise on the general distribution of matter: the cosmological principle, which states that *the Universe, on sufficiently large scales, is homogeneous and isotropic*.
- A small number of physical parameters: the *cosmological parameters* (see Table 1.1).

Ω_Λ	Ω_m	Ω_b	h	n_s	σ_8
0.6825	0.3175	0.0489	0.6711	0.9624	0.8344

TABLE 1.1: The basic set of cosmological parameters from the Planck mission (Planck Collaboration et al., 2015). The first three are the density parameters for vacuum energy, total matter and baryonic matter, respectively (see the derivation of Eq. 1.8 for a precise definition). h is the Hubble's constant in units of $100\,\mathrm{km\,s^{-1}\,Mpc^{-1}}$, n_s is the scalar spectral index and σ_8 is the density fluctuations at the scale $8\,\mathrm{Mpc\,h^{-1}}$.

The only interaction that is effective on large scales in the Universe is the gravitational one. All other interactions (i.e. electromagnetic, weak and strong) are effective only on much smaller astrophysical scales, e.g. the stellar interiors. For centuries the Newtonian gravitational theory worked remarkably well in predicting most of the observations. At

the beginning of the XX century, the Special and the General Theories of Relativity provided a larger and more accurate framework to describe the gravitational interaction between massive particles. The General Relativity describes the space-time structure of the Universe as a result of the matter distribution and can be applied to describe its general dynamics. Its predictions are completely different from those of the Newtonian gravity only for particles moving at velocities comparable with the speed of light and/or inside strong gravitational fields.

The Einstein's equations were initially employed assuming very simple premises for the Universe, i.e. its homogeneity and its isotropy. *Homogeneity* means uniform conditions everywhere and at any time, *isotropy* means that there is no privileged direction in space. The combination of these two simplifying conditions is known under the name *cosmological principle*. Initially, these conditions were chosen only in order for the equations of General Relativity to be actually solvable. As it turned out, several observations indicate that the Universe is actually homogeneous and isotropic on the largest observable scales to within one part over 10^5, as the analysis of the Cosmic Microwave Background proves (Smoot et al., 1992).

There are no stable solutions to Einstein's equations for an homogeneous and isotropic Universe: it must be either expanding or contracting. Indeed, less than a decade after the publication of the theory of General Relativity, Edwin Hubble observed for the first time that the "nebulae" (objects that nowadays we know to be external galaxies) are receding at a speed, v, that is proportional to their distance from us, r. The constant of proportionality is named Hubble constant H:

$$v = H_0 r \,. \tag{1.1}$$

The Hubble constant is time-dependent and we define H_0 its present-day value, $H_0 \sim 67.11\,\mathrm{km\,s^{-1}\,Mpc^{-1}}$ (see Table 1.1). This constant also sets a fundamental time-scale in the Universe: its inverse is roughly equal to the age of the Universe, $T \approx 14\,\mathrm{Gyr}$. From our vantage point on the planet Earth, we observe all galaxies receding from us, but, due to the cosmological principle, the same observation is true in every place in the Universe, which is isotropic and homogeneous. Due to its astonishing simplicity, the large-scale dynamics of the Universe is described by a small number of parameters (see Table 1.1).

In the theoretical framework of the General Relativity, the space-time geometry is mathematically expressed by the so-called metric tensor $g_{\mu\nu}$, which allows to measure the space-time interval ds between two events:

$$ds^2 = g_{\mu\nu} dx^\mu dx^\nu \, . \tag{1.2}$$

Here, dx is a four-vector containing the space-time coordinates of the event, i.e. $dx = (ct, r, \theta, \phi)$ in spherical coordinates and with the usual rescaling of the time coordinate by the speed of light c. The space-time line ds is commonly defined to vanish for a photon, moving at c: $ds = 0$.

The expression of ds for a spatially homogeneous and isotropic space, which is expanding or contracting, is the one that results from the Friedman-Robertson-Walker metric, in spherical comoving coordinates:

$$ds^2 = c^2 dt^2 - a(t) \left[\frac{dr^2}{1 - kr^2} - r^2 d\Omega \right] \, , \tag{1.3}$$

where $a(t)$ is the cosmic scale factor that describes the expansion of the Universe as function of time, k is the curvature and $d\Omega = d\theta^2 + sin^2\theta d\phi^2$. Several observations show that the total space-time curvature of the Universe is nearly flat, so that $k \sim 0$ (de Bernardis et al., 2000).

The metric expressed in Eq. 1.3 enters in the Einstein's field equations:

$$R_{\mu\nu} - \frac{1}{2} g_{\mu\nu} R = \frac{8\pi G}{c^4} T_{\mu\nu} + \Lambda g_{\mu\nu} \, , \tag{1.4}$$

where $R_{\mu\nu}$ is the Ricci tensor, which describes the local curvature of space-time, R is the curvature scalar, $T_{\mu\nu}$ is the energy-momentum tensor and Λ is the cosmological constant (dark energy or vacuum energy, with the modern terminology). The Einstein's field equations are a set of 10 equations that describes the fundamental interaction of gravitation as a result of space-time being curved by matter and energy. They equate the local space-time curvature (the left-hand side) with the local energy and momentum within that space-time (expressed by the energy-momentum tensor).

The cosmological constant is named in this way due to the fact that the energy density associated with this source is constant in space and time. Given that the space is actually

expanding, the pressure associated to the vacuum is negative, i.e. its gravitational effect is positive, repulsive. This effect gives rise to the accelerated expansion of the Universe, which is underway in the last 6 Gyr of cosmic history. The nature of the dark energy is unclear at the present time.

It is interesting to note that, naming R_c the comoving coordinate, a source located at a separation of $r = a(t)R_c$ from us will move away from our position with a velocity $v = dr/dt = \dot{a}R_c = (\dot{a}/a)r = Hr$, with $H(t) \equiv \dot{a}(t)/a(t)$, re-obtaining the Hubble's law.

In the scenario currently described, the cosmology is completely specified by the evolution of $a(t)$. The expansion factor $a(t)$ is also simply related to the redshift z of the source, by the relation:

$$a(t) = \frac{1}{1+z}\,, \tag{1.5}$$

defining $a_0 = 1$. Eq. 1.4 drives to the so-called Friedman equation:

$$\left(\frac{\dot{a}}{a}\right)^2 = H^2(t) = \frac{8\pi G}{3}\rho - \frac{kc^2}{a^2} + \frac{\Lambda c^2}{3}\,, \tag{1.6}$$

which relates the expansion of the Universe, mathematically expressed by the Hubble constant $H(t)$, to the matter-energy density and to the curvature k.

The density ρ can be expressed as a sum of three contributes $\rho = \rho_m + \rho_r + \rho_\Lambda$ where ρ_m is the non-relativistic matter energy density, ρ_r is the radiation energy density, and ρ_Λ is the vacuum energy density. Defining the critical density as:

$$\rho_c = \frac{3H^2}{8\pi G} \approx 5 \times 10^{-30}\,\mathrm{g\,cm^{-3}}\,, \tag{1.7}$$

we can introduce the density parameter Ω for each type of energy density: $\Omega_m = \rho_m/\rho_c$, $\Omega_r = \rho_r/\rho_c$, $\Omega_\Lambda = \rho_\Lambda/\rho_c$. The Friedmann equation finally becomes:

$$\frac{H(t)}{H_0} = \sqrt{\frac{\Omega_m}{a^3} + \frac{\Omega_r}{a^4} + \Omega_\Lambda}\,. \tag{1.8}$$

It is clearly visible from Eq. 1.8 that the matter content of the Universe is diluted as $\sim a^{-3}$ due to the expansion of the Universe while the radiation content is diluted as $\sim a^{-4}$ due to the fact that the energy associated to the photons are also redshifted with the scale factor. Finally, the vacuum energy is constant throughout the cosmic time.

This last equation relates the matter-energy content of the Universe to its overall evolution over time, and may be interpreted as a compact version of the entire cosmological model.

1.2 From the Big Bang to the Reionization

In this section we provide a brief overview of the main phases that characterized the evolution of the Universe from the original singularity of the Big Bang to the reionization phase, which began at $z \sim 30 - 20$ and lasted until $z \sim 6$. This overview is not meant to be exhaustive, its only aim being to provide a very general scheme of the first phases of the cosmic evolution.

1.2.1 The first second of the Universe

The Big Bang is the initial singularity that originated the Universe $\sim 13.7\,\mathrm{Gyr}$ ago.

Several properties of the Universe, e.g. its geometrical flatness (see Section 1.1), suggest that immediately after the Big Bang, during a brief period ($t \sim 10^{-35} - 10^{-33}\,\mathrm{s}$) called inflation, an exponential expansion happened. In this period the Universe might have increased its size by ~ 60 orders of magnitudes (see e.g. the seminal paper Linde 1982 for reference). The actual existence of this inflationary period has not been observationally proved so far. Nonetheless, it is of considerable importance to explain many properties of the Universe. Before the inflation, quantistic fluctuations might have produced extremely large density variations, which would have been stretched to cosmological scales if a linear expansion happened. Instead, the extremely fast expansion predicted by the inflationary theory erased the density fluctuations on large scales, producing an Universe uniform up to 1 part over 10^5. On small spatial scales, the density fluctuations remained as seeds of the large structures that we see today in the Universe, e.g. galaxies and clusters of galaxies.

After the inflationary stage, an unknown process named baryogenesis generated an excess of particles over antiparticles. Nowadays, we observe the Universe to be composed of particles, their respective antiparticles having been annihilated during this stage. As the expansion continued, the Universe cooled to a temperature $T \sim 100\,\mathrm{MeV}$: protons

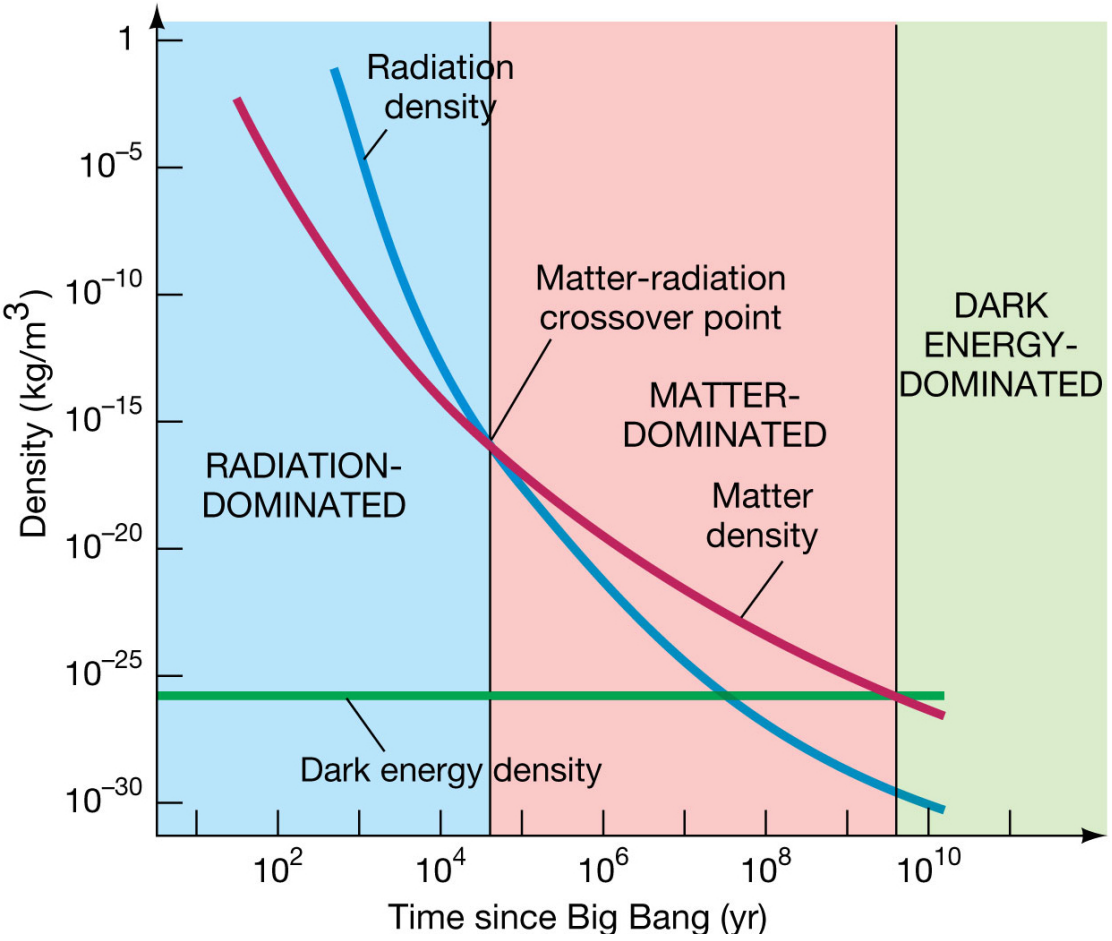

FIGURE 1.1: A brief history of the Universe with a focus on the domination of its different components. The radiation-dominated era, from the Big Bang until $z \sim 3300$, the matter-dominated era for $3300 > z > 0.3$ and the dark energy era for $z < 0.3$, i.e. for the last 6 Gyr. Copyright: Pearson Education, Inc. (2011).

and neutrons condensed out of the primordial quark-gluon plasma through the so-called quantum chromo-dynamics phase transition. At about one second after the Big Bang, the temperature declined to $T \sim 1$ MeV and the weakly interacting neutrinos decoupled.

1.2.2 The formation of the first elements

Just after the inflation, the content of the Universe was firstly dominated by radiation. The radiation-dominated era lasted until $z \sim 3300$. The Universe was then dominated by its matter content for $3300 > z > 0.3$ and finally by dark energy for $z < 0.3$, i.e. for the last 6 Gyr (see Fig. 1.1). During the radiation-dominated era the expansion rate was $a(t) \propto t^{2/3}$, then in the matter-dominated era was $a(t) \propto t^{1/2}$ and finally during the vacuum-dominated era the expansion is exponential, i.e. $a(t) \propto e^t$. These relations are simply derived from Eq. 1.8.

Along with the expansion, the temperature T of the Universe was decreasing with the redshift, as $T \propto (1+z)$ in the radiation-dominated era. About three minutes after the Big Bang, when $T \sim 10^9\,\mathrm{K}$, the cosmic gas consisted of a plasma of free electrons, protons, photons and neutrinos. Each species remained coupled until the rate of interactions $\Gamma(t)$ with the others was greater than the rate of cosmic expansion (the Hubble's constant), i.e. until $\Gamma(t) > H(t)$. In the following few minutes, nuclear fusion reactions produced light atomic nuclei more massive than hydrogen, such as deuterium, helium and lithium. Though simple atomic nuclei formed within the first minutes after the Big Bang, thousands of years passed before the first electrically neutral atoms formed.

1.2.3 The matter-radiation decoupling

Although the transition to the matter domination occurred at $z \sim 3300$, the Universe remained hot enough for the matter to be fully ionized, while Thomson scattering efficiently coupled it to the radiation. At $z \sim 1100$ the temperature decreased below $\sim 3000\,\mathrm{K}$ and the free electrons recombined with protons to form neutral hydrogen atoms. This is one of the most crucial phase transition in the cosmic history: the Universe became transparent to the propagation of light. The recombination is imprinted into the Cosmic Microwave Background, successively imaged and measured by several experiments (e.g. Boomerang, COBE, WMAP, Planck, see Fig. 1.2).

At this point of the cosmic history, at $z \sim 1100$ or $\sim 380\,000\,\mathrm{yr}$ after the Big Bang, photons were able to freely propagate, but the Universe was still dark. The only radiation emitted was the 21 cm spin line of neutral hydrogen. There is currently a huge observational effort underway to detect this faint radiation, as it is in principle an even more powerful tool than the Cosmic Microwave Background for studying the early Universe. The Dark Ages of the Universe lasted until $z \sim 30 - 20$: in this relatively short period, the first bound structures were forming from the collapse of dark matter halos, as Sec. 1.3 describes.

1.2.4 The formation of the first stars

Nowadays, we dispose of an image of the Universe when it was only $\sim 380\,000\,\mathrm{yr}$ old (the Cosmic Microwave Background) and images of several galaxies living in the infant

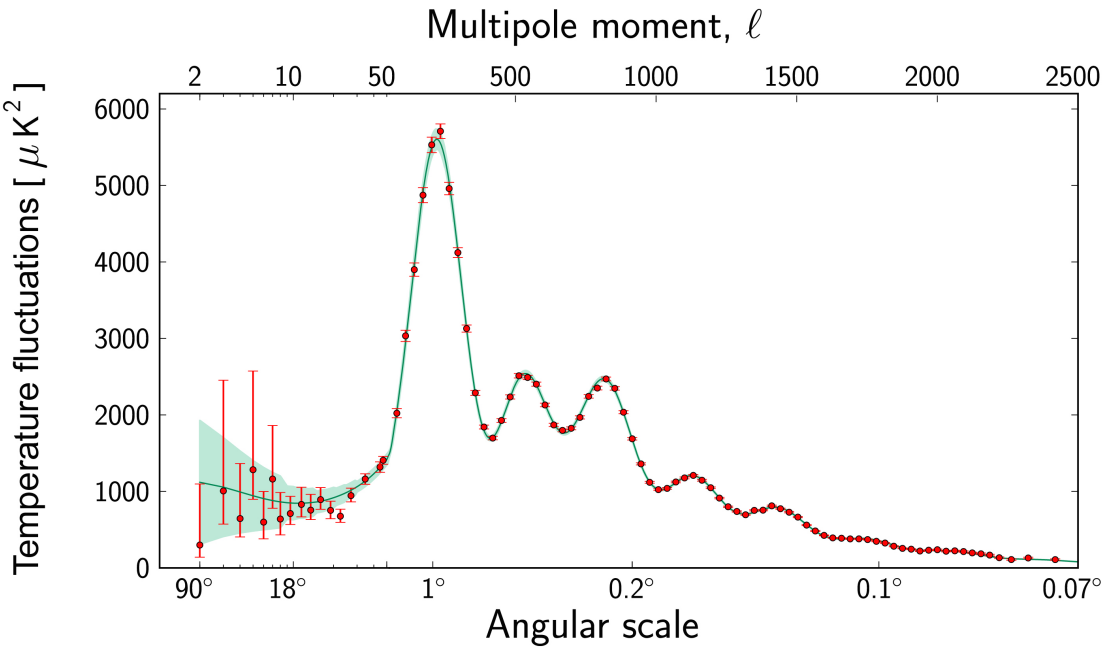

FIGURE 1.2: The temperature fluctuations in the Cosmic Microwave Background detected by the Planck satellite at different angular scales on the sky. The red dots are measurements made with Planck, shown with error bars that account for measurement errors as well as for an estimate of the uncertainty that is due to the limited number of points in the sky at which it is possible to perform measurements. This so-called cosmic variance is an unavoidable effect that becomes most significant at larger angular scales. Copyright: ESA and the Planck Collaboration.

Universe. To date, the farthest galaxy ever observed is at $z \approx 11$ (Oesch et al., 2016), when the Universe was only $\sim 400\,\mathrm{Myr}$ old. Between these two epochs there was a period during which the Universe was dark, since no stars were formed and the Cosmic Microwave Background no longer traced the distribution of matter. As already discussed, the only radiation emitted was the 21 cm spin line of neutral hydrogen.

This period (between $z \sim 30-20$ and $z \sim 6$) is a crucial transition in the early Universe since it marked the passage from the very simple initial conditions of the Universe (see Table 1.1) to the birth of the complexity we observe today (e.g. planets, stars, galaxies, clusters). The Dark Ages is the period when the first gravitationally bound objects, like galaxies, black holes and stars, were formed. The building blocks of the Universe we observe today were slowly constructed in the darkness. As soon as the first stars formed, complex chemical and radiative processes entered the scene and contributed to form all the astonishing structures we observe nowadays in the Universe. This event opened up the way to the reionization of the Universe, which will be described more thoroughly in the next subsection.

The formation of the first large-scale structures in the Universe was associated with

the collapse of dark matter halos starting from the primordial density fluctuations, left-overs of the inflationary period. The first star formation, instead, is linked to the fate of baryons which collapsed under the gravitational effect of the dark matter. This collisional process resulted in the formation of the first generation of stars, named Pop III.

Many advancements have been made in the field of the first star formation, nonetheless the physics of the fragmentation process and its relationship with the thermodynamical conditions of the gas are still far to be fully understood. For detailed reviews of the first start formation process described in this subsection, the interested reader is referenced to Barkana & Loeb (2001) and Bromm (2013).

Pop III stars are thought to be very different from local stars. They were characterized by (i) very low metallicities, (ii) large masses, (iii) high surface temperatures. Their metallicity[1] should be comparable with the one produced during the Big Bang, i.e. $Z \sim 10^{-10}$. For comparison, the metallicity of standard Pop II stars is nowadays $Z \sim 10^{-3} - 10^{-4}$. The temperature of the Universe during the period when Pop III stars formed was much higher than the mean present-day value. Since the Jeans mass M_J (i.e. the minimum mass needed for a molecular cloud to collapse and form a bounded object) scales with the temperature as $M_J \propto T^{3/2}$, the characteristic mass scale of these first stars is large compared with the present-day value: Pop III stars are currently thought to have masses in the range $\sim 10^2 - 10^3\,\mathrm{M}_\odot$. In addition, the large masses are also due to the lack of metal cooling agents, which drives to a fragmentation only occurring into relatively large units (see also the next Chapter 2 on the formation of the first black holes). Only massive stars, reaching very high temperatures and densities, are able to produce enough energy by nuclear fusion through the *p*-*p* chain. In fact, due to the lack of carbon, nitrogen, and oxygen the CNO cycle was not active in the first stellar population.

In order to collapse, the gas needs to cool. The cooling was mainly driven by radiative de-excitation of molecular hydrogen, H_2 (see Fig. 1.3). Hence, the fate of a gas clump depends on its ability to rapidly increase its H_2 content during the collapse phase. The description of the Pop III star formation needs the understanding of the various channels

[1] Here the usual definition of metallicity is employed: $Z = 1 - X - Y$, where X and Y are the hydrogen and helium mass fractions, respectively. The mass fraction of the species i with mass m_i is given by m_i/M where M is the total mass of the system.

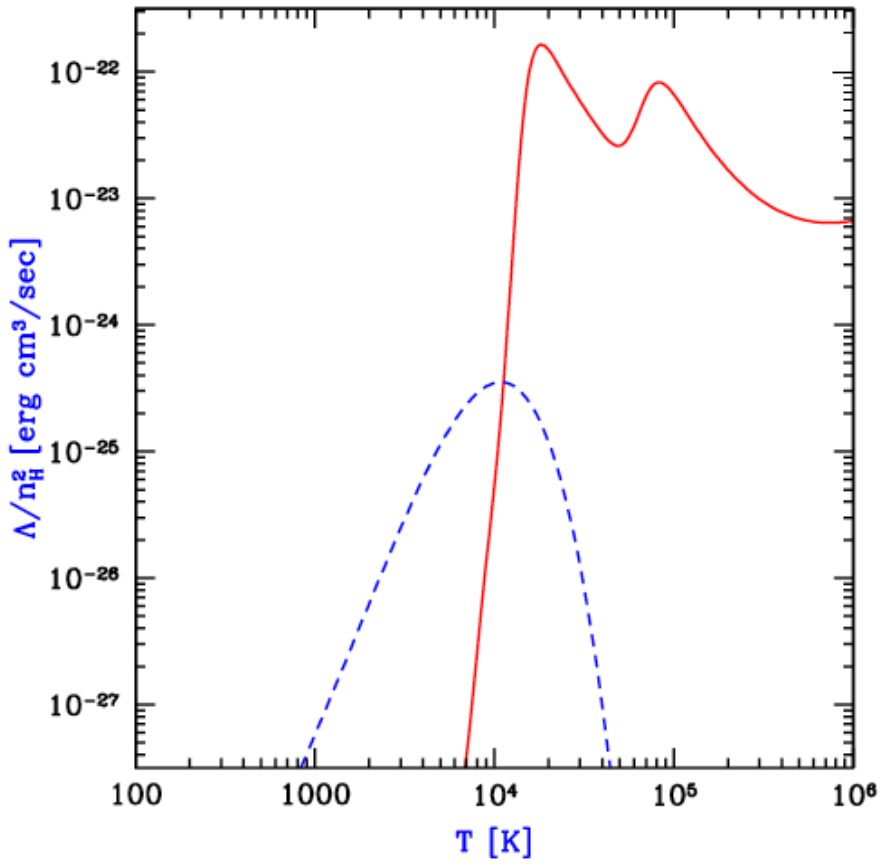

FIGURE 1.3: Cooling rates as a function of temperature for a primordial gas composed of atomic hydrogen and helium, as well as molecular hydrogen, in the absence of any external radiation. The solid line shows the cooling curve for an atomic gas, with the characteristic peaks due to collisional excitation of H I and He II. The dashed line shows the additional contribution from molecular cooling. Image taken from Barkana & Loeb (2001).

available for the gas to cool, the evaluation of their efficiency and the modeling of the physical processes that set the mass scale of the fragments.

These unusually massive stars burned their fuel in a short period of time (the stellar lifetime τ is inversely proportional to the cube of its mass: $\tau \propto M_*^{-3}$): they eventually exploded as supernovae and possibly collapsed into compact objects. The metals produced during the lifetime of these stars were then dispersed during the supernova explosion, enriching the surrounding gas and opening the way to the next generation of metal-enriched stars.

The amount of UV ionizing photons produced by Pop III stars and the fraction that escapes from the star-forming sites (usually named f_{esc}) are fundamental parameters that have to be taken into account to model the evolution of the subsequent phase of the

cosmic history: the epoch of reionization. The dark and neutral IGM, as a consequence of the expansion and of the continuous emission of ionizing photons from the Pop III stars, became once again ionized.

1.2.5 The epoch of reionization

The formation of the first stars led to the emission of high-energy photons that progressively ionized the surrounding IGM at larger and larger scales. Current constrains strongly suggest that the epoch of reionization occurs within the redshift range $z \sim 10-6$ (Planck Collaboration et al., 2016). At $z \sim 6$ many observations (e.g. Fan et al. 2001 and references therein) show that the reionization of the Universe should be complete. For the second time in its history, the matter inside the Universe is ionized: the reionization marked the second phase transition for the cosmic gas, after the matter-radiation decoupling (see e.g. Zaroubi 2013 and references therein for an extensive review).

The reionization process can be divided in three phases (see Gnedin 2000 for a broad description): (i) pre-overlap stage, (ii) overlap stage and (iii) post-overlap stage. During the first stage, several sources of photons with energy $E_\gamma > 13.6\,\mathrm{eV}$ started to produce ionizing radiation, while the ionization fronts were still detached. In the overlap stage, individual ionized regions overlapped and reionized the diffuse IGM: the ionization fronts touched and the process accelerated since each point inside the overlapped regions was irradiated by at least a couple of sources. This is what is usually termed as the "moment of reionization". During the last stage, the remaining high-density regions were progressively ionized.

From a theoretical point of view, an accurate modeling of galaxy formation and a proper treatment of radiative transfer are imperative to follow the evolution of the reionization process. An important parameter for the modeling of radiative transfer is the so-called escape fraction (f_{esc}), the fraction of ionizing radiation that escapes the galaxy into the IGM. Observational and theoretical studies agree to bound the value of the escape fraction in the range $f_{esc} = 0.1 - 0.5$ (see e.g. Ferrara & Loeb 2013).

The main parameter used to describe the evolution of the cosmic reionization is the filling factor $Q_{H\,II}$, i.e. the fraction of the volume of the Universe which is filled by H II regions. Fig. 1.4 is a simulation of the redshift evolution of the filling factor for different

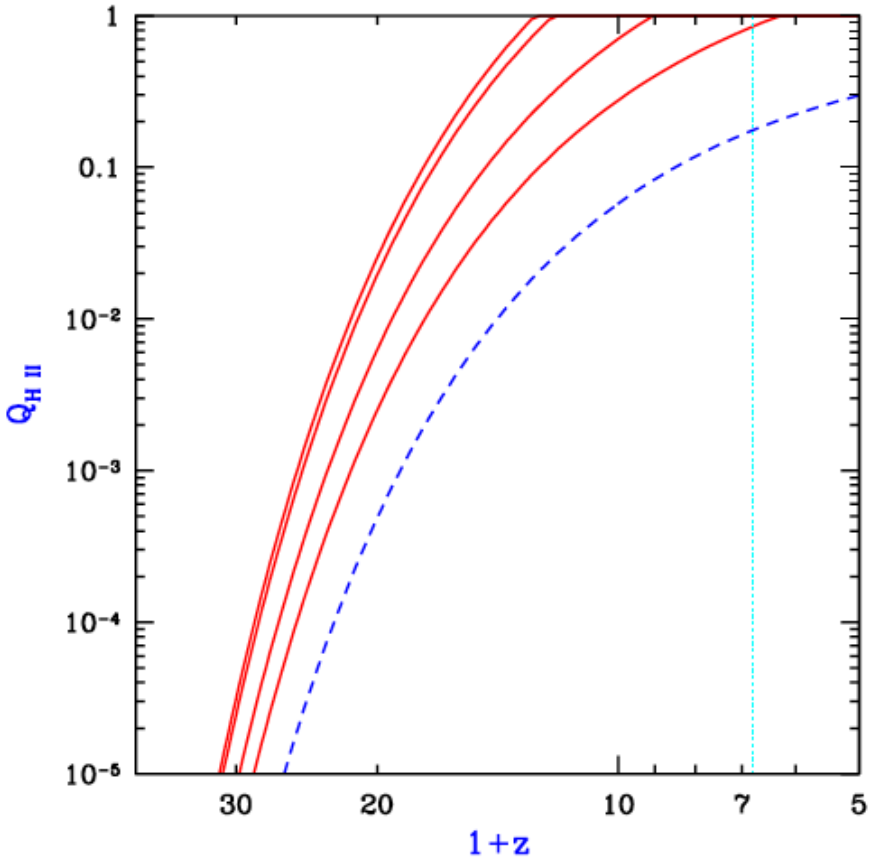

FIGURE 1.4: Simulation of the redshift evolution of the filling factor for different values of the clumping factor ($C = 0, 1, 10, 30$ from left to right). The dashed curve shows the collapse fraction F_{col}, i.e. the fraction of baryons that is collapsed in galaxies, and the vertical dotted line shows the $z = 5.8$ observational lower limit (Fan et al., 2001) on the reionization redshift. Image taken from Barkana & Loeb (2001).

values of the clumping factor $C =< n_H^2 > / < n_H >^2$, where n_H is the hydrogen number density. The figure clearly shows that the more the Universe is clumped, the longer is the time required for the reionization to be completed.

The three major observational methods to investigate the epoch of reionization are: (i) the observation of the emission spectra of quasars (through the Gunn-Peterson effect), (ii) the study of Cosmic Microwave Background anisotropy and polarization and (iii) the observation of the 21 cm line emission of neutral hydrogen.

There is still an open debate about the specific kind of sources, and their relative importance, that caused the reionization of the Universe. Anyway, five possible classes of sources have been identified: (i) first Pop III stars, (ii) galaxies, (iii) quasars, (iv) gamma ray bursts and (v) decaying/annihilating dark matter particles.
Pop III stars, due to their high internal and surface temperatures, were able to release a

large amount of ionizing photons. Currently, Pop III stars are thought to have exerted the leading contribution to the reionization process of the Universe. To constrain the contribution of the first galaxies to the reionization process it is necessary to model the ionizing photon emission rate as well as the escape fraction f_{esc}. Much work has been done on the theoretical side, while on the observational one, a major contribution will be provided by the forthcoming JWST telescope, which will be able to observe the infant Universe much farther than current observatories. Quasars are very efficient sources of ionizing photons and were already formed at high redshifts: the farthest quasar discovered to date is at $z \approx 7$ (Mortlock et al., 2011), well inside the reionization period. The emission spectrum of quasars is harder than that of stellar sources, meaning that the fraction of emitted ionizing photons is larger. In addition, also the escape fraction f_{esc} from the host galaxy is in general higher, meaning that a larger fraction of ionizing photons is able to escape into the inter-galactic medium. Gamma ray bursts are the most powerful electromagnetic emissions known in the Universe. They are flashes of gamma rays associated with extremely energetic explosions, whose origin is still debated nowadays. They produce a flux that is comparable to that of an entire quasar and therefore they outshine any other sources of radiation. Currently, the most distant gamma ray burst event observed is at $z \approx 8.2$ (Tanvir et al., 2009), again well inside the reionization process. To conclude, also the photons produced by the decaying dark matter particles could exert an additional, small contribution.

1.3 The Formation of the First Structures

The main problem of the field of structure formation may be summarized as follows. We know that the Universe began in a nearly uniform state, but we now observe galaxies, stars, planets, as well as voids: how did all of this come about from the very uniform initial conditions of the early Universe? Nowadays, large-scale isotropy is well established (for an extensive review see Wu et al. 1999) from the distribution of faint radio sources, optically selected galaxies, the X-ray background and most importantly the Cosmic Microwave Background at $z \sim 1100$. In the previous Sec. 1.2 we presented a general picture of the cosmic history. However, to understand the formation of gravitationally bound structures, it is necessary to follow and describe the evolution of the

small inhomogeneities that appeared in the primordial Universe, as early as in the inflationary period. For an extensive review on the basic equations of structure formation, the interested reader is again referenced to Barkana & Loeb (2001).

The fate of the primordial fluctuations is described by the gravitational instability scenario. The standard model of structure formation explains how small initial density fluctuations originated gravitationally bound halos: regions that were denser than the average value, first on small spatial scales and later on larger ones, collapsed due to their enhanced self-gravity. When the deviations from homogeneity are small, the dark matter may be treated as a pressure-less fluid and evolves by very simple equations, following the so-called linear regime. In regions that are significantly denser than the background, the full Newtonian theory of gravity must be included in the so-called non-linear regime. The equations derived in the linear regime apply both to dark and baryonic matter, because the densities are still too small to require all the complications of baryonic physics (radiation transfer, fluid dynamics etc.), while the ones derived for the non-linear regime are strictly applicable to dark matter.

As explained in Sec. 1.1, the cosmological principle states that the Universe is homogeneous and isotropic on large scales: all the gravitationally bound objects that we observe nowadays originated from the growth of unstable fluctuations in the density field $\rho(\mathbf{x})$ of the baryonic and non-baryonic matter. The dimensionless over-density $\delta(\mathbf{x})$ is defined as:

$$\delta(\mathbf{x}) \equiv \frac{\rho(\mathbf{x})}{\rho_0} - 1\,, \tag{1.9}$$

where ρ_0 denotes the average matter density over a volume V, sufficiently large such that the Universe can be considered as fulfilling the cosmological principle inside it.

Of course, we are not able to predict the exact value of $\delta(\mathbf{x})$ in the primordial Universe, so that we imagine $\delta(\mathbf{x})$ as a random variable and δ to be a continuous random field, usually assumed to be gaussian. The random values that δ takes at two nearby points $\mathbf{x}$ and $\mathbf{x} + d\mathbf{x}$ must be correlated. The degree to which $\delta(\mathbf{x})$ and $\delta(\mathbf{x} + d\mathbf{x})$ are correlated is expressed by the correlation function:

$$\zeta(\mathbf{x}) = < \delta(\mathbf{x})\delta(\mathbf{x} + d\mathbf{x}) >\,, \tag{1.10}$$

where the brackets indicate the expectation value.

It is possible to demonstrate that the Fourier transform of the correlation function, under specific periodic boundary conditions, is the power spectrum of the fluctuations:

$$\zeta(\mathbf{x}) = \frac{1}{V}\sum_{k} P(k)e^{i\mathbf{k}\cdot\mathbf{x}}\,. \tag{1.11}$$

Here, $P(k) \equiv < |\delta_k|^2 > /V$ is the power spectrum of the random field on the scale k. The power spectrum is extremely important in order to study the spatial scale distribution of fluctuations. From the inflationary theory, the power spectrum is predicted to be scale invariant, i.e. $P(k) \propto k^{n-1}$ with $n = 1$, while the amplitude of the fluctuations has to be determined experimentally.

1.3.1 Linear regime

At early times, $\delta(x) \ll 1$ everywhere and we can derive linear equations for the evolution of the over-density. We consider only the derivation for non-relativistic fluids, which are valid after the radiation-dominated period, for $z \lesssim 3000$: in this period, most of the structures formed.

Basically, the structure formation is a competition between: (i) the gravitation that facilitates the growth of over-densities and (ii) the cosmic expansion and the gas pressure that dampen them. We start by modeling the Universe as a fluid with an average mass density ρ. Consider a slightly over-dense region in $\mathbf{x}'$ with a density $\rho + d\rho$ at $t = t_0$: the matter is then attracted toward $\mathbf{x}'$ and, as a consequence, the density increases even more.

In order to model the growth of perturbations we need a set of equations that give the evolution of the density ρ of a fluid in a gravitational field with potential $\Phi(\mathbf{x})$. From classical fluid dynamics we know that, for a fluid with velocity $\mathbf{v}$, this set of equations holds:

$$\frac{\partial \rho}{\partial t} + \nabla_r \cdot (\rho \mathbf{v}) = 0 \quad \text{(continuity)} \tag{1.12}$$

$$\frac{\partial \mathbf{v}}{\partial t} + (\mathbf{v}\cdot\nabla)\mathbf{v} = -\frac{1}{\rho}\nabla_r p - \nabla_r \phi \quad \text{(Euler)} \tag{1.13}$$

$$\nabla_r^2 \phi = 4\pi G\rho \quad \text{(Poisson)} \tag{1.14}$$

It is possible to demonstrate that the comoving equivalents (i.e. written in a reference frame expanding with the Universe) of continuity and Euler's equations are, respectively:

$$\frac{\partial \rho}{\partial t} + 3H\rho\nabla_r \cdot (\rho \mathbf{v}) = 0\,, \tag{1.15}$$

$$\frac{\partial \mathbf{v}}{\partial t} + (\mathbf{v}\cdot\nabla)\mathbf{v} + 2H\mathbf{v} + \frac{\ddot{a}}{a}\mathbf{x} = -\frac{1}{a^2}\left(\frac{1}{\rho}\nabla_r p + \nabla_r \phi\right)\,. \tag{1.16}$$

If we neglect non-linear terms, we combine continuity and Euler's equations, we assume that the pressure $p = c_s^2 \rho_0 \delta_k$ is a function of density alone ($c_s^2 = dp/d\rho$ is the speed of sound and δ_k is the perturbation of the k-mode) and we consider the Fourier transform of the perturbation $\delta(x,t)$, we finally obtain the evolution equation of the perturbation for each k-mode:

$$\frac{d^2\delta_k}{dt^2} + 2\left(\frac{\dot{a}}{a}\right)\frac{d\delta_k}{dt} = \left(4\pi G\rho - \frac{k^2 c_s^2}{a^2}\right)\delta_k\,. \tag{1.17}$$

The growth of the perturbations due to gravitational collapse is counteracted by both the pressure and the expansion of the Universe.

We begin to examine this equation in the large-scale perturbations case, i.e. when k is small, so that the term $\sim k^2$ may be neglected. In the matter-dominated period, the solutions to Eq. 1.17 are the sum of a decaying and a growing power laws. After a transient period, the growing solution dominates:

$$\delta_k(t) \propto t^{2/3}\,. \tag{1.18}$$

In the current and future epoch of dark energy domination, the general solution for large scale perturbations is, instead:

$$\delta_k(t) \propto \exp\left(-2Ht\right). \tag{1.19}$$

To summarize, large scale density fluctuations grow as $t^{2/3}$ during the matter domination and freeze once the Universe becomes dominated by dark energy.

To examine Eq. 1.17 more deeply, we define the Jeans length as:

$$\lambda_j = \frac{2\pi a}{k_j} = c_s \sqrt{\frac{\pi}{G\rho}} \,. \tag{1.20}$$

At this critical scale length the competing pressure and gravitational forces are equivalent. We have two possible situations:

1. if $\lambda < \lambda_j$ we have $\omega^2 = k^2 c_s^2 - 4\pi G\rho = c_s^2(k^2 - k_j^2) > 0$: the solutions of Eq. 1.17 are $\delta_k = \delta_0 e^{i(kr \pm \omega t)}$. In this situation the pressure is able to prevent the collapse and the density perturbation propagates as waves with the speed of sound c_s: the perturbations do not grow.

2. if $\lambda > \lambda_j$ we have $\omega^2 = k^2 c_s^2 - 4\pi G\rho = c_s^2(k^2 - k_j^2) < 0$: the solution of Eq. 1.17 represents a non-propagating stationary wave with an amplitude that increases with time exponentially.

As in the theory of star formation then, the Jeans length provides the minimum scale length which is required for a non-relativistic fluid in the linear regime to collapse under its self-gravity.

1.3.2 Non-linear regime

The density in a standard galaxy halfway from its center is more than 10^5 times the critical density ρ_c: it is clear that galaxy formation involves highly non-linear density fluctuations. In order to have a complete picture of the structure formation process, we need to follow it into the non-linear regime, with analytic approximations or numerical simulations. We start with a very simplified model which, nonetheless, allows to introduce the principal concepts.

In a matter-dominated, flat Universe assume that at some time t_i there is a spherically symmetric density fluctuation such that its associate over-density is $\delta_i \ll 1$. The total mass inside the sphere of radius r_i is:

$$M = \frac{4}{3}\pi(1 + \delta_i)\rho_m(t_i) r_i^3 \,, \tag{1.21}$$

where ρ_m is the average density outside the sphere.

We now follow the evolution of the radius $r(t)$ of the material, assuming that the mass inside the sphere is constant. From Newton's law:

$$\frac{d^2r(t)}{dt^2} = -\frac{GM}{r^2(t)}\,. \tag{1.22}$$

Assuming that the velocity of the shell at radius $r(t)$ is below the escape speed, the solution to the previous equation may be written parametrically as:

$$r(t) = b(1-\cos\eta)\,, \tag{1.23}$$

$$t = \sqrt{\frac{b^3}{GM}}(\eta - \sin\eta)\,, \tag{1.24}$$

where $r_{max} = 2b$ is the turnaround radius at which the expansion stops and the collapse phase begins, which occurs at $\eta = \pi$.

The average over-density inside the radius $r(t)$ is then:

$$\delta(t) = \frac{\rho_s(t)}{\rho_m(t)} - 1 = \frac{9}{2}\frac{(\eta-\sin\eta)^2}{(1-\cos\eta)^3} - 1\,, \tag{1.25}$$

where ρ_s is the density of the shell, namely $\rho_s(t) = 3M/[4\pi r^3(t)]$. At the turnaround (TA) point the over-density is:

$$\delta_{TA} = \delta(\eta=\pi) \approx 4.55\,. \tag{1.26}$$

Similarly, it is possible to compute the turnaround radius and time:

$$r_{TA} = 2b \approx \left(\frac{243}{250}\right)^{1/3}\frac{(GMt_i^2)^{1/3}}{\delta_i}\,, \tag{1.27}$$

$$t_{TA} = \pi\sqrt{\frac{b^3}{GM}} \approx 1.095\frac{t_i}{\delta_i^{3/2}}\,. \tag{1.28}$$

The last equation states that the larger is the initial over-density δ_i, the sooner the collapse begins.

This is an over-simplified model, because the density fluctuations are neither spherically symmetric nor isolated and the collapsing material undergoes relaxation and phase mixing and eventually settles into an equilibrium configuration, called a halo. This collapse

and relaxation process is named virialization because at the end the halo satisfies the virial theorem.

A more sophisticated and accurate modeling of the non-linear regime (see e.g. Barkana & Loeb 2001) leads to the following analytic expressions for the virial radius, the circular velocity and the virial temperature of the halo of mass M that collapses at redshift z:

$$r_{vir} = 0.784 \left(\frac{M}{10^8 h^{-1} M_\odot}\right)^{1/3} \left(\frac{\Omega_m \Delta_c}{18\pi^2 \Omega_m(z)}\right)^{-1/3} \left(\frac{1+z}{10}\right)^{-1} h^{-1}\mathrm{kpc}\,, \tag{1.29}$$

$$v_h = 23.4 \left(\frac{M}{10^8 h^{-1} M_\odot}\right)^{1/3} \left(\frac{\Omega_m \Delta_c}{18\pi^2 \Omega_m(z)}\right)^{1/6} \left(\frac{1+z}{10}\right)^{1/2} \mathrm{km\,s^{-1}}\,, \tag{1.30}$$

$$T_{vir} = 2 \times 10^4 \left(\frac{\mu}{0.6}\right) \left(\frac{M}{10^8 h^{-1} M_\odot}\right)^{2/3} \left(\frac{\Omega_m \Delta_c}{18\pi^2 \Omega_m(z)}\right)^{1/3} \left(\frac{1+z}{10}\right)^{-1} \mathrm{K}\,, \tag{1.31}$$

where m_p is the proton mass, μ is the mean molecular weight, and Δ_c is the final overdensity relative to the critical density at the collapse redshift. This last term, for a closed Universe with $\Omega_m + \Omega_\Lambda = 1$, is given by the fitting formula (Bryan & Norman, 1998):

$$\Delta_c = 18\pi^2 + 82[\Omega_m(z) - 1] - 39[\Omega_m(z) - 1]^2 \tag{1.32}$$

This method provides excellent predictions for the main physical quantities describing the halos. Other than characterizing the properties of individual haloes, a crucial prediction of the structure formation theory is the halo abundance i.e. the number density of haloes as a function of mass at any redshift. To do that, it is necessary to describe the density field and its fluctuations on a given scale. We introduce the concept of window function $W_R(r)$. This function, normalized such that $\int dr^3 W(r) = 1$ allows us to follow the growth of perturbations on any spatial scale R. We then obtain the smoothed density perturbation field $\int d\delta(x) W(r)$ on the scale R, denoted with δ_r or δ_m where $M = (4/3)\pi\rho R^3$. The variance of $< \delta_m >$ is computed to be:

$$\sigma^2(M) = \sigma^2(R) = \int_0^\infty \frac{dk}{2\pi^2} k^2 P(k) |\tilde{W}_R(k)|^2\,, \tag{1.33}$$

where $\tilde{W}_R(k)$ is the Fourier transform of the real-space window function $W_R(r)$. The variance σ_M is a key parameter in order to compute the abundance of dark matter halos of a given mass.

There are two possibilities to evaluate this last quantity: (i) numerical computations that solve the equations of gravitational collapse and (ii) analytic techniques that approximate these results with simple one-dimensional functions. The most commonly adopted analytic method was developed by Press & Schechter (1974). The abundance of halos at redshift z is determined from the linear density field by applying a model of spherical collapse to associate peaks in the field with virialized objects in a full non-linear treatment. This method is greatly successful in describing the formation of structures and in reproducing the numerical results. The method provides the comoving number density of halos, dn, with mass between M and $M + dM$ as:

$$M\frac{dn}{dM} = -\left(\frac{2}{\pi}\right)^{1/2}\frac{dln(\sigma)}{dln(M)}\frac{\rho_0}{lnM}\nu_c e^{-\nu_c^2/2}\,, \tag{1.34}$$

where ρ_0 is the present mean mass density, σ is the standard deviation of the density contrast smoothed through a certain window function $W(r)$ and $\nu_c = \delta_{crit}(z)/\sigma(M)$ is the number of standard deviations which the critical collapse over-density $\delta_{crit}(z)$ represents on the mass scale M.

Chapter 2

Black Holes in the Early Universe

This chapter starts with a general description of astrophysical black holes and with a brief introduction on the main equations describing the space-time around them. Later on, we present the problem of the existence of SMBHs as early as $z \sim 7$, i.e. less than a billion years after the Big Bang. Then, we describe the processes that may have led to the formation of the first black holes in the Universe, mainly focusing on the differences with the formation process that occurs in the local Universe. Understanding this primordial formation pathway could represent an important step forward in the solution of the SMBHs problem. In particular, we focus on the DCBH scenario.

2.1 Introduction to Black Holes

A black hole is the final product of the complete gravitational collapse of a material object. The compactness (i.e. the ratio between its mass $M_\bullet$ and its radius r) of a black hole is so extreme that its escape velocity:

$$v_{esc} = \sqrt{\frac{2GM_\bullet}{r}}\,, \tag{2.1}$$

is larger than the speed of light c: even a photon cannot escape from the horizon of a black hole.

A black hole is fully characterized by three parameters only: (i) its mass, (ii) its spin and (iii) its charge. Astrophysical black holes are neutral so that, practically, they can be described by the first two parameters only.

Ironically enough, a black hole is characterized by at least two contradictions. Firstly, black holes are very simple solutions of Einstein's equations of General Relativity, but they are also the most diverse from their Newtonian analogues. Secondly, black holes do not emit photons from their horizons, but the environments around them are the most luminous of the Universe, due the huge energy irradiated by the infalling material.

The origin of the radiated energy is the release of gravitational binding energy as the gas falls into the deep gravitational potential well of the black hole. More than $\sim 10\%$ of the accreting mass can be converted into energy: this is more than an order of magnitude larger the maximum efficiency of nuclear fusion: the gravitational engine is far more efficient than the nuclear fusion. The total luminosity L of the black hole is usually expressed in the following way:

$$L = \epsilon \dot{M} c^2 \,, \tag{2.2}$$

where ϵ is the efficiency (generally $\epsilon \sim 0.1$, with an important dependence on the black hole spin, see Equation 2.8) and $\dot{M}$ is the mass accretion rate. The black hole accretes the non-radiated component as:

$$\dot{M}_\bullet = (1-\epsilon)\dot{M} \,. \tag{2.3}$$

Astrophysical black holes are usually classified into three categories, based on their mass: (i) stellar mass BHs, (ii) Intermediate Mass BHs (IMBHs) and (ii) Super-Massive BHs (SMBHs). While this categorization is not strictly defined, the usual mass division is reported in Table 2.1.

	Mass Range
Stellar Mass BHs	$2\,M_\odot \lesssim \mathrm{M}_\bullet \lesssim 10^2\,M_\odot$
Intermediate Mass BHs	$10^2 M_\odot \lesssim \mathrm{M}_\bullet \lesssim 10^6 M_\odot$
Super-Massive BHs	$10^6 M_\odot \lesssim \mathrm{M}_\bullet \lesssim 10^{10} M_\odot$

TABLE 2.1: Generally accepted categories of black holes, classified according to their mass.

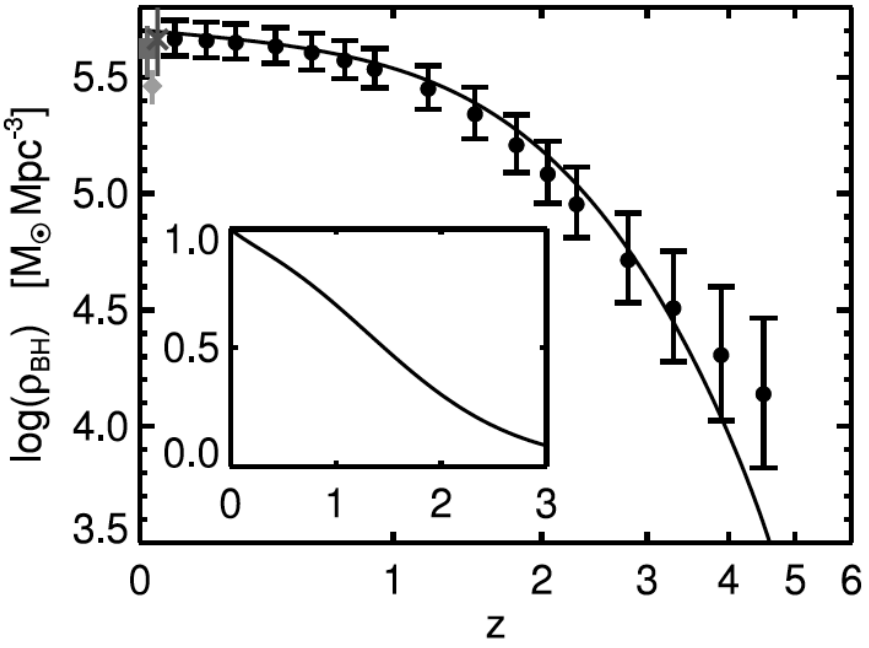

FIGURE 2.1: The comoving BH mass density of quasars from data and the best-fit luminosity function. The inset shows the fraction of the mass density relative to today's value. The presence of AGNs has been observed up to very high redshifts ($z \sim 7$). Image taken from Hopkins et al. (2007).

Stellar mass BHs are the direct end-product of the final phases of stellar evolution for massive stars, which usually terminate their life with a supernova explosion, ejecting most of the original stellar material. If the remnant is more massive than the so-called Oppenheimer–Volkoff limit ($\sim 2\,M_\odot$, see e.g. Bombaci 1996), the final evolution of the core is the collapse into a black hole. This is the standard (and also the better understood) way to build up a black hole. The recent detection of gravitational waves (Abbott et al., 2016b) proved the existence of stellar-mass black hole binaries, with a single component mass of order $\sim 30\,M_\odot$.

SMBHs are found at the center of almost every galaxy. Their activity may be minimal (like in the Milky Way case), or they can be observed swallowing up huge amounts of gas, like in the AGNs. These objects are galaxies hosting at their center an accreting SMBHs that emits huge amounts of radiation. It is actually studying these accreting SMBHs that most of the observational evidence on black holes has been currently built up. AGN activity is observed in a small fraction of galaxies at practically any cosmic epoch (Hopkins et al., 2007), see Fig. 2.1.

There is a clear and direct evidence for the existence of SMBHs also beyond the AGN population. At the center of our own Galaxy, stars are observed to orbit around the

Galactic center at velocities up to $10^5\,\mathrm{km\,s^{-1}}$, owing to the strong gravitational acceleration near the central black hole, with a mass $\sim 4 \times 10^6\,\mathrm{M_\odot}$ (Schödel et al., 2002).

Indeed, searches for black holes in local galaxies have shown that most of them harbor a SMBHs at its center (Antonucci, 1993). This suggests that AGN are rare only because their activity is short-lived ($50 - 100\,\mathrm{Myr}$): SMBHs at the center of galaxies show AGN activity only when they are fed with a large amount of material. When their environment is finally devoid of gas, the AGN activity is ceased. The gas inside the galaxy may be depleted by accretion onto the black hole or even expelled from the galaxy by the radiative feedback of the SMBH, through powerful outflows. This may be better understood with the fact that the binding energy per unit mass in a typical galaxy corresponds roughly to a fraction 10^{-6} of the binding energy per unit mass near a black hole: a small amount of gas that releases its energy near the central compact object may have a strong impact on the surrounding environment.

2.1.1 The metric of the space-time around a black hole

We now move to a mathematical description of these objects, which necessarily requires the use of General Relativity. A spherically symmetric gravitational field, in the vacuum, is described by the so-called Schwarzschild metric:

$$ds^2 = -\left(1 - \frac{R_S}{r}\right) c^2 dt^2 + \left(1 - \frac{R_S}{r}\right)^{-1} dr^2 + r^2 d\Omega\,, \tag{2.4}$$

with the usual notation and with $R_S = 2\frac{GM}{c^2}$ being the Schwarzschild radius, which is related only to the mass $M_\bullet$ of the object:

$$R_S = \sqrt{2\frac{GM_\bullet}{c^2}}\,. \tag{2.5}$$

The horizon of the black hole (R_S, in this case) is a spherical boundary from which nothing can escape. It is also interesting to note that for small masses $R_S \to 0$ and the Schwarzschild metric reduces to the Minkowski one (see Chapter 1, Equation 1.3).

The metric of the space-time for a spinning black hole was derived in 1963 by Kerr and it represents the most general solution of Einstein's equations for objects of this kind. Calling J the angular momentum of the spinning black hole ($j = J/(M_\bullet c)$ is its

value normalized to the black hole mass), the dimensionless ratio $a = J/(GM_\bullet/c^2)$ is named the spin parameter and it ranges between 0 and 1: $a = 0$ is a Schwarzschild (non-spinning) black hole, while $a = 1$ is a maximally-rotating (Thorne, 1974) black hole (see e.g. Volonteri et al. 2013 and references therein).

The orbits followed by photons or massive particles strongly depend on the black hole spin. This fact has deep implications for the radiative efficiency ϵ (see the following Equation 2.8). The circular orbit followed by a photon around a black hole of mass $M_\bullet$ with a spin parameter a is given by (see e.g. Teo 2003):

$$r_{ph} = R_S \left[1 + \cos\left(\frac{2}{3} \cos^{-1}(\pm a) \right) \right] , \tag{2.6}$$

where the upper sign refers to an orbit which rotates in a direction opposite to that of the black hole (retrograde orbit), while the lower sign is for prograde orbits. For a non-spinning black hole, $r_{ph} = (3/2)R_S$.

For massive particles, the radius of the Innermost Stable Circular Orbit (ISCO) defines the inner edge of any possible disk of particles that may form around the black hole. At smaller radii, massive particles plunge into the black hole on a dynamical time scale. The smaller the ISCO, the larger is the fraction of their gravitational energy that massive particles can radiate away: as a consequence, the higher is the radiative efficiency ϵ. The radius of the ISCO is given by (Bardeen et al., 1972):

$$r_{ISCO} = \frac{1}{2} R_S \left[3 + Z_2 \pm [(3 - Z_1)(3 + Z_1 + 2Z_2)]^{1/2} \right] , \tag{2.7}$$

where Z_1 and Z_2 are functions of the spin parameter a only.

The radiative efficiency is given by (Loeb & Furlanetto, 2013):

$$\epsilon = 1 - \frac{r^2 - R_S r \mp j\sqrt{0.5 R_S r}}{r(r^2 - \frac{3}{2} R_S r \mp 2j\sqrt{0.5 R_S r})^{1/2}} . \tag{2.8}$$

This function ranges from $\epsilon \sim 5.72\%$ for a Schwarzschild ($a = 0$) black hole to $\epsilon \sim 42.3\%$ for a maximally rotating ($a = 1$) black hole with the gas accreting on a prograde orbit.

2.1.2 Accretion regimes

The simplest accretion regime onto a black hole of mass $M_\bullet$ is the so-called Bondi accretion (Bondi, 1952). If a static black hole is embedded in an hydrogen plasma of uniform density ρ_0 and temperature T_0, the thermal protons in the gas move approximately at the sound speed $c_s = \sqrt{k_b T_0/m_p}$, where k_b is the Boltzmann constant and m_p is the proton mass. Hence, the sphere of gravitational influence of the central object is given by the Bondi radius $r_B = GM_\bullet/c_s^2$. Under these conditions, it is possible to demonstrate that the (stationary) accretion rate is given by:

$$\dot{M}_B = \pi r_B^2 \rho_0 c_s \approx 15 \left(\frac{M_\bullet}{10^8\,\mathrm{M}_\odot}\right)^2 \left(\frac{n_H}{1\,\mathrm{cm}^{-3}}\right) \left(\frac{T_0}{10^4\,\mathrm{K}}\right)^{-3/2} \mathrm{M}_\odot\,\mathrm{yr}^{-1}\,, \tag{2.9}$$

The maximum value of the accretion rate onto a black hole of mass $M_\bullet$, under the assumption of spherical accretion, is given by the so-called Eddington rate (Frank et al., 2002). The luminosity emitted in this case is simply derived from balancing the inward force of gravity on each proton by the outward radiative force on its companion electron at a distance r from the center:

$$\frac{GM_\bullet m_p}{r^2} = \frac{L_E}{4\pi r^2 c}\sigma_T\,, \tag{2.10}$$

where σ_T is the Thomson cross section for electron scattering. Interestingly, the limiting luminosity L_E does not depend on the radius r. The final expression is the following:

$$L_E = \frac{4\pi G M_\bullet m_p c}{\sigma_T} \approx 3.2 \times 10^4 \left(\frac{M_\bullet}{\mathrm{M}_\odot}\right) L_\odot\,. \tag{2.11}$$

From the Eddington luminosity L_E it is possible to derive the Eddington accretion rate $\dot{M}_E$:

$$\dot{M}_E = \frac{L_E}{\epsilon c^2}\,. \tag{2.12}$$

2.1.3 Accretion disks

Black holes are usually characterized by accretion disks. This is due to the fact that the accretion inflow normally has a non-zero angular momentum with respect to the central body: if this is the case, the gas will reach a centrifugal barrier from which it can

accrete further inward only if its angular momentum is transported away. The existence of this barrier is a consequence of the steeper radial scaling of the centrifugal acceleration ($\sim r^{-3}$) with respect to the gravitational acceleration ($\sim r^{-2}$): for decreasing radii, the centrifugal acceleration increases faster. Near the centrifugal barrier an accretion disk will form around the black hole, on the plane perpendicular to its rotation axis. Then, the accretion time is determined by the time needed to transport away the angular momentum and it can be significantly larger than the free-fall time. Once the accretion disk is formed, there are two significant regimes for the accretion: (i) the thin disk regime and (ii) the thick disk regime.

In the thin disk regime the cooling time of the gas is shorter than the viscous time and it is characterized by high gas inflow rates ($\dot{m} \equiv \dot{M}/\dot{M}_E > 10^{-2}$). This accretion regime is usually the one active in AGNs. In this regime, the angular momentum is transported away by both the gas viscosity and by magneto-rotational instability effects (Chandrasekhar, 1960). The radial temperature distribution of the disk in the thin regime is interesting in order to estimate the electromagnetic emission radiated from these sources. It is possible to show that the temperature profile is given by (Loeb & Furlanetto, 2013):

$$T_d \approx 10^5 \left(\frac{M_\bullet}{10^8\,\mathrm{M}_\odot}\right)^{-1/4} \left(\frac{\dot{m}}{0.1}\right)^{1/4} \left(\frac{r}{10R_S}\right)^{-3/4} \left[1 - \left(\frac{r}{r_{ISCO}}\right)^{1/2}\right] \mathrm{K}\,. \tag{2.13}$$

Note than the disk surface temperature increases with decreasing mass and reaches the X-rays regime in the case of stellar mass black holes. The accretion disks around smaller black holes are generally hotter. For SMBHs, the accretion disk can be divided radially into three distinct regions: (i) the inner region where radiation pressure and electron scattering opacity dominate, (ii) the middle region where gas pressure and electron scattering opacity dominate and (iii) the outer region where gas pressure and free-free opacity dominate.

When the accretion flow is considerably smaller than the Eddington value ($\dot{m} \equiv \dot{M}/\dot{M}_E < 10^{-2}$) the gas inflow switches to the so-called advection-dominated accretion flow (ADAF), a radiatively inefficient accretion regime which is characterized by a thick accretion disk. Their analytic description is much more complex than in the thin regime. Since the gas reservoirs in the local Universe are scarce (due to the lack of major mergers events and

due to the star formation which depletes them), most of the local SMBHs are characterized by a very low accretion rate and are then described by the thick disk model. This mode of accretion can persist over a period of time which is orders of magnitude longer than the AGN mode ($\sim 100\,\mathrm{Myr}$).

Widespread theoretical and observational indications suggest that accretion at rates larger than the Eddington rate ($\dot{M} > \dot{M}_E$, i.e. super-Eddington accretion) may occur. This apparent violation may be explained by: (i) non spherical accretion flows, or (ii) efficient photon trapping inside an high-density accretion disk. More details are provided in Chapter 3 and in Chapter 4.

2.2 The First Black Holes in the Universe

In this section we present the problem of the early ($z \sim 7$) SMBHs, explaining why they challenge the standard black hole growth theory. Then, we present the general theory for the formation of the first black holes, highlighting the differences with respect to the local formation channel.

2.2.1 The problem of the early super-massive black holes

Currently, the highest redshift AGN known is at $z = 7.085$, only $0.77\,\mathrm{Gyr}$ after the Big Bang (Mortlock et al., 2011). This object has a bolometric luminosity of $6.3 \times 10^{13}\,\mathrm{L}_\odot$ with an estimated black hole mass of $2 \times 10^9\,\mathrm{M}_\odot$. Even more massive objects, on the mass scale $\sim 10^{10}\,\mathrm{M}_\odot$ (Wu et al., 2015), have been discovered at comparable redshifts (see Fig. 2.2). It is interesting to note that the mass of these objects is close to the theoretical maximum black hole mass predicted by several papers (e.g. Natarajan & Treister 2009, King 2016, Inayoshi & Haiman 2016).

Given that structures in the ΛCDM cosmological model are formed hierarchically, in principle it could be possible to explain a handful of extreme objects, like the most massive ones in Fig. 2.2, as outliers characterized by some peculiar growth histories. However, the discovery of populations of massive quasars at progressively higher redshifts suggests that a more general physical explanation is required.

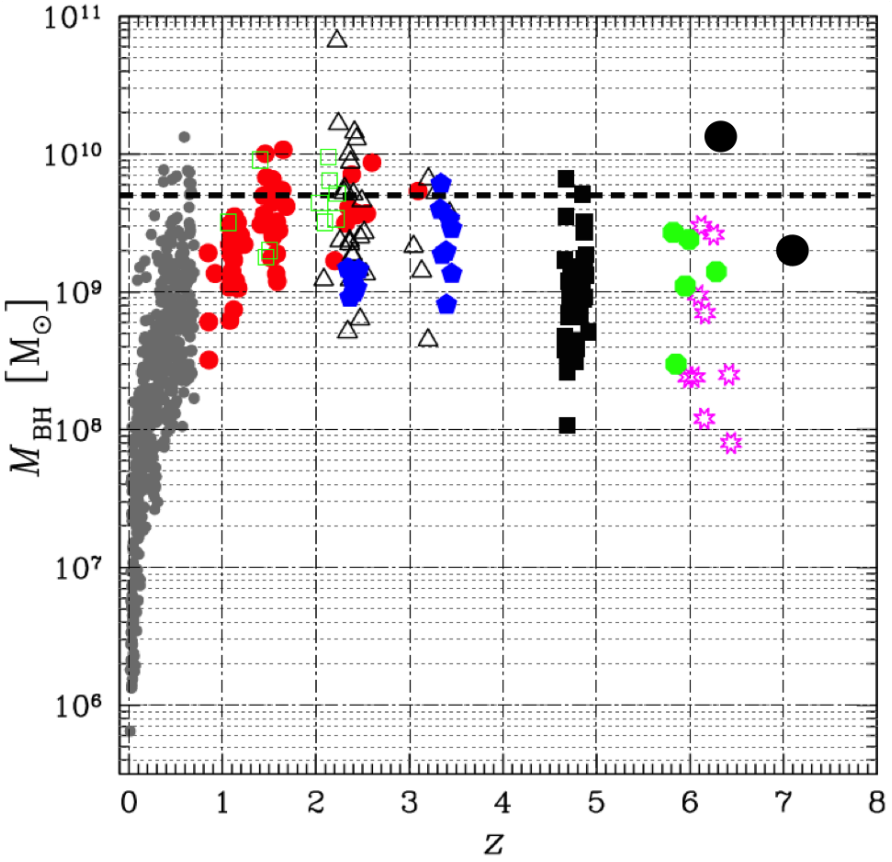

FIGURE 2.2: This chart, taken from Marziani & Sulentic (2012), reports the massive black holes discovered so far, shown as a function of their redshift and estimated mass. A small group of these objects is at very high redshifts ($z \gtrsim 6$), and they have very large masses, in excess of about $10^8\,M_\odot$. This group has been updated with both the most distant black hole (Mortlock et al., 2011) and the most massive high-z object discovered (Wu et al., 2015), shown with black circles.

These observational evidences imply an important, and still unanswered, question: how is it possible to build up such huge objects in such a short time? The standard formation pathway for a black hole, the collapse of massive stars, produces a stellar-mass black hole, with $M_\bullet \lesssim 100\,M_\odot$. From this seed, the black hole growth can proceed through two different channels: (i) accrete mass from the surrounding environment and (ii) merge with other black holes. Both channels are favored by galaxy mergers. In fact, these events deliver large amounts of low angular momentum gas to the deepest point of the gravitational potential well of both the interacting galaxies, where the most massive black hole usually reside. Moreover, galactic mergers may favor the merger of the black holes that they host.

We already derived in Section 2.1 that there is a limiting accretion rate, the Eddington rate $\dot{M}_E$, at which a black hole is able to accrete. At least under the assumption

of spherical symmetry and radiatively efficient accretion disks, larger accretion rates are not allowed because the radiation pressure would overcome the gravitational force. Assuming that a black hole constantly accretes at the Eddington rate $\dot{M}_E$, the equation that describes the growth of the black hole mass is the following:

$$\dot{M}_{BH} = \frac{M_{BH}}{t_E}\,, \tag{2.14}$$

where t_E is the Eddington time-scale given by:

$$t_E = 4 \times 10^7 \left[\frac{\epsilon}{0.1(1-\epsilon)}\right] \left(\frac{L_E}{L}\right) \text{ yr}\,. \tag{2.15}$$

Assuming that the mass inflow is constantly provided at the Eddington rate, the black hole mass grows exponentially, i.e. $M_{BH}(t) \propto e^{t/t_E}$, with t_E being the e-folding time. The growth time suggested by these equations is significantly shorter than the age of the Universe when the first SMBHs are observed, i.e. $\sim 10^9$ yr.

Unfortunately, several reasons make it very unlikely that a stellar mass seed is actually able to accrete at the Eddington rate for ~ 1 Gyr. One limitation is provided by the supply of low-angular momentum gas, its absence inevitably interrupting the black hole growth. An evident example is the SMBH at the center of our own Galaxy, which is in a dormant state, accreting only intermittently very small amounts of gas, from erratic stars falling too close to it. Another relevant process that may interrupt the growth of the black hole is gravitational recoil. Galaxy mergers were very common in the early Universe and these events provided most of the inflowing mass to the early black holes. When the central black holes of two interacting galaxies merge, the non-isotropic emission of gravitational waves, predicted by the theory of General Relativity, may provide a strong kick to the merged compact object. The amplitude of the gravitational recoil depends sensitively on spin orientations of the black holes prior to merger and on their masses: it can provide recoiling velocities of hundreds of kilometers per second, a velocity which is usually much higher than the typical escape velocity of a high-z dwarf galaxy (Campanelli et al., 2007). Once the merged object is expelled from the galaxy, the mass inflow is abruptly quenched.

These difficulties in accreting continuously at the Eddington rate suggest that there should exist other pathways to produce SMBHs in a time-scale of ~ 1 Gyr. In the

following we provide some possible pathways to achieve this goal.

2.2.2 Formation of the first black holes

We showed that it is very challenging to reach black hole masses of $\sim 10^9\,\mathrm{M}_\odot$ at $z \sim 7$ starting from stellar mass seeds, with an accretion rate capped at the Eddington value. Two different scenarios have been proposed to overcome this problem, which are briefly summarized in the following.

- **Start big, grow normal**: in this scenario, a large black hole seed is formed, with a mass up to $10^{4-5}\,\mathrm{M}_\odot$. Once formed, it grows up at or close to the Eddington rate, possibly reaching the $10^9\,\mathrm{M}_\odot$ stage at $z \sim 7$. The necessity to form a large mass seed is, of course, to give a jump start to the accretion process: the Eddington rate of a $10^5\,\mathrm{M}_\odot$ object is 10^4 times larger than the Eddington rate of a $10\,\mathrm{M}_\odot$ object. For instance, Loeb & Furlanetto (2013) showed that in order to assemble at $z = 7.085$ a SMBH with mass $M \sim 2 \times 10^9\,\mathrm{M}_\odot$ it is necessary to start from black hole seeds with masses $\gg 400\,\mathrm{M}_\odot$.

- **Start small, grow fast**: in this scenario, a small black hole seed is formed, with a mass up to $\sim 100\,\mathrm{M}_\odot$. Forming these small black hole seeds is straightforward from Pop III stars, which were formed in the early Universe, with low or zero metallic content. Starting from such small black holes, it is challenging to form a SMBH at $z \sim 7$ by accreting at the Eddington rate. It is then necessary to find a way to accrete faster than Eddington, or super-Eddington.

When it comes to the first scenario, there is a whole plethora of different models to explain the formation of these massive black hole seeds, that then grows at or below the Eddington rate. The pure DCBH scenario, the one we mostly focused our attention on in this Thesis, will be described below, in Sec. 2.3. For instance, under specific conditions (low inflow rates at the center of the collapsing halo) a super-massive star is formed (Ferrara et al., 2014). This star evolves rapidly and collapses into a massive black hole seed. Another possibility is that a dense stellar cluster merges, by collisions among the members at the center of the halo, leading to a massive black hole seed again (Devecchi & Volonteri 2009, Davies et al. 2011). Moreover, a pre-galactic disk may

collapse, in mildly metal enriched environments, leading to the formation of a massive seed (Lodato & Natarajan 2006, Begelman et al. 2006, Lodato & Pringle 2007). In all these models, the predicted masses of the black hole seed are different, but the idea is the same: forming a massive black hole, to give a jump start to the growth process, which may take place at or even below the Eddington rate.

When it comes to the second scenario, one possibility is that the accretion disks of these objects are radiatively inefficient, making the trapping of photons dynamically important (Abramowicz et al. 1988, Paczynski & Abramowicz 1982, Mineshige et al. 2000, Sadowski 2009, 2011, McKinney et al. 2014 for the slim disk model). In fact, if a large fraction of photons is trapped inside the accretion disk, the effective radiation pressure acting on the surrounding gas is decreased (see e.g. Begelman 1978, Ohsuga et al. 2002) and the luminosity is only mildly (e.g. logarithmically) dependent on the accretion rate. This may lead to accretion rates that are several times larger than the Eddington rate, without overshooting the Eddington luminosity. Theoretical studies and simulations have confirmed the possibility of reaching accretion rates several hundred times the Eddington rate. Since the black hole mass grows exponentially with the accretion rate, the black hole growth is significantly faster, and it may be possible to reach the SMBH stage at $z \sim 7$ even starting from low-mass seeds. Again, several theoretical models have been proposed to allow super-Eddington rates. Alternatives of the slim disk solution exist, e.g the ZEro-BeRnoulli Accretion (ZEBRA, Coughlin & Begelman, 2014) and the ADiabatic Inflow-Outflow Solutions (ADIOS, Blandford & Begelman, 1999, Begelman, 2012) models, which allow for a fraction of the inflowing mass to be lost during the accretion process.

Before analyzing in detail the DCBH model in the next Sec. 2.3, we briefly investigate the reason why the early Universe may have hosted high-mass black hole seeds. The reasons are related to the environmental conditions that existed in the early Universe. These conditions are essentially based on the interconnected evolution of the first stars and the first black holes. Firstly, the early Universe was almost completely metal-free, due to the fact that the first stars did not already pollute it with metals. Secondly, the first stars were much more massive (and much hotter, see Chapter 1) than local stars: their emission of ionizing photons was copious.

In order to collapse and form gravitationally bound objects, the primordial halos needed

to cool. The only coolants available during this early phase of the cosmic evolution were atomic and molecular hydrogen. In particular, molecular hydrogen is a key species for gas cooling and fragmentation in the primordial Universe (see Fig. 1.3). Then, the suppression of H_2 molecules by Lyman-Werner (LW, $11.2\,\mathrm{eV} < E_\gamma < 13.6\,\mathrm{eV}$) photons strongly quenches the gas cooling process and, as a consequence, the fragmentation. When large ($T_{\rm vir} \gtrsim 10^4\,\mathrm{K}$), metal-free atomic cooling halos are illuminated by a sufficiently strong UV flux, the conditions for the creation of high-mass compact objects may be reached (Loeb & Rasio 1994, Begelman et al. 2006, Lodato & Natarajan 2006, Johnson et al. 2012, Latif et al. 2013a).

Numerical simulations have shown that stars with mass up to $\sim 10^6\,\mathrm{M}_\odot$ could have formed at the center of early dwarf galaxies that were only able to cool down their gas via atomic hydrogen and had $T_{vir} \sim 10^4\,\mathrm{K}$ and no H_2 molecules due to the UV suppression (Bromm & Loeb, 2003). Such stellar systems had a total mass several orders of magnitude larger than local stars and their formation was possible only under these strict conditions, available during a short period of the cosmic history. In these cases, the gas lacks the ability to cool down well below its virial temperature and the entire halo is only allowed to fragment into two of three major clumps, which inevitably form massive black holes, see Fig. 2.3.

2.3 Direct Collapse Black Holes

The DCBH scenario, firstly suggested by Bromm & Loeb (2003), provides one of the possibilities to form high-mass black hole seeds at high redshifts. In recent years, this scenario is maybe the best-known one, likely due to the following reasons: (i) it is theoretically elegant and well tailored to the physical conditions of the early Universe, (ii) the (predicted) observational signatures of these objects are easier to check in actual observations, e.g. the absence of metal lines, and (iii) the predicted masses are sufficiently large to allow for their direct observation with current or upcoming surveys.

As already stated in this section, a necessary condition to allow for the collapse of high-mass halos in the primordial Universe is the existence of a strong LW flux $J_\nu > J_\nu^\bullet$, which destroys the H_2 molecules of atomic cooling, metal-free halos, quenching in this way the cooling process and their fragmentation in smaller and smaller clumps.

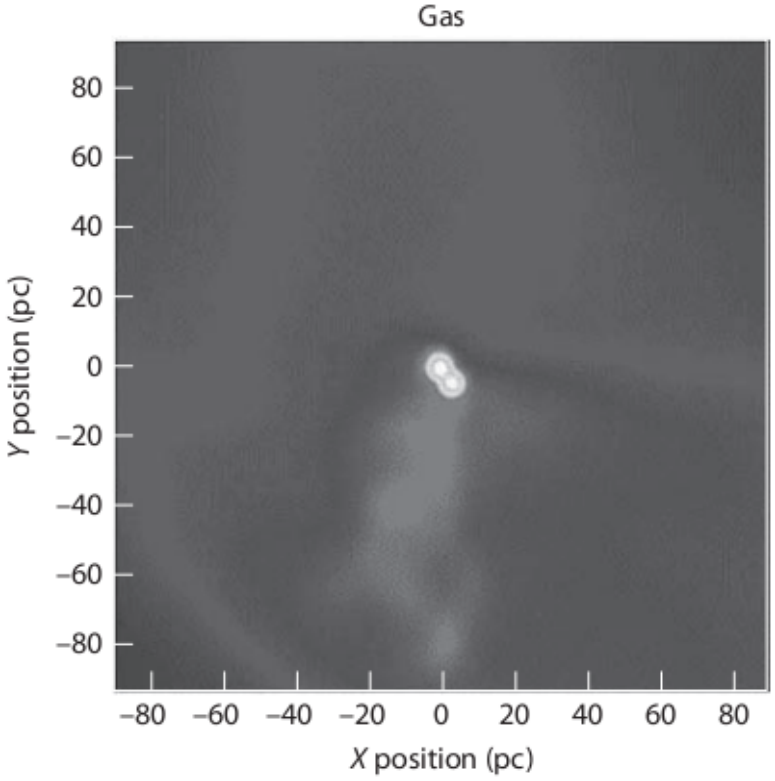

FIGURE 2.3: Numerical simulation of the collapse of an early dwarf galaxy with no molecular hydrogen and a virial temperature just above the cooling threshold of atomic hydrogen. The snapshot shows the density distribution of gas $\sim 500\,\mathrm{Myr}$ after the Big Bang and indicates the formation of two massive objects near the center of the galaxy, with masses $M_1 \approx 2.2 \times 10^6\,\mathrm{M}_\odot$ and $M_2 \approx 3.1 \times 10^6\,\mathrm{M}_\odot$. Image taken from Bromm & Loeb (2003).

The precise value of the threshold $J_\nu^\bullet$ depends on a multitude of factors, namely the radiative transfer, the chemistry and the spectral shape of the sources, which are only approximately known. However there is a broad agreement that $30 < J_\nu^\bullet < 1000$ in units of $10^{-21}\,\mathrm{erg\,s^{-1}\,cm^{-2}\,Hz^{-1}\,sr^{-1}}$ (see e.g. Agarwal et al. 2012, Latif et al. 2013a, Ferrara et al. 2014).

A collapsing metal-free, atomic cooling halo, embedded in a LW flux $J_\nu > J_\nu^\bullet$, may follow two different pathways to form an IMBH (i.e. a black hole with mass $\lesssim 10^6\,\mathrm{M}_\odot$) at high redshift (see Ferrara et al. 2014 and references therein).

- Continuously accreting mass until it reaches the limit of General Relativity instability and directly collapses into a black hole: the high-mass black hole seed is formed via the *Direct Collapse Black Hole* scenario.
- Passing through a *phase of Super-Massive Star* (SMS) that in a very short time ($\lesssim 1\,\mathrm{Myr}$) terminates its nuclear fuel and collapses into a black hole.

The formation process of the black hole seed starts with the growth of a proto-SMS inside metal-free atomic cooling halos embedded in a strong LW radiation field. The collapse is isothermal and coherent, with accretion rates comparable or larger than the thermal accretion rate:

$$\dot{M} = \frac{\pi^2}{8G} c_s^2 \approx 0.162 \left(\frac{T}{10^4\,\mathrm{K}} \right)^{3/2} \mathrm{M}_\odot\,\mathrm{yr}^{-1}\,. \tag{2.16}$$

At these rates, it only takes $\sim 10^5\,\mathrm{yr}$ to build a $\sim 10^4\,\mathrm{M}_\odot$ SMS.

The growth of the proto-SMS, fed by accretion rates typically larger than $\sim 0.1\,\mathrm{M}_\odot\,\mathrm{yr}^{-1}$, can be blocked by at least two type of events: (i) accretion of polluted gas or (ii) major mergers. The accretion of polluted gas may be brought by minor mergers or smooth accretion from the IGM. Metals would enhance the cooling rate, driving thermal instabilities which finally lead to the fragmentation of the gas into clumps: they cannot be accreted as their angular momentum is hard to dissipate. In addition, major mergers may generate vigorous turbulence, again disrupting the smooth accretion flow onto the central proto-SMS star. These mergers were very common in the early Universe, when these objects presumably formed.

If these events indeed occur, the star stops the accretion and rapidly evolves towards a very hot Zero Age Main Sequence SMS emitting copious amonts of UV photons, clearing the remaining halo gas out of the potential well. After a very brief lifetime ($\lesssim 1\,\mathrm{Myr}$) the SMS dies and leaves a black hole seed with comparable mass. If, on the contrary, the high accretion rate can be sustained for a longer time, the star can continue to grow. Because of its low effective temperature, radiative feedback is unable to stop the halo gas from accreting. The growth continues until the object finally encounters a General Relativity instability that induces a rapid ($\sim 10^5\,\mathrm{s}$) direct collapse into a DCBH, i.e. without passing through a genuine stellar phase. The limiting mass for a non-rotating proto-SMS is the following (Ferrara et al., 2014):

$$M_{GR} \approx 8.48 \times 10^5 \left(\frac{\dot{M}}{1\,\mathrm{M}_\odot\,\mathrm{yr}^{-1}} \right)^{2/3} \mathrm{M}_\odot\,. \tag{2.17}$$

The two cases are strongly different, because virtually no ionizing photons are produced in the second one, since the collapse is isothermal and the temperature is kept at low levels. Therefore, the newly formed DCBH will find itself embedded in the gas reservoir

of the halo and starts to accrete again. This accretion phase remains highly obscured and it is only in the latest phases that the DCBH is able to clear the remaining gas. The DCBH should be allowed to grow up to $M_\bullet = 10^{4-6}\,\mathrm{M}_\odot$, when the photospheric temperature reaches about $3 \times 10^4\,\mathrm{K}$, allowing the radiative feedback to clear the gas, stop the accretion and determine the final mass of the black hole seed.

Recent studies (see e.g. Yue et al. 2014) suggest that the formation of DCBHs was possible only during a brief era of cosmic evolution, between $z = 20$ and $z = 13$: after this time, the gas in the potential formation sites (i.e. unpolluted halos with virial temperature slightly above the atomic cooling threshold) is photo-evaporated.

Part II

Theoretical Framework

General Introduction to the Theoretical Framework

This part describes the theoretical framework of our study. In Chapter 3 the radiation hydrodynamics code that we developed is presented, along with the main assumptions on the physical environment we focus our attention upon. Moreover, the typical accretion process on a DCBH with initial mass $\sim 10^5\,\mathrm{M}_\odot$ is described. In Chapter 4 we provide a general theory for the accretion process on a DCBH with mass in the range $\sim 10^{4-6}\,\mathrm{M}_\odot$ and different radiative efficiencies of the accretion disk. We identify two different accretion regimes: feeding dominated accretion and feedback limited accretion. The former leads to an high-efficient growth of the black hole seed, while the latter requires a longer time and a larger mass reservoir to reach the same final black hole mass. Finally, we investigate the possibility of a bimodal cosmic evolution in mass of the first black hole seeds.

Chapter 3

Simulating the Growth of Intermediate Mass Black Holes

3.1 Introduction

In the popular ΛCDM cosmological model, the formation of the first stars occurred in the redshift range $20 \lesssim z \lesssim 30$ (Barkana & Loeb 2001, Miralda-Escudé 2003, Bromm & Yoshida 2011, Stacy & Bromm 2014, Hummel et al. 2015, for a recent and extensive review see also Bromm 2013) in minihalos, i.e. dark matter structures with virial temperatures $T_{\rm vir} \leq 10^4\,{\rm K}$ and total masses $M_h \lesssim 10^8\,{\rm M}_\odot$. The concurrent formation of the first black holes (Bellovary et al. 2011, Volonteri & Bellovary 2012, Agarwal et al. 2013, 2014, see Haiman 2013 for an updated review), as a final product of the evolution of the first massive stars, represents a second key event during the same cosmic epoch. The appearance of these classes of objects likely had a very strong impact on both the interstellar and the intergalactic medium, due to their radiative and mechanical feedback (Park & Ricotti, 2011, Petri et al., 2012, Park & Ricotti, 2012, Jeon et al., 2012, Tanaka et al., 2012, Maiolino et al., 2012, Park & Ricotti, 2013, Nakauchi et al., 2014).

The process of cooling and fragmenting the gas plays a role of key importance in this cosmic epoch. Minihalos primarily cool their metal-free gas through molecular hydrogen line emission. Under intense irradiation in the Lyman-Werner band (LW, $E_\gamma = 11.2 - 13.6\,{\rm eV}$), H_2 is photo-dissociated via the two-step Solomon process (see the original study by Draine & Bertoldi 1996), so that cooling (and, consequently, the formation of

stars and stellar mass black holes) is quenched (Visbal et al., 2014). The UV specific intensity in the LW band, $J_\nu = J_{21}^* \times 10^{-21} \mathrm{erg\,s^{-1} cm^{-2} Hz^{-1}\,sr^{-1}}$, required for quenching is somewhat uncertain, but lies in the range $J_{21}^* = 0.1 - 1$ (see, e.g., Machacek et al. 2001 and Fialkov et al. 2013).

When instead primordial, atomic-cooling halos ($T_{\rm vir} > 10^4\,\mathrm{K}$) are exposed to a LW flux of even higher intensity, $J_\nu > J_\nu^\bullet$ (Loeb & Rasio 1994, Eisenstein & Loeb 1995, Begelman et al. 2006, Lodato & Natarajan 2006, Regan & Haehnelt 2009, Shang et al. 2010, Johnson et al. 2012, Agarwal et al. 2012, Latif et al. 2013a) the destruction of H_2 molecules allows a rapid, isothermal collapse, initially driven by H I Lyα line cooling, later replaced by two-photon emission. The precise value of $J_\nu^\bullet$ depends on several factors, but there is a general consensus that it should fall in the range $30 < J_{21}^\bullet < 1000$, depending on the spectrum of the sources (Sugimura et al., 2014).

Several theoretical works (Bromm & Loeb 2003, Begelman et al. 2006, Volonteri et al. 2008, Shang et al. 2010, Johnson et al. 2012) have shown that the result of this collapse is the formation of a DCBH of mass $M_\bullet \approx 10^{4-5}\,\mathrm{M_\odot}$, likely passing through the intermediate super-massive protostar phase, either directly collapsing into a compact object due to general relativistic instability (Shibata & Shapiro 2002, Montero et al. 2012) or at the end of the very rapid evolution if the super-massive stars reaches the Zero-Age Main Sequence (for a more detailed discussion, see Ferrara et al. 2014). Once formed, the subsequent accretion of the remaining gas from the parent halo leads to a further growth of the DCBH into a fully-fledged IMBH of mass $M_\bullet \approx 10^{5-6}\,\mathrm{M_\odot}$.

This scenario is confirmed by cosmological simulations, as those presented by Latif et al. (2013a), who have shown that under the previous conditions (atomic-cooling halos irradiated by $J_\nu > J_\nu^\bullet$) very strong accretion flows up to $\approx 1\,\mathrm{M_\odot\,yr^{-1}}$ may take place. As calculations by Hosokawa et al. (2013) and Schleicher et al. (2013) suggest that the effects of radiative feedback from the accreting protostar is weak, due to its cool (≈ 6000 K) photosphere, it has been possible to safely extend the simulations to longer time scales (Latif et al., 2013b), up to the formation of a $\sim 10^5\,\mathrm{M_\odot}$ central condensation[1].

In this chapter, we follow the accretion history onto a newly formed DCBH, with special emphasis on the dynamical and radiative properties of the inner parts of the parent halo, providing most of the accretion material to the central black hole. In particular,

[1]Even higher masses can result if magnetic fields, suppressing fragmentation, are included (Latif et al., 2014a).

we aim at clarifying a number of aspects, including (i) the accretion time scale; (ii) the time-dependent emitted luminosity; (iii) the final outcome of the accretion phase, with a progressive depletion of the gas or a final outburst; (iv) the fraction of the halo gas accreted by the black hole and that ejected in the outskirts by radiative feedback.

Previous works have already attempted to describe the accretion process onto black holes of different sizes. Sakashita & Yokosawa (1974) employed the method of similarity solutions to describe the time evolution of the accretion process in the optically thin regime (i.e. $\tau \lesssim 1$, where τ is the optical depth). Tamazawa et al. (1975), instead, used a full radiative transfer approach to describe the process in the optically thick regime (i.e. $\tau \gtrsim 1$) assuming steady state, i.e. without any explicit time dependence in the accretion flow. In contrast with these previous works, we aim at a full time-dependent description in the optically thick regime, similarly to the somewhat idealized approach used by (Park & Ricotti, 2011, 2012, 2013, Johnson et al., 2013), but extending these studies in several aspects and including a more complete physical description of the accretion process.

Recent works (Alexander & Natarajan 2014, Volonteri et al. 2015, Madau et al. 2014) have proposed the occurrence of brief, recurring but strongly super-critical accretion episodes (with rates even $50-100$ times larger than the Eddington limit) to explain the rapid black hole mass build-up at high redshifts. An early phase of stable super-critical quasi-spherical accretion in the BHs was also proposed in Volonteri & Rees (2005). Such large accretion rates may be sustainable in the so-called "slim disk" solution (Begelman & Meier 1982, Paczynski & Abramowicz 1982, Mineshige et al. 2000, Sadowski 2009, 2011), an energy-advecting, optically thick accretion flow that generalize the standard thin disk model (Shakura & Sunyaev, 1976). See also the description provided in Sec. 2.1. In these radiatively inefficient models the radiation is trapped into the high-density gas and is advected inward by the accretion flow: as a consequence, the luminosity is only logarithmically dependent on the accretion rate and very large flows are sustainable (see the discussion in Chapter 4). These works, while investigating the accretion flow at much smaller spatial scales, offer an interesting perspective in the discussion of the implications of our efforts, as detailed in Sec. 3.5.

The present work is the first necessary step towards a precise prediction of the observable properties of DCBHs, whose existence has remained so far in the realm of theoretical,

albeit physically plausible, speculations. This effort seems particularly timely given the advent of powerful telescopes as the JWST, becoming available in the next few years, and high-z ultra-deep surveys like the HST Frontier Fields (Coe et al., 2014). In practice, we aim at determining the SED of DCBHs in order to build diagnostic tools able to uniquely identify these sources among the other high-z ones (see Chapter 5 and Chapter 6). If successful, this strategy would not only represent a breakthrough in the study of the first luminous objects in the Universe, but it would also shed some light on the puzzles provided by the interpretation of the formation of SMBH (see e.g. Fan et al. 2001, Petri et al. 2012, Mortlock et al. 2011) and the excess recently found in the power spectrum of the cosmic Near Infrared Background fluctuations (for an overview, see Yue et al. 2013). These issues will be discussed in more details in Sec. 3.5 of the present chapter.

The outline of this chapter is as follows. In Sec. 3.2 we describe the physics and equations of the radiation-hydrodynamic problem we aim at solving, along with the numerical implementation and initial conditions (further details in Sec. 3.3). In Sec. 3.4 we present the results of our simulations, providing a full picture of the accretion and feedback processes. Finally, in Sec. 3.5 we provide some discussion and a summary. Throughout, we adopt recent Planck cosmological parameters (Planck Collaboration et al., 2015) as reported in Table 1.1. Moreover, we define $f_{Edd} \equiv \dot{M}_\bullet/\dot{M}_{Edd}$: the accretion is super-critical (super-Eddington) if $f_{Edd} > 1$.

3.2 Physical and Numerical Implementation

The present study is based on a series of radiation-hydrodynamic simulations. Our code is designed to execute a fully consistent treatment of spherically-symmetric hydrodynamic (HD) equations and a simplified version of the Radiative Transfer (RT) equations.

The simulated spatial region is large enough to allow us to neglect deviations from spherical symmetry, e.g. the presence of an accretion disk which may form at much smaller scales. As detailed in de Souza et al. (2013), the primordial halos which generated the DCBHs rotate very slowly, with a mean value of the spin parameter $\lambda = Jc/(GM_h^2) = 0.0184$, where J is the angular momentum of the halo with mass M_h. Under these

conditions, deviations from the spherical symmetry become important at the centrifugal radius $R_c = \lambda^2 G M_h^2/(c^2 M_\bullet) \sim 10^{-6}\,\mathrm{pc} \sim 100\,R_\mathrm{S}$, with R_S the Schwarzschild radius: this value is $\sim 10^5$ times smaller than the internal boundary of our simulations. Our resolution is designed to resolve the Bondi radius (or gravitational radius, see Bondi 1952):

$$R_B = \frac{2GM_\bullet}{c^2_{s(\infty)}} = 1.5\,\mathrm{pc} = 5 \times 10^{-4}\,R_\mathrm{vir} = 10^8\,R_\mathrm{S}\,, \tag{3.1}$$

where $c_{s(\infty)}$ is the sound speed at large distances from the accretion flow, R_vir is the virial radius of the halo and R_S is the Schwarzschild radius of the black hole. The Bondi radius largely varies during our simulations, but, for clarity reasons, all distances in the plots are expressed in terms of its initial value $R_B(t = t_0)$. Interestingly, even Adaptive Mesh Refinement cosmological simulations cannot resolve this spatial radius (see, e.g. Pallottini et al. 2013 where the maximum resolution is $\sim 5\,\mathrm{kpc}$) and therefore they have to resort to some kind of sub-grid prescriptions for the black hole growth. In this context, the usual methodology to deal with IMBHs is to suppose that they irradiate with luminosities $L \approx L_{Edd}$ where:

$$L_{Edd} = 3.2 \times 10^4 \left(\frac{M_\bullet}{M_\odot}\right) \mathrm{L}_\odot\,, \tag{3.2}$$

is the Eddington luminosity. The domain of our simulations spans approximately from $0.1\,R_B$ to $2\,R_B$. This spatial dynamic range is designed to focus on the smallest possible spatial region of interest for the full simulation (obtaining the highest possible spatial resolution), i.e. from the radius of gravitational influence ($\sim R_B$) down to the smallest radius ($\sim 0.2\,R_B$) reached by the propagating density wave at the end of the simulation.

The natural time scale of the problem is given by the free-fall time at the Bondi radius:

$$t_{ff} \simeq \frac{1}{\sqrt{G\rho(R_B)}} \simeq 10^5\,\mathrm{yr}\,. \tag{3.3}$$

The time scale for the full RT simulation is about $\sim 10^3\,t_{ff}$, due to the presence of radiation pressure which slows down the collapse.

In the following subsections we describe the physics included in the simulations, separating the HD and the RT parts for clarity reasons. Some more technical aspects (heating and cooling terms, photon diffusion and boundary conditions) are deferred to the Sec. 3.3.

3.2.1 Hydrodynamics

We solve the standard system of ideal, non-relativistic Euler's equations, i.e. neglecting viscosity, thermal conduction and magnetic fields, for a primordial (H-He) composition gas, spherically accreting onto a central IMBH, assumed at rest; we assign to the gas a null angular momentum with respect to the central object. The code evolves in time the following system of conservation laws for mass, momentum and energy, solving for the radial component:

$$\frac{\partial \rho}{\partial t} + \nabla \cdot (\rho \mathbf{v}) = 0\,, \tag{3.4}$$

$$\frac{\partial \mathbf{q}}{\partial t} + \nabla \cdot (\mathbf{q} \times \mathbf{v}) = -(\gamma - 1)\nabla E - \nabla p_{rad} + \mathbf{g}\rho\,, \tag{3.5}$$

$$\frac{\partial E}{\partial t} + \nabla \cdot (E\mathbf{v}) = -(\gamma - 1)E\nabla \cdot \mathbf{v} + (H - C)\,, \tag{3.6}$$

where ρ is the gas mass density, $\mathbf{v}$ is the gas velocity (taken to be positive in the outward direction), $\mathbf{q} = \rho\mathbf{v}$ is the momentum density and E is the energy density. Moreover $\gamma = 5/3$ is the ratio of specific heats, p_{rad} is the additional radiation pressure, $\mathbf{g}(r)$ is the gravitational field generated by the central black hole and $(H - C)$ are the heating and cooling terms. In the following, we neglect the vector notation since we only consider the radial components of the previous quantities. The total energy density E is given by the relation:

$$E = \rho\epsilon + \frac{\rho v^2}{2}\,, \tag{3.7}$$

where ϵ is the specific gas thermal energy:

$$\epsilon = \frac{1}{\gamma - 1}\frac{1}{\mu}RT\,, \tag{3.8}$$

where T is the gas temperature, R is the gas constant and μ is the mean molecular weight which, for a primordial gas with helium fraction $Y_P = 0.24665$ (Planck Collaboration et al., 2015) and no metals $Z_p = 0$, is equal to $\mu = 1.15$. The gas thermal pressure is given by the usual equation for ideal gases:

$$P_g = \frac{1}{\mu}\rho RT\,, \tag{3.9}$$

while the gravitational acceleration is

$$g(r,t) = \frac{GM_\bullet(t)}{r^2}\,. \tag{3.10}$$

The value of the black hole mass $M_\bullet(t)$ changes with time, due to the accretion, with the following set of rules, where $\dot{M}_\bullet = 4\pi r^2 \rho |v|$:

$$\begin{cases} \dot{M}_\bullet(t) \neq 0 \;\; \Leftrightarrow \;\; v(r = r_{min}, t) < 0 \\ M_\bullet(t) = M_0 + (1-\epsilon) \int_0^t \dot{M}_\bullet \, \mathrm{d}t \end{cases} \tag{3.11}$$

where $M_0 = 10^5 \, \mathrm{M}_\odot$ is the initial value for the mass we adopt for the IMBH, $\dot{M}_\bullet$ denotes the time derivative of $M_\bullet$ and ϵ is the efficiency factor for mass-energy conversion (see the RT subsection below for more details).

The system Eqs. 3.4 - 3.6 are solved with a Linearized Roe Riemann solver (Roe, 1981), a method based on Roe's matrix characteristic decomposition, which offers superior quality in treating the diffusion in hydrodynamic quantities. The time-stepping algorithm is a classical Runge-Kutta third-order scheme.

3.2.2 Radiative transfer

In our simulations, matter and radiation are coupled via (frequency-independent) Thomson scattering with interaction strength σ_T, the Thomson scattering cross section. At low temperatures, due to the decrease of the ionized fraction, we introduce an additional dependence which will be made explicit in the following. All radiation-related quantities are integrated over frequencies: this treatment serves as a good approximation for the main radiative features. Our RT modeling builds upon the works by Tamazawa et al. (1975) for what concerns the general theoretical framework; we also exploit the computationally effective scheme by Novak et al. (2012). In the following we first introduce the relevant RT equations and then discuss their numerical implementation.

In the usual notation, J is the intensity of the radiation field, S is the source function, H (K) is the first (second) moment of intensity. All these quantities are functions of time and position.

The closure relation between the second moment of intensity K and the intensity J is given by the so-called Eddington factor f (Hummer & Rybicki 1971, Tamazawa et al. 1975), here defined as:

$$f = \frac{K}{J} = \frac{1 + \tau/\tau_0}{1 + 3\tau/\tau_0} \, , \tag{3.12}$$

where τ_0 is the optical depth at which the Eddington factor becomes equal to 1/2.

The source total luminosity L and H are related at any point of the spatial domain by $L = 16\pi^2 r^2 H$. In turn, L depends on the gas accretion rate $\dot{M}_\bullet$ onto the IMBH (for $v < 0$):

$$L = \epsilon c^2 \dot{M}_\bullet = \epsilon c^2 \left(4\pi r^2 \rho |v|\right) , \tag{3.13}$$

where we employ an efficiency factor $\epsilon = 0.1$ (see e.g. Yu & Tremaine 2002, Madau et al. 2014). Generally speaking, the efficiency factor ranges from $\epsilon = 0.057$ for a Schwarzschild (i.e. non-rotating) black hole to $\epsilon = 0.32$ for a maximally rotating object (see Thorne 1974). We then define $L_\bullet$ the luminosity evaluated at the innermost grid cell, located at $r = r_{min}$:

$$\begin{cases} L_\bullet \equiv \epsilon c^2 \left[4\pi r_{min}^2 \rho(r_{min}) |v(r_{min})|\right] & \text{if } v(r_{min}) < 0 \\ L_\bullet \equiv 0 & \text{if } v(r_{min}) \geq 0 \end{cases} \tag{3.14}$$

The acceleration caused by radiation pressure is then:

$$a_{rad} = \frac{\kappa(T) L}{4\pi r^2 c} , \tag{3.15}$$

where c is the speed of light and $\kappa(T)$ is the opacity of the gas, calculated following the temperature-dependent prescription given in Begelman et al. (2008), namely:

$$\kappa(T) = 0.2(1+\mu) \frac{1}{1 + (T/T_*)^{-\beta}} \, \mathrm{cm^2 \, g^{-1}}, \tag{3.16}$$

with $\beta = 13$. Below $T \sim T_* = 8000\,\mathrm{K}$, the opacity rapidly falls due to the decrease of the ionized fraction: as a consequence, also the effectiveness of the radiation pressure is quenched.

Our definition of the optical depth τ is:

$$\tau(R) \equiv -\int_0^R \kappa \rho \, \mathrm{d}r = -\sigma_T \int_0^R \frac{\rho(r)}{1 + (T/T_*)^{-\beta}} \, \mathrm{d}r \, , \tag{3.17}$$

where we have included the temperature dependence of the opacity. The quantity reported in the graphs is the optical depth for an external observer.

As we will see, due to feedback effects, accretion onto the IMBH occurs in an intermittent manner. It is then useful to introduce the duty-cycle, defined as the fraction of time

spent accreting within a given time frame of duration T_{tot}:

$$\mathcal{D} = \frac{\Delta t_{accr}}{T_{tot}} \,. \tag{3.18}$$

The instantaneous value of the duty-cycle is computed dividing the total integration time T_{tot} in slices and computing the duty-cycle with respect to each slice.
The equations for steady and spherically-symmetric transfer of radiation have been derived, e.g. by Castor (1972) and Cassinelli & Castor (1973). For our problem, it is appropriate to assume steady-state RT equations since the light-crossing time at the Bondi radius, $R_B/c \approx 5\,\mathrm{yr}$, is negligible with respect to the free-fall time, see Eq. 3.3. The full RT equations are:

$$\begin{aligned} &\frac{v}{c}\frac{d}{dr}\left(\frac{4\pi J}{\rho}\right) + 4\pi K \frac{v}{c}\frac{d}{dr}\left(\frac{1}{\rho}\right) - \frac{4\pi}{\rho}\frac{v}{c}\left(\frac{3K-J}{r}\right) = \\ &= -\frac{1}{4\pi\rho r^2}\frac{dL}{dr} - 4\pi\kappa(J-S)\,, \end{aligned} \tag{3.19}$$

$$\frac{dK}{dr} + \left(\frac{3K-J}{r}\right) + \frac{v}{c}\frac{dH}{dr} - \frac{2}{r}\frac{v}{c}H - \frac{2}{\rho}\frac{v}{c}\frac{d\rho}{dr}H = -\rho\kappa H\,. \tag{3.20}$$

The term $\kappa(J-S)$ handles the gas heating and cooling, as the $(H-C)$ terms in the energy equation, see Eq. 3.6. These equations are correct up to the first order in $\beta = v/c$ and are suitable for high-speed accretion flows, where β is not negligible. In the previous equations, the transition from the optically thin to the optically thick regime is described by the density-dependent Eddington factor f (decreasing from 1 to 1/3 with increasing optical depth) and by the term $\sim \rho\kappa(T)$.

Novak et al. (2012) presented several computationally-effective non-relativistic RT formulations which yield the correct behavior both in optically thin and optically thick regimes. These formulations are convenient because they allow to obtain accurate results with a lower computational complexity. We defer the interested reader to the full derivation in Novak et al. (2012) and we write down only the final formulation.

$$\frac{dL}{dr} = 4\pi r^2(\dot{E} - 4\pi\rho\kappa J)\,, \tag{3.21}$$

$$\frac{dJ}{dr} = -\frac{2Jw}{r} - \frac{(3-2w)\rho\kappa L}{16\pi^2 r^2}\,. \tag{3.22}$$

In these expressions, w is an interpolation parameter that controls the transition from optically thin to optically thick regimes and is a function of the position: it ranges from $w = 0$ (for an isotropic radiation field, i.e. in the optically thick regime) to $w = 1$ in the optically thin regime. Furthermore, $\dot{E}$ is the source term, playing the same role of S in the relativistic treatment, see Sec. 3.3 for a more detailed description. Eq. 3.21 is derived from the full RT Eqs. 3.19-3.20 by neglecting the v/c terms and using $\dot{E}$ instead of S. Eq. 3.22, instead, is derived by using the specific values of the Eddington factor $f \equiv K/J$ and the interpolation factor w in each regime: ($f = 1$, $w = 1$) for the optically thin and ($f = 1/3$, $w = 0$) for the optically thick.

Finally, we need to specify the boundary conditions. As in the study of stellar interiors, the second order differential equation for $L(r)$, or the two first-order ODEs in $L(r)$ and $J(r)$ (Eqs. 3.21-3.22), requires two boundary conditions, at the inner and outer boundaries. The innermost cell of the grid radiates the luminosity produced by the accretion flow onto the black hole (see Eq. 3.14), so that $L(r_{min}) \equiv L_\bullet$. Far from the black hole, the luminosity is expected to resemble a point source because the scattering becomes negligible, so that:

$$J(r_{max}) \equiv \frac{L(r_{max})}{16\pi^2 r_{max}^2} \,. \tag{3.23}$$

In order to solve the set of boundary-value differential Eqs. 3.21-3.22, the so-called shooting method with Newton-Raphson iteration (Press et al., 1992) works remarkably well up to the optical depth of a few. Beyond this limit, the shooting method becomes unstable and it is necessary to switch to a more powerful relaxation method (Press et al., 1992). However, following the evolution of the system for physically relevant time scales ($\sim 100\,\mathrm{Myr}$) requires such a large number of steps that even the relaxation method becomes computationally unviable. To overcome this problem, we follow the method outlined in the Appendix B of Novak et al. (2012) and sketched in our Sec. 3.3.

3.2.3 Initial conditions

We model the spherically-symmetric gas accretion onto a seed black hole of initial mass $M_0 = 10^5\,\mathrm{M}_\odot$, assumed at rest at the center of a dark matter halo of total mass (dark matter and baryons) $M_h = 6.2 \times 10^7\,\mathrm{M}_\odot$ at redshift $z = 10$; the gas mass is $M_{gas} = (\Omega_b/\Omega_m)\,M_h = 9.6 \times 10^6\,\mathrm{M}_\odot$. The angular momentum of the halo with respect to its center of mass is zero. We assume that the gas follows the density profile derived from

the simulations in Latif et al. (2013a), which is well approximated by the following functional form:

$$\rho(r) = \frac{\rho_0}{1 + (r/a)^2}\,, \tag{3.24}$$

where a is the core radius, estimated from the Fig. 1 of Latif et al. (2013a) as $a \sim 10^{-3}$ pc; this scale is too small to be resolved by our simulations, while the virial radius of the halo is much larger than our computational domain, being $R_{\rm vir} \sim 3$ kpc. Normalization to the gas mass content, M_{gas}, gives the central density value $\rho_0 \sim 10^{-11}\,{\rm g\,cm^{-3}}$. From the initial prescription for the density field and assuming an isothermal profile with $T = 2 \times 10^4$ K as in Latif et al. (2013a), the initial conditions for the pressure field are derived directly from the equation of state, Eq. 3.9. The initial conditions for the radial velocity are set to a very small, spatially constant value $v_0 < 0$. After a very brief ($\ll t_{ff}$) transient, the system adjusts to a velocity profile consistent with a rapid accretion across the inner boundary of the grid. In addition, the initial density profile is also rapidly modified within the Bondi radius, while outside the gravitational influence of the black hole it remains almost unaltered.

The spatial grid for all simulations extends from $r_{min} = 5.0 \times 10^{17}$ cm ≈ 0.16 pc to $r_{max} = 1.0 \times 10^{19}$ cm ≈ 3.2 pc, with 3000 logarithmically spaced bins. This range is optimized for our computational target, allowing to follow the entire displacement of the density wave (see Sec. 3.4) and extending out to the Bondi radius. In addition, the choice of the minimum radius r_{min} is tied to the time step Δt, which is computed from the well-known CFL condition:

$$v\,\frac{\Delta t}{\Delta r} = C < C_{max}\,, \tag{3.25}$$

where C is the dimensionless Courant number and $C_{max} = 0.8$. Higher velocities need smaller time steps: hence, decreasing the value of r_{min} requires an additional decrease of Δt. For further details about the simulations, e.g. the boundary conditions, see the following Sec. 3.3.

3.3 Further Details on the Implementation

This section contains some more technical details about the modules HD and RT, such as the boundary conditions for velocity and density, the heating and cooling terms and

the photon diffusion condition.

3.3.1 Additional boundary conditions

In addition to the boundary conditions for the luminosity, we need to specify the behavior of velocity and density at the innermost and outermost cells of the spatial grid. The spatial boundary conditions are: (i) outflow for the inner boundary (with restrictions on velocities, see below) and (ii) void for the outer boundary.

An outflow boundary condition forces the derivatives of the quantities of interest to be zero, i.e., artificially extends spatial domain outside the boundary. The restriction for the boundary velocity v_b is the following:

$$v_b = \begin{cases} v(r_{min}) & \text{if } v(r_{min}) < 0 \\ 0 & \text{if } v(r_{min}) > 0 \end{cases} \tag{3.26}$$

and is meant to prevent the replenishment of the computational domain by the gas coming from unresolved scales.

A void boundary condition, on the contrary, constrains the quantity of interest to be zero outside the computational domain: the system composed by the IMBH and its parent halo is isolated in space.

3.3.2 Heating and cooling

This paragraph deals with the non-adiabatic regime, i.e. the source/sink term $\dot{E}$ (Eqs. 3.21-3.22). Differently from the implementation in Novak et al. (2012), where $\dot{E}$ accounts for energy transfer among different frequency bands, in our case the interaction between matter and radiation is purely elastic (i.e. the frequency of the interacting photon is unchanged) and this term expresses the energy emitted or absorbed by matter per unit time and per unit volume.

For a gas at $T \lesssim 10^4\,\mathrm{K}$ (i.e. below the atomic hydrogen cooling threshold) the energy equation is purely adiabatic. Instead, for a gas at $T \gtrsim 10^4\,\mathrm{K}$, the term $\dot{E}$ takes into

account only the bremsstrahlung losses and is given by (in CGS units):

$$\dot{E} = 2\left(\psi - \frac{1}{2}\right)\chi_{ion} n^2 \mathcal{S}\,, \tag{3.27}$$

with $\mathcal{S} = -3.8\times10^{-27}\sqrt{T}$. Here, n is the hydrogen number density and ψ is the fraction of photons emitted at a given radius that are likely to belong to the outgoing stream (see Sec. 3.2). The term $2\left(\psi - \frac{1}{2}\right)$ is the fraction of transmitted (i.e. not absorbed) photons, since ψ is defined as $\psi = (1 + p_{trans}/2)$.

Moreover, the term χ_{ion} is the ionized fraction, which accounts for the fraction of hydrogen atoms that can contribute to the bremsstrahlung. This last term is calculated as $\chi_{ion} = (\alpha_b/\gamma + 1)^{-1}$, where α_b is the recombination rate and γ is the collisional ionization rate. Both of them are expressed in $\mathrm{cm}^3\,\mathrm{s}^{-1}$ and are defined as (see e.g. Maselli et al. 2003):

$$\alpha_b = \frac{8.4\times10^{-11}}{\sqrt{T}}\left(\frac{T}{1000}\right)^{-0.2}\left[1.0 + \left(\frac{T}{10^6}\right)^{0.7}\right]^{-1}, \tag{3.28}$$

$$\gamma = 1.27\times10^{-11}\sqrt{T}\,e^{-157809.1/T}\left[1.0 + \left(\frac{T}{10^5}\right)^{0.5}\right]^{-1}. \tag{3.29}$$

3.3.3 Photon diffusion condition

Given the very high values of the optical depth (up to ~ 100 in our simulations), it is important to check whether a proper treatment for photon diffusion is required. Photons in the diffusive regime are advected inward with the gas, rather than diffuse out of the accretion flow. In this condition, the trapped infalling material should be considered a "quasi-star", similar to the phase advocated by Begelman et al. (2008), with an atmosphere in local thermodynamic equilibrium: the emission from the inner section of the accreting flow would then be thermal.

Begelman (1978) gives a very practical way to assess the occurrence of the diffusive behavior of photons. Photons displaced at some radius r are trapped-in if:

$$\tau(r)\,\frac{v(r)}{c} > 1\,. \tag{3.30}$$

Throughout this chapter, we refer to this formula as the diffusion condition, which is never met in our grid, because the maximum values reached are of order $\tau(r)\, v(r)/c \approx 10^{-3}$.

This proves that the photons inside the simulated spherical volume in our work are never in the diffusive regime. It is likely that this condition is actually met at smaller radii, where the gas may form a structure quite similar to a stellar atmosphere. We defer the investigation of this possibility to future work.

3.3.4 The two-stream approximation

The RT method we used is based on Novak et al. (2012) and relies on the two-stream approximation, i.e. the luminosity is expressed as the sum of an ingoing and an outgoing radiation stream. When the optical depth is low, photons of the ingoing stream at any given radius r_0 are likely to successfully traverse the inner parts of the halo ($r < r_0$) and emerge as outgoing photons at the same radius, but with $\varphi = \varphi + \pi$ if φ is the azimuthal angle. In this case, all the radiation emitted by a source term is to be added to the outgoing stream. The source term, in our case, is given by bremsstrahlung emission. If, instead, the optical depth is large, the ingoing photons are likely to be absorbed for $r < r_0$. Then, only half of the emitted photons should be added to the outgoing stream. The other half should be added to the ingoing stream, where they will in due course be absorbed. The resulting equations for the two radiation streams are:

$$\frac{dL_{out}}{dr} = 4\pi r^2 \psi \dot{E} - \rho\kappa L_{out}\,, \tag{3.31}$$

$$\frac{dL_{in}}{dr} = 4\pi r^2 (1-\psi) \dot{E} - \rho\kappa L_{in}\,, \tag{3.32}$$

where $\psi(r)$ is the fraction of photons emitted at a given radius that are likely to belong to the outgoing stream. The simplest estimate of the quantity $\psi(r)$ is given in Novak et al. (2012):

$$\psi(r) = 1 - \frac{1}{2}\left[\frac{1}{1+e^{-\tau}}\right]\left[\frac{r_1^2}{\max(r_1^2, r^2)}\right]\,, \tag{3.33}$$

where τ is the optical depth from r to infinity and r_1 is the radial distance from the center where τ reaches unity. These equations must be complemented with the boundary

TABLE 3.1: Simulation parameters for the two test simulations (T1 and T2) and for the full one (FS) which includes a complete solution of the radiative transfer.

Parameter	T1	T2	FS
r_{min} [pc]	0.16	0.16	0.16
r_{max} [pc]	3.2	3.2	3.2
Integration time [yr]	3.2×10^4	3.2×10^4	1.4×10^8
Radiation pressure	no	yes	yes
Energy equation	adiabatic	adiabatic	non-adiabatic

conditions:

$$\begin{cases} L_{in}(r_{max}) = 0 \\ L_{out}(r_{min}) = L_\bullet \end{cases} \tag{3.34}$$

and the expression for the radiative acceleration, Eq. 3.15, must be changed into the following one:

$$a_{rad} = \frac{\kappa(T)(L_{out} - L_{in})}{4\pi r^2 c} \,. \tag{3.35}$$

3.4 Results

We present our results starting from the two test simulations T1 (pure hydro) and T2 (hydro + radiation pressure) in order to highlight some physical key features of the problem. Next, we turn to the analysis of the full simulation, FS, that in addition includes the complete solution of the radiative transfer; the FS simulation contains our main findings. The simulation parameters used in the three runs are reported in Table 3.1.

The total integration time T_{tot} for the runs T1 and T2 has been chosen in order to show the most important features of their radiation-hydrodynamic evolution, while for the FS simulation it corresponds to the total history of the system.

3.4.1 Test simulation T1: pure hydro

Simulation T1 is a pure adiabatic hydrodynamic simulation. The only two forces acting on the gas are produced by the gravitational field of the black hole and by the pressure gradient; therefore, it corresponds to the "classical" Bondi solution (Bondi, 1952), with

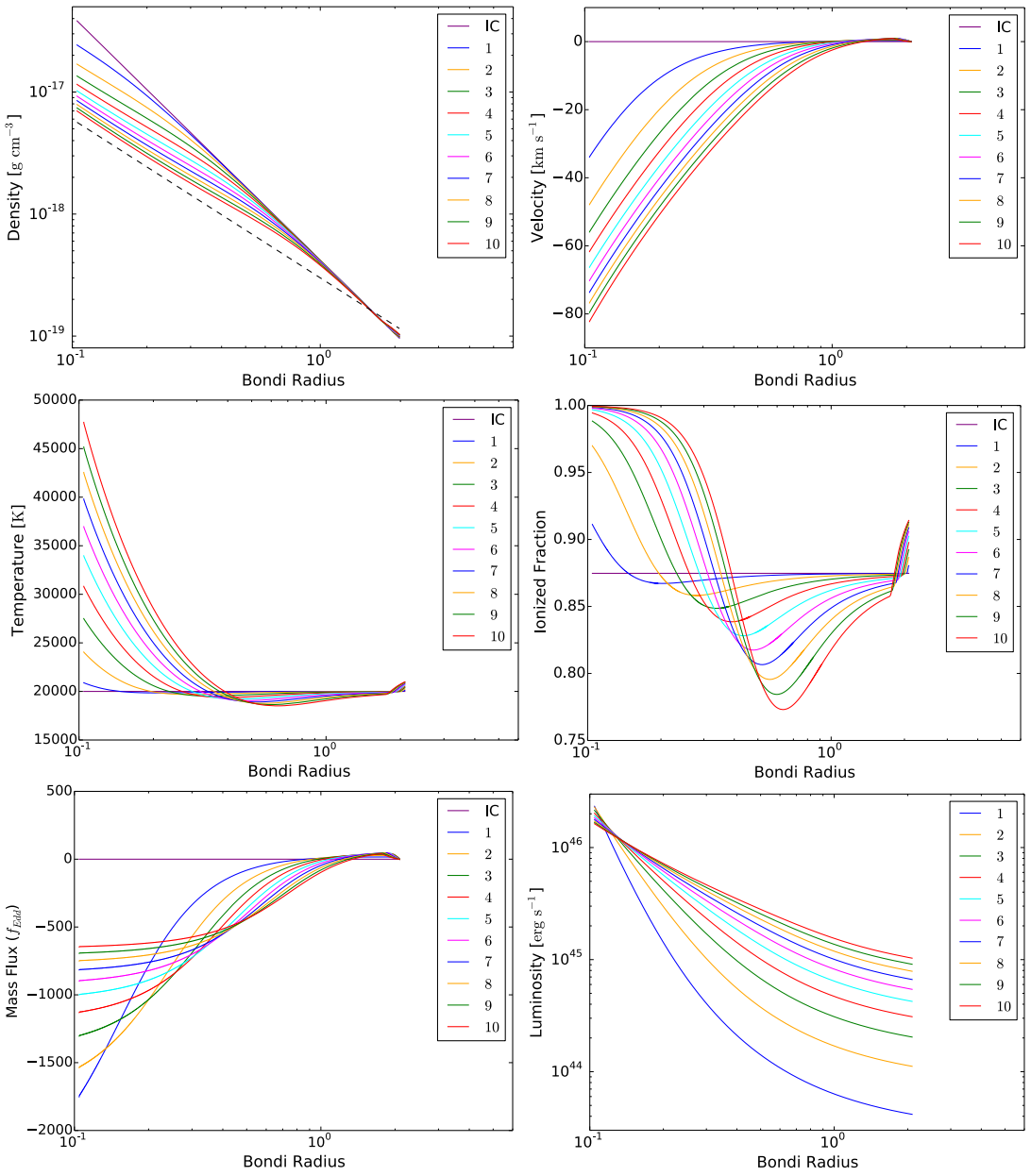

FIGURE 3.1: Spatial profiles for the T1 simulation: total integration time is $T_{tot} \approx 3.2 \times 10^4$ yr. The purple line labeled as "IC" represents the initial conditions: where this line is not present the corresponding initial condition is impossible to show on the plot. The colored lines correspond to different times of the simulation, equally spaced such that $T_{tot} = i\,\Delta t$ with $\Delta t = 3200$ yr and $i = 1, \ldots 10$. All horizontal axes are in units of R_B. The accretion rate is plotted with the velocity sign. The density panel reports the classical Bondi solution with a dashed black line.

the only exception consisting in the limited gas reservoir, which prevents a genuine steady state to take place. The spatial profiles predicted by T1 are shown in Fig. 3.1.

The evolution occurs over a free-fall time scale, $t_{ff} \sim 3.2 \times 10^4$ yr during which the system progressively approaches the Bondi solution, reported on the density panel as a

dashed black line, in which the gas density scales as:

$$\rho(r) \propto \left(\frac{r}{r_B}\right)^{-3/2} . \tag{3.36}$$

This scaling cannot be sustained for $t \gg t_{ff}$, due to the limitedness of the gas reservoir (unlimited in the classical Bondi solution) and ceases to be valid near the Bondi radius, where the gravitational influence of the black hole terminates.

The system is progressively emptied from the inner part of the environment, due to the absence of radiation pressure: the density near the inner boundary drops by a factor ~ 5 during the simulation time and the effect is propagated outward, up to the Bondi radius. The velocity of the gas increases with time as well, due to the overall decrease of gas pressure. The flow stabilizes to a velocity of order $\sim 100\,\mathrm{km\,s^{-1}}$ at the inner boundary. The temperature of the infalling gas increases, reaching peaks of $5 \times 10^4\,\mathrm{K}$ in the inner regions. The temperature profile is reflected in the behavior of the ionized fraction (see Sec. 3.3 for the relevant equations), which is smaller than 1 only when the temperature drops below the $\sim 2 \times 10^4\,\mathrm{K}$ level. The flow accretes at strongly super-Eddington rates at all times, reaching peaks of $f_{Edd} \sim 2000$: the Eddington limit does not apply in this case due to the absence of radiation pressure. The accretion rate progressively decreases due to the density drop: this causes the slow reduction in magnitude of the luminosity at the innermost cell, clearly visible in the bottom-right panel of Fig. 3.1. The emitted luminosity is obscured by high column densities at the beginning of the simulation, while the drop of the density decreases the optical depth with time, down to a value ~ 5. The spatial scaling of the emitted luminosity is described by Eq. 3.21 and caused by obscuration. The small jumps visible at the outer boundary, outside the sphere of gravitational influence of the black hole, are caused by the thermal pressure of the gas and are unimportant for the overall evolution of the system. The IMBH mass at the end of the T1 simulation is $M_\bullet \approx 2.0 \times 10^5\,\mathrm{M_\odot}$.

3.4.2 Test simulation T2: adding radiation pressure

In the T2 simulation an outward radiative force, corresponding to a fixed (i.e. not tied to $\dot{M}_\bullet$) value of the luminosity $\hat{L} = 2 \times 10^{43}\mathrm{erg\,s^{-1}}$, is added to the gravitational force and the pressure gradient, while the energy equation is still adiabatic. The radiative force is active only when the black hole is accreting, i.e. when $v(r_{min}) < 0$. The aim of

the T2 simulation is to show in a simplified way the effect of the radiation pressure on the gas.

Fig. 3.2 is a comparison between the fixed value of the luminosity employed in T2 and the luminosity resulting from the T1 simulation, computed through the accretion rate $\dot{M}_\bullet$ at $r = r_{min}$ with Eq. 3.14 (but not included in T1). The latter is ~ 3 orders of magnitude larger, due to the absence of radiation pressure, and reaches a steady value after a free-fall time $\sim 3000\,\mathrm{yr}$. The Eddington luminosity is also shown for comparison, its progressive increase being due to the change in $M_\bullet$. The value of $\hat{L}$ is set in order to be at any time larger than the corresponding L_{Edd}.

The radiation pressure can modify the accretion flow in two ways. If $f_{Edd} < 1$, the effect is a decrease of the accretion rate $\dot{M}_\bullet$. Naming $\dot{M}_{T1}$ the accretion rate without any radiative force (i.e. the one in the T1 simulation) and $\dot{M}_R$ the accretion rate with the addition of a radiative force with $f_{Edd} < 1$, it is easy to show that the following relation holds:

$$\dot{M}_R = \dot{M}_{T1}\sqrt{1 - f_{Edd}}\,. \tag{3.37}$$

If, instead, $f_{Edd} \geq 1$, the accretion is intermittent (i.e. $\mathcal{D} < 1$): the infalling gas is swept away by the radiation pressure and some time is needed to re-establish the accretion. Under the simplifying assumption that the initial infalling velocity of the gas is slow, it is possible to show that, if $f_{Edd} \geq 1$, an estimate of the value of the duty-cycle is given by:

$$\mathcal{D} = (2f_{Edd} - 1)^{-1}\,. \tag{3.38}$$

Under these assumptions, $\mathcal{D} \equiv 1$ for $f_{Edd} = 1$ (as in the pure hydro case), while for $f_{Edd} > 1$ it steadily decreases.

The T2 simulation is an example of the latter case, with $f_{Edd} \sim 1.5$. From the previous analysis we expect two major differences with respect to the T1 simulation, namely: (i) the IMBH accretes $\sim 50\%$ less mass (if the total integration times are equal) because $\mathcal{D}$ is smaller by a factor ~ 0.5, and (ii) the IMBH produces some feedback effect on the surrounding gas.

This is exactly what we observe in the T2 simulation. The final mass is $M_\bullet = 1.4 \times 10^5\,\mathrm{M}_\odot$, i.e. the black hole accreted $\sim 60\%$ less mass than in the T1 simulation, in complete agreement with our rough estimate in Eq. 3.38. In addition, the spatial profiles

for this simulation, shown in Fig. 3.3, manifestly provide some evidence of the effect that the radiation pressure exerts on the gas. A density wave, produced by the radiative feedback, propagates in the outward direction with velocities up to $\sim 20\,\mathrm{km\,s^{-1}}$; in addition, the positive values of the accretion flow measured in a large part of the spatial domain indicate the occurrence of a gas outflow from the external boundary. The high-density wave is followed by a rarefaction zone, with a density jump as high as $\sim 60\%$, which is visible also in the optical depth plot. The temperature in the high-density wave reaches values $\sim 2.5 \times 10^4\,\mathrm{K}$, while in the rarefaction zone it drops to $\sim 7000\,\mathrm{K}$ (the temperature profile follows the pressure, i.e. the cooling is adiabatic), decreasing the ionized fraction to very small ($\sim 10^{-3}$) values as well. The accretion flow promptly (after $\sim 6000\,\mathrm{yr}$) stabilizes to a value $f_{Edd} \sim -500$ at the innermost cell: this value is set by the fixed radiation pressure of the T2 simulation, which indirectly sets also the velocity at which the accretion flow is re-started at the end of each idle phase (the larger the radiation pressure is, the longer is the time needed for accretion to re-start, then the larger is the resulting mass inflow).

This general framework is explained by the following scenario: when the black hole accretes, the fixed super-critical emitted luminosity sweeps away the surrounding gas, affecting a spherical region of radius r_τ, defined such that $\tau(r_\tau) = 1$. The gas located at $r \gg r_\tau$ is also accelerated upward, not by the radiation pressure in this case but by the shock wave, and acquires a positive velocity. When the irradiation is temporarily shut down, the gas located at $r \ll r_\tau$ is affected by the strong gravitational field of the black hole and falls back in due course.

3.4.3 The full simulation

The aim of the FS simulation is to describe the accretion flow onto an IMBH with $M_0 = 10^5\,\mathrm{M_\odot}$. The final integration time for this simulation, when all the gas contained in the halo is expelled by radiation pressure, is $\sim 142\,\mathrm{Myr}$. The forces acting on the gas are the gravity of the black hole, the pressure gradient and the radiation pressure. The differences with respect to the previous T1 and T2 simulations are: (i) the radiation pressure is computed self-consistently, i.e. with Eq. 3.14 and (ii) the energy equation is non-adiabatic, with cooling determined by the bremsstrahlung radiation (see Sec. 3.3).

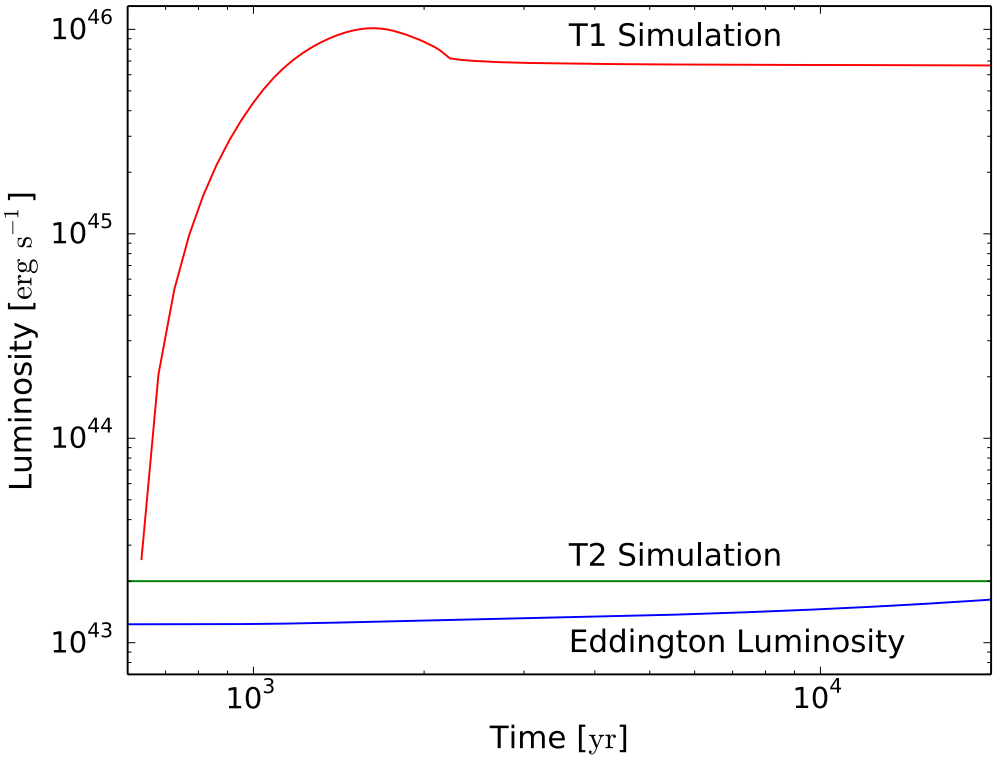

FIGURE 3.2: Comparison between the emitted luminosity for different simulations. The red line is the luminosity of the T1 simulation (computed from $\dot{M}_\bullet$ at $r = r_{min}$ with Eq. 3.14, but not included in the physics). In green, the fixed luminosity value used for the T2 simulation $\hat{L} = 2 \times 10^{43}\,\mathrm{erg\,s^{-1}}$. In blue, for comparison, the Eddington luminosity for the T2 simulation, whose value increases along with $M_\bullet$. The value of $\hat{L}$ is always above, but very close to, the Eddington limit.

3.4.3.1 Spatial structure and time evolution

Broadly speaking, the simulation allows the identification of three distinct evolutionary phases of the system, described in turn below.

1. **Initial Transient Phase**: the gas, initially almost at rest (as detailed in Sec. 3.2), is accelerated downward, progressively increasing $\dot{M}_\bullet$ and, as a consequence, the emitted luminosity L, as shown in Fig. 3.4. This plot shows that the emitted luminosity increases by $\sim$ 3 orders of magnitude in only $\sim 200\,\mathrm{yr}$, a fraction $\sim 10^{-6}$ of the full evolution of the system. This process is self-regulated, due to the interconnection between gravity, accretion rate and radiation pressure. The gravity tends to increase the accretion rate by accelerating the gas downward, while the emitted luminosity acts against the infall by providing an outward acceleration. This evolutionary phase lasts until the emitted luminosity becomes comparable to the Eddington limit, i.e. $L_{Edd}(t) = 3.4 \times 10^4 [M(t)/M_\odot]\,\mathrm{L}_\odot$, approximately

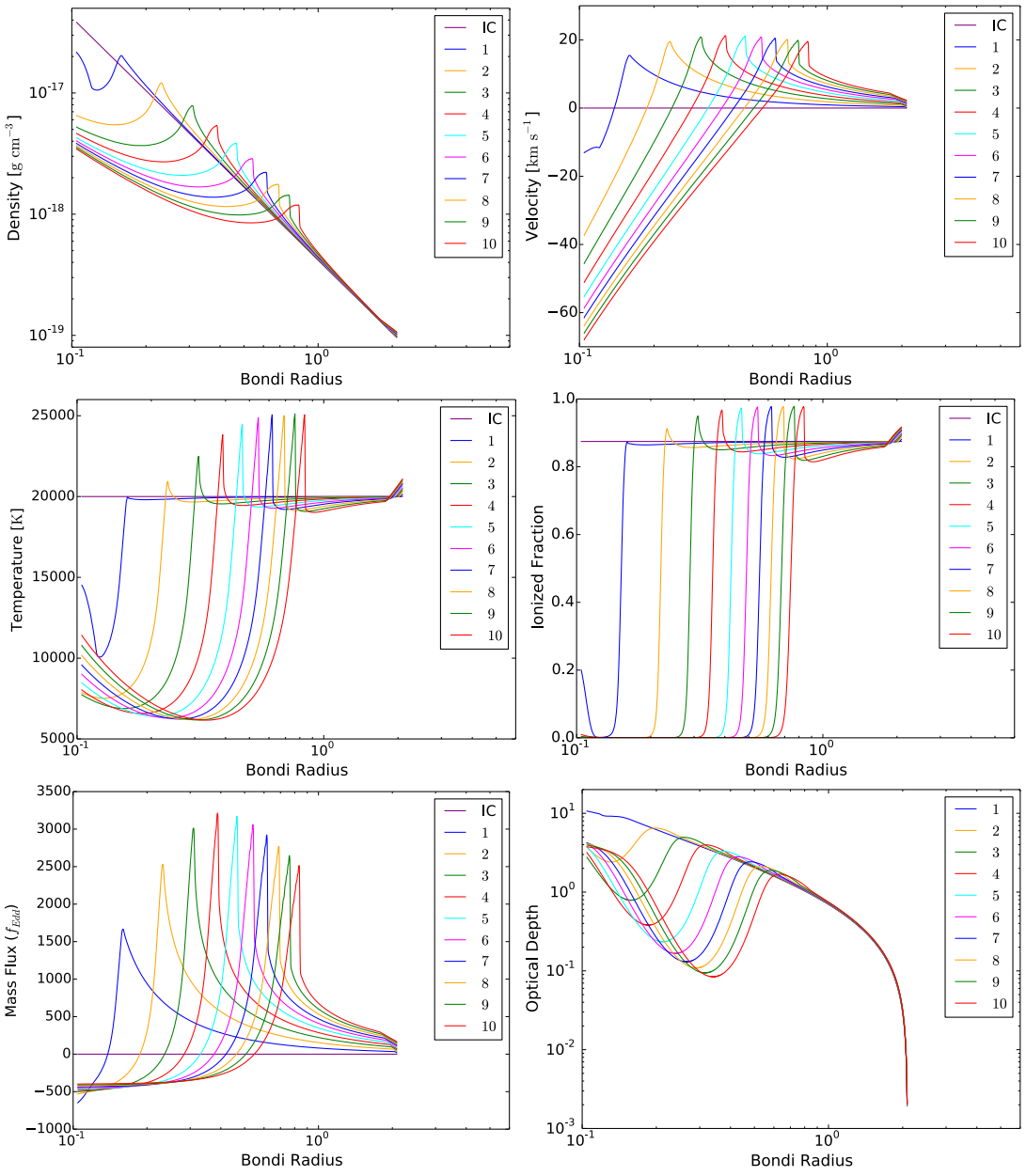

FIGURE 3.3: Spatial profiles for the T2 simulation: total integration time is $T_{tot} \approx 3.2 \times 10^4$ yr. A fixed radiative force, determined by the luminosity $\hat{L} = 2 \times 10^{43}\,\mathrm{erg\,s^{-1}}$ and active only when $v(r_{min}) < 0$, is added to the gravity and to the pressure gradient, as explained in the text. The colored lines correspond to different times of the simulation, equally spaced such that $T_{tot} = i\,\Delta t$ with $\Delta t = 3200\,\mathrm{yr}$ and $i = 1, \ldots 10$.

$10^{43}\,\mathrm{erg\,s^{-1}}$ at the beginning of the simulation. Above this threshold, the radiation pressure is able to sweep the gas away from the inner boundary and the accretion process becomes intermittent ($\mathcal{D} < 1$).

This initial phase lasts $\sim 200 - 300\,\mathrm{yr}$: the emitted luminosity and the fractional mass accreted:

$$\frac{\Delta M_t}{M_0} = \frac{(M_t - M_0)}{M_0}\,, \tag{3.39}$$

are shown in Fig. 3.4. An estimate of the duration T_t of this initial phase is easily computed from the following argument. We request that during T_t the luminosity $L = \epsilon c^2 \dot{M}_\bullet$ becomes equal to the Eddington luminosity:

$$L = \epsilon c^2 \frac{dM}{dt} \equiv L_{Edd} = \frac{4\pi G m_p c}{\sigma_T} M\,. \tag{3.40}$$

By means of integrating between $t = 0$ when $M(t) = M_0$ and T_t when $M(t) = M_t$ and calling $\Delta M_t = M_t - M_0$ we obtain:

$$T_t = \frac{\epsilon c \sigma_T}{4\pi G m_p} \ln\left(1 + \frac{\Delta M_t}{M_0}\right) \approx \frac{\epsilon c \sigma_T}{4\pi G m_p} \frac{\Delta M_t}{M_0}\,, \tag{3.41}$$

where the last approximation is valid for $\Delta M_t / M_0 \ll 1$. This equation, with the value $\Delta M / M_0 \approx 7 \times 10^{-6}$ taken from Fig. 3.4, gives the expected time scale $T_t \sim 300\,\mathrm{yr}$. Defining $t_{Edd} \equiv (c\sigma_T)/(4\pi G m_p)$ the Eddington time scale, the previous formula becomes:

$$T_t \approx \epsilon t_{Edd} \frac{\Delta M}{M_0}\,. \tag{3.42}$$

Interestingly, if we assume that $M(t) \propto M_0$ (see e.g. Volonteri et al. 2015, Madau et al. 2014), as in:

$$M(t) = M_0 \exp\left[\left(\frac{1-\epsilon}{\epsilon}\right)\frac{t}{t_{Edd}}\right], \tag{3.43}$$

the time scale T_t is strictly independent on the black hole mass M_0.

It is relevant to investigate in detail the mechanism that leads the system from a stable accretion at $L \sim L_{Edd}$ to the unstable and intermittent phase shown in Fig. 3.4 for $t \gtrsim 270\,\mathrm{yr}$. When the IMBH starts to accrete at $\dot{M}_\bullet \sim \dot{M}_{Edd}$, the gas near the inner boundary is swept away, so that the accretion is temporarily blocked and the radiation pressure is turned off. The emitted luminosity does not affect the outer parts of the domain, where $r \gg r_\tau$, see the similar discussion for the T2 simulation. The gas located in this section continues its infall, counteracted only

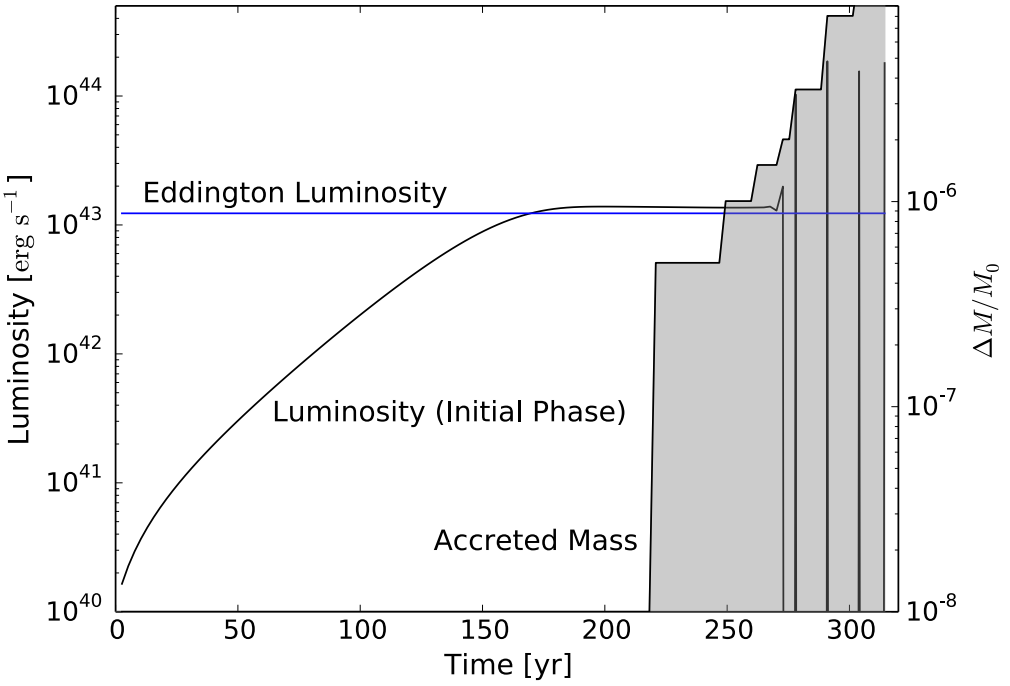

FIGURE 3.4: Luminosity emitted and fractional mass accreted ($\Delta M_t/M_0 = (M_t - M_0)/M_0$) during the initial phase, lasting $\sim 200-300$ yr. The corresponding Eddington luminosity is also shown, for comparison.

by the thermal pressure exerted from the internal layers, and eventually feeds the black hole with increasingly larger mass inflows. The difference with respect to the T2 simulation is due to the direct dependence of the emitted luminosity from the mass inflow in the FS case. More specifically, this mechanism is schematically explained in Fig. 3.5. In the first panel, the black hole is accreting mass from the innermost shell, which is collapsing just as the outer one. When the black hole irradiates with $L \gtrsim L_{Edd}$, the radiation pressure acts only on the innermost shell (supposing for simplicity that the outer shell is located at $r \gg r_\tau$) which is swept outward, while the outer shell continues the infall. During this period, the IMBH is not irradiating. The innermost shell eventually terminates its outward movement, due to the gravitational pull of the black hole. The innermost shell merges with the outer one, so that its density is increased. Eventually, the merged shells approach the accretion boundary and re-start the cycle with a larger accretion flow, i.e. with the emission of a higher luminosity.

2. **Main Accretion Phase**: this phase lasts ~ 142 Myr and is characterized by a duty-cycle $\mathcal{D} \sim 0.48$ and an average accretion rate $f_{Edd} \simeq 1.35$: the accretion is super-critical on average. This value is computed as a global average of f_{Edd} over

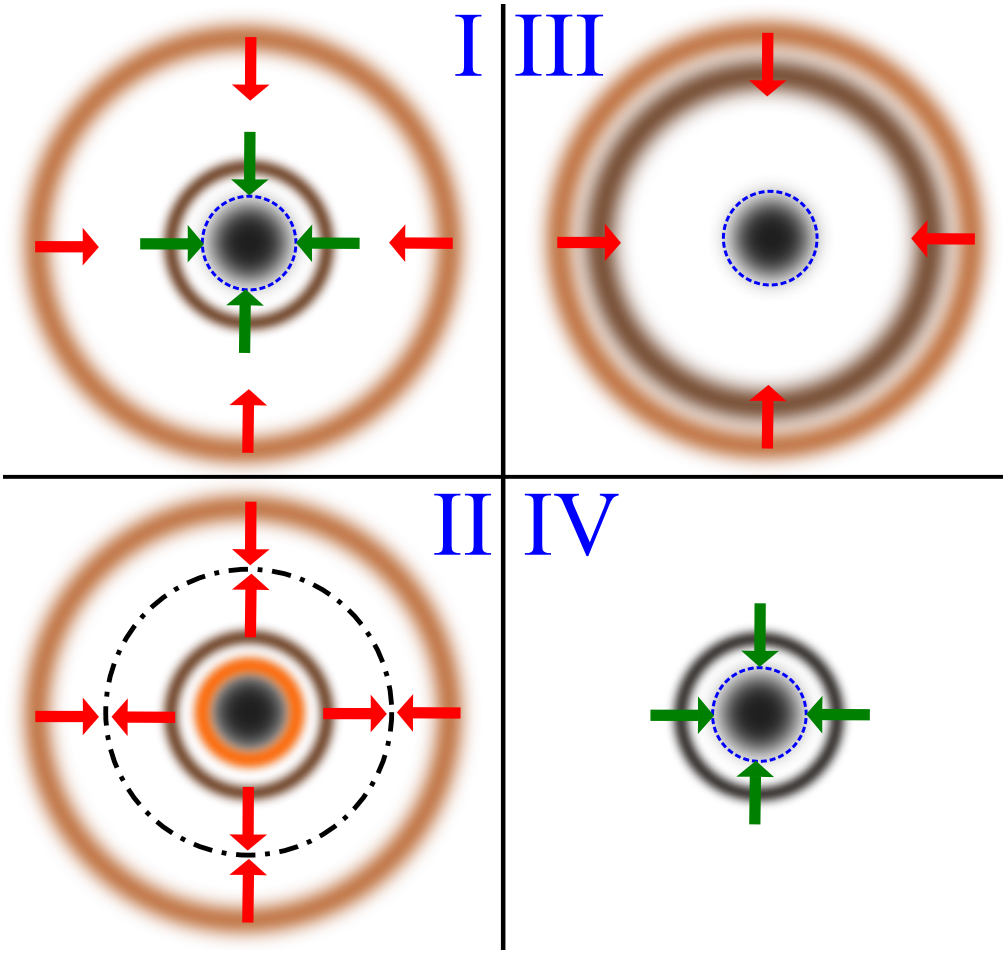

FIGURE 3.5: Schematic description of the mechanism that progressively increases the emitted luminosity. Here we consider only two mass shells, but the system must be thought to be composed of an infinite number of them. The black hole is at the center of the four panels, in black. Brown circles are mass shells: the darker the shell, the higher the density. The smallest circle is the accretion boundary: it becomes orange when the black hole irradiates. Green arrows indicate accretion through the inner boundary, red arrows indicate a movement of the mass shell. The black dot-dashed line indicates the radius r_τ. See the text for a detailed description of the panels.

the entire integration time, including the idle phases (when the accretion does not take place) and it is in substantial agreement with the approximated (i.e. valid for small inflow velocities) relation given in Eq. 3.38. Fig. 3.6 shows the spatial profiles for the FS simulation.

From the analysis of the spatial profiles, three main features are evident: (i) a density wave approaching the center, (ii) large pressure waves moving towards larger radii, visible from the velocity profile and (iii) the progressive emptying of the outer regions (discussed below).

The density wave, with over-densities as high as $\sim$ 1 order of magnitude with

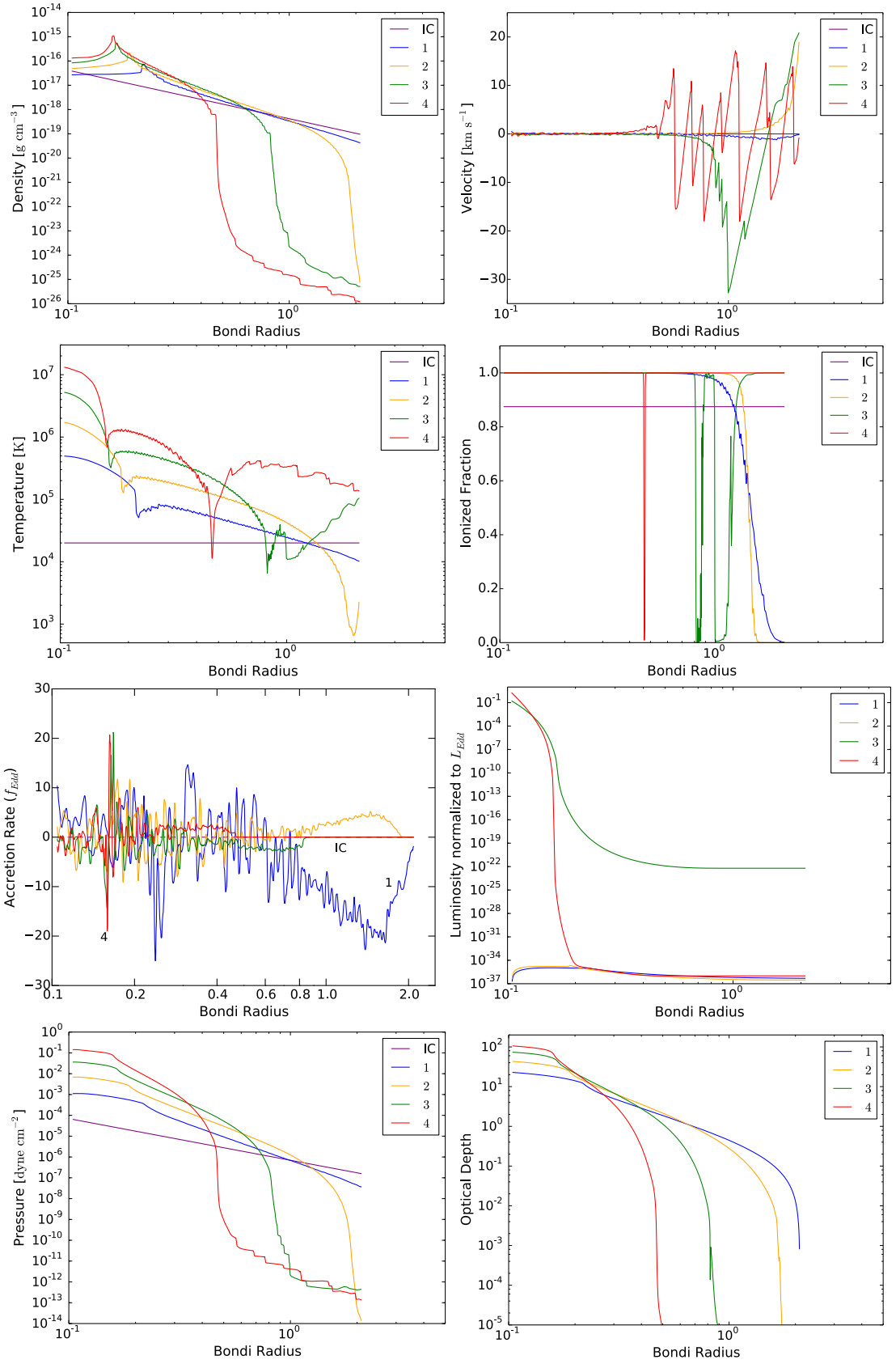

FIGURE 3.6: Spatial profiles for the FS simulation: total integration time is $T_{tot} \approx 1.4 \times 10^8$ yr and $T_{tot} = i\,\Delta t$ with $\Delta t = 35$ Myr and $i = 1, \ldots 4$.

respect to the surrounding volume, moves in the inward direction, contrarily to the T2 simulation. This difference is due to the fact that in the FS simulation the radiation pressure and the accretion rate are interconnected, while in the T2 run the former is fixed: this joint evolution leads to a smooth increase in the emitted luminosity and to a different response of the system.

When the IMBH accretes at super-critical rates, the emitted radiation promptly interrupts the mass inflow and consequently the radiation pressure. The accelerated gas moves in the outward direction creating a pressure jump of $\sim 50\%$ between the two sides of the shock front (see the pressure spatial profile in Fig. 3.6). Eventually, the gravitational acceleration of the IMBH inverts the velocity and the accretion starts again.

The radiation pressure affects only a small volume, in the inner section of the accretion flow where $\tau \sim 10 - 100$, as the optical depth spatial profile shows: the internal layers ($r \ll r_\tau$) of the gas distribution are intermittently reached by the radiation pressure, while the external layers ($r \gg r_\tau$) are in a quasi free-fall state. For this reason, similarly to the mechanism detailed in Fig. 3.5, the density wave progressively moves towards the center, leading to an increase of ~ 1 order of magnitude in the density measured at the innermost cell, as Fig. 3.7 shows. The top of the density wave R_{dw} moves inward with the time scaling: $R_{dw} \propto t^{-0.7}$.

The optical depth of the inner regions is increased along with the density: this additional effect progressively decreases the volume where the radiation pressure is effective. The luminosity panel is described in a separate subsection below.

The velocity spatial profile shows that the outer regions ($R \gtrsim 0.5 R_B$) are swept by waves of high-speed ($10 - 20\,\mathrm{km\,s^{-1}}$) gas. This volume, while not affected by radiation pressure, is strongly affected by the thermal pressure exerted from the internal layers: the pressure spatial profile shows, in the external regions, pressure jumps as high as $\sim 6 - 7$ orders of magnitude. As the radiation pressure is intermittent, the net result is the formation of waves in the surrounding gas, whose magnitude and frequency increase with time: an always increasing energy is transported outward by this mechanism.

Finally, the temperature spatial profile shows values as high as $\sim 10^7\,\mathrm{K}$ in the proximity of the inner boundary, at late stages of accretion, caused by the very

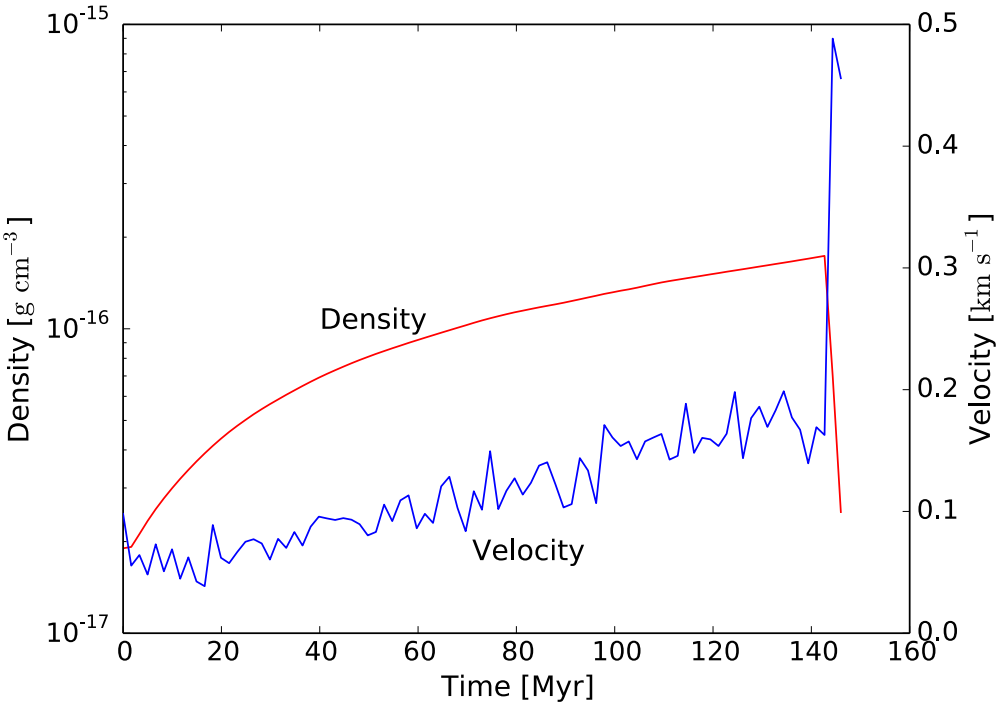

FIGURE 3.7: Time evolution of density and velocity computed at the innermost cell of the spatial grid. It most clearly shows, along with the following Fig. 3.8, the final evolution phase. At the time $\sim 142\,\mathrm{Myr}$, a jump of a factor ~ 3 in the velocity marks the final act in the evolution of the system: the remaining gas is eventually ejected outward.

large pressure and density. The temperature spatial profile is reflected in the ionized fraction: the ionized volume expands outward with time.

The complicated behavior of the mass flux spatial profile is a symptom of chaotic motions occurring in the environment, caused mainly by the intermittent irradiation. The last two data dumps of the FS simulation show a very small mass flux in the external layers, due to the fact that $\dot{M}_\bullet(r) \propto \rho(r)$.

3. **Final Burst**: this events marks the end of the accretion flow onto the IMBH, $\sim 142\,\mathrm{Myr}$ in the simulation. The gas is swept away and the accretion rate goes to zero: the black hole becomes a dark relic, having exhaled its "last gasp".

   As the central density increases, the emitted luminosity rises as well, as shown in Fig. 3.8, standing always a factor $\sim 2-3$ higher than the Eddington luminosity. This trend is highlighted by the shaded region in the same plot, which shows the value of f_{Edd}: after an initial transient period lasting $\sim 20\,\mathrm{Myr}$ and due to the necessity of stabilizing the accretion flow, the gap with respect to the Eddington luminosity increases with time: the emission is progressively more super-critical.

The value of f_{Edd} here is computed including the idle phases: being the duty-cycle ~ 0.48, the value of f_{Edd} computed considering only the active phases would be doubled.

The radiated luminosity reaches the value $\sim 3 \times 10^{45}\,\mathrm{erg\,s^{-1}}$ ($f_{Edd} \sim 3$) and the density in the external layers drops: the remaining mass inside the computational domain is a factor ~ 25 lower than the initial one, due to both the accretion onto the compact object and the outflow. Differently with respect to the T2 simulation, when the radiation pressure was fixed to a super-critical value, its direct linkage to the mass inflow progressively voids the halo outside-in. The external layers are not able to exert a sufficient pressure to contain the expansion of the radiation-driven shell and, as a consequence, the remaining gas is ejected from the system.

This effect is most clearly visible in Fig. 3.7, which shows the velocity evolution measured at the innermost cell. The general increasing trend ($\sim 10^{-3}\,\mathrm{km\,s^{-1}\,Myr^{-1}}$) in magnitude of the central velocity is abruptly changed by a jump of a factor ~ 3. The internal layer starts to move outward with velocities of $\sim 0.5\,\mathrm{km\,s^{-1}}$. The same effect is hinted at in the Fig. 3.8, where the accretion (and consequently the emitted luminosity) is abruptly blocked. After a transient period, the velocity might be re-inverted, but the very low value of the gas mass still inside R_B strongly suggests that the evolution time scale of this system with $M_0 = 10^5\,\mathrm{M_\odot}$ is indeed of order 100 Myr.

3.4.3.2 Black hole growth

After having investigated the space and time evolution of the accretion flow, we devote some further analysis to the black hole growth, more specifically to the accretion time scale and the final mass balance.

An important diagnostic quantity for the accretion process is the duty-cycle, defined in Sec. 3.2. A direct comparison between the three simulations shows that the evolutionary time scales are quite different. As a simple estimator, the Table 3.2 reports for each simulation the time t_{2M_0} needed for the IMBH to double its initial mass, along with the final mass reached at the end of the integration time. These time scales are very different between the T1-T2 simulation (both of order $\sim 10^4\,\mathrm{yr}$) and the FS simulation ($\sim 5 \times 10^6\,\mathrm{yr}$) because their average accretion duty-cycles are different, i.e. the FS

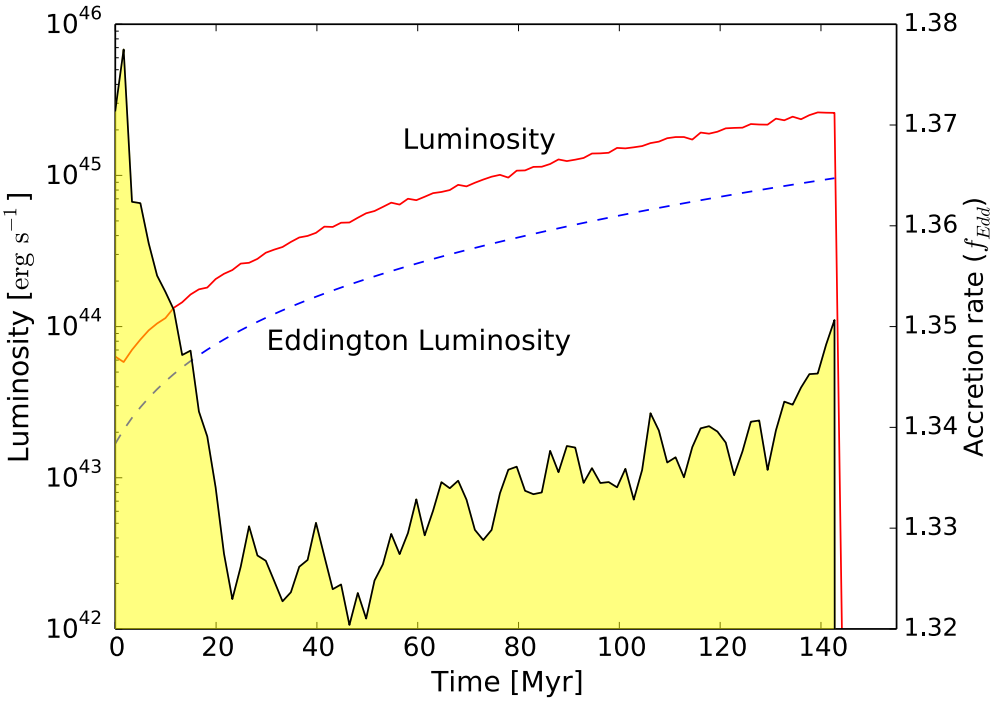

FIGURE 3.8: Time evolution of the emitted luminosity and of f_{Edd} (the accretion rate normalized to the Eddington value) computed at the innermost cell. The smoothness of the lines is due to an averaging process over a time much longer than the typical idle periods of the accretion. The value of f_{Edd} is computed as a running average over a window period much longer than the typical duration of the duty-cycle and includes the idle phases. The blue dashed line shows the corresponding time evolution of the Eddington luminosity, which increases as the black hole mass grows. At the time ~ 142 Myr the accretion is abruptly terminated by the final burst.

TABLE 3.2: Diagnostic quantities for the two test (T1 and T2) simulations and for the full one (FS), specifically the time t_{2M_0} needed to double the initial mass of the black hole and its final mass reached at T_{tot}.

Parameter	T1	T2	FS
t_{2M_0} [yr]	$\sim 3 \times 10^4$	$\sim 4 \times 10^4$	$\sim 5 \times 10^6$
Final BH mass [$M_\odot$]	$\sim 2.0 \times 10^5$	$\sim 1.4 \times 10^5$	$\sim 7.0 \times 10^6$

system spends a smaller fraction of the integration time accreting. The duty-cycle is strictly dependent on the magnitude of the radiative force, as we have shown in the subsection dedicated to the T2 simulation with simple analytic arguments. In the FS simulation the luminosity is computed self-consistently and it reaches large values, due to the super-critical f_{Edd}. The duty-cycle stabilizes on average to a value ~ 0.48, in agreement with the prediction of the approximated Eq. 3.38 (see also Park & Ricotti 2012), but varies in the range $0.2 \lesssim \mathcal{D} \lesssim 1$.

Furthermore, we have calculated the quantity of gas accreted by the IMBH and the

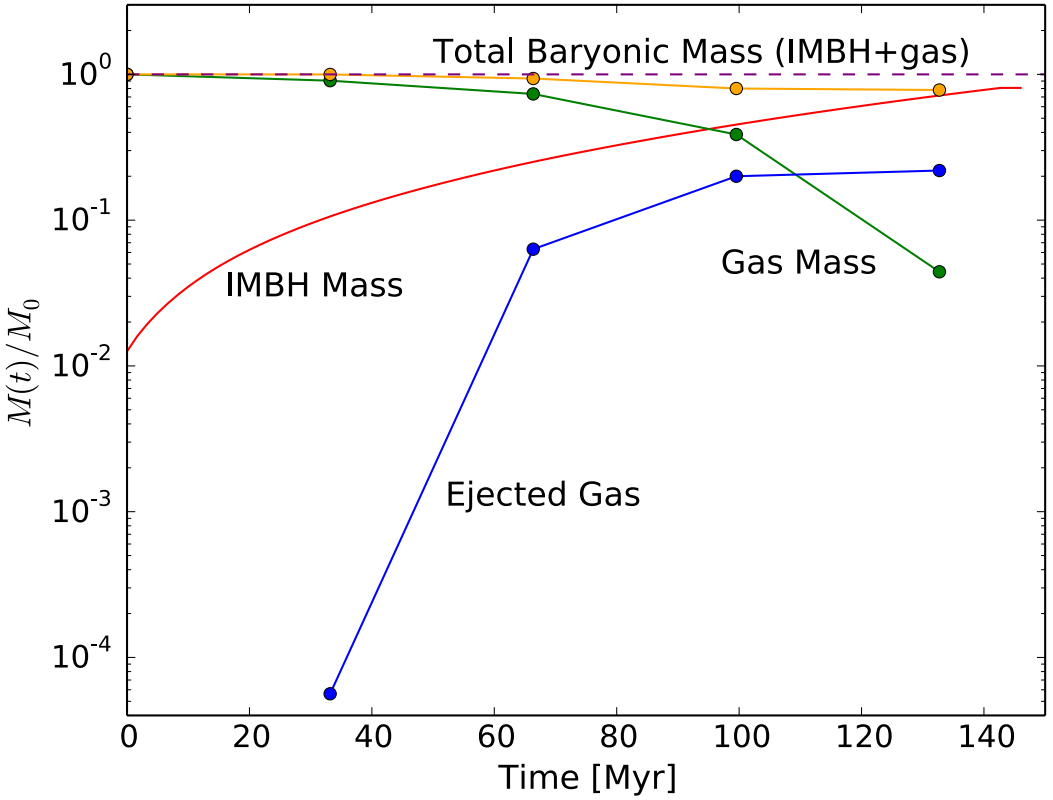

FIGURE 3.9: Final mass balance for the FS simulation. All masses are normalized to the initial value of the gas mass, $M_{gas} \sim 9.6 \times 10^6\,\mathrm{M}_\odot$. The dashed purple line is only a reference for the unitary value. The IMBH mass line is smoother and extended to a longer time than the others because the corresponding output value is saved at a very high frequency, while other quantities are more discretized.

amount ejected from the system, before the final burst. The density spatial profile in Fig. 3.6 shows that at the end the outer layers of the volume are almost empty: in about $\sim 120\,\mathrm{Myr}$ (the time of the last complete data dump) the density drops by ~ 7 orders of magnitude. The matter is partly accreted by the central object, partly ejected from the outer boundary of the system by high-speed pressure waves, as described above.

Our final results for the mass balance are summarized in Fig. 3.9. The baryonic mass of the halo is reduced by a factor ~ 25 from the beginning of the simulation. Most of this mass ($\sim 90\%$) is accreted onto the black hole, while $\sim 10\%$ is ejected from the outer boundary of the system. Starting from a DCBH of mass $M_0 = 10^5\,\mathrm{M}_\odot$, the final mass of the black hole is $M_\bullet \sim 7 \times 10^6\,\mathrm{M}_\odot$, a fully fledged SMBH.

3.4.3.3 Radiation emission

The study of the luminosity emitted from the IMBHs is one of the main objectives in this work. Due to the high values of the optical depth (see its spatial profile in Fig. 3.6), the luminosity is almost completely obscured for an external observer. The column density reaches values $\sim 10^{25}\,\mathrm{cm}^{-2}$ in the late stages of the FS simulation.

The spatial profile of the emitted luminosity is shown in Fig. 3.6. The luminosity emitted via bremsstrahlung (lower lines of the luminosity panel in Fig. 3.6, corresponding to data dumps when the black hole is not accreting) is, in this spatial range, completely negligible. The lines show two important facts: (i) the luminosity emitted near the accretion boundary slowly increases, due to the mechanism already detailed in this section and (ii) the radiation that escapes from the outer boundary decreases and is blocked at progressively smaller radii. The latter effect is due to the accumulation of matter at smaller distances from the center. In fact, the density measured at the innermost cell increases by a factor ~ 10 during the time evolution of the system, as the density spatial profile in Fig. 3.6 demonstrates. Combining this fact with the density dependence of the spatial derivative of the luminosity ($dL/dr \propto -\rho\kappa L$, see Sec. 3.3) completely explains the behavior of the luminosity panel in Fig. 3.6. To conclude, the luminosity emitted during the accretion process onto an IMBH at high-z is obscured for most of the evolution of the system. We predict that it might be observable during the initial phase of the accretion, when the central density is still low, and during the final burst of radiation.

In order to have a rough estimate of the observability of the latter phase, we assume that the peak luminosity $L_{peak} \sim 3 \times 10^{45}\,\mathrm{erg\,s}^{-1}$ is emitted in a small ($\Delta\lambda/\lambda \ll 1$) range of Far-IR wavelengths centered at $\lambda = 2\,\mu$m with a flat spectrum (for a detailed study of the contribution of DCBHs sources to the cosmic infrared background, see Yue et al. 2013). For a source located at $z = 10$, the radiation intensity would be $\mathcal{I} \approx 10^{-6}\,$Jy, which is observable by the future JWST with only $\sim 100\,$s of integration, yielding a Signal-to-Noise ratio[2] of ~ 250. Of course, in order to produce more accurate predictions for the observability, it is necessary to take into account the frequency of these events at high-z and the exact emission spectrum of the source: we defer this to future work.

[2]Estimate performed with the JWST prototype Exposure Time Calculator (ETC).

3.5 Discussion and Summary

In this chapter we have investigated the radiation-hydrodynamic evolution of the spherical accretion flow onto an IMBH with initial mass $M_0 = 10^5\,\mathrm{M}_\odot$ and gas mass in the parent halo $M_{gas} = 9.6 \times 10^6\,\mathrm{M}_\odot$.

The IMBH accretes for $\sim 142\,\mathrm{Myr}$ with an average duty-cycle ~ 0.48 and accretion rates super-critical on average, with $f_{Edd} \simeq 1.35$, i.e. $\dot{M}_\bullet \simeq 0.1\,\mathrm{M}_\odot\,\mathrm{yr}^{-1}$. The emitted luminosity increases with time, as a consequence of the progressive growth of the accretion flow. The radiation pressure creates large density waves moving, with velocities as high as $\sim 20\,\mathrm{km\,s}^{-1}$, in the outer ($r \gtrsim 0.5\,R_B$) section of the accretion flow.

At the end of the simulation $\sim 90\%$ of the gas mass has been accreted onto the compact object, while $\sim 10\%$ has been ejected. The accretion is terminated when the emitted luminosity reaches the value $\sim 3 \times 10^{45}\,\mathrm{erg\,s}^{-1} \sim 3\,L_{Edd}$ and the related radiation pressure ejects all the remaining gas mass (which, at the final time, is a factor of ~ 25 lower than the initial one). We estimate that this final burst of radiation should be observable by the future JWST. We have identified three different phases of the accretion (the initial phase, the main accretion phase and the final burst), detailing their main characteristics in turn.

We predict that the accretion flow, on average, occurs at mildly super-critical rates for the total evolution of the system (except the very initial transient phase). Recently, Alexander & Natarajan (2014), Volonteri et al. (2015) and Madau et al. (2014), but see also Volonteri & Rees 2005, have suggested that brief but strongly super-critical accretion episodes (with rates as large as $f_{Edd} \gtrsim 50$) might explain the rapid black hole mass build-up at $7 \lesssim z \lesssim 20$. Very large and prolonged accretion rates may be sustainable in the so-called "slim disk" solution (Begelman & Meier 1982, Paczynski & Abramowicz 1982, Mineshige et al. 2000, Sadowski 2009, 2011), an energy-advecting, optically thick flow that generalize the standard thin disk model (Shakura & Sunyaev, 1976). In these radiatively inefficient models the radiation is trapped (see also the diffusion condition in Sec. 3.3) into the high-density gas and is advected inward by the accretion flow: this happens when the photon diffusion time exceeds the time scale for accretion. This would allow a very mild dependence of the emitted luminosity L on the normalized accretion rate f_{Edd}, which is usually described as a logarithmic dependence

(Mineshige et al. 2000, Wang & Netzer 2003): $L/L_{Edd} \sim 1[1 + 2\ln(f_{Edd}/50)]$, valid for $f_{Edd} \geq 50$. The following Chapter 4 provides a much broader description of the slim disk solution and, in general, of radiatively inefficient accretion flows.

In our work, we analyze the accretion flow on very large scales ($R \sim R_B$, i.e. the accretion disk is beyond our resolution limit) and photons are never trapped (see Sec. 3.3). For this reason, the accretion flow is radiatively efficient so that $L/L_{Edd} \sim f_{Edd}$ and the accretion rates are only mildly super-critical: $f_{Edd} \simeq 1.35$ on average. In our case, the idle phases are caused by the necessity to re-establish the downward accretion flow after the radiation burst, while in the strongly super-critical models they are caused by the need for replenishing the gas reservoirs (e.g. by galaxy mergers, see e.g. Volonteri et al. 2015). In our simulation, at smaller radial distances ($R \ll R_B$) we expect that the radiation eventually reaches the trapping condition. This is neglected in the present implementation of the simulation, but could critically modify the radiative properties of the source, especially in the light of recent studies on strongly super-critical accretion.

Some aspects of the simulation may be improved, namely:
(i) The accreting gas, at smaller radii, should form an accretion disk. If the accretion flow has a non-zero angular momentum with respect to the central body, the gas will reach a centrifugal barrier (caused by the steeper radial scaling of the centrifugal acceleration, $\sim r^{-3}$, with respect to the gravitational acceleration, $\sim r^{-2}$) from which it can accrete further inward only if its angular momentum is transported away. This would at least partly modify the irradiation mechanism.
(ii) A full spectral analysis of the source needs a more accurate description of the interaction between radiation and matter, also including additional heating/cooling mechanisms.
(iii) At smaller radial distances the photons should be trapped and the accretion flow should become energy-advective, i.e. radiatively inefficient, as described above. An appropriate modeling of the inefficient accretion flow would then be required.
(iv) The magnetic field may also significantly affect the accretion flow structure and behavior, as already pointed out in e.g. Sądowski et al. (2015) and McKinney et al. (2014). The inclusion of an appropriate modeling of the magnetized plasma would then be required.
Some of these issues are already tackled in the following Chapter 4.

This work is the basis upon which a full spectral analysis of these sources is to be constructed: this would be the key to unveil the eventual existence of IMBHs during the Cosmic Dawn era (see Chapter 5).

The existence of IMBHs at high redshifts, although not observationally confirmed at the present time, would represent a breakthrough in our knowledge of the primordial Universe. We summarize their theoretical relevance with the following two statements:
(i) The formation of IMBHs in the early Universe would ease the problem of the presence of SMBHs with masses $M_\bullet \sim 10^9\,\mathrm{M}_\odot$ at redshifts as high as $z \approx 7.085$ (Mortlock et al., 2011). These massive seeds would play a role of paramount importance in giving a jump start to the accretion process.
(ii) The formation of IMBHs at high redshifts could provide a possible interpretation of the near-infrared cosmic background fluctuations (Yue et al., 2013) and its recently detected cross-correlation with the X-ray background (Cappelluti et al., 2013). This interpretation would be even more plausible if the primordial population of IMBHs is proved to be highly obscured.

The observation of IMBHs could then provide the missing pieces for the solution of these intriguing puzzles.

Chapter 4

The Growth Efficiency of High-Redshift Black Holes

4.1 Introduction

As already detailed in Chapter 3, recent observations (Mortlock et al., 2011, Wu et al., 2015) have detected the presence of optically bright quasars at redshifts as high as $z \sim 7$. These high-energy sources are powered by accretion onto SMBHs, suggesting the presence of compact objects with mass $M_\bullet \sim 10^{9-10}\,\mathrm{M}_\odot$ less than 1 Gyr after the Big Bang (Fan et al., 2006). This evidence contrasts with the standard theory of black hole growth, which requires a longer time to build up such massive objects (see Haiman 2013 for a recent review), due to: (i) the low mass of some of the proposed seeds, born out of first-generation (Pop III) stars, with masses $M_\bullet \lesssim 10^3\,\mathrm{M}_\odot$ (Madau & Rees, 2001, Bromm & Loeb, 2003, Petri et al., 2012), and (ii) the maximum growth rate allowed for a radiatively efficient and spherical inflow, the Eddington rate, which provides a lower limit for the time scale of the process (Jeon et al., 2012). Generally speaking, the luminosity L emitted due to a gas inflow with an accretion rate $\dot{M} \equiv dM/dt$ is $L = \epsilon c^2 \dot{M}$, where ϵ is the matter-radiation conversion factor and c is the speed of light. In the standard scenario, a black hole grows in mass exponentially, with a time scale given by the Salpeter time $t_S \sim 0.045\epsilon_{0.1}\,\mathrm{Gyr}$, where $\epsilon_{0.1}$ is normalized to the standard value of 10%: starting from a low-mass seed ($M_\bullet \sim 100\,\mathrm{M}_\odot$), this process would require a *constant* accretion at the Eddington rate up to $z \sim 7$ to build up a $\sim 10^9\,\mathrm{M}_\odot$ SMBH.

Several ways to overcome these limitations have been proposed in the literature. The possibility of giving a jump start to the growth process through more massive seeds has been investigated thoroughly (see e.g. Volonteri 2010) with a variety of mechanisms: (i) the direct collapse of self-gravitating pre-galactic disks at high-redshifts (Lodato & Natarajan 2006, Begelman et al. 2006, Lodato & Pringle 2007), (ii) the formation of a very massive star from runaway stellar mergers in a dense cluster (Devecchi & Volonteri 2009, Davies et al. 2011) and (iii) the collapse of a primordial atomic-cooling halo, exposed to a Lyman-Werner flux of sufficient intensity, into a DCBH, through a general relativistic instability (Shang et al. 2010, Johnson et al. 2012, Ferrara et al. 2014).

An alternative scenario assumes that accretion rates are not capped by the Eddington limit (Volonteri & Rees, 2005). Recent works (Alexander & Natarajan 2014, Madau et al. 2014, Volonteri et al. 2015) have proposed the occurrence of short and recurring, but strongly super-critical (i.e. super-Eddington) accretion episodes at high-redshifts, with rates as large as $50 - 100$ times the Eddington limit $\dot{M}_{Edd} \equiv L_{Edd}/(\epsilon c^2)$, where:

$$L_{Edd} \equiv \frac{4\pi G M_\bullet c}{\kappa_T} \,. \tag{4.1}$$

In the definition of the Eddington luminosity, G is the gravitational constant and κ_T is the Thomson opacity. The radiative efficiency of the gas inflow depends on the accretion rate. Recalling the definition of the Eddington luminosity (Eq. 4.1), we define $f_{Edd} \equiv \dot{M}_\bullet/\dot{M}_{Edd}$, i.e. the accretion rate normalized to the Eddington value, like in Chapter 3. It is expected that if matter is accreted at moderate rates $0.01 \lesssim f_{Edd} \lesssim 1$, the inflowing material creates a radiatively efficient, geometrically thin and optically thick accretion disk (Shakura & Sunyaev, 1973). In this case the radiative efficiency depends only on the black hole spin, and varies from $\sim 6\%$ for Schwarzschild black holes to $\sim 32\%$ for maximally rotating ones (Thorne, 1974). If, instead, accretion occurs super-critically ($f_{Edd} > 1$) the structure of the accretion disk is modified because of advection: the energy produced in the disk is carried inwards, in the black hole, rather than being radiated away (see, e.g., Abramowicz & Fragile, 2013, Lasota, 2015). The disk thickness increases and the disk becomes geometrically thick. The most common solution proposed for such accretion flows is the "slim disk" (Abramowicz et al. 1988, Paczynski & Abramowicz 1982, Mineshige et al. 2000, Sadowski 2009, 2011, McKinney et al. 2014), radiatively inefficient and with a thick geometric structure, in which photon

trapping is significant inside the trapping radius R_{pt}:

$$R_{pt} = \frac{R_S}{\epsilon} \frac{\dot{M}}{\dot{M}_{Edd}}, \tag{4.2}$$

where R_S is the Schwarzschild radius. Only a fraction of the photons produced by the viscous process inside the accretion flow is able to free stream out of the trapping radius, because the photon diffusion time exceeds the time scale for accretion. Consequently, the effective radiation pressure acting on the surrounding gas is decreased (see e.g. Begelman 1978, Ohsuga et al. 2002) and the luminosity is only mildly (e.g., logarithmically) dependent on the accretion rate. Alternatives of the slim disk solution exist, e.g the ZEro-BeRnoulli Accretion (ZEBRA, Coughlin & Begelman, 2014) and the ADiabatic Inflow-Outflow Solutions (ADIOS, Blandford & Begelman, 1999, Begelman, 2012) models, which allow for a fraction of the inflowing mass to be lost during the accretion process.

The present chapter investigates, both analytically and numerically, the growth of high-redshift ($z \sim 10$) black hole seeds. The growth process may be controlled by the amount of gas available in the halo (feeding-dominated) or by the radiative feedback (feedback-limited). The growth is feeding-dominated if the radiative back-reaction of the black hole is negligible: the rapidity of the process is mainly determined by the gas accretion rate that the host halo can provide. The black hole growth is more efficient and rapid if the flow is feeding-dominated, assuming that a sufficient amount of gas is present in its host halo.

We devise a very general analytic model that is able to predict the growth efficiency from the physical properties of the system formed by the black hole seed and its host halo. Furthermore, we employ a radiation-hydrodynamic code to follow the growth process from small (0.002 pc) to large scales ($\gg R_B$, where R_B is the Bondi radius), spanning a spatial dynamic range of four orders of magnitude, with special emphasis on the properties of the inner regions of the host halo, providing most of the accretion material to the central object. The spatial dynamic range employed in the current simulations is much bigger than the one detailed in Chapter 3. The growth is monitored as a function of different parameters, namely: the accretion model (radiatively efficient or inefficient), the density profile of the halo $\rho(r)$ and the initial mass of the seed $M_0 = 10^{3-6}\,\mathrm{M}_\odot$.

This chapter extends the work detailed in Chapter 3, where we simulated in great detail

the accretion process onto a $z \sim 10$ black hole seed of initial mass $10^5\,M_\odot$, embedded in a dark matter halo with a gas mass of $\sim 10^7\,M_\odot$ and with extreme density conditions (a number density of hydrogen particles at ~ 0.1 pc from the center of the halo $\sim 10^7\,cm^{-3}$), finding that in ~ 142 Myr about 90% of the gas mass of the halo has been accreted onto the compact object.

In this general framework, we aim at clarifying several aspects, including (i) do the radiatively inefficient accretion models provide an effective way to rapidly increase the mass of the seed? If so, why? (ii) What is the final fate of black hole seeds as a function of their initial mass? How long can they accrete? (iii) Is it possible to predict the growth efficiency of the accretion process from the physical properties of the (black hole + host halo) system? In the cosmological context, answering these questions will provide some insights into the mass that has been locked inside black holes during the cosmic evolution. This would be of great interest to understand both the formation of high-redshift SMBHs and their remnant population.

The outline of this chapter is as follows. In Sec. 4.2 we briefly describe the physics and equations of the radiation-hydrodynamic problem, along with the initial conditions for the density profiles. In Sec. 4.3 we present our analytic model for the black hole growth, while in Sec. 4.4 we show the results of our simulations. Finally, in Sec. 4.5 we provide some further discussion and a summary. Throughout, we adopt recent Planck cosmological parameters (Planck Collaboration et al., 2015) as reported in Table 1.1.

4.2 Physical and Numerical Implementation

The present study employs a series of radiation-hydrodynamic simulations to test the predictions of our growth model. Our code (see Chapter 3) is designed to perform a fully consistent treatment of uni-dimensional spherically-symmetric hydrodynamic equations and a simplified, frequency-integrated, version of radiative transfer equations. While the spherical symmetry is an idealization of a real accretion flow, several works have shown that 1D simulations provide a reliable description of many of its most important features. For instance, in Novak et al. (2011) the authors performed a comparative analysis between the outputs of a code run in 1D and 2D, finding similar results in

terms of black hole growth and duty cycle. The main difference, for which the multi-dimensional approach is a significant improvement, concerns the fact that the additional degrees of freedom allow classical instabilities (e.g. the Rayleigh-Taylor and the Kelvin-Helmholtz ones) to operate. Their net effect is to produce a somewhat higher accretion rate, a less effective feedback and a more irregular pattern of bursts, compared with the 1D case. Notwithstanding the dimensionality of the code, our implementation cannot take into account the full complexity of the accretion flow, which only a more advanced treatment of angular momentum transport would allow. Due to the triaxiality of the host halo, the angular momentum field is extremely complex and variable in time, at every location inside the inflow (see Choi et al. 2013, 2015). Overall, the outward angular momentum transfer is very efficient (Choi et al., 2015), due to the gravitational torques induced by both the dark matter and the gas distributions. The gas loses its angular momentum efficiently and flows well beyond its centrifugal barrier: the gas that reaches the black hole is expected to have low angular momentum. Therefore, despite its simplifications, our approach helps in acquiring physical insight on the process of black hole growth. In this section we present a general overview of the most important aspects of the physical implementation, while the interested reader is referred to Chapter 3 for a detailed description of the code.

The domain of our simulations[1] spans approximately from 0.002 pc to 20 pc. The characteristic spatial scale for accretion is the Bondi radius R_B:

$$R_B = \frac{GM_\bullet}{c_{s(\infty)}^2} \,. \tag{4.3}$$

Here, $c_{s(\infty)}$ is the sound speed at large distances from the black hole, defined as:

$$c_{s(\infty)} = \sqrt{\frac{\gamma R T_\infty}{\mu}} \,, \tag{4.4}$$

where $\gamma = 5/3$ is the ratio of specific heats, R is the gas constant, T_∞ is the gas temperature at large distances and $\mu = 1.15$ is the mean molecular weight for a primordial gas. For instance, the Bondi radius corresponding to a seed with initial mass $M_\bullet = 10^5\,\mathrm{M}_\odot$ with $c_{s(\infty)} \sim 12\,\mathrm{km\,s^{-1}}$ (i.e. $T_\infty \sim 10^4\,\mathrm{K}$) is $R_B = 3\,\mathrm{pc} \sim 10^{-3}\,R_{\mathrm{vir}} \sim 10^8\,R_{\mathrm{S}}$, where R_{vir}

[1] We performed a series of convergence tests on the extension of the spatial range (see Chapter 3) that confirmed that the main outputs of our simulations (e.g. duty cycles and accretion rates) do not depend on it as long as (i) it covers a sufficiently large radial range around R_B (e.g. from $\sim 0.1R_B$ to $\sim 2R_B$) and (ii) the centrifugal radius, where the accretion disk starts to form, is not resolved.

is the virial radius of the halo. Our spatial range, spanning ~ 4 orders of magnitude, covers the entire range of R_B corresponding to an initial mass of the seed within the range $10^{3-6}\,\mathrm{M}_\odot$.

In the hydrodynamic module we solve the standard system of ideal, non-relativistic Euler's equations (conservation laws for mass, momentum and energy, neglecting viscosity, thermal conduction and magnetic fields) for a primordial (H-He) composition gas with helium fraction $Y_P = 0.24665$ (Planck Collaboration et al., 2015) and no metals, spherically accreting onto a central black hole, assumed at rest and already formed at the beginning of the runs, with a given initial mass $M_0 \equiv M_\bullet(t=0)$. The infalling gas has zero angular momentum with respect to the black hole.

The forces acting on the gas are: (i) the thermal pressure, (ii) the gravitational pull of the black hole and (iii) the radiation pressure. The thermal pressure is given by the usual equation for ideal gases:

$$P_g = \frac{\rho R T}{\mu}\,, \tag{4.5}$$

where ρ is the mass density. The gravitational acceleration at the distance r from the central object is:

$$g(r,t) = -\frac{G M_\bullet(t)}{r^2}\,. \tag{4.6}$$

The value of the black hole mass $M_\bullet(t)$ changes with time, due to gas accretion, with the following set of rules, where $\dot{M}_\bullet = 4\pi r^2 \rho |v|$:

$$\begin{cases} \dot{M}_\bullet(t) \neq 0 \;\;\Leftrightarrow\;\; v(r=r_0,t) < 0 \\ M_\bullet(t) = M_0 + (1-\epsilon)\int_0^t \dot{M}_\bullet \,\mathrm{d}t \end{cases} \tag{4.7}$$

where v is the velocity of the gas and ϵ ranges[2] from $\epsilon = 0.057$ for a Schwarzschild (i.e., non-rotating) black hole to $\epsilon = 0.32$ for a maximally rotating object (see Thorne 1974). The mass flow $\dot{M}_\bullet$ is computed at the accretion radius r_0 (the innermost cell of our spatial grid) and it is equivalent, by definition, to the accretion rate onto the black hole. The acceleration caused by the radiation pressure is:

$$a_{rad}(r) = \frac{\kappa(\rho,T) L(r)}{4\pi r^2 c}\,, \tag{4.8}$$

[2]We assume that the matter-radiation conversion factor ϵ is numerically equal to the accretion efficiency η, i.e. all the gas reaching the inner boundary is actually accreted by the black hole (see e.g. Sadowski et al. 2014, McKinney et al. 2014, Jiang et al. 2014).

where L is the emitted luminosity and $\kappa(\rho, T)$ is the opacity of the gas, which includes the Thomson term (with the additional inclusion of a temperature dependence, as in Begelman et al. 2008) and bound-free terms. In our code, all radiation-related quantities are integrated over frequencies: matter and radiation are coupled via Thomson (electron) scattering and bound-free interactions. The radiative transfer employs a simplified two-streams approximation presented in Novak et al. (2012), to which the interested reader is deferred for a detailed description.

The relation between the emitted luminosity $L_0 \equiv L(r_0)$ and the accretion rate $\dot{M}_\bullet$ is:

$$\begin{cases} L_0 \equiv \epsilon c^2 \mathcal{F}(\dot{M}_\bullet) & \text{if } v(r_0) < 0 \\ L_0 \equiv 0 & \text{if } v(r_0) \geq 0 \end{cases} \tag{4.9}$$

where $\mathcal{F}(\dot{M}_\bullet)$ is a generic function of the accretion rate. In the simple case of radiatively efficient accretion (treated in Chapter 3) the following relation holds:

$$\frac{L}{L_{Edd}} = f_{Edd}\,. \tag{4.10}$$

In the radiatively inefficient accretion mode (for instance, the slim disk solution) the luminosity L depends on f_{Edd} as in the following prescriptions (Mineshige et al., 2000, Volonteri et al., 2015):

$$\frac{L}{L_{Edd}} = \frac{f_{Edd}}{25} \quad (f_{Edd} < 50)\,, \tag{4.11}$$

$$\frac{L}{L_{Edd}} = 2\left[1 + \ln \frac{f_{Edd}}{50}\right] \quad (f_{Edd} \geq 50)\,. \tag{4.12}$$

In this scenario, only a fraction of the emitted luminosity escapes to infinity, and the effective radiation pressure depends only weakly on the accretion rate: note that $L = 2L_{Edd}$ for $f_{Edd} = 50$. In the radiatively inefficient accretion mode the matter-radiation conversion efficiencies are $\epsilon = 0.04$ for $f_{Edd} < 50$ and:

$$\epsilon = \frac{1}{25}\left(\frac{f_{Edd}}{50}\right)^{-1}\left[1 + \ln\left(\frac{f_{Edd}}{50}\right)\right] \leq 0.04\,, \tag{4.13}$$

for $f_{Edd} \geq 50$.

Due to radiation pressure, the accretion may occur in an intermittent manner. Therefore, it is useful to introduce the duty cycle, defined as the fraction of time spent accreting

within a given time frame of duration t_{tot}:

$$\mathcal{D} \equiv 1 - \frac{t_{idle}}{t_{tot}} \,. \tag{4.14}$$

Here, t_{idle} is the idle time, i.e. the time spent without accretion taking place.

4.2.1 The initial density profile

In this work we simulate the spherically-symmetric gas accretion onto a black hole seed at the center of a dark matter halo of virial temperature $T_{vir} \sim 10^4\,\mathrm{K}$ and total mass (dark matter and baryons) $M_h = 6.7 \times 10^8\,\mathrm{M}_\odot$ at $z = 10$. For $r \ll R_{vir}$, as in our computational domain, most of the mass is baryonic. We assume that the gas initially follows the isothermal ($T \sim 10^4\,\mathrm{K}$) density profile derived from the simulations in Latif et al. (2013a), well approximated by the functional form:

$$\rho(r) = \frac{\rho_0}{1 + (r/a)^2} \,, \tag{4.15}$$

where a is the core radius.

In order to study how the black hole growth depends on the host halo, we implemented two different density profiles, schematically shown in Fig. 4.1. A high density profile (HDP) with a central density $\rho_0 = 10^{-12}\,\mathrm{g\,cm^{-3}}$ and a core radius $a = 1.6 \times 10^{-3}\,\mathrm{pc}$ and a low density profile (LDP) with a central density $\rho_0 = 10^{-18}\,\mathrm{g\,cm^{-3}}$ and a core radius $a = 2\,\mathrm{pc}$. Both density profiles yield a total baryonic mass $M_{gas} \sim 10^7\,\mathrm{M}_\odot$ over the entire spatial domain. In the HDP case the spatial domain has been slightly enlarged, with respect to the LDP one, to fulfill this condition. The yellow-shaded area in Fig. 4.1 shows that the LDP may be interpreted as the density profile resulting after the formation of a black hole of mass $\sim 10^5\,\mathrm{M}_\odot$ at the center of the halo (see Latif et al. 2013b, 2014b). Consequently, the HDP may be interpreted as the density profile resulting after the formation of a very small ($\lesssim 10^3\,\mathrm{M}_\odot$) black hole seed, which leaves the matter distribution of the halo almost unaltered. In summary, we study four models: HDP with radiatively efficient accretion, HDP with radiatively inefficient accretion, LDP with radiatively efficient accretion, and LDP with radiatively inefficient accretion.

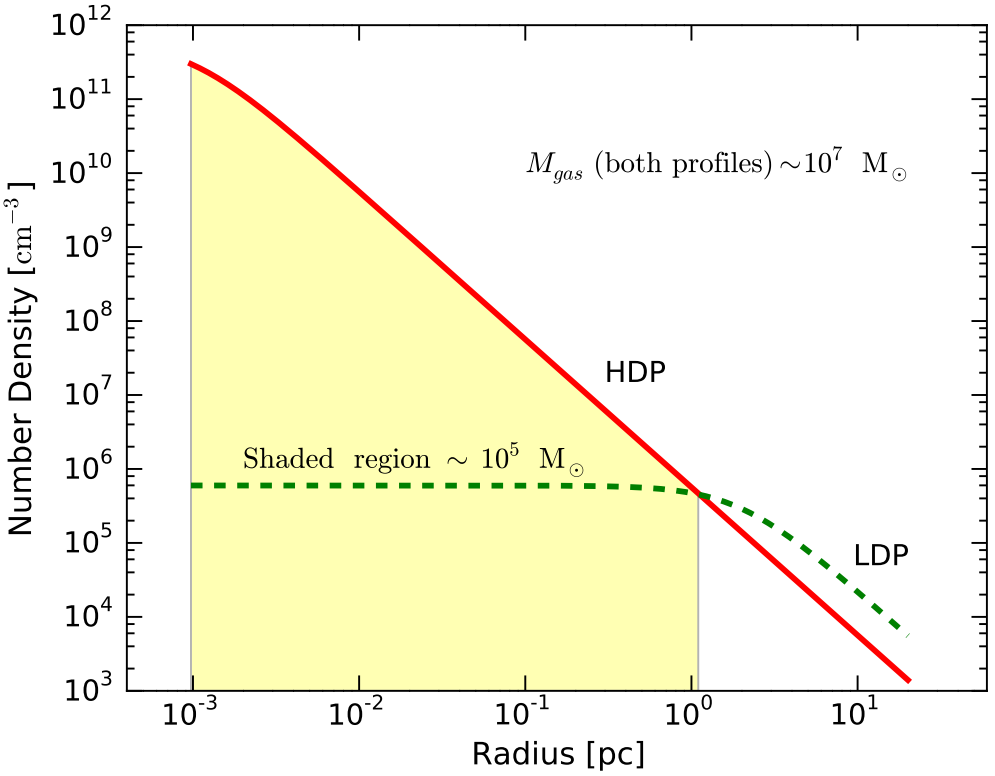

FIGURE 4.1: The two density profiles employed, both yielding a total baryonic mass of $\sim 10^7\,\mathrm{M}_\odot$ over the integration range. The LDP has a much larger core radius, but the central density is smaller by ~ 6 orders of magnitude. The yellow-shaded region contains a total mass of $10^5\,\mathrm{M}_\odot$ and may be interpreted as the gas which has been extracted from the HDP to produce a black hole of the same mass. Consequently, the HDP profile may be interpreted as the density profile resulting after the formation of a small black hole of mass $M_\bullet \lesssim 10^3\,\mathrm{M}_\odot$.

4.3 Analytical Insights

In this section we present our analytic model to describe the growth of high-redshift black holes. We predict whether the mass inflow is feeding-dominated or feedback-limited, as a function of the main physical properties of the (black hole + host halo) system. This analytic framework is then employed to determine a time-evolving spatial scale outside of which the radiative feedback is highly effective and outflows dominate. Moreover, we envisage the existence of a mass scale above which the accretion flow is always feeding-dominated.

4.3.1 Modeling the mass inflow

Our analytic model takes into account the following properties: (i) the density of the gas in the inner sections of the halo ρ_0, (ii) the mass of the black hole seed $M_\bullet$, (iii) the matter-radiation conversion factor ϵ, (iv) the Eddington factor f_{Edd}. Starting from quasi-static conditions, the accretion rate increases, due to the black hole's gravitational pull. The build-up of the accretion rate causes an increasing emission of radiation, which eventually might be able to stop the gas inflow, or even invert its velocity: this depends on the intensity of the radiation field and on the inertia of the gas. The rate at which the linear momentum of the gas is changed relies on the comparison between two time scales: (i) the feedback time scale, t_{fb}, defined as the time needed by the radiation pressure to significantly (i.e. by a factor e) change $\dot{M}_\bullet$, and (ii) the accretion time scale, t_{acc}, which estimates the time needed to consume the gas mass inside the inner regions of the accretion flow.

Given the general expression for the acceleration caused by the radiation pressure (Eq. 4.8) and the relations between the luminosity L and the Eddington factor f_{Edd} for radiatively efficient and inefficient flows (Eqs. 4.10, 4.11, 4.12), we calculate t_{fb}. The impulse theorem (radial component) states that $dp = Fdt$, where p is the linear momentum per unit volume of the gas, F is the force applied on the gas per unit volume and t is the time:

$$d(\rho v) = \rho a_{rad} dt = \rho \frac{\kappa}{4\pi c} \frac{L}{r^2} dt \,. \tag{4.16}$$

This equation needs to be evaluated at some radius representative of the accretion process onto the black hole. In a simulation, this radius is the innermost cell of the spatial grid, where the gas is assumed to be accreted by the black hole. From a purely theoretical point of view, it may be considered as the radius where the accretion disk forms. In either cases, we designate this spatial scale r_0, the accretion radius. Evaluating the previous equation at $r = r_0$ gives:

$$d(4\pi r_0^2 \rho_0 v_0) = \frac{\rho_0 \kappa_0}{c} L_0 \, dt \,. \tag{4.17}$$

Here, L_0 is computed with Eq. 4.9 and the mass flux is computed at the accretion boundary, corresponding to the accretion rate $\dot{M}_\bullet$. Therefore:

$$d\dot{M}_\bullet = \frac{\rho_0 \kappa_0}{c} L_0 \, dt \, . \tag{4.18}$$

We solve this ordinary differential equation with the initial condition $\dot{M}_\bullet(t = 0)$, assuming that the accretion rate decreases with time: in the case of an increasing mass flux, only the sign of the exponential solution changes. The general solution is:

$$\dot{M}_\bullet(t) = \dot{M}_\bullet(t = 0) e^{-t/t_{fb}} \, , \tag{4.19}$$

where

$$t_{fb} = \frac{\psi}{\epsilon \rho_0 \kappa_0 c} \, , \tag{4.20}$$

and

$$\psi = f_{Edd} \frac{L_{Edd}}{L} \, . \tag{4.21}$$

In the standard radiatively efficient scenario $\epsilon = 0.1$ and $\psi = 1$, while in the radiatively inefficient case $\epsilon = 0.04$ and $\psi = 25$ (for $f_{Edd} < 50$) and $\epsilon < 0.04$ and $\psi > 25$ (for $f_{Edd} \geq 50$). The feedback time scale is not related to the black hole mass $M_\bullet$, but only to the mass of the inflowing gas, via ρ_0. In the slim disk case, for a given density ρ_0, the feedback time scale is $\gtrsim 60$ times longer: the system reacts to a modification of the accretion rate in a much slower way.

To calculate t_{acc}, we estimate the time scale for the consumption (due to accretion) of the gas mass inside some radius r, given an accretion rate $\dot{M}_\bullet$:

$$t_{acc} = \frac{M_g(< r)}{\dot{M}_\bullet} = \frac{\epsilon c \kappa}{4 \pi G f_{Edd}} \frac{M_g(< r)}{M_\bullet} \, , \tag{4.22}$$

where on the right-hand side we have parametrized the luminosity through the Eddington factor f_{Edd}. The accretion time scale[3] is inversely proportional to the black hole mass $M_\bullet$ and directly proportional to the gas mass within the radius r.

Defining the ratio of the two time scales as:

$$\mathcal{T}(r, t) \equiv \frac{t_{fb}}{t_{acc}} \, , \tag{4.23}$$

[3]The accretion time scale is also very well approximated by a fraction 1/3 of the crossing time for a particle at some radius r: $M/\dot{M} = r/(3\dot{r})$.

a transition radius, r_T, exists such that:

$$t_{acc}(r_T) = t_{fb}(r_T)\,. \tag{4.24}$$

The flow is *feeding-dominated* in the region where $r \ll r_T$, $t_{acc} \ll t_{fb}$, $\mathcal{T}(r,t) \gg 1$ and gas is easily available for the accretion. The flow is instead *feedback-limited* where $r \gg r_T$, $t_{acc} \gg t_{fb}$, $\mathcal{T}(r,t) \ll 1$ because outflows dominate over inflows and accretion proceeds in an intermittent way, or can be even halted if the gas reservoir is empty. The parameter $\mathcal{T}(r,t)$ allows us to determine whether an accretion flow is feeding-dominated or feedback-limited. The expressions for r_T and $\mathcal{T}(r,t)$ are as follows:

$$r_T = \left[\psi \frac{3G f_{Edd} M_\bullet}{(\epsilon \rho_0 \kappa_0 c)^2}\right]^{1/3}\,, \tag{4.25}$$

and

$$\mathcal{T}(r,t) = \psi \frac{3G f_{Edd} M_\bullet}{(\epsilon \rho_0 \kappa_0 c)^2 r^3} = \left(\frac{r_T}{r}\right)^3\,. \tag{4.26}$$

Note that the black hole mass $M_\bullet$ increases with time, while ρ_0 decreases as gas is consumed, therefore the transition radius increases with time: a larger fraction of the host halo enters the feeding-dominated region, and accretion becomes progressively easier. Moreover, we define $\mathcal{T}(r_0,t) \equiv \mathcal{T}_0$.

Eq. 4.26 shows that the efficiency of an accretion flow depends on several variables that we discuss in turn. Firstly, the smaller the internal density of the halo, ρ_0, the longer is t_{fb}. This is because when the gas density is low the physical accretion rate on the black hole is small, and, at a given black hole mass, radiation pressure is less effective. It will be easier to have a feeding-dominated flow in the LDP than in the HDP case. Secondly, a smaller radiative efficiency ϵ yields a less effective radiation pressure, and consequently radiatively inefficient accretion would be more likely feeding-dominated. Thirdly, a larger Eddington factor $f_{Edd} \propto \dot{M}_\bullet \propto v$ implies a higher inward linear momentum of the gas. In this case, the inward velocity of the gas mass is less easily inverted. Lastly, the black hole mass $M_\bullet$: since $\dot{M}_{Edd} \propto M_\bullet$, a smaller mass corresponds to a smaller physical critical accretion rate: in a given halo a small black hole is more likely to be fed at rates that, for its mass, give rise to high radiation pressure. A small black hole is therefore more likely to find itself in the feedback-limited regime.

As an example, Fig. 4.2 shows a comparison between the accretion time scale (t_{acc})

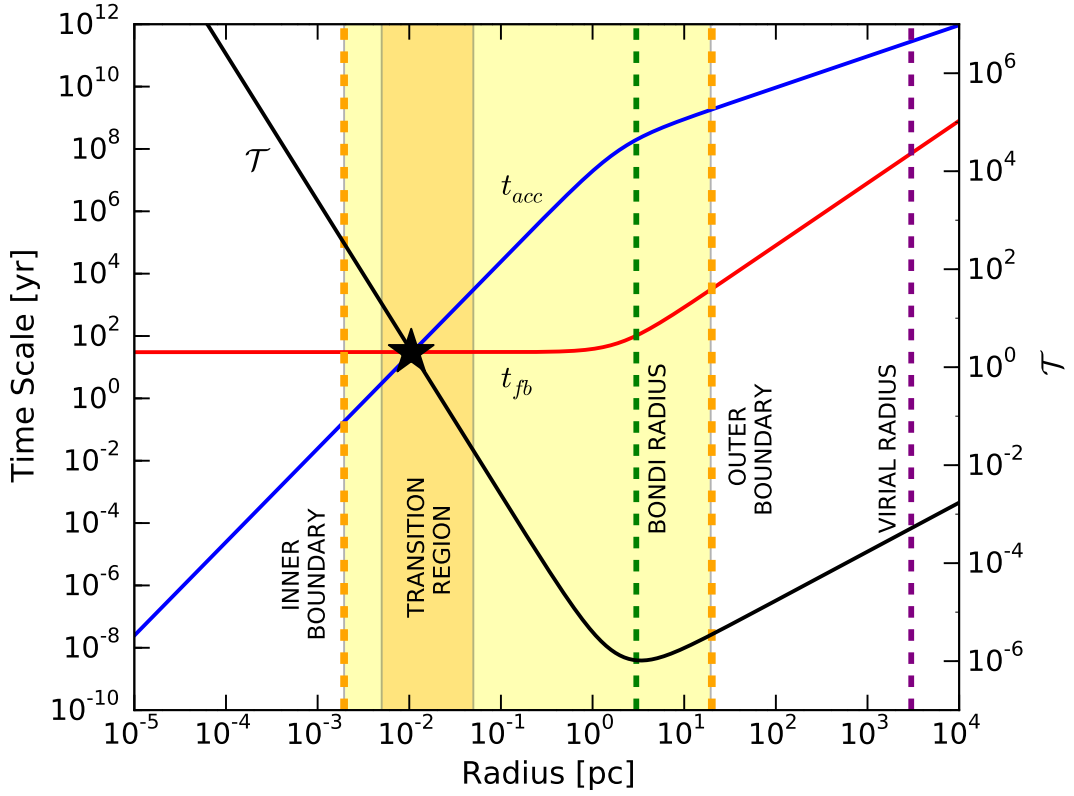

FIGURE 4.2: Comparison, at $t = 0$, between the accretion time scale (t_{acc}) and the feedback time scale (t_{fb}) for the accretion flow onto a black hole of initial mass $10^5\,M_\odot$ in the radiatively efficient and LDP case. The black line is the value of $\mathcal{T}(r, t_0)$. The yellow-shaded area is the region of integration in the present work, while the orange-shaded region indicates the transition region, where $0.1 \lesssim \mathcal{T} \lesssim 10$. The inner and outer boundaries, the Bondi radius and the virial radius of the halo are shown. The black star indicates the position of the transition radius.

and the feedback time scale (t_{fb}), both computed at $t = 0$, for the accretion flow onto a black hole of initial mass $10^5\,M_\odot$ embedded in an LDP in the radiatively efficient case (Eq. 4.10). The transition radius $r_T \sim 2 \times 10^{-2}$ pc is larger than the accretion radius ($r_0 \sim 2 \times 10^{-3}$ pc), so we expect the black hole growth to be feeding-dominated. Moreover, an overall modification of the spatial velocity profile of the accretion flow should be visible around the position of the transition radius, in the spatial range that we schematically call transition region, where $0.1 \lesssim \mathcal{T} \lesssim 10$. These effects are discussed in Sec. 4.4, dedicated to the results of our numerical simulations.

In the HDP case the transition radius would be smaller than the accretion radius and the growth would be feedback-limited. On the contrary, in the radiatively inefficient cases, both HDP and LDP, the transition radius would be even larger than the one shown in Fig. 4.2, leading to a more extended feeding-dominated region.

4.3.2 Relation between $\mathcal{D}$ and $\mathcal{T}_0$

In the following we derive an analytic relation between our model, through the quantity $\mathcal{T}_0$ (Eq. 4.26), and $\mathcal{D}$, the duty cycle for the black hole growth (Eq. 4.14), which is a phenomenological way, computable only *a posteriori*, to describe if the gas inflow is continuous. Even Adaptive Mesh Refinement cosmological simulations cannot resolve the typical spatial scale of accretion, therefore they have to resort to some kind of sub-grid prescriptions to model the black hole growth, like assuming that they *continuously* accrete at the Bondi-Hoyle-Lyttleton rate (Bondi 1952, see also Chapter 2), capped at the Eddington rate (see e.g. Springel et al. 2005, Di Matteo et al. 2008, Dubois et al. 2013, Costa et al. 2014, Dubois et al. 2015). Our model may provide in such cases more realistic values for the duty cycles of these sources.

Calling t_{idle} the fraction of t_{tot} during which the black hole is not accreting, it is possible to show that this relation holds:

$$\frac{t_{idle}}{t_{tot}} = e^{-t_{fb}/2t_{acc}}\,, \tag{4.27}$$

by solving the following differential equation (where χ is the time scale for the variation of $\dot{M}_\bullet$):

$$-\frac{d\chi}{dt} = \frac{\chi}{2t_{acc}}\,. \tag{4.28}$$

The factor 2 accounts for the fact that, once the radiation pressure exerts an action on the infalling gas for some time Δt, a time $2\Delta t$ is needed to re-establish the accretion rate preceding the acceleration (see Eq. 4.19). We obtain:

$$\mathcal{D} = (1 - e^{-\mathcal{T}_0/2})\,. \tag{4.29}$$

With our definition, $\mathcal{D}(\mathcal{T}_0 = 1) \sim 0.4$. A proof of the validity of Eq. 4.29 is provided in Fig. 4.7.

4.3.3 The black hole - host halo connection

The transition radius, which separates the feeding-dominated region ($r \ll r_T$) from the feedback-limited region ($r \gg r_T$), increases with time (see Eq. 4.25). Consequently, if the black hole growth is feeding-dominated at r_0 and $t = 0$, it will always be so. Asking

that $\mathcal{T}(r_0, t_0) \gtrsim 1$ translates into a black hole mass above which the flow will always be feeding-dominated:

$$M_{crit} = \frac{3 \times 10^6}{\psi f_{Edd}} \left(\frac{\epsilon}{0.1}\right)^2 \left(\frac{\rho_0}{5 \times 10^{-15}\,\mathrm{g\,cm^{-3}}}\right)^2 \left(\frac{r_0}{10^{-4}\,\mathrm{pc}}\right)^3 \mathrm{M}_\odot\,. \tag{4.30}$$

Here, we considered $r_0 \sim 10^{-4} - 10^{-3}\,\mathrm{pc} \sim 20 - 200\,\mathrm{AU}$ as a typical spatial scale for accretion disks.

In the HDP case for the standard accretion scenario the previous limit reads:

$$\mathcal{T}(r_0, t_0) > 1 \;\text{ if }\; M_\bullet > M_{crit} \sim 3 \times 10^6\,\mathrm{M}_\odot \;\;(\mathrm{HDP} - \mathrm{Std})\,, \tag{4.31}$$

while both in the LDP case and in the slim disk accretion scenario (both density profiles) the limit is negligible:

$$\mathcal{T}(r_0, t_0) > 1 \;\text{ if }\; M_\bullet > M_{crit} \sim 10 - 100\,\mathrm{M}_\odot \;\;(\text{other cases})\,. \tag{4.32}$$

The physical meaning of M_{crit} requires a clarification, since one normally expects that feedback halts the black hole growth above a given mass, rather than below (see e.g. Silk & Rees 1998, King 2003, 2010). The meaning of the lower limit we find is that when $M_\bullet > M_{crit}$ the accretion rate needed to exert a sufficiently strong feedback is so high, for the halo in question, that the accretion flow cannot produce it. In other words, the inflow rate is determined by the halo properties, and is, at least initially, independent of the black hole mass. If a given halo provides the same $\dot{M}_\bullet$ to a small black hole or a large black hole, it will be the smaller black hole that will reach the Eddington limit first, having its growth stunted. As a general result, smaller black hole seeds should encounter great challenges during the first stages of the growth, characterized by outflows and very low values of the duty cycle. This effect could play an important role at high redshifts, where black hole seeds of different mass may form from the same host halo, depending on the thermal and radiative properties of the environment.

4.4 Numerical Results

The following two subsections describe our numerical simulations and their analysis through the growth model outlined so far.

4.4.1 Inflows and outflows

As an example, we discuss a simulation of the accretion flow onto a black hole of initial mass $10^5\,M_\odot$ in the radiatively efficient and LDP case. Starting from static and isothermal conditions, the gravity of the black hole rapidly pulls in the gas, building up the accretion flow. Fig. 4.3 shows the time evolution of the velocity and temperature spatial profiles, which may be interpreted as the dynamical and thermal counterparts of Fig. 4.2, bearing in mind that $r_T(t)$ always increases. The transition and the outflow regions are defined as the set of radii r where, at least once during the time evolution of the system, the relations $0.1 \lesssim \mathcal{T}(r) \lesssim 10$ and $\mathcal{T}(r) \lesssim 0.1$ respectively hold. In the region close to the accretion boundary the inflow is very smooth, with inward velocities up to $\sim 15\,\mathrm{km\,s^{-1}}$ and temperatures rising up to $\sim 2.4 \times 10^4\,\mathrm{K}$. In the transition region, the flow starts to be disturbed by radiative feedback, which becomes more effective due to the increase of t_{acc}, with frequent velocity inversions and a more complex temperature profile. In the outflow region the radiative feedback is dominant, with large (up to $\sim 5\,\mathrm{km\,s^{-1}}$) outflowing velocities and a temperature profile which reconnects to the thermal floor ($T \sim 10^4\,\mathrm{K}$) of the host halo.

For the same simulation, Fig. 4.4 shows the time evolution of the mass flux at the inner boundary (i.e. the accretion rate), at the outer boundary and inside the transition region, in which the computed values are a spatial average over the cells belonging to this region at each time of the simulation. The inner region is characterized by a slow, but *constant*, accretion of order $\sim 2.0 \times 10^{-3}\,M_\odot\,\mathrm{yr^{-1}}$. The outer region is swept by large outflows, whose magnitude increases with time, reaching a peak of $\sim 0.8\,M_\odot\,\mathrm{yr^{-1}}$, while the transition region is characterized by a mild outflow.

In the HDP case (for the same accretion scenario), $r_T \lesssim r_0$ and the growth is feedback-limited: the accretion is discontinuous and the transition region would extend down to the accretion boundary, while the outflows would be more intense. On the contrary, in the radiatively inefficient cases, both HDP and LDP, $r_T \gg r_0$: the accretion flow would be smooth and continuous over a large fraction of the spatial domain, with the transition region starting to be visible only close to the outer radius.

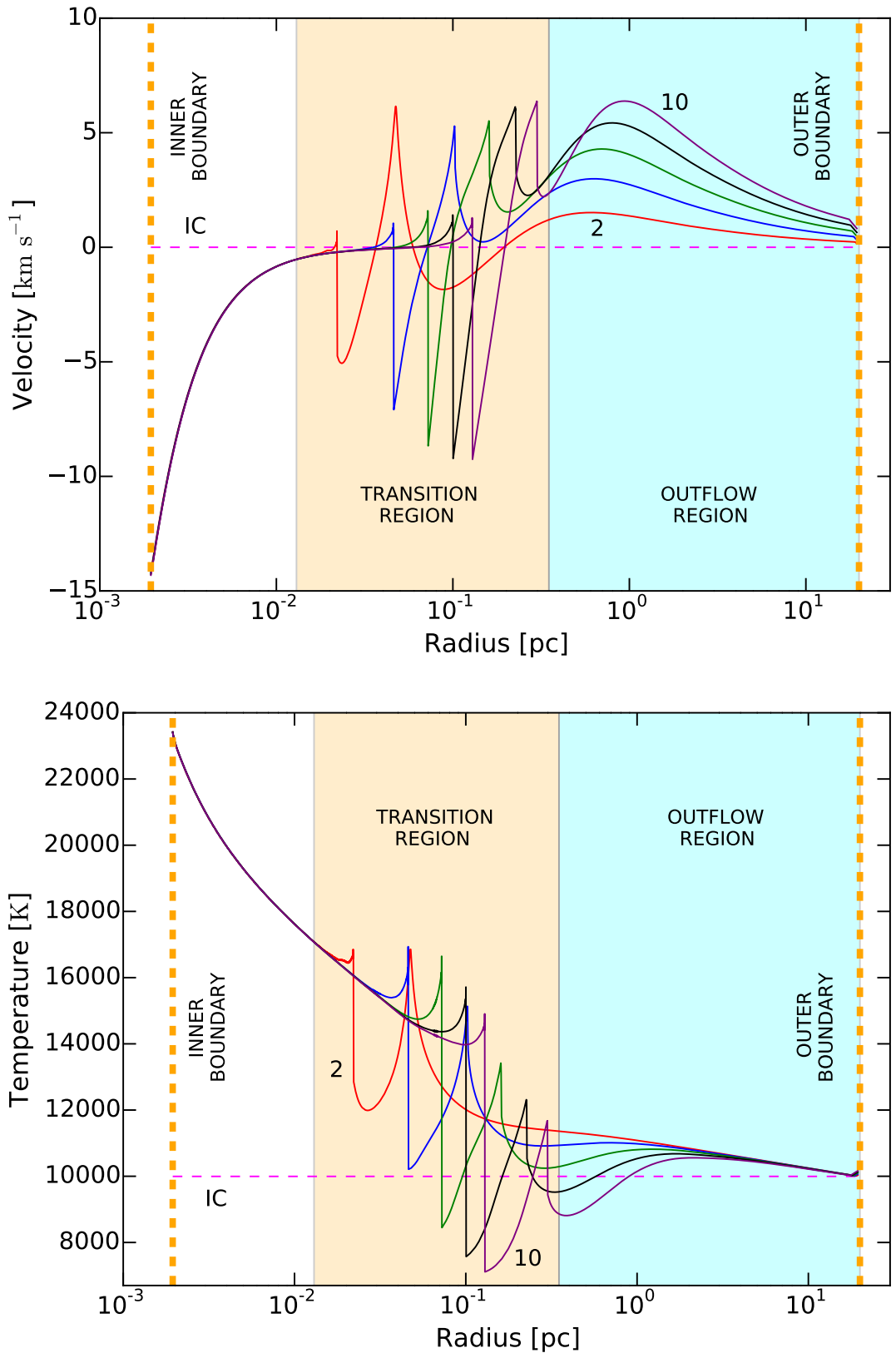

FIGURE 4.3: Velocity and temperature spatial profiles for the accretion flow onto a $M_0 = 10^5\,\mathrm{M}_\odot$ black hole embedded in a LDP density profile, accreting in the radiatively efficient mode. The total integration time is $t_{tot} = 10^5\,\mathrm{yr}$ ($t_{tot} = i\,\Delta t$ with $\Delta t = 10^4\,\mathrm{yr}$ and $i = 0, 2, 4, 6, 8, 10$). The initial conditions are marked with the label "IC". The transition and outflow regions are defined by $0.1 \lesssim \mathcal{T}(r) \lesssim 10$ and $\mathcal{T}(r) \lesssim 0.1$ respectively. The inner and outer boundaries are shown with orange dashed lines.

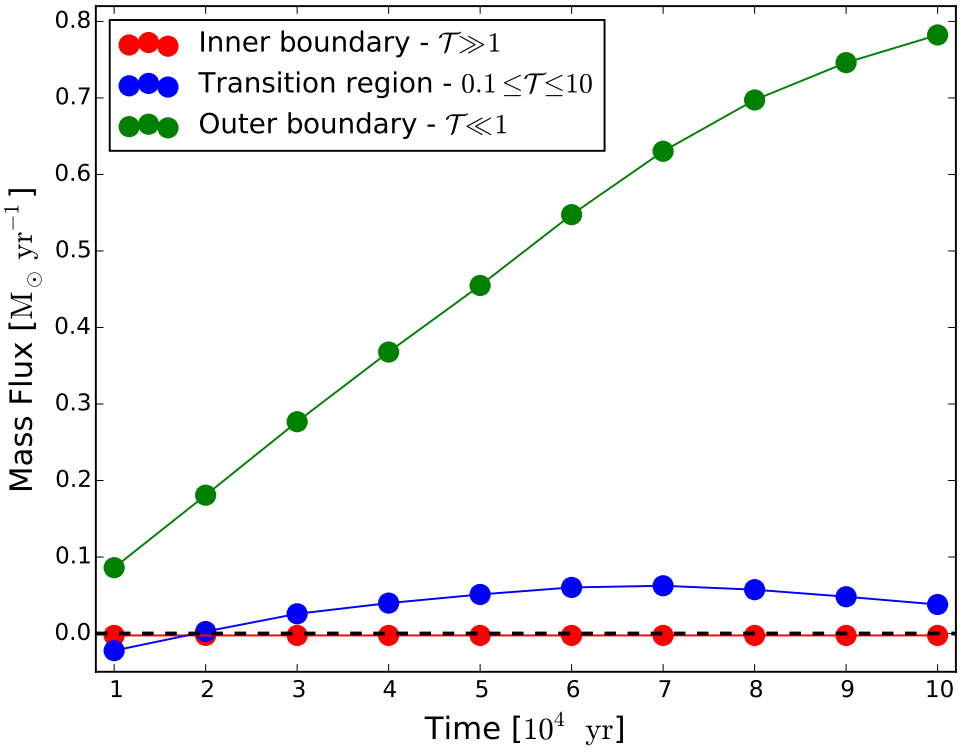

FIGURE 4.4: Time evolution of the mass flux computed at the inner boundary, outer boundary and inside the transition region highlighted in Fig. 4.3. There is a slow but constant ($\sim 2.0 \times 10^{-3}\,\mathrm{M}_\odot\,\mathrm{yr}^{-1}$) accretion at the inner boundary, while the outer region is characterized by a strong outflow, with a mass flux up to $\sim 0.8\,\mathrm{M}_\odot\,\mathrm{yr}^{-1}$. The transition region is characterized by a mild outflow, on average.

4.4.2 The growth efficiency

In the following we numerically test the predictions of our model with 16 runs, in order to adequately explore the range of density profiles (HDP and LDP), black hole seed masses ($10^{3-6}\,\mathrm{M}_\odot$) and radiative efficiencies ($L \propto f_{Edd}$ and $L \propto \ln f_{Edd}$). The simulations are run for $\sim 10^5\,\mathrm{yr}$ to allow all the simulated accretion flows to reach steady-state conditions without reaching a complete depletion of the gas reservoir. The parameters reported in the figures, $\langle\mathcal{T}(r_0)\rangle$, $\langle f_{Edd}\rangle$ and $\langle\mathcal{D}\rangle$, are an average over the entire simulation time, while the parameter $\Delta M/M_0$ expresses the total mass growth at the end of the simulation, normalized to the initial value of the seed mass. Fig. 4.5 shows the results in the radiatively efficient case, while Fig. 4.6 refers to the radiatively inefficient one. The top panels refer to HDP, while the bottom ones to LDP.

4.4.2.1 The $M_\bullet = 10^{3-6}\,\mathrm{M}_\odot$ runs

The HDP case in the radiatively efficient scenario (Fig. 4.5, top panel) is particularly interesting because $\mathcal{T}$ crosses unity twice, allowing us to test the $\mathcal{D}-\mathcal{T}$ relation. The simulated masses are all below $M_{crit} \sim 3\times10^6$ characteristic of this density profile and radiative efficiency for $f_{Edd}=1$, therefore one expects the flow not be feeding-dominated at all times. However, in Chapter 3 we showed that super-critical accretion is feasible, for short times, also in radiatively efficient scenarios. Indeed, in the mass range $10^{3-4}\,\mathrm{M}_\odot$ the entire galaxy is in outflow ($r_T \sim r_0$), but the radiation pressure is active only when the gas accretion is underway, while during the remaining time the inflow builds up again. As a consequence, the radiation pressure is unable to sweep *all* the gas away from the accretion boundary, and a small physical accretion rate is sufficient to grow such small black holes, so the flow can sustain, on average, $f_{Edd}\sim 25$, with duty cycles $\mathcal{D}\sim 0.8-0.9$. The relevant M_{crit}, therefore, is not the one for $f_{Edd}\sim 1$, but for $f_{Edd}\sim 25$. The values of $\mathcal{T}$ and r_T slowly increase as the initial mass of the seed $M_\bullet$ approaches $M_{crit}\sim 1.2\times10^5\,\mathrm{M}_\odot$ for $f_{Edd}\sim 25$ (see the left-most vertical line in Fig. 4.5, top panel).

In the range $10^{5-6}\,\mathrm{M}_\odot$ a super-Eddington flow is no more sustainable, since the radiation pressure is progressively more powerful: the flow stabilizes at $f_{Edd}\sim 1$. For an Eddington-limited flow, $M_{crit}\sim 3\times10^6\,\mathrm{M}_\odot$ (see the right-most vertical line in Fig. 4.5, top panel). In the process of going from $f_{Edd}\sim 25$ to $f_{Edd}\sim 1$ the flow becomes mildly feedback-limited ($\mathcal{T}\sim 0.7$ for $M_\bullet = 10^6\,\mathrm{M}_\odot$, $\mathcal{D}\sim 0.3-0.5$). The physical accretion rates in the HDP case are within the range $10^{-3}-10^{-4}\,\mathrm{M}_\odot\,\mathrm{yr}^{-1}$ (see Fig. 4.5 for further details).

In the LDP case of the radiatively efficient scenario, the critical mass value M_{crit} is $< 10^3\,\mathrm{M}_\odot$: as a consequence the growth is feeding-dominated ($\mathcal{D}\sim 1$ and $\mathcal{T}\gtrsim 10^2$) for all runs and accretion rates are stable, close to the Eddington value ($f_{Edd}\sim 1$). The physical accretion rates are within the range $10^{-2}-10^{-5}\,\mathrm{M}_\odot\,\mathrm{yr}^{-1}$, increasing with the mass $M_\bullet$ just as the Eddington rate.

In the HDP case of the radiatively inefficient scenario (Fig. 4.6, top panel) the situation is similar, because $M_{crit} < 10^3\,\mathrm{M}_\odot$: so $r_T \gg r_0$ and the growth is always feeding-dominated ($\mathcal{T}$ up to $\sim 10^4$). Accretion is not capped at the Eddington rate, so we reach

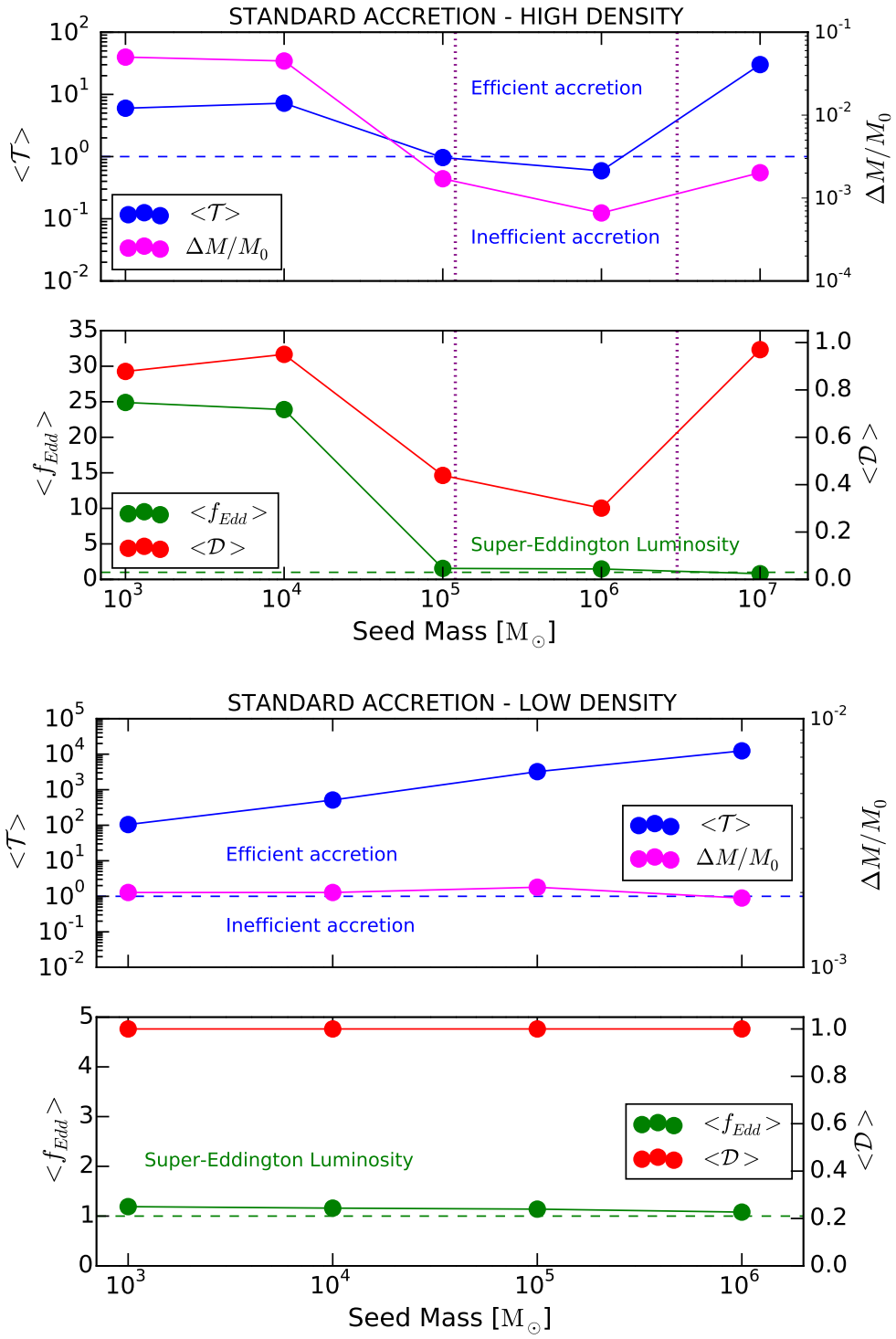

FIGURE 4.5: Radiatively efficient case - Comparison between the parameters used to describe the accretion flow ($\mathcal{T}$, $\Delta M/M_0$, f_{Edd} and $\mathcal{D}$), for black hole seed masses in the range $10^{3-6}\,M_\odot$ and two density profiles (HDP above and LDP below). The vertical purple lines show the values of M_{crit} for $f_{Edd} = 25$ and $f_{Edd} = 1$, from left to right. The physical accretion rates are, in ascending order of mass: $4.0\times10^{-4}\,M_\odot\,yr^{-1}$, $4.5\times10^{-3}\,M_\odot\,yr^{-1}$, $1.5\times10^{-3}\,M_\odot\,yr^{-1}$, $6.5\times10^{-3}\,M_\odot\,yr^{-1}$ for the HDP, and $2.0\times10^{-5}\,M_\odot\,yr^{-1}$, $2.0\times10^{-4}\,M_\odot\,yr^{-1}$, $2.0\times10^{-3}\,M_\odot\,yr^{-1}$, $2.0\times10^{-2}\,M_\odot\,yr^{-1}$ for the LDP. The simulation with $M_0 = 10^7\,M_\odot$ shows a very large value for the physical accretion rate, $\sim 2.0\times10^{-1}\,M_\odot\,yr^{-1}$. See the main text for further details.

rates as high as $f_{Edd} \sim 300$, leading to a *super-Eddington* emitted luminosity $L \sim 5 L_{Edd}$ (Eq. 4.12). The physical accretion rates reach large values, with a peak of $14\,\mathrm{M}_\odot\,\mathrm{yr}^{-1}$.

Similarly, in the LDP case of the radiatively inefficient scenario (Fig. 4.6, bottom panel) all accretion flows are feeding-dominated, with physical accretion rates within the range $10^{-1} - 10^{-4}\,\mathrm{M}_\odot\,\mathrm{yr}^{-1}$. While the Eddington factor is $f_{Edd} \sim 5$ for all masses, the emitted luminosity is strongly *sub-Eddington*, due to the low mass density of the LDP scenario, which is unable to produce a mass inflow leading to super-critical luminosities.

In summary, radiatively inefficient accretion allows for largely feeding-dominated growths of the central black hole, while standard accretion scenarios may be feedback-limited when the gas density is very high. Moreover, the main difference between the two density profiles, notwithstanding the accretion mode, is related to the accretion rates that they can sustain to feed the black hole: the HDP produces an accretion rate up to $f_{Edd} \sim 300$, decreasing dramatically the growth time of the central object.

With the average values of $\mathcal{T}$ and $\mathcal{D}$ computed so far for the 16 runs, we are in the conditions of testing our model for the $\mathcal{D} - \mathcal{T}$ relation, given by Eq. 4.29. Fig. 4.7 shows that our analytic model offers a very good fit to the points in the $(\mathcal{D}, \mathcal{T})$ plane.

In order to have a general overview of the mass accreted (across the inner boundary) and ejected (across the outer boundary) in the different simulations performed, Fig. 4.8 provides a mass balance summary. The mass growth ($\Delta M_\bullet \equiv M_\bullet(t) - M_0$) for a black hole seed of initial mass $10^5\,\mathrm{M}_\odot$ is shown with solid lines, while the dashed lines indicate the mass ejected through outflows. The black solid diamonds indicate the final mass that the same seed would reach accreting *continuously* at the Eddington rate ($\mathcal{D} = 1$, $f_{Edd} = 1$) with $\epsilon = 0.1$. The ejected mass is larger than the accreted mass, except for the HDP in the slim disk scenario (brown line), due to the large values of f_{Edd} available under these physical conditions. The mass growth in the standard radiatively efficient scenario is smaller than or equal to the one predicted by a continuous accretion at the Eddington rate, while in the slim disk scenario it is $2 - 3$ orders of magnitude larger (in particular, the slim disk and HDP accretion provides a final mass that is ~ 1000 times larger).

In Chapter 3, we found that only $\sim 10\%$ of the halo mass is expelled with outflows during the accretion process. In the present work, during the first $10^5\,\mathrm{yr}$ of evolution of a $10^5\,\mathrm{M}_\odot$ seed embedded in a HDP halo the outflowing gas is $\sim 85\%$ of the total.

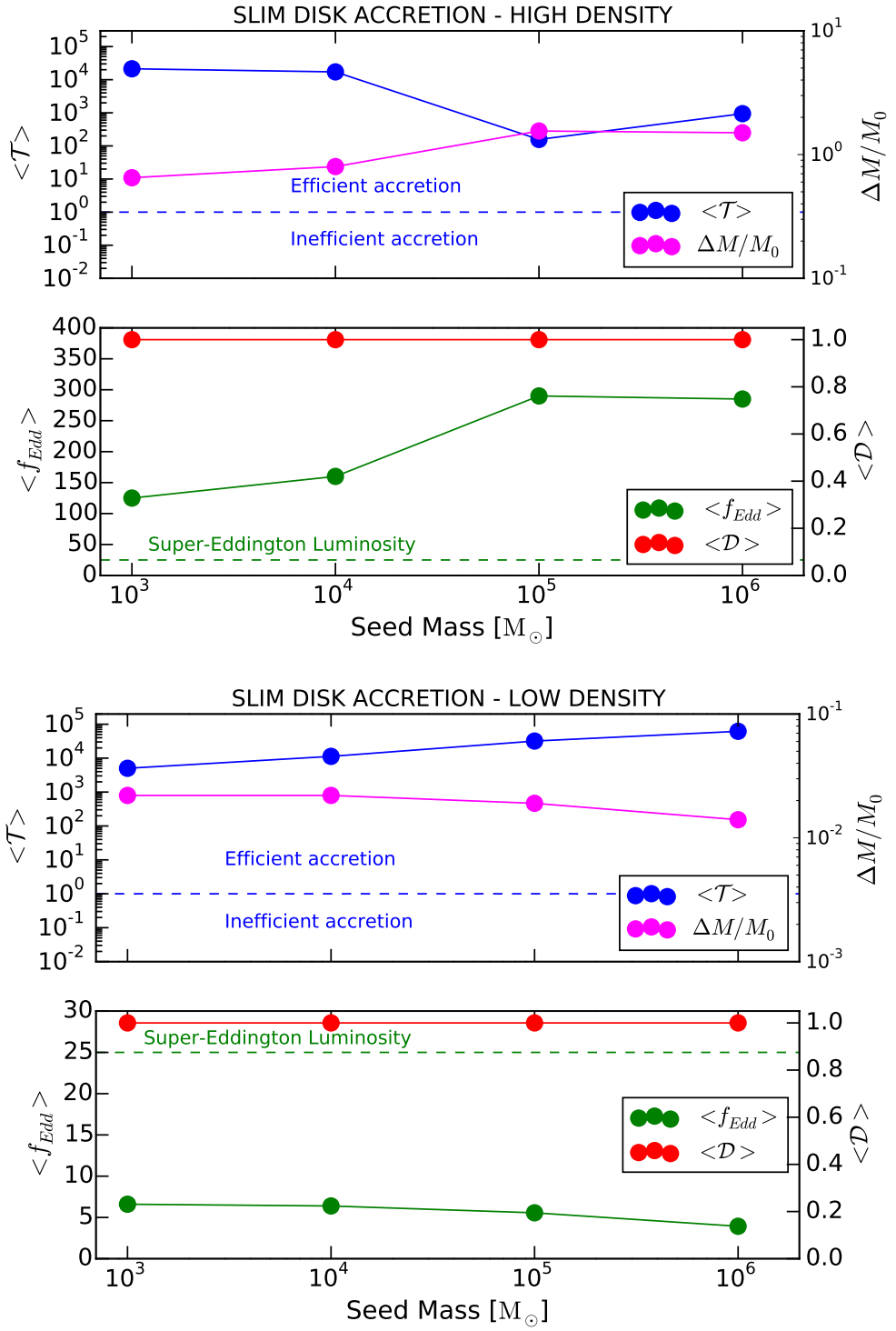

FIGURE 4.6: Radiatively inefficient case (slim disk) - Same as Fig. 4.5. The physical accretion rates are, in ascending order of mass: $7.0\times10^{-3}\,M_\odot\,yr^{-1}$, $7.0\times10^{-2}\,M_\odot\,yr^{-1}$, $1.5\,M_\odot\,yr^{-1}$, $1.4\times10^{1}\,M_\odot\,yr^{-1}$ for the HDP, and $2.0\times10^{-4}\,M_\odot\,yr^{-1}$, $2.0\times10^{-3}\,M_\odot\,yr^{-1}$, $2.0\times10^{-2}\,M_\odot\,yr^{-1}$, $1.5\times10^{-1}\,M_\odot\,yr^{-1}$ for the LDP. See the main text for further details.

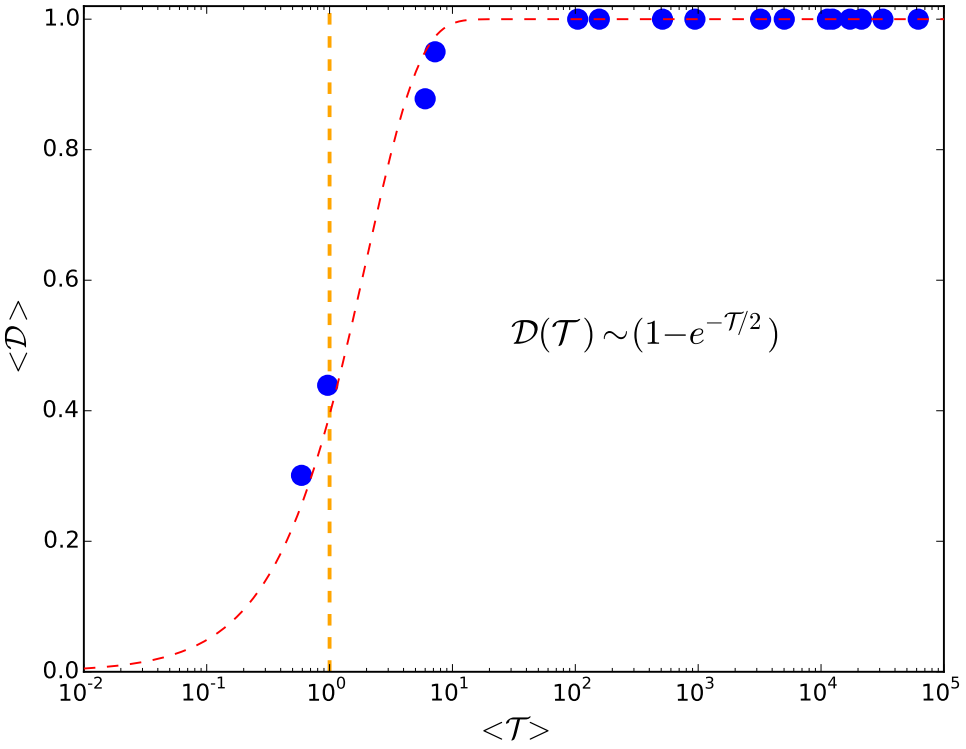

FIGURE 4.7: Data points in the $(\mathcal{D}, \mathcal{T})$ plane, obtained from the 16 runs performed (Figs. 4.5 and 4.6). The overplotted line is the theoretical relation between $\mathcal{D}$ and $\mathcal{T}$, discussed in the main text (Eq. 4.29).

This difference is explained by three reasons. Firstly, the relative importance of outflows decreases with time, due to the fact that the gradient of $r_T(t)$ is positive: the simulation presented in Chapter 3 is ~ 1000 times more extended in time than the ones analyzed here. Secondly, the spatial range of the present work is much larger, then more apt to probe the outflow regions. Lastly, the halo density profiles are different, since the one employed in Chapter 3 had a higher central density. Most of the baryonic mass of a $T_{vir} \sim 10^4\,\mathrm{K}$ halo at $z \sim 10$ was confined inside a sphere of radius $\sim 3\,\mathrm{pc}$, leading to values of the optical depths of order $N_H \sim 9 \times 10^{25}\,\mathrm{cm}^{-2}$ at the beginning of the collapse, which may have strongly reduced the impact of outflows.

4.4.2.2 The $M_\bullet = 10^7\,\mathrm{M}_\odot$ run: a test case for M_{crit}

In the radiatively efficient case with HDP (Fig. 4.5, top panel) the value of $\mathcal{T}$ reaches a minimum (~ 0.7) around $M_\bullet \sim 10^6\,\mathrm{M}_\odot$ and rises up to ~ 60 again for $M_\bullet \sim 10^7\,\mathrm{M}_\odot$, allowing us to test the value of $M_{crit} \sim 3 \times 10^6\,\mathrm{M}_\odot$ (Eq. 4.30) predicted for this scenario.

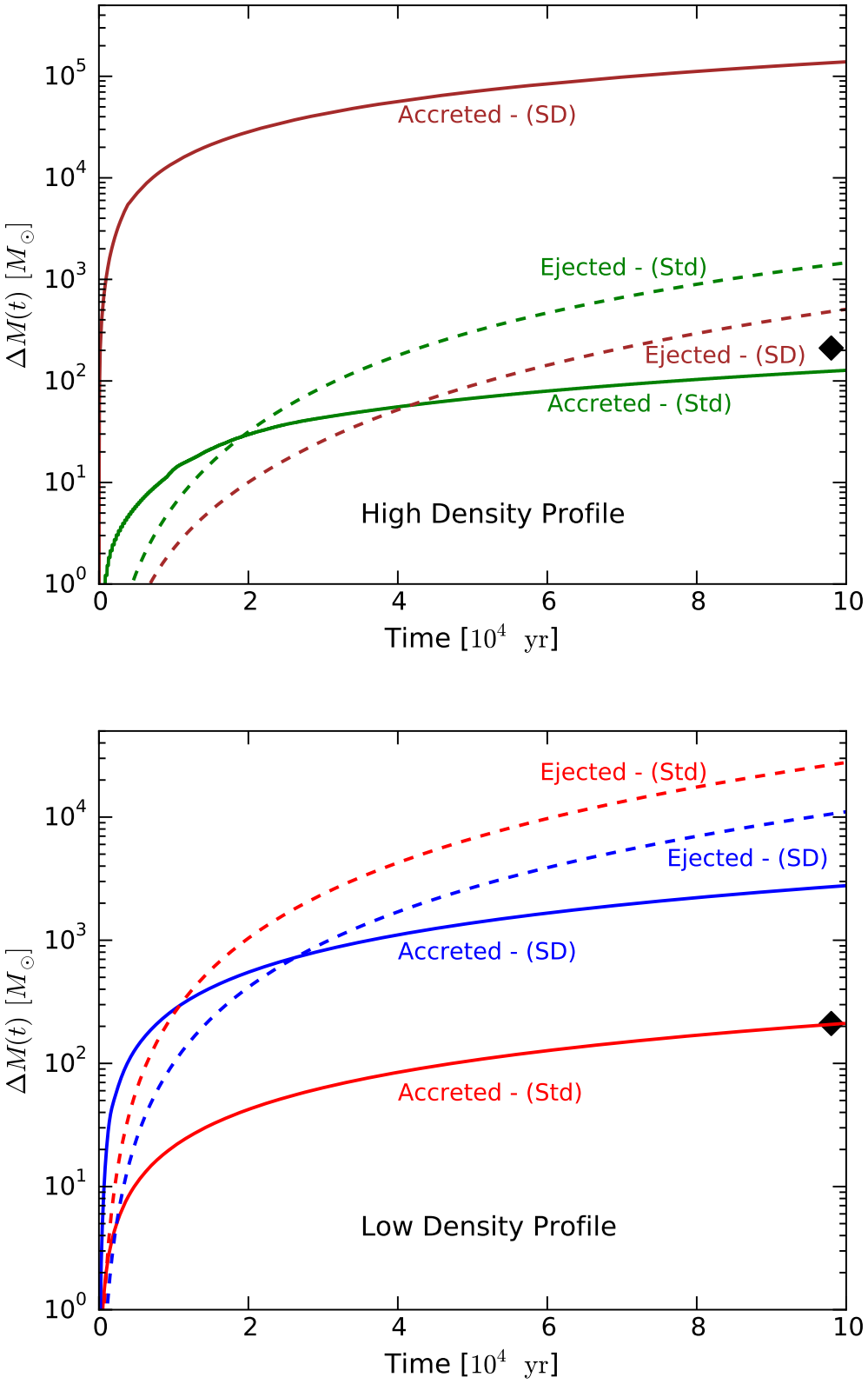

FIGURE 4.8: Mass accreted (solid lines) and ejected (dashed lines) for a black hole seed with initial mass 10^5 $M_\odot$, embedded in a HDP (top panel) and in a LDP (bottom panel), in radiatively efficient and inefficient scenarios. The black solid diamonds indicate the final mass that the same seed would reach accreting continuously at the Eddington rate with $\epsilon = 0.1$.

TABLE 4.1: Analytic estimate of the accretion history for a black hole seed with initial mass $M_\bullet = 10^5\,\mathrm{M}_\odot$ in the four scenarios investigated so far.

Accretion scenario	t_{end} [Myr]	$M_\bullet(t_{end})$ [$\mathrm{M}_\odot$]	$M_\bullet(t_{end})/M_{gas}$
Standard accretion - HDP	225	7.4×10^5	7%
Standard accretion - LDP	110	1.5×10^6	15%
Slim Disk accretion - HDP	14	1.0×10^7	100%
Slim Disk accretion - LDP	9	8.3×10^6	83%

For $M_\bullet \gtrsim M_{crit}$, the Eddington rate is so large ($\gtrsim 0.3\,\mathrm{M}_\odot\,\mathrm{yr}^{-1}$) that the accretion flow from the halo simply cannot provide it (the free-fall rate at $t = 0$ is $\sim 0.2\,\mathrm{M}_\odot\,\mathrm{yr}^{-1}$). As a consequence, the Eddington factor remains below unity ($f_{Edd} = 0.7$) while $\mathcal{D} \sim 1$. In this case, the physical accretion rates are very large ($\sim 0.2\,\mathrm{M}_\odot\,\mathrm{yr}^{-1}$), a factor ~ 100 higher than the values for other seed masses (see the caption of Fig. 4.5). This feeding-dominated simulation has produced continuous accretion with very large rates and with sub-Eddington luminosities.

4.4.3 The final black hole mass

The integration time for all simulations is much shorter than the typical evolutionary time scale for these systems (see Chapter 3 and Chapter 5). In this section we estimate the depletion time t_{end} needed to void the inner regions of the host halo from its gas content, due to both gas accreted by the black hole, and ejected through outflows. Furthermore, from t_{end} we can provide a rough estimate of the final black hole mass, by extrapolating the average accretion rates up to t_{end}.

Extrapolating the lines in Fig. 4.8, we find the depletion time t_{end} with the following condition:

$$M_{acc}(t = t_{end}) + M_{ej}(t = t_{end}) = M_{gas}\,, \tag{4.33}$$

where $M_{acc}(t)$ is the accreted mass, $M_{ej}(t)$ is the ejected mass and $M_{gas} = 10^7\,\mathrm{M}_\odot$ is the total gas mass within our computational domain. Table 4.1 provides a general outline of the accretion history for a black hole seed with initial mass $M_\bullet = 10^5\,\mathrm{M}_\odot$ in the four scenarios investigated so far, including the depletion time t_{end}, the extrapolated final mass of the black hole $M_\bullet(t_{end})$ and its ratio with the initial baryonic mass of the host halo $M_\bullet(t_{end})/M_{gas}$.

While in standard accretion scenario the typical time scale is $\sim 100\,\mathrm{Myr}$ (see the simulation in Chapter 3) and the black hole can accrete $\sim 5\% - 15\%$ of the baryonic mass of the host halo, in radiatively inefficient modes the growth is much more rapid and efficient. Specifically, in the slim disk scenario we predict that the evolutionary time scale is of order $\sim 10\,\mathrm{Myr}$ (see the following Chapter 5), with outflows playing a negligible role: the black hole is able to accrete $\sim 80\% - 100\%$ of the host halo gas.

4.4.4 A bimodal evolution of the black hole seeds

Several works in literature (e.g. Silk & Rees 1998, King 2003, 2010) have investigated various forms of the so-called $M_\bullet - \sigma$ relation, which provides an upper limit for the black hole mass: a compact object embedded in a halo with velocity dispersion $\sigma \sim v_{esc}$ (the halo escape speed) can grow up to a mass given by the $M_\bullet - \sigma$ relation, while the remaining gas is dispersed by radiation-driven (Silk & Rees, 1998) and/or momentum-driven (King, 2003) outflows. The usual assumption adopted in these works is that the momentum flux ($\dot{M}_{out} v$) of the outflowing gas is comparable to the one in the Eddington-limited radiation field: $\dot{M}_{out} v \sim L_{Edd}/c$. In this work we have taken an alternative view where, comparing the time scales for gas infall and gas ejection as a function of radius, we prove that the momentum flux may be very different from the Eddington value: for instance, in the slim disk model where super-critical accretion rates may be associated with sub-Eddington luminosities.

Our approach predicts the existence of a critical black hole mass M_{crit} *above* which the accretion is negligibly affected by outflows: this, in turn, may lead to a bimodal evolution of the initial mass function of high-redshift black hole seeds. The lower-mass seeds ($M_\bullet < M_{crit}$) would go through a feedback-limited growth, with recurring episodes of strong outflows which deplete the inner regions of the host halo from its mass content: the black hole cannot accrete more than a few percent of the gas reservoir. On the contrary, higher-mass seeds ($M_\bullet > M_{crit}$) would go through a feeding-dominated growth, with outflows playing a negligible role: the black hole grows in mass very rapidly, possibly even consuming most of the host halo mass, reaching the SMBH stage early in time. For the LDP case, and for slim disk accretion in either density profile M_{crit} is very low ($\sim 10 - 100\,\mathrm{M}_\odot$), and therefore of relevance only if black hole seeds are stellar-mass or

so. For the HDP case, and standard accretion, $M_{crit} \sim 3 \times 10^6\,\mathrm{M}_\odot$ is relevant for most seed masses proposed in the literature.

As a proof-of-concept of this bimodal development, Fig. 4.9 shows the cosmological evolution, between $z = 10$ and $z = 7$ (the epoch when the first SMBHs are observed), of two initial mass functions for high-redshift black hole seeds: a simple flat distribution in the mass range $Log_{10}(M_\bullet[\mathrm{M}_\odot]) = 4.5 - 5.5$ (top panel) and the initial mass function modeled (at $z = 10$) in Ferrara et al. (2014) (bottom panel). This evolution, far from being a precise prediction of the actual black hole growth, is a proof-of-concept based on the theoretical framework described in the present work. The basic equation for the mass growth is the following one:

$$M_\bullet(t) = M_\bullet(t=0)\exp\left[\mathcal{D} f_{Edd}\frac{t}{0.045\,\mathrm{Gyr}}\right], \tag{4.34}$$

where the values for $\mathcal{D}(M_\bullet)$ and $f_{Edd}(M_\bullet)$ are interpolated for each $M_\bullet$ from the solid lines in Fig. 4.5, in the HDP case. The bimodal evolution is evident and the mass gap at $Log_{10}(M_\bullet) \sim 5.7$ is expected to rapidly spread during the cosmic time. Importantly, this effect does not depend on the shape of the initial mass function.

In the HDP case with a radiatively inefficient accretion the bimodal evolution is expected to occur as well since, while $\mathcal{D} \sim 1$ for all masses, the value of f_{Edd} does show a mass dependence (see the upper panel of Fig 4.6).

In halos with a LDP density profile, in any accretion scenario, the bimodal evolution is not expected to occur, since f_{Edd} and $\mathcal{D}$ are nearly independent of the seed mass (see bottom panels of Figs. 4.5 and 4.6). Nonetheless, we expect this evolutionary effect to play a remarkable role in the growth process, since we believe that dark matter halos with a HDP density profile harbored at their center the black hole seeds with smaller masses ($M_\bullet \lesssim 10^{3-4}\,\mathrm{M}_\odot$), the ones which are affected the most by feedback-limited growth.

4.5 Discussion and Summary

The aim of this work is to provide a theoretical framework, supported by numerical simulations, to describe the growth of high-redshift ($z \sim 10$) black hole seeds. The

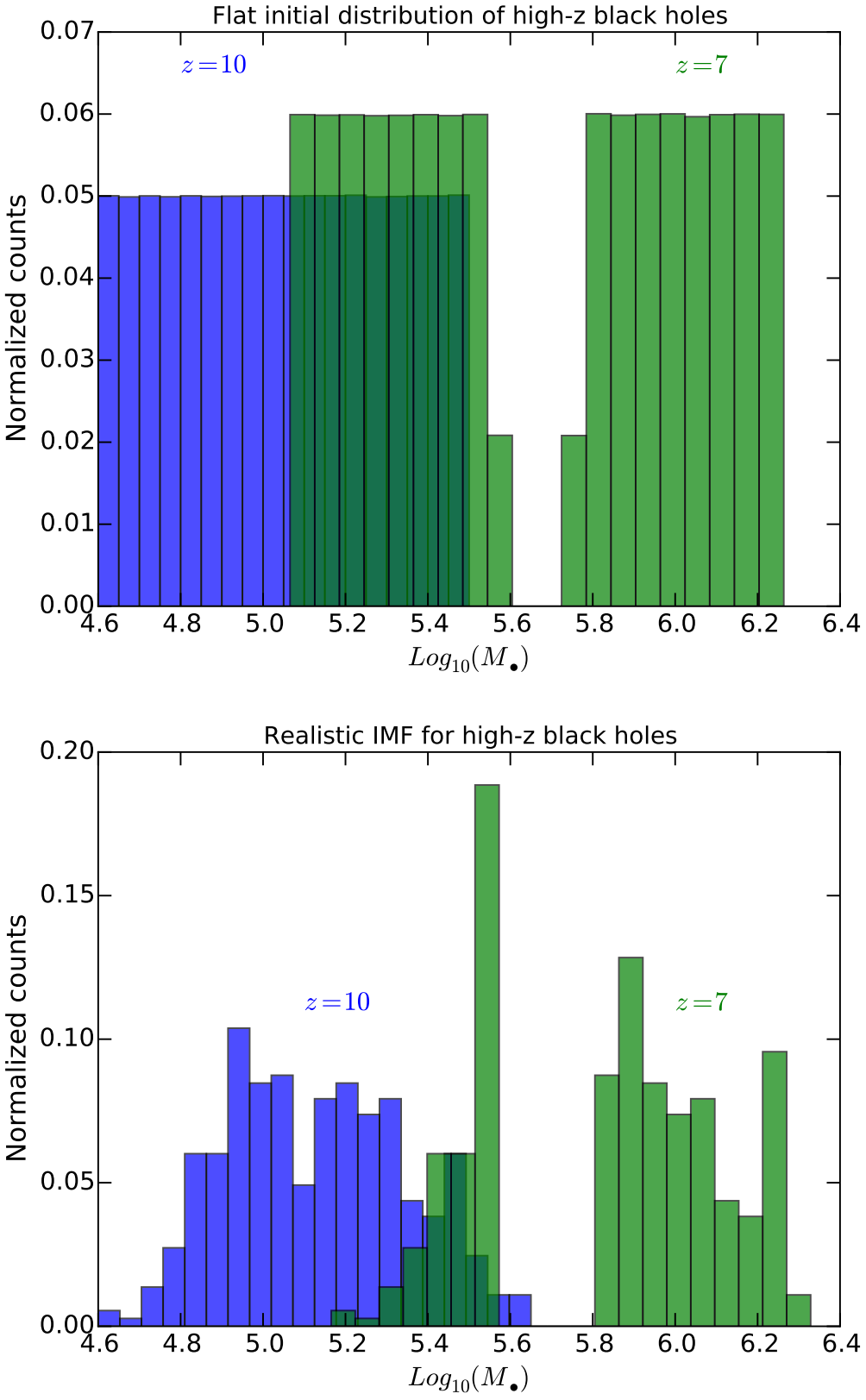

FIGURE 4.9: Proof-of-concept bimodal evolution, between $z = 10$ and $z = 7$, of two initial mass functions for black hole seeds: a flat one (top) and a more realistic one (bottom). The evolution is computed along the theoretical lines described in this paper, with values for $\mathcal{D}(M_\bullet)$ and $f_{Edd}(M_\bullet)$ interpolated from the HDP simulations in the standard accretion scenario.

growth can be either feeding-dominated or feedback-limited. It is feeding-dominated if the radiative back-reaction of the black hole is negligible: the rapidity of the process is mainly determined by the gas accretion rate that the host halo can provide. In a feeding-dominated accretion flow the black hole: (i) increases its mass during most of its time evolution, and (ii) exerts a relatively small mechanical and/or radiative feedback on its surrounding gas reservoir. For these reasons, a feeding-dominated accretion is the desirable way to grow the black hole efficiently.

Within this theoretical framework, we investigated, with the aid of 1D radiation hydrodynamic simulations, the growth of black hole seeds with a set of astrophysically-motivated initial conditions to explore the consequences of our model: seed masses in the range $10^{3-6}\,\mathrm{M}_{\odot}$, embedded in a dark matter halo of total mass (dark matter and baryons) $M_h = 6.7 \times 10^8\,\mathrm{M}_{\odot}$ with two different density profiles and with different prescriptions for the accretion efficiency, namely a radiatively efficient mode ($\epsilon = 0.1$) and a slim disk mode ($\epsilon \lesssim 0.04$).

Three points in particular are worthy of being retained from this chapter.

- We confirmed that radiatively inefficient accretion modes (for instance the slim disk model) may ensure a continuous growth with rates largely exceeding the Eddington limit (reaching $\sim 300\dot{M}_{Edd}$ in our simulations). Radiatively inefficient accretion flows allow for feeding-dominated growths of the central black hole, while standard accretion scenarios may be feedback-limited with high values of the host halo gas density. The feedback time scale for these radiatively inefficient modes is $\gtrsim 60$ times longer than in the standard accretion scenario: the system reacts to a modification of the accretion rate in a much slower way because at a given accretion rate the production of radiation is reduced, decreasing the feedback effectiveness. In addition, we numerically proved the feasibility of accretion flows with *sub-Eddington luminosities* and *super-Eddington rates*.

- We theoretically derived the existence of a time-evolving transition radius, r_T, which discriminates between feeding-dominated and feedback-limited growths. The transition radius, in addition, determines the spatial scale at which outflows take place, and provides a mass scale, M_{crit}, above which the black hole growth is always feeding-dominated. The critical black hole mass is $10 - 10^6\,\mathrm{M}_{\odot}$, depending

on the accretion scenario and on the host halo properties. Consequently, we foresee the possibility of a bimodal evolution of the population of black hole seeds: low-mass seeds grow much less efficiently than high-mass ones.

- Our model may be employed in modeling the growth of high-redshift black holes in large cosmological simulations, which cannot resolve the typical spatial scales of accretion.

To conclude, the aim of our model is to study high-redshift accretion flows leading to the growth of the first black holes. In particular, we provided the theoretical framework needed to understand why radiatively inefficient accretion models are likely to be a crucial ingredient in explaining the presence of SMBHs of mass $\sim 10^{9-10}\,\mathrm{M}_{\odot}$ less than 1 Gyr after the Big Bang (Mortlock et al., 2011, Wu et al., 2015). In order to build such extremely massive objects already at $z \sim 7$, an Eddington-capped accretion would require, starting from a stellar mass ($M_{\bullet} \sim 50\,\mathrm{M}_{\odot}$) seed, a constant Eddington flow. However, a low-mass seed would be hindered in its initial growth by its own feedback, making continuous accretion at Eddington levels unlikely (see also Johnson & Bromm, 2007, Alvarez et al., 2009, Milosavljević et al., 2009, Park & Ricotti, 2012).

Part III

Observational Framework

General Introduction to the Observational Framework

This part describes the observational framework of our study: from our theoretical model, developed in the previous chapters, we predict the observables of DCBHs. In Chapter 5 we study the time-evolution of the spectrum emerging from the host halo of a DCBH. Comparing our theoretical predictions with observations, we provide constraints on the high-redshift DCBH mass density, in radiatively efficient and inefficient accretion models. In Chapter 6 we develop a photometric method to select DCBH candidates in deep multi-wavelength fields, at $z \gtrsim 6$. We employ our method to the CANDELS/GOODS-S survey, selecting two high-redshift objects that are to date our best candidates for being the first DCBHs ever detected. Finally, in Chapter 7 we investigate the emission of gravitational waves during the formation process of a DCBH, suggesting that this signal may be detected by future gravitational waves observatories, like Ultimate-DECIGO.

Chapter 5

Shining in the Dark: the Spectral Evolution of the First Black Holes

5.1 Introduction

The cosmic epoch in the redshift range $10 \lesssim z \lesssim 30$ was characterized by the formation of the first stars (Pop III) and of the first black holes (see Bromm & Yoshida 2011, Volonteri 2010, Volonteri & Bellovary 2012, Haiman 2013 for recent reviews). Detecting these sources directly is at, or beyond, the sensitivity edge of current observatories. While recently Sobral et al. (2015) have shown that a very luminous Lyα emitter at $z \approx 6.6$ may be consistent with having a mixed composition of Pop III and second-generation (Pop II) stars, to date there are no confirmed observations of the first black holes, partly due to the uncertainty on their observational signatures. The next generation of observatories will most likely detect the first glimpses of light in the Universe, both in the electromagnetic spectrum (e.g. ALMA, JWST, ATHENA) and in the gravitational waves domain (e.g. e-LISA, DECIGO, see also Chapter 7).

The formation process of the first black holes is likely to produce a strong imprint on their observational signatures, as well as on their mass growth. The standard theory of Eddington-limited accretion predicts that black holes grow in mass over a time scale $\sim 0.045\epsilon_{0.1}\,\mathrm{Gyr}$, where $\epsilon_{0.1}$ is the matter-energy conversion factor normalized to the standard value of 10%. With black hole seeds of initial mass $\sim 100\,\mathrm{M}_{\odot}$, formed at the end of the very short ($\sim 1 - 10\,\mathrm{Myr}$) lifetime of Pop III stars, it is, at best, challenging

to explain recent observations of optically bright quasars with $M_\bullet \sim 10^{9-10}\,\mathrm{M}_\odot$ at $z \sim 7$ (Mortlock et al., 2011, Wu et al., 2015). An alternative, attractive solution is based on Massive Black Hole (MBH) seeds ($10^{3-5}\,\mathrm{M}_\odot$) appearing at $z \sim 10 - 15$, giving a jump start to the growth process (e.g., Spaans & Silk, 2006, Begelman et al., 2006, Lodato & Natarajan, 2006). Under specific conditions (Bromm & Loeb 2003, Begelman et al. 2006, Volonteri et al. 2008, Shang et al. 2010, Johnson et al. 2012, Agarwal et al. 2014), the collapse of a primordial atomic-cooling halo may lead to the formation of MBHs with a birth mass function peaked at $M_\bullet \sim 2\times10^5\,\mathrm{M}_\odot$ (Ferrara et al., 2014). The subsequent gas accretion from the host halo leads to further growth into $\gtrsim 10^7\,\mathrm{M}_\odot$ objects.

The expected abundance of MBHs is largely unconstrained. Salvaterra et al. (2012) and Treister et al. (2013) provided upper limits of order $\rho_\bullet \lesssim 10^{3-4}\,\mathrm{M}_\odot\,\mathrm{Mpc}^{-3}$, using the X-ray background and the stacked X-ray luminosity of high-redshift galaxies, respectively. Upper limits for the $z = 6$ MBH mass density provided by Willott (2011), Fiore et al. (2012) and Cowie et al. (2012) are even lower ($\rho_\bullet \lesssim 10^{2-3}\,\mathrm{M}_\odot\,\mathrm{Mpc}^{-3}$), although none of these constraints take into account Compton-thick sources that can be buried deep inside dense nuclei in proto-galaxies. Yue et al. (2013, 2014) noted that if MBHs are responsible for the near-infrared background fluctuations, their high-redshift mass density should be comparable to the present-day value: $\rho_\bullet(z = 0) \sim 2 \times 10^5\,\mathrm{M}_\odot\,\mathrm{Mpc}^{-3}$, see Yu & Tremaine (2002). The population of high-redshift MBHs would produce gravitational waves, during their collapse (see Chapter 7) or ensuing MBH-MBH mergers (Sesana et al., 2007, 2011), detectable with upcoming observatories.

Previous chapters (Chapter 3 and Chapter 4) focused, through accurate 1D radiation-hydrodynamic simulations, on the dynamical evolution of $z \sim 10$ MBH seeds with initial mass $M_\bullet \sim 10^{3-6}\,\mathrm{M}_\odot$, embedded in dark matter halos with total mass $M_h \sim 10^8\,\mathrm{M}_\odot$ and accreting in the standard Eddington-limited scenario, or including a model for super-Eddington accretion through slim disks (see also Volonteri & Rees 2005, Volonteri et al. 2015). In the present chapter we focus on their emission spectrum with three objectives: (i) predict the time evolution of the spectrum, (ii) assess the observability with current (Chandra Deep Field South, CDF-S) and future (JWST, ATHENA) surveys, and (iii) estimate the mass density $\rho_\bullet$ of high-redshift MBHs.

The outline of this chapter is as follows. In Sec. 5.2 we describe the physical and numerical implementation, while in Sec. 5.3 we present our results for the spectral

evolution of high-redshift MBHs. Finally, in Sec. 5.4 we provide some further discussion and a summary. Throughout, we adopt recent Planck cosmological parameters (Planck Collaboration et al., 2015) as reported in Table 1.1.

5.2 Physical and Numerical Implementation

The present work is based on radiation-hydrodynamic simulations post-processed with `CLOUDY`, a spectral synthesis code (Ferland et al., 2013).

The physical framework is the following: a high-redshift ($z = 10$) MBH seed with initial mass $10^5\,\mathrm{M}_\odot$ is located at the center of a dark matter halo with primordial composition and total mass $M_h \sim 10^8\,\mathrm{M}_\odot$ ($T_{\rm vir} \sim 10^4\,\mathrm{K}$). The MBH accretes mass from the inner parts (within $\sim 10\,\mathrm{pc}$) of the host halo until complete gas depletion.

Our radiation-hydrodynamic code takes into account the frequency-integrated radiative transfer through the gas, with appropriate: (i) cooling and heating terms, (ii) matter-to-radiation coupling, and (iii) energy propagation through a two-stream approximation method. The code computes the accretion rate through the inner boundary of the simulation domain, from which we derive the total bolometric energy radiated by accretion, assuming a radiatively efficient or inefficient disk. The full *frequency-dependent* radiative transfer through the host halo is then performed in a post-processing step using `CLOUDY`. This code computes the detailed time-evolving spectrum emerging from the host halo using as input the matter distribution obtained from our radiation-hydrodynamics simulations and the realistic irradiation spectrum at the inner boundary, scaled to the appropriate bolometric luminosity. Additional details are given in Sec. 5.2.1 and Sec. 5.2.2.

5.2.1 Dynamics and thermodynamics

Our radiation-hydrodynamic code (see Chapter 3 for an extensive description) solves the 1D spherically-symmetric equations of hydrodynamics and a frequency-integrated version of radiative transfer equations. The code evolves self-consistently the radial component of the standard system of ideal, non-relativistic Euler's equations (neglecting viscosity, thermal conduction and magnetic fields) for a gas accreting, with no angular

momentum, onto the central MBH, assumed at rest and already formed at the time $t = 0$, with a given initial mass $M_\bullet(t = 0)$. The simulation domain spans from 0.1 pc to 10 pc, largely encompassing the characteristic spatial scale for accretion, the Bondi radius:

$$R_B = \frac{GM_\bullet}{c^2_{s(\infty)}} \sim 3.0\,\mathrm{pc}\,, \tag{5.1}$$

where G is the gravitational constant and $c_{s(\infty)} = \sqrt{\gamma R T_\infty/\mu} \sim 12\,\mathrm{km\,s^{-1}}$ is the sound speed at large distances from the accretion boundary; $\gamma = 5/3$ is the ratio of specific heats, R is the gas constant, T is the gas temperature and $\mu = 1.15$ is the mean molecular weight for a primordial H-He composition gas with helium fraction $Y_P = 0.24665$ (Planck Collaboration et al., 2015) and no metals. For a $10^5\,\mathrm{M}_\odot$ object, the inner boundary of our spatial domain is $\sim 10^7$ times larger than the Schwarzschild radius and $\sim 10^5$ times larger than the centrifugal radius, i.e. the spatial scale below which deviations from spherical symmetry become important and an accretion disk may form. Moreover, the angular momentum transfer in the outward direction of the accretion flow is very efficient, due to gravitational torques induced by dark matter and gas distributions of the halo (Choi et al., 2015). The gas loses its angular momentum efficiently and flows well beyond its centrifugal barrier. Therefore, despite its simplifications, our 1D approach is significantly helpful in acquiring physical insights on the mechanisms regulating the black hole growth. For the same reason, neglecting viscosity, thermal conduction and magnetic fields is a safe choice, since they play an important role only on spatial scales comparable with the radius of the accretion disk.

The gas accretion through the inner boundary of our spatial domain produces an accretion rate $\dot{M}_\bullet$, which in turn generates an emitted luminosity L via two different accretion models: (i) a standard Eddington-limited model in which $L = \epsilon c^2 \dot{M}$, $\epsilon = 0.1$, and (ii) a radiatively inefficient model, the slim disk, in which $L \propto \ln(M_\bullet)$ and $\epsilon \lesssim 0.04$ is a function of $\dot{M}_\bullet$. The main physical quantity that determines the properties of the accretion disk, and consequently the radiative efficiency, is the accretion rate. Accretion of gas at moderate rates ($0.01 \lesssim f_{Edd} \lesssim 1$) is expected to form a radiatively efficient, geometrically thin and optically thick accretion disk, which is typically modelled with the standard α-disk model (Shakura & Sunyaev, 1973). In a Shakura & Sunyaev disk the radiative efficiency is determined only by the location of the innermost stable circular orbit, which in turn depends only on the spin of the black hole, and it varies between $\sim 6\%$ and $\sim 32\%$ for a non-spinning and a maximally spinning black hole, respectively

(Thorne 1974, see also Chapter 2). In a super-critical ($f_{Edd} > 1$) accretion environment the structure of the accretion disk is, instead, expected to be geometrically and optically thick and radiatively inefficient (but see Jiang et al. 2014, McKinney et al. 2015). The most common solution proposed for such accretion flows is the slim disk (Paczynski & Abramowicz 1982, Abramowicz et al. 1988, Mineshige et al. 2000, Sadowski 2009, 2011, McKinney et al. 2014). In these scenarios, part of the energy produced inside the disk is advected inwards (see, e.g., Abramowicz & Fragile 2013, Lasota 2015) out to a spatial scale named the photon trapping radius ($R_{tr} \sim R_s f_{Edd}$, where R_s is the Schwarzschild radius). Therefore, only a fraction of the photons produced in the accretion disk is able to free stream out of R_{tr}: consequently, the effective radiation and radiation pressure escaping to infinity is decreased (see e.g. Begelman 1978, Ohsuga et al. 2002). While the slim disk solution is the simplest and most tested model for super-critical accretion, alternatives exist, e.g the ZEro-BeRnoulli Accretion (ZEBRA, Coughlin & Begelman 2014) and the ADiabatic Inflow-Outflow Solutions (ADIOS, Blandford & Begelman 1999, Begelman 2012) models. These theoretical models also include a parameter that describes the fraction of the inflowing mass which is lost due to radiation pressure.

Radiation pressure accelerates the gas via:

$$a_{rad}(r) = \frac{\kappa(\rho, T) L(r)}{4\pi r^2 c}\,, \tag{5.2}$$

where the gas opacity $\kappa(\rho, T)$ includes Thomson and bound-free terms, with the inclusion of a temperature dependence (Begelman et al., 2008). The radiation pressure may be able to temporarily interrupt the gas inflow, resulting in an intermittent accretion and outflows. The physical parameters regulating this occurrence are investigated in Chapter 4.

We assume that the gas initially follows the isothermal ($T \sim 10^4\,\mathrm{K}$) density profile derived from the simulations in Latif et al. (2013a), approximated by the functional form:

$$\rho(r) = \frac{\rho_0}{1 + (r/a)^2}\,, \tag{5.3}$$

where a is the core radius and ρ_0 is the central density. To understand how the matter distribution influences both the accretion and the emerging spectrum (through the hydrogen column density), we implemented two different density profiles, both of them yielding a gas mass $\sim 10^7\,\mathrm{M}_\odot$: (i) a high density profile (HDP) with a central density

$\rho_0 = 10^{-12}\mathrm{g\,cm^{-3}}$ and a core radius $a = 0.002\,\mathrm{pc}$, and (ii) a low density profile (LDP) with a central density $\rho_0 = 10^{-18}\mathrm{g\,cm^{-3}}$ and a core radius $a = 2\,\mathrm{pc}$. The LDP may be thought as the density profile resulting after the formation of a MBH of mass $\sim 10^5\,\mathrm{M_\odot}$ at the halo center (see Latif et al. 2013b, 2014b), while in the HDP case the seed formed is very small ($\lesssim 10^3\,\mathrm{M_\odot}$). These density profiles are the same employed in Chapter 4. A density floor of $10^{-24}\,\mathrm{g\,cm^{-3}} \sim 1\,\mathrm{cm^{-3}}$, a factor at least 10^6 times smaller than the central density for both profiles, is imposed for numerical stability reasons. In summary, we have four models: standard accretion - LDP, standard accretion - HDP, slim disk accretion - LDP, slim disk accretion - HDP.

5.2.2 Spectrum

Our code evolves the system in time until gas depletion and provides `CLOUDY` with data to compute the spectrum emerging from the host halo. This code takes into account: (i) the spatial profiles for hydrogen number density $n_H(r)$ and temperature $T(r)$, (ii) the source spectrum of the central object, and (iii) the bolometric luminosity L of the source, computed self-consistently from $\dot{M}_\bullet$. The spherical cloud of gas is assumed to be metal-free, so that only H and He recombination lines are present. The addition of a small amount of metals, formed by the first Pop III stars, would increase the number of lines and the absorption of high-energy photons. The source SED is taken from Yue et al. (2013) and can be described as the sum of three components: (i) a multi-colour blackbody, (ii) a power-law, and (iii) a reflection component. The source spectrum is extended from far-infrared to hard X-ray ($\sim 1\,\mathrm{MeV}$).

5.3 Results

We describe in the following the standard accretion - LDP case, and discuss the differences with the other cases when needed.

The balance between the inward gravitational acceleration and the outward radiation pressure keeps the accretion rate close to the Eddington level ($f_{Edd} \approx 1.2$) for most of the time, ensuring a continuous accretion (see Chapter 3). The top panel of Fig. 5.1 shows the time evolution of f_{Edd} and of $M_\bullet$ in this accretion scenario. Defining the duty cycle, $\mathcal{D}$, as the fraction of time spent accreting during the total evolutionary time

of the system, we find that in the LDP cases $\mathcal{D} = 1$, while other accretion scenarios may be characterized by quiescent phases ($\mathcal{D} < 1$, see Table 5.1). The system evolves for $\sim 120\,\mathrm{Myr}$, until complete depletion of the $\sim 10^7\,\mathrm{M}_\odot$ gas reservoir within $\sim 10\,\mathrm{pc}$. However, this time scale is a lower limit, since in a real galaxy the gas would extend much further.

Fig. 5.2 (top panel) shows the time evolution of the bolometric luminosity emitted at the inner boundary, before traversing the host halo gas. The corresponding Eddington luminosity:

$$L_{Edd} \equiv \frac{4\pi G M_\bullet c}{\kappa_T} \propto M_\bullet\,, \tag{5.4}$$

with κ_T being the Thomson opacity, is also shown for comparison. The luminosity increases for the first $\sim 115\,\mathrm{Myr}$, reaching a peak of $\sim 5 \times 10^{44}\,\mathrm{erg\,s^{-1}}$ and is, on average, mildly super-Eddington as long as the amount of gas is sufficient to sustain this accretion rate. Afterwards, the luminosity plummets, when all the available gas has been consumed. For comparison, the interested reader is referred to Chapter 3, where a plot of the same physical quantities is shown in Fig. 3.8. Moreover, Fig. 5.2 also shows the values of the hydrogen column density, N_H, computed at selected times ($t_s = 5$, 75, 110, 115, 120 Myr) when also the emergent spectrum is computed. The system is initially Compton-thick ($N_H \gtrsim 1.5 \times 10^{24}\,\mathrm{cm^{-2}}$, see the horizontal line). As the gas is progressively accreted by the MBH, N_H steadily decreases before a sudden drop ($t_s \approx 115$ Myr) corresponding to the remaining gas evacuation by radiation pressure. Table 5.1 lists duty cycles and accretion time scales for all four models.

The bottom panels of Fig. 5.1 and Fig. 5.2 show the time evolution of f_{Edd}, $M_\bullet$, L and N_H in the slim disk - LDP case. In this accretion scenario, the Eddington rate reaches high values ($f_{Edd} \sim 20$) only for a short amount of time ($\sim 2\,\mathrm{Myr}$), while afterwards the accretion rates are sub-Eddington. The evolution is much more rapid (the available gas is consumed in $\sim 6\,\mathrm{Myr}$, a factor of ~ 16 faster than in the standard case) and the host halo becomes Compton-thin ($N_H \lesssim 1.5 \times 10^{24}\,\mathrm{cm^{-2}}$) in $\lesssim 2\,\mathrm{Myr}$. As already noted in Chapter 4, in the slim disk accretion - LDP case, the black hole is able to accrete up to $\sim 80\%$ of the gas mass within $\sim 10\,\mathrm{pc}$, with respect to the $\sim 15\%$ in the standard accretion scenario, and the black hole grows to $\sim 8 \times 10^6\,\mathrm{M}_\odot$ in $\sim 6\,\mathrm{Myr}$, while in the standard case the black hole grows to $\sim 1.5 \times 10^6\,\mathrm{M}_\odot$ in $\sim 100\,\mathrm{Myr}$.

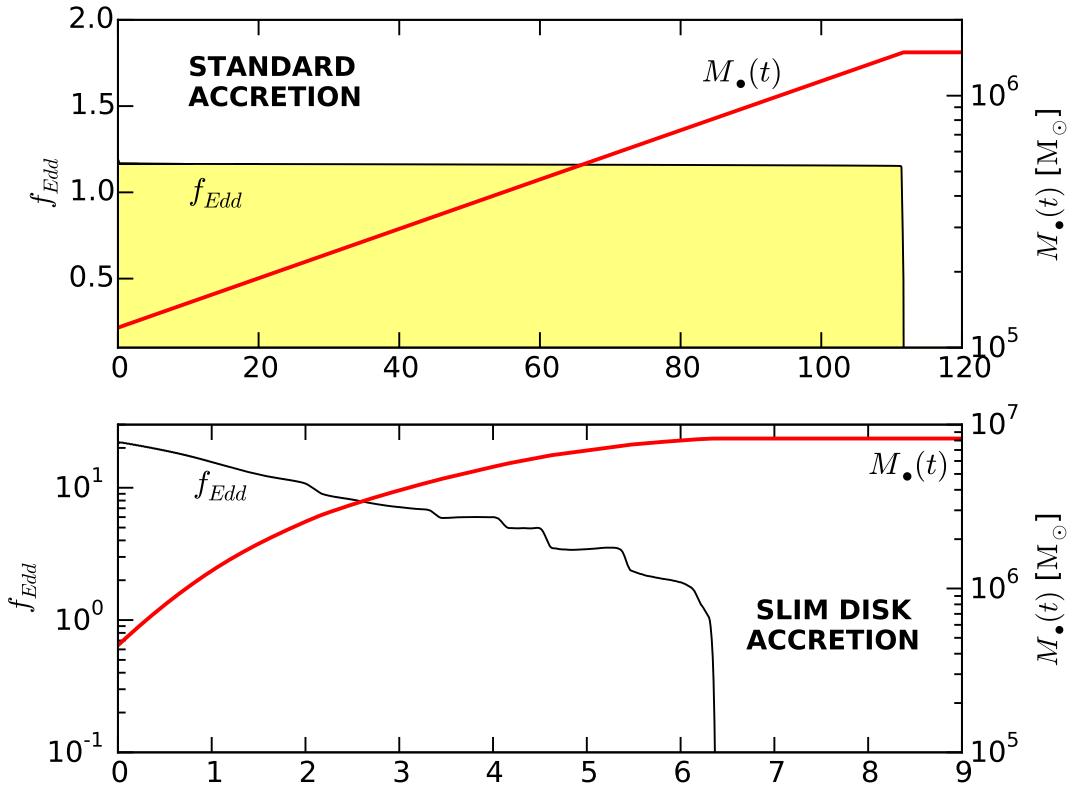

FIGURE 5.1: Time evolution of the Eddington factor f_{Edd} and of the black hole mass $M_\bullet$, in the standard accretion - LDP (top) and the slim disk accretion - LDP (bottom) scenarios. The Eddington ratio is reported as a running average over periods of $\sim 0.1\,\mathrm{Myr}$.

5.3.1 Spectral evolution

The time-evolving spectrum emerging from the host halo, in the standard accretion - LDP case, is shown in Fig. 5.3 at $z = 9$, i.e. $\sim 100\,\mathrm{Myr}$ after the beginning of the simulation ($z = 10$). The spectrum is composed by: (i) the continuum emitted by the source and attenuated by the gas, and (ii) the diffuse emission of the gas. Most of the energy emerges in the *observed* infrared and X-ray bands. The latter is characterized by a bell-shaped spectrum peaked around 1 keV, while in the infrared band a large number of H-He nebular lines is present. Photons with frequency shortwards than the Lyα line are absorbed by the intervening matter at column densities $N_H \gtrsim 10^{23}\,\mathrm{cm}^{-2}$ and reprocessed at lower energies, boosting the infrared emission of the halo. X-ray emission occurs predominantly within the rest-frame energy range $4\,\mathrm{keV} < E_\gamma < 10\,\mathrm{keV}$. The mean free path of such photons is much larger than the Hubble radius at $z = 9$: $\lambda_X \gtrsim 8\,\mathrm{Gpc} \gg R_H(z = 9) = 165\,\mathrm{Mpc}$. Hence growing MBH seeds negligibly contribute to reionization. The increase with time of the continuum normalization in

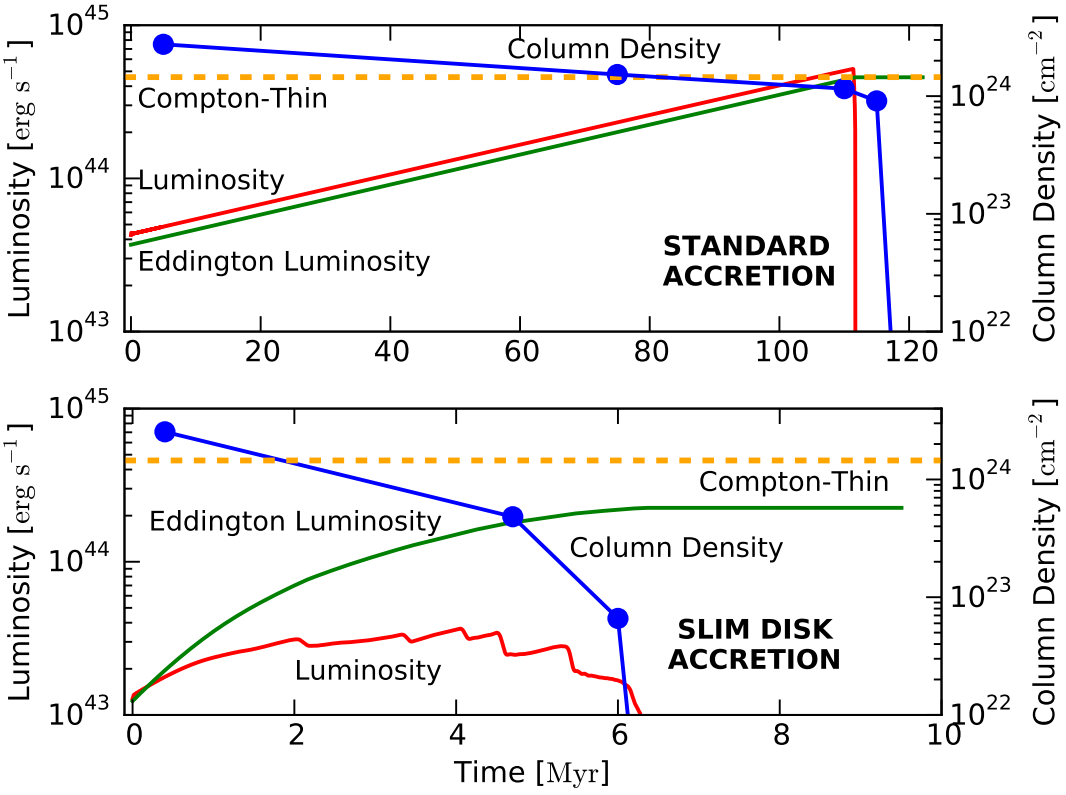

FIGURE 5.2: Time evolution of the bolometric luminosity emitted at the inner boundary, before traversing the host halo gas, in the standard accretion - LDP (top) and the slim disk accretion - LDP (bottom) scenarios. The luminosity is reported as a running average over periods of ~ 0.1 Myr. The corresponding Eddington luminosity, $L_{Edd} \propto M_{\bullet}$, and the values of the hydrogen column density (blue curves, right axis) are also shown.

the X-ray is mainly due to the progressive rise of the bolometric luminosity of the central object. The ratio between the infrared and the X-ray continua depends on the column density, since in the Compton-thick case ($N_H \gtrsim 1.5 \times 10^{24}\,\mathrm{cm}^{-2}$) the high-energy frequencies are heavily absorbed and reprocessed at lower energies, leading to an overall increase of the infrared emission. When the gas becomes Compton-thin at ~ 75 Myr, the X-ray continuum progressively increases, while the infrared one starts to decrease. Approaching the complete gas depletion within ~ 10 pc, at ~ 120 Myr, the column density is so low (see Fig. 5.2, top panel) that the outgoing radiation is nearly unimpeded (the emerging spectrum is very similar to the source spectrum, reported, at peak luminosity, $t = 115$ Myr, as a dashed line) and the continuum normalization drops by ~ 3 (~ 4) orders of magnitude in the X-ray (infrared) band.

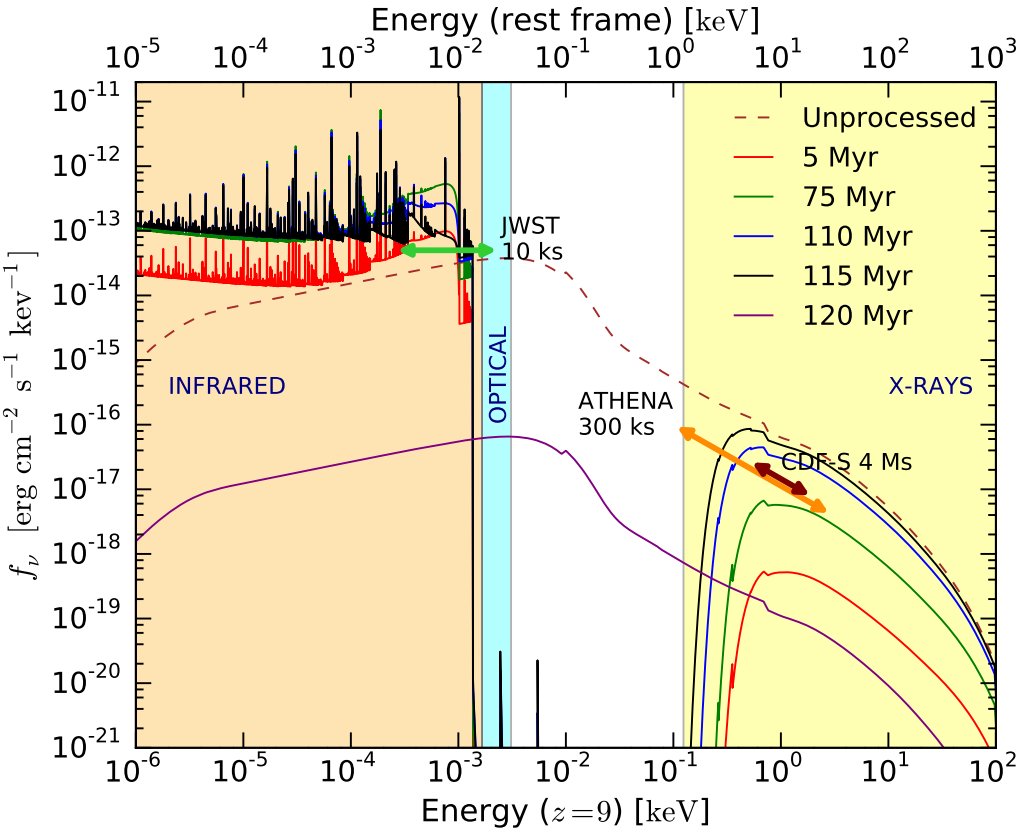

FIGURE 5.3: Time evolution of the spectrum emerging from the host halo for a source located at $z = 9$, in the standard accretion - LDP case. The infrared, optical and X-ray bands are highlighted with shaded regions, while the unprocessed spectrum is reported, at peak luminosity ($t = 115$ Myr), with a dashed line. The flux limits for future (JWST, ATHENA) and current (CDF-S) surveys are also shown.

5.3.2 High-redshift massive black hole density

The approximate flux thresholds for two future-generation observatories (JWST[1] in the infrared band, ATHENA[2] in the X-ray) and for the CDF-S[3] survey are shown in Fig. 5.3. We predict that the JWST will be able to observe most ($\gtrsim 95\%$) of the accretion process onto a $10^5\,M_\odot$ MBH seed up to a comoving distance corresponding to $z \sim 25$, while ATHENA will only detect $\sim 25\%$ of the total evolution, around the peak luminosity, up to $z \sim 15$.

Comparing the predicted peak flux (in the 1 keV observed band) with the CDF-S sensitivity, we find that this ultra-deep survey could have observed the accretion process onto a typical MBH up to $z_{max} \sim 15$. In the CDF-S survey, $N_C = 3$ AGN candidates at $z \gtrsim 6 \equiv z_{min}$ have been identified (Giallongo et al. 2015, but see also Weigel

[1]For a NIRcam observation with a Signal-to-Noise ratio of 10 and a total integration time of 10^4 s.
[2]For a 3σ detection with a total integration time of 3×10^5 s.
[3]Ultra-deep survey in the X-ray with a total integration time of 4×10^6 s.

et al. 2015 where the authors question some of these candidates) inside a sky region of $\sim 170\,\mathrm{arcmin}^2$. An upper limit for the number density of MBH seeds can be derived as:

$$n_\bullet(6 < z < 15) \lesssim \frac{N_C}{\Omega_{CDF}\mathcal{V}\mathcal{D}\mathcal{F}}\,, \tag{5.5}$$

where $\Omega_{CDF} = 1.1\times10^{-6}$ is the sky fraction observed by the CDF-S, $\mathcal{V} = 2.3\times10^{12}\,\mathrm{Mpc}^3$ is the comoving volume of the Universe between z_{min} and z_{max}, $\mathcal{D}$ is the duty cycle for accretion and $\mathcal{F} \equiv t_{det}/t_{obs}$ is the fraction of time during which the object is detectable within the time frame $t_{obs}(6 < z < 15) = 670\,\mathrm{Myr}$, assuming a single episode of MBH growth at these redshifts[4]. The predicted flux, within the spectral range $0.5 - 2.0\,\mathrm{keV}$, is above the CDF-S sensitivity between $\sim 85\,\mathrm{Myr}$ and $\sim 115\,\mathrm{Myr}$, so that $t_{det} = 30\,\mathrm{Myr}$ and $\mathcal{F} = 0.045$. Using these values we obtain the following upper limit for the number density of MBH seeds:

$$n_\bullet(6 < z < 15) \lesssim \frac{2.5\times10^{-5}}{\mathcal{D}}\left(\frac{0.045}{\mathcal{F}}\right)\,\mathrm{Mpc}^{-3}\,. \tag{5.6}$$

Considering MBHs of initial mass $10^5\,\mathrm{M}_\odot$ growing up to $\sim 10^7\,\mathrm{M}_\odot$ (see Chapter 3), we finally obtain the following upper limit for the MBH seeds mass density:

$$\rho_\bullet(6 < z < 15) \lesssim \frac{2.5\times10^{2}}{\mathcal{D}}\left(\frac{0.045}{\mathcal{F}}\right)\,\mathrm{M}_\odot\,\mathrm{Mpc}^{-3}\,. \tag{5.7}$$

The discussion so far has been limited to the scenario in which a MBH with an initial mass close to the peak of the birth mass function devised in Ferrara et al. (2014) accretes gas from a LDP host halo in the Eddington-limited mode. However, this is not the only possible scenario. Table 5.1 provides a general outline of the accretion history and CDF-S observability for a MBH seed with initial mass $10^5\,\mathrm{M}_\odot$ in three additional scenarios: standard accretion - HDP, slim disk accretion - LDP and slim disk accretion - HDP. Table 5.1 includes the depletion time t_{end}, the duty cycle $\mathcal{D}$, the detection time t_{det} with its related value of $\mathcal{F}$ and the upper limit on $\rho_\bullet$. In the Eddington-limited cases the depletion times are lower limits since, while our simulations are run in isolation, in a cosmological framework the halo growth by mergers and accretion would not be negligible within $\sim 100\,\mathrm{Myr}$. In the slim disk case, given the depletion times of order

[4]This calculation assumes spherical symmetry of the host halo and an isotropic irradiation of the MBH. If the density along the poles is much lower, then a fraction of the sources would be completely unobscured.

TABLE 5.1: Accretion history and CDF-S observability for a MBH seed with initial mass $M_\bullet = 10^5\,\mathrm{M}_\odot$ in the four indicated accretion scenarios.

Accretion scenario	Observable	t_{end} [Myr]	$\mathcal{D}$	t_{det} [Myr]	$\mathcal{F}$	$\rho_\bullet$ [$\mathrm{M}_\odot\,\mathrm{Mpc}^{-3}$]
Standard - LDP	YES	120	1.0	30	0.045	$\lesssim 2.5 \times 10^2$
Standard - HDP	YES	240	0.4	110	0.16	$\lesssim 1.8 \times 10^2$
Slim disk - LDP	NO	7	1.0	0	0	No constraints
Slim disk - HDP	YES	12	1.0	1	0.0015	$\lesssim 7.6 \times 10^3$

$\sim 10\,\mathrm{Myr}$, the hierarchical growth of the halo plays a minor role.

Interestingly, the accretion process is undetectable by the CDF-S in the slim disk - LDP case, whose time-evolving spectrum is shown in Fig 5.4. Therefore no constraints on $\rho_\bullet$ can be obtained in this case. The slim disk - HDP case is instead observable, albeit only for a very short time, $t_{det} \sim 1\,\mathrm{Myr}$, due to the larger accretion rates in this scenario, which produce a sufficiently high luminosity despite radiation trapping. The very low value of $\mathcal{F} \sim 1.5 \times 10^{-3}$ produces an upper limit for $\rho_\bullet$ higher than in other accretion scenarios by a factor ~ 35.

Let us now focus on the reason why the slim disk case leads to a very different value for $\rho_\bullet$ with respect to the standard accretion case. The amount of mass that is available for accretion is equal in both cases ($\sim 10^7\,\mathrm{M}_\odot$) and, to a first-order approximation, also the mass actually accreted is similar. This is not strictly true, since the radiation pressure is more efficient in the standard case in creating mass outflows (see Chapter 4), but the produced outflows are fairly weak regardless of the accretion scenario. The real difference between the slim disk and the standard cases is due to radiation trapping, which decreases the effective bolometric luminosity (i.e. the luminosity escaping to infinity) in the former case, with respect to the latter. Since the accreting black hole is intrinsically fainter in the slim disk case, it will be observable for a smaller fraction of time, $\mathcal{F}$ (with the extreme $\mathcal{F} = 0$ for the LDP case), during its evolution: this eventually leads to a larger upper limit on $\rho_\bullet$.

The initial mass of the MBH seed influences the time scale of the process and its observability. If, for instance, the high-redshift population of MBHs is characterized by a larger average mass, the evolutionary time scale would be smaller (since $t_{end} \propto \dot{M}_{Edd}^{-1} \propto M_\bullet^{-1}$, where $\dot{M}_{Edd}$ is the Eddington accretion rate), but the emitted luminosity would be higher (since $L \propto L_{Edd} \propto M_\bullet$). The effect on $\mathcal{F}$ may vary from case to case, but in general a larger average mass is likely to decrease $\mathcal{F} \equiv t_{det}/t_{obs}$ since $t_{det} \leq t_{end} \propto M_\bullet^{-1}$.

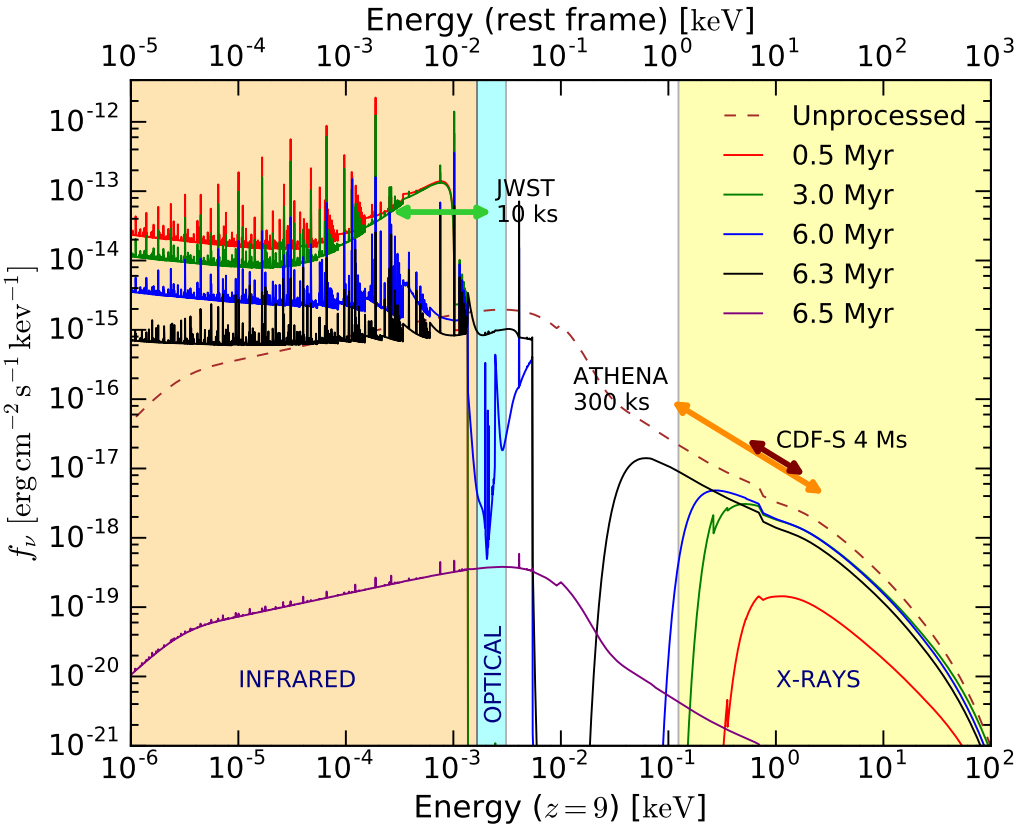

FIGURE 5.4: As in Fig. 5.3, but for the slim disk accretion - LDP case.

This would lead to a less stringent upper limit on $\rho_\bullet$.

5.4 Discussion and Summary

Using a combination of radiation-hydrodynamic and spectral synthesis codes, we have investigated the time-evolving spectral energy distribution of an accreting $z \sim 10$ MBH. The MBH seed, whose initial mass is $10^5\,\mathrm{M}_\odot$, is embedded in a dark matter halo of total mass $10^8\,\mathrm{M}_\odot$. Employing two gas density profiles and two accretion modes (Eddington-limited and slim disk) we simulated the system until complete gas depletion and we accurately calculated the time-evolving spectrum of the radiation emerging from the host halo. The main results of this work are summarized in the following.

- The spectrum of the emerging radiation, for a MBH observed at $z = 9$, is dominated by the infrared-submm ($1 - 1000\,\mu$m) and X-ray ($0.1 - 100\,$keV) bands. Photons with frequency shortwards than the Lyα line are absorbed by the intervening matter at column densities $N_H \gtrsim 10^{23}\,\mathrm{cm}^{-2}$ and reprocessed at lower

energies, in the infrared band. Due to the very large mean free path $\lambda_X > 1\,\mathrm{Gpc}$ of X-ray photons, growing MBH seeds negligibly contribute to reionization. The continuum normalization is set by: (i) the bolometric luminosity of the source and (ii) the column density of the host halo. The former determines the overall normalization, while the latter determines the ratio between the low-energy and the high-energy continua.

- Our predictions show that the JWST will detect in the infrared a fraction $\gtrsim 95\%$ of the accretion process onto a typical MBH seed observed at $z \sim 9$, while ATHENA should observe it in the high-energy bands only around the peak luminosity, a fraction $\sim 25\%$ of the total evolution. Similarly, long-exposure surveys in the X-ray, like the CDF-S, could have already observed the accretion process on a $z \sim 9$ object for a comparable fraction of time. The redshift of the sources sets their luminosity distance, hence influences their detectability. For instance, the standard accretion - LDP system is observable by the CDF-S for $\sim 41\%$ of the time at $z_{min} = 6$, while it becomes undetectable at $z \gtrsim z_{max} = 15$.

- From the $z \gtrsim 6$ candidates detected in the CDF-S survey (Giallongo et al., 2015) we estimate the following upper limits on the $z \gtrsim 6$ MBH mass density: (a) $\rho_\bullet \lesssim 2.5 \times 10^2\,\mathrm{M_\odot\,Mpc^{-3}}$ assuming Eddington-limited accretion; (b) $\rho_\bullet \lesssim 7.6 \times 10^3\,\mathrm{M_\odot\,Mpc^{-3}}$ if accretion occurs in the slim disk, highly obscured mode. However, the accretion process is undetectable with the CDF-S sensitivity in the slim disk accretion - LDP case, due to the flux suppression caused by radiation trapping, and no constraints on $\rho_\bullet$ can be given.

Very recently, we proposed that the first detection of a high-redshift MBH seed could have already occurred. Indeed, in Pallottini et al. (2015) we showed that the observational features of CR7 (Sobral et al., 2015), a bright Lyα emitter at $z = 6.604$, may be explained by accretion onto a MBH of initial mass $\sim 10^5\,\mathrm{M_\odot}$.

For Eddington-limited accretion, our upper limit, $\rho_\bullet \lesssim 2.5 \times 10^2\,\mathrm{M_\odot\,Mpc^{-3}}$, is compatible with the one set by Cowie et al. (2012) using observations of faint X-ray sources in the CDF-S, while it is more stringent than limits by Willott (2011), Fiore et al. (2012) and Treister et al. (2013) ($\rho_\bullet \lesssim 10^3\,\mathrm{M_\odot\,Mpc^{-3}}$) and particularly by Salvaterra et al. (2012) ($\rho_\bullet \lesssim 10^4\,\mathrm{M_\odot\,Mpc^{-3}}$, using the unresolved X-ray emission). The current observational constraints, however, do not take into account heavily buried, Compton-thick objects or

radiatively inefficient accretion. Recently, indeed, Comastri et al. (2015) suggested that recent revisions to the local SMBHs mass density, up to $\rho_\bullet(z = 0) \sim 10^6\,\mathrm{M}_\odot\,\mathrm{Mpc}^{-3}$, seem to imply that a significant fraction of the local SMBHs have grown in heavily buried, Compton-thick phases, or by radiatively inefficient accretion. Our model is a first step towards testing the role of Compton-thick or radiatively inefficient phases in the early growth of MBHs.

In the present chapter, we provided a general picture of the interconnection between the main accretion mode at work in the high-redshift Universe and the black hole mass density. To summarize our rationale: assuming that, for MBHs at $z \gtrsim 6$, the main accretion channel is the standard, Eddington-limited one, we are able to provide an upper limit on $\rho_\bullet$ which is consistent (and competitive) with current estimates. In the standard disk scenario, MBHs have grown in heavily buried, Compton-thick phases for about 70% of the total evolution time (e.g., $\sim 70\,\mathrm{Myr}$ for the LDP), but they are long-lived and intrinsically bright, and visible for a substantial amount of time. Assuming instead that at super-critical accretion rates the accretion disk thickens, with radiation trapping playing a significant role, the suppressed radiative efficiency leads to a much lower intrinsic luminosity. These sources are intrinsically faint, not obscured: the Compton-thick phase is short ($\sim 2\,\mathrm{Myr}$, 30% of the total evolution time for the LDP) because the obscuring gas is consumed rapidly. Our slim disk simulations suggest, as one would expect, that these short-lived and fainter MBHs are more difficult to detect in current surveys compared to brighter objects accreting in the Eddington-limited mode. As a consequence, the upper limit on $\rho_\bullet$ is inevitably higher than currently predicted, up to a factor ~ 35.

5.5 Supplementary Figures

In the following we include additional figures showing the time evolution of the emerging spectrum (in νf_ν units) for the four accretion scenarios discussed so far.

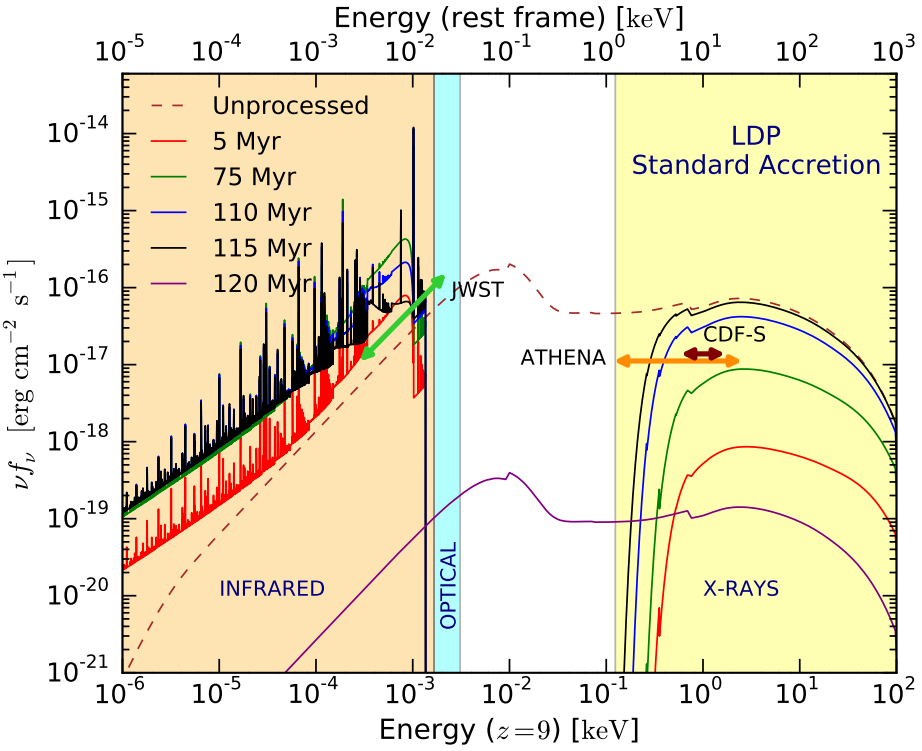

FIGURE 5.5: Standard accretion - LDP case.

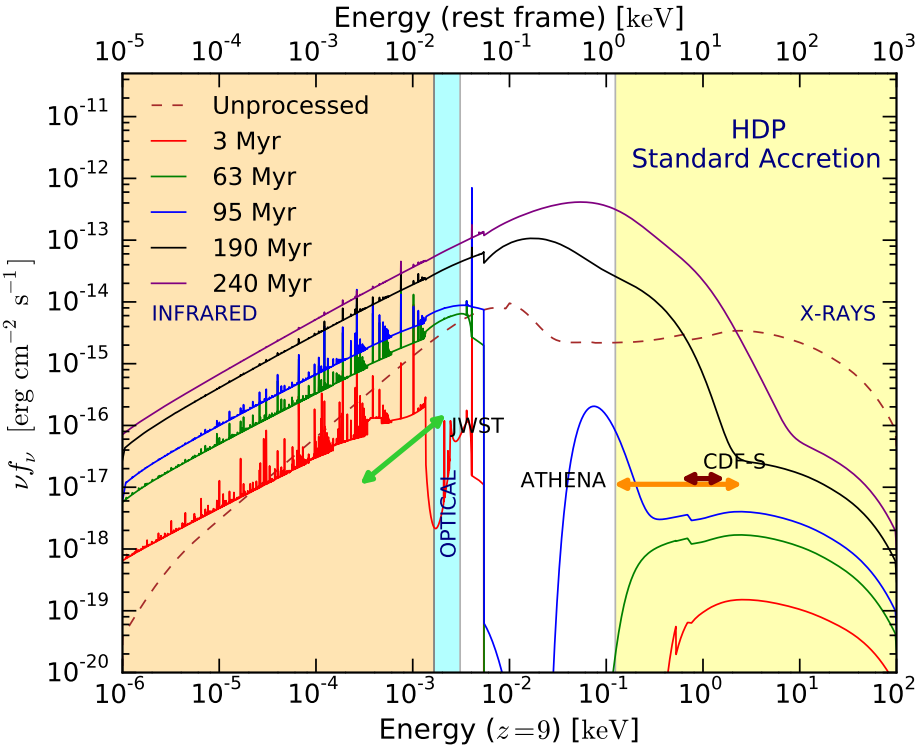

FIGURE 5.6: Standard accretion - HDP case.

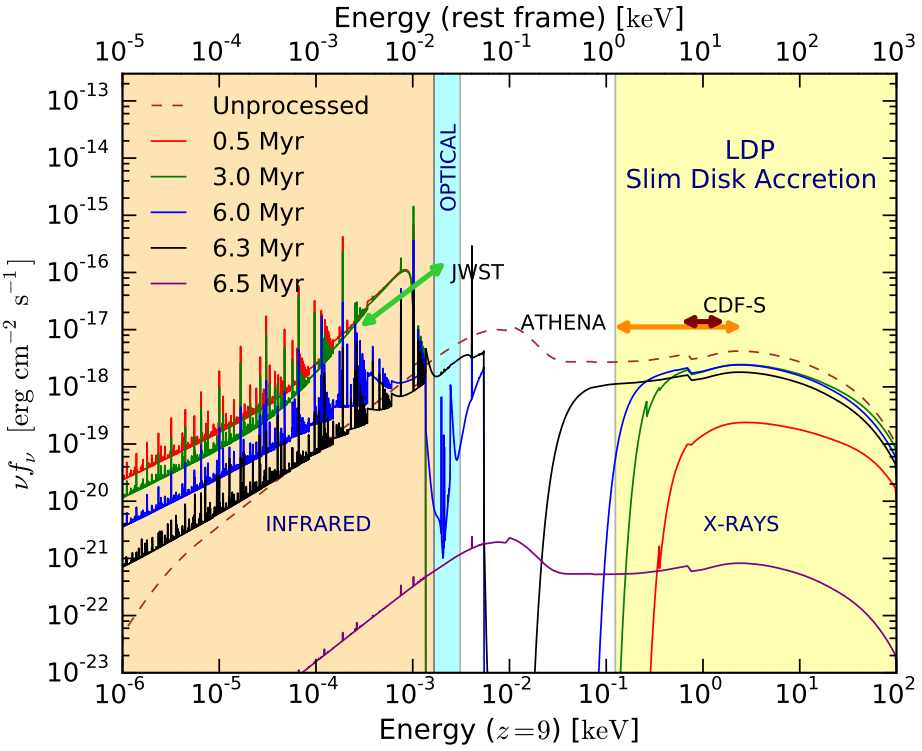

FIGURE 5.7: Slim disk accretion - LDP case.

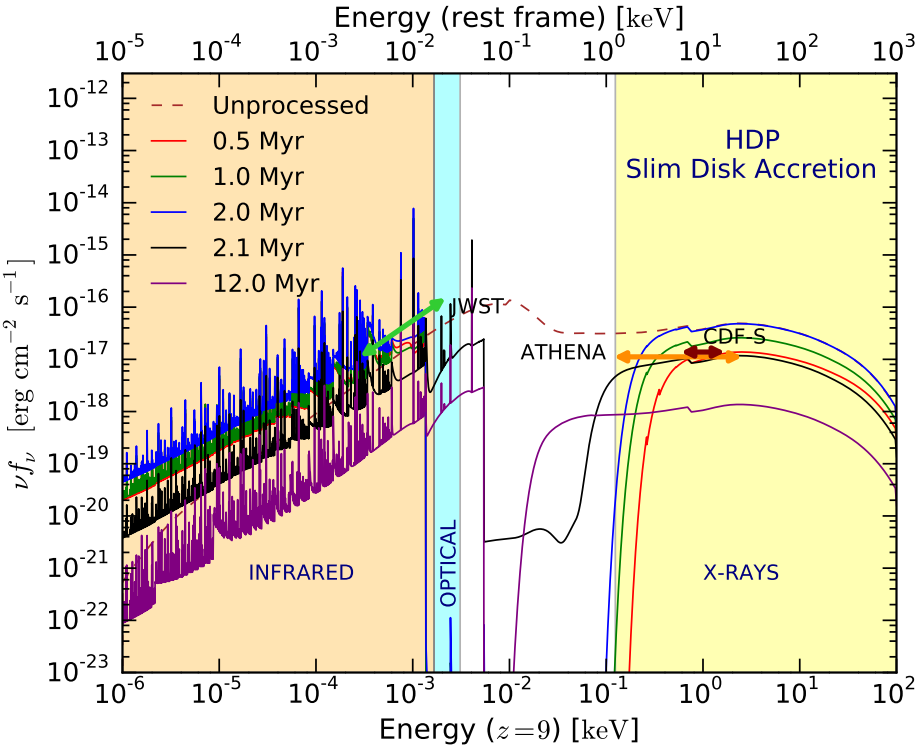

FIGURE 5.8: Slim disk accretion - HDP case.

Chapter 6

First Identification of Direct Collapse Black Hole Candidates in the Early Universe in CANDELS/GOODS-S

6.1 Introduction

The most distant objects with a spectroscopic redshift measurement detected in the Universe to date are extremely powerful gamma-ray bursts ($z \sim 8.2$, Tanvir et al. 2009), and Lyman-break galaxies ($z \sim 11.1$, Oesch et al. 2016). In the same period of the cosmic time, the reionization epoch, the first SMBHs were already in place, but the seeds out of which these extremely massive objects were born have not been observed yet. Several observations (e.g. Mortlock et al. 2011, Wu et al. 2015) have detected the presence of accretion-powered objects with masses in excess of $10^{9-10}\,M_{\odot}$ already at $z \sim 7$, when the Universe was less than 1 billion years old. These observations are in tension with the standard theory of black hole growth, which would require, assuming Eddington-limited accretion, a longer time to produce these massive objects (Fan et al., 2006, Haiman, 2013) from stellar-mass seeds, born out of the first population of stars (Pop III). Assuming that low angular momentum gas is always available for feeding, a black hole grows in mass exponentially, with an e-folding time $\sim 0.045\,\mathrm{Gyr}$, for radiatively efficient accretion models. Starting from a stellar-mass seed ($\lesssim 100\,M_{\odot}$), this process

would require a constant accretion at the Eddington rate to produce a $\sim 10^9\,\mathrm{M}_\odot$ SMBH by $z \sim 7$, a physically unlikely condition.

Two main solutions to the mass growth enigma have been proposed (Volonteri, 2010). Firstly, the black hole seeds from which the accretion started could have been as massive as $\sim 10^{4-6}\,\mathrm{M}_\odot$ (Lodato & Natarajan, 2006, Devecchi & Volonteri, 2009, Davies et al., 2011). One possibility to build up massive black hole seeds at $z \sim 10-15$ is through the DCBH scenario (Shang et al., 2010, Johnson et al., 2012). The collapse of a primordial atomic-cooling halo (with a virial temperature $T_{\rm vir} \gtrsim 10^4\,\mathrm{K}$) may lead, in the presence of a strong flux of Lyman-Werner photons (energy $h\nu = 11.2-13.6\,\mathrm{eV}$) dissociating the H_2 and thus preventing gas fragmentation, to the formation of DCBHs with a typical mass around $10^5\,\mathrm{M}_\odot$ (Ferrara et al., 2014). Secondly, the growth rates might not be capped by the Eddington value (Volonteri & Rees, 2005, Alexander & Natarajan, 2014, Madau et al., 2014, Volonteri et al., 2015, Pacucci et al., 2015) $\dot{M}_{\rm Edd} \equiv L_{\rm Edd}/(\epsilon c^2)$, where $L_{\rm Edd} \approx 1.2 \times 10^{38} M_\bullet\,\mathrm{erg\,s^{-1}}$, $M_\bullet$ is the black hole mass in solar masses, ϵ is the efficiency factor for mass-energy conversion and c is the speed of light. In highly-obscured environments, radiation trapping could allow super-Eddington accretion rates to take place, dramatically speeding up the black hole growth.

At the present time no detection of early SMBH progenitors has been confirmed. This may be due to their extreme faintness, but possibly also to the current lack of clear theoretical indications about their mass, host halo properties and typical accretion rates, resulting in large uncertainties in the prediction of their observational signatures. We proposed (Pallottini et al. 2015, see also Agarwal et al. 2015, Hartwig et al. 2015, Visbal et al. 2016, Smith et al. 2016, Smidt et al. 2016, Dijkstra et al. 2016a) that a $z \approx 6.6$ object named CR7, the brightest Ly-α emitter discovered so far (Sobral et al., 2015), could be powered by a DCBH with an initial mass $\sim 10^5\,\mathrm{M}_\odot$, associated with a standard stellar emission. This was motivated by the peculiarities of its spectrum, namely: (i) very strong Ly-α and He II lines emission, and (ii) absence of metal lines, within the detection threshold. This proposition needs deeper X-ray observations to be confirmed or rejected.

In the previous chapters, in particular Chapter 3 and Chapter 5, employing a combination of radiation-hydrodynamic simulations and spectral synthesis codes, we computed the time-evolving spectrum emerging from the halo hosting a black hole seed. The

bulk of the emission occurs in the observed infrared-submm ($1 - 1000\,\mu$m) and X-ray ($0.1 - 100\,$keV) bands. Here we present a method to select DCBH candidates in ultra-deep fields purely based on infrared photometry.

The outline of this chapter is as follows. In Sec. 6.2 we describe the numerical setup of our simulations, while Sec. 6.3 presents the photometric tool that we developed. In Sec. 6.4 we show our results, including the identification of two DCBH candidates in CANDELS/GOODS-S. Finally, in Sec. 6.5 we discuss the caveats of this work and in Sec. 6.6 we provide some further discussion and a summary. Throughout, we adopt recent Planck cosmological parameters (Planck Collaboration et al., 2015) as reported in Table 1.1.

6.2 Numerical Implementation

In this section we introduce the physical and numerical implementation of our simulations. The interested reader is referred to Chapter 3 (radiation-hydrodynamic module) and to Chapter 5 (spectral module) for a much more detailed description.

6.2.1 General physical framework

A high-z black hole seed, with initial mass $M_\bullet(t=0)$ in the range $10^{4-5}\,\mathrm{M}_\odot$, is placed at the center of a dark matter halo with primordial composition gas (H and He, with helium fraction $Y_P \approx 0.247$, Planck Collaboration et al. 2015), total mass (baryonic and dark matter) M_h and virial temperature $T_{\rm vir} = T_{\rm vir}(M_h, z) \sim 10^4\,$K (Barkana & Loeb, 2001):

$$T_{\rm vir} \approx 1.98 \times 10^4 \left(\frac{\mu}{0.6}\right) \left(\frac{M_h}{10^8\ h^{-1}\ \mathrm{M}_\odot}\right)^{2/3} \left(\frac{1+z}{10}\right)\ \mathrm{K}\,. \tag{6.1}$$

In this formula, μ is the mean molecular weight and h is the reduced Hubble constant. At $z \sim 10$, $T_{\rm vir} \sim 10^4\,$K corresponds to $M_h \sim 10^8\,\mathrm{M}_\odot$. In this work, we do not assume any specific relation between the initial black hole mass $M_\bullet(t=0)$ and its host halo mass M_h. The mass of a black hole seed is assigned following the initial mass function derived in Ferrara et al. (2014). The black hole accretes mass from the inner regions of the host halo, with an accretion rate, $\dot{M}$, self-regulated by the combined effects of gravity, gas pressure and radiation pressure.

6.2.2 Radiation-hydrodynamics

Our radiation-hydrodynamic code (described in Chapter 3) evolves self-consistently the standard system of ideal, non-relativistic Euler's equations for a gas accreting radially onto the central black hole, assumed at rest and already formed at $t = 0$. We do not simulate the formation process of the massive black hole, but our implicit assumption is that it forms via the DCBH scenario, since: (i) the host halo is metal-free, and (ii) the surrounding gas has not been photo-evaporated by Pop III stellar emission. Other formation channels would not comply with these two assumptions.

The spatial domain of the simulations spans from 0.002 pc to 200 pc, largely encompassing the characteristic spatial scale for accretion, the Bondi radius, which, for a $10^5\,M_\odot$ black hole, is ~ 3 pc. The gas initially follows the isothermal density profile derived from the simulations in Latif et al. (2013a), where $\rho(r) \propto (r/a)^{-2}$ and $a \sim 2$ pc is the core radius of the baryonic matter distribution. This density profile is the one resulting after the formation of a massive seed of mass $\sim 10^5\,M_\odot$ at the halo center (Latif et al., 2013b, 2014b).

The value of the black hole mass $M_\bullet(t)$ changes with time, due to the accretion, modeled with the accretion rate $\dot{M}_\bullet = 4\pi r^2 \rho |v|$ (r is the radial coordinate, ρ the gas density and v is the radial velocity, all computed at the inner boundary of the spatial domain). The accretion rate generates an emitted bolometric luminosity $L_{\rm bol}$ computed as:

$$L_{\rm bol} \equiv \epsilon c^2 \dot{M}\,, \tag{6.2}$$

where $\epsilon \approx 0.1$. The radiation pressure accelerates the gas via

$$a_{rad}(r) = \frac{\kappa(\rho, T) L_{\rm bol}(r)}{4\pi r^2 c}\,, \tag{6.3}$$

where the gas opacity $\kappa(\rho, T)$, function of the gas density and temperature, includes Thomson (Begelman et al., 2008) and bound-free terms.

6.2.3 Observed DCBH spectrum

Our radiation-hydrodynamic code computes the frequency-integrated radiative transfer through the gas, taking into consideration the appropriate: (i) cooling and heating

terms, (ii) matter-to-radiation coupling, and (iii) energy propagation through a two-stream approximation method. Full details are provided in Chapter 3. The *frequency-dependent* radiative transfer through the host halo is then performed using the spectral synthesis code `CLOUDY` (Ferland et al., 2013). This code computes the time-evolving spectrum emerging from the host halo (see Chapter 5) employing as input data: (i) the spatial profiles for hydrogen number density and temperature, (ii) the source spectrum of the central object, and (iii) the bolometric luminosity of the source (computed self-consistently with Eq. 6.2). The source SED, extended from far-infrared to hard X-ray, is a standard AGN spectrum, computed for a metal-free gas (Yue et al., 2013). The source spectrum depends on the black hole mass, and therefore evolves with time as $M_\bullet$ increases.

6.3 Photometry and SED Fitting

In this section we describe the main photometric tool used in this work, along with the optical/infrared and X-ray data employed.

6.3.1 The color-color plot

The shape of the spectrum emerging from a high-z dark matter halo hosting a DCBH depends on the black hole mass and on the absorbing hydrogen column density of the surrounding gas. If the halo is Compton-thick ($N_H \gtrsim 1.5 \times 10^{24}\,\mathrm{cm}^{-2}$) high-energy photons ($\lesssim 10 - 50\,\mathrm{keV}$) are largely absorbed and the DCBH may be invisible in the X-ray. Nonetheless, sufficiently massive black hole seeds, $M_\bullet(t = 0) \gtrsim 10^{4-5}\,\mathrm{M}_\odot$, are always visible in the infrared, as we showed in Chapter 5, due to the reprocessing of high-energy radiation into lower-energy photons. Moreover, the infrared spectrum is less dependent on the specifics of the accretion flow.

For these reasons, we devised a method to select DCBH candidates through infrared photometry. The computation of the predicted photometry for a DCBH follows from: (i) the time evolution of the spectrum emerging from the host halo, and (ii) the shapes of the photometric filters employed. Denoting by $\mathcal{F}(F)$ the flux measured through the filter F, the generic color index for the couple of filters A and B is defined as follows: $A - B \equiv -2.5\,\mathrm{Log}_{10}\,[\mathcal{F}(A)/\mathcal{F}(B)]$.

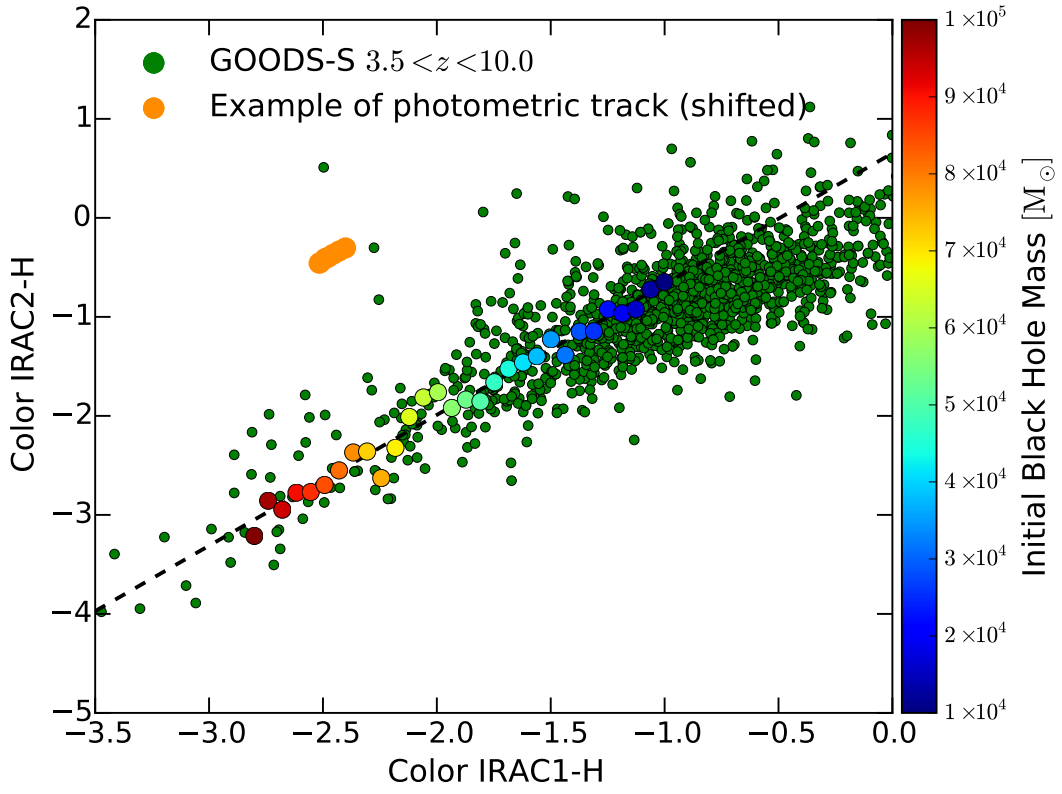

FIGURE 6.1: Color-color diagram for the infrared filters H, IRAC1 and IRAC2. GOODS-S objects, brighter than the 27th magnitude in the H band (H < 27) and with $3.5 \lesssim z \lesssim 10$, are shown with green points. Numerical predictions for the colors of DCBHs are shown, at $z \sim 7$, with filled circles, whose color depends on the initial mass of the seed (see the color-bar). Larger black hole masses are associated with redder spectra (i.e. more negative colors). All colors are *observed quantities*. An example of a photometric track (see Sec. 6.4.1) for a DCBH of initial mass $\sim 8 \times 10^4\,\mathrm{M}_\odot$ is shown in orange. Its position has been shifted vertically to avoid information overload.

We employ three photometric filters to probe the infrared spectrum: the HST H (1.6 μm), the Spitzer IRAC1 (3.6 μm) and IRAC2 (4.5 μm). We construct a color-color diagram (Fig. 6.1) in which we plot both data points for objects in the CANDELS/GOODS-S multi-wavelength survey (see Sec. 6.3.2 for a description of the data) and our predictions for the colors of DCBHs. All colors are *observed quantities*. The data points roughly fall on a line since the observed infrared spectra are to a good approximation power laws, with a broad range of slopes. The position in the color-color plot of DCBH seeds with initial masses in the range $10^{4-5}\,\mathrm{M}_\odot$, computed via radiation-hydrodynamic simulations, is shown with filled circles whose color depends on $M_\bullet(t = 0)$, as shown in the color-bar.

To compute the photometric points for DCBHs as a function of their mass, a total number of ~ 100 simulations have been performed, initializing the black hole seed with

masses in the range $10^{4-5}\,M_\odot$. For each simulation, the mass of the host halo has been modified in order to set the virial temperature $T_{\rm vir} \sim 10^4\,K$ for the redshift of choice (Eq. 6.1). Different sets of simulations have been performed at redshifts $z = 13$, $z = 10$ and $z = 7$. Since the shape of the SED at the wavelengths of our interest is roughly a power law, the effect of a redshift change on the position of the photometric points is small. Each simulation has been run for a time which varies with M_h and with $M_\bullet(t = 0)$, between $\sim 10\,$Myr and $\sim 80\,$Myr, in order to reach a steady state accretion without depleting the gas reservoir. Sec. 6.4.1 and Sec. 6.4.2 describe the dependence of DCBH colors on column density and on black hole mass.

Our method is perfectly adaptable to the JWST photometric system. The photometric filters F150W (center wavelength $\lambda_0 = 1.5\,\mu$m), F356W ($\lambda_0 = 3.6\,\mu$m) and F444W ($\lambda_0 = 4.4\,\mu$m) are equivalents to the H, IRAC1 and IRAC2 filters, respectively, and may be used to implement our selection method with the JWST.

6.3.2 The CANDELS/GOODS-S survey

The photometric data employed in this work are based on the GOODS-S field of the official CANDELS catalogues (Guo et al., 2013). Object selection has been performed in the H band of the near-infrared Wide Field Camera-3. The covering area of the GOODS-S survey is $\sim 170\,$arcmin^2, to a mean 5σ depth of 27.5 magnitudes in the H band. These imaging data include photometry over a wide range of wavelengths, from the U band ($0.36\,\mu$m) to the IRAC4 band ($7.9\,\mu$m). Importantly for our purposes, the catalog includes very deep imaging with the IRAC instrument from the Spitzer Extended Deep Survey (Ashby et al., 2013), covering the CANDELS fields to a 3σ depth of 26 AB magnitude at both $3.6\,\mu$m (IRAC1) and $4.5\,\mu$m (IRAC2). Overall, the detection of objects in the GOODS-S field is realistic up to $27.5 - 28.0$ magnitudes in the H band, at $\sim 90\%$ completeness limit (Grazian et al., 2015).

For the photometric data that we employed in this work, each source has been visually inspected. The total number of sources detected in the GOODS-S field is 34930. In our redshift range of interest, $3.5 \lesssim z \lesssim 10$ (see Fig. 6.1), the total number of objects is 2037, while at high redshifts ($6 \lesssim z \lesssim 10$) is 97. In our analysis we included only GOODS-S objects with a precise value (i.e. not upper limits) for the three magnitudes H, IRAC1 and IRAC2. In total, there are 2272 spectroscopic redshifts of good quality

in the GOODS-S field. The number of spectroscopic redshifts available at $z > 3.5$ is 173 (25 at $z > 6.5$). For sources lacking spectroscopic information, photometric redshifts were computed by optimally-combining six different photometric redshifts (Dahlen et al., 2013). For a broader discussion on the uncertainties in the redshift determination, see Sec. 6.5.2.

6.3.3 X-ray detected objects in the GOODS-S survey

In a recent work (Giallongo et al., 2015), 22 faint AGN candidates were identified in the GOODS-S field as having an X-ray counterpart (but see Weigel et al. 2015 and Cappelluti et al. 2015). The selection method is the following one: high-z galaxies are selected in the H band down to very faint levels (H $\leq$ 27) using reliable photometric redshifts. At $z > 4$, this corresponds to a selection criterion based on the galaxy rest-frame UV flux. AGN candidates are picked up from this parent sample if they show X-ray fluxes above a threshold of $F_X \sim 1.5 \times 10^{-17}\,\mathrm{erg\,cm^{-2}\,s^{-1}}$ in the soft energy band $(0.5 - 2\,\mathrm{keV})$.

For 3 of these sources the photometric redshift is $z \gtrsim 6$: object 33160 at $z \approx 6.06$, object 29323 at $z \approx 9.73$ and object 28476 at $z \approx 6.26$. H band images of the first two sources, with X-ray contours from the Chandra 7 Ms field, are shown in Fig. 6.2. As we will show in Sec. 6.4, these two sources are our DCBH candidates. The photometric redshift of 29323 is more uncertain, but its probability distribution function suggests that $z \gtrsim 6$ with high confidence (see Fig. 6.2). Objects 33160 and 29323, both at $z \gtrsim 6$, are to be considered robust detections, being also included in the Xue et al. (2011) catalog, with identification numbers 85 and 156, respectively. Moreover, the source 29323 is also detected in Cappelluti et al. (2015), but these authors suggest that the determination of its photometric redshift could be affected by potential artifacts in the SED.

Instead, object 28476 is a possible X-ray detection: for this source there are 15 detected counts in the soft-band $(0.5-2\,\mathrm{keV})$, compared to ~ 5 background counts within a radius of 3 pixel, corresponding to a probability of spurious detection of $\sim 10^{-4}$. Anyway, the association between this X-ray source and its optical counterpart is more problematic. A full description, including coordinates, of all the 22 X-ray detected sources is provided in Giallongo et al. (2015).

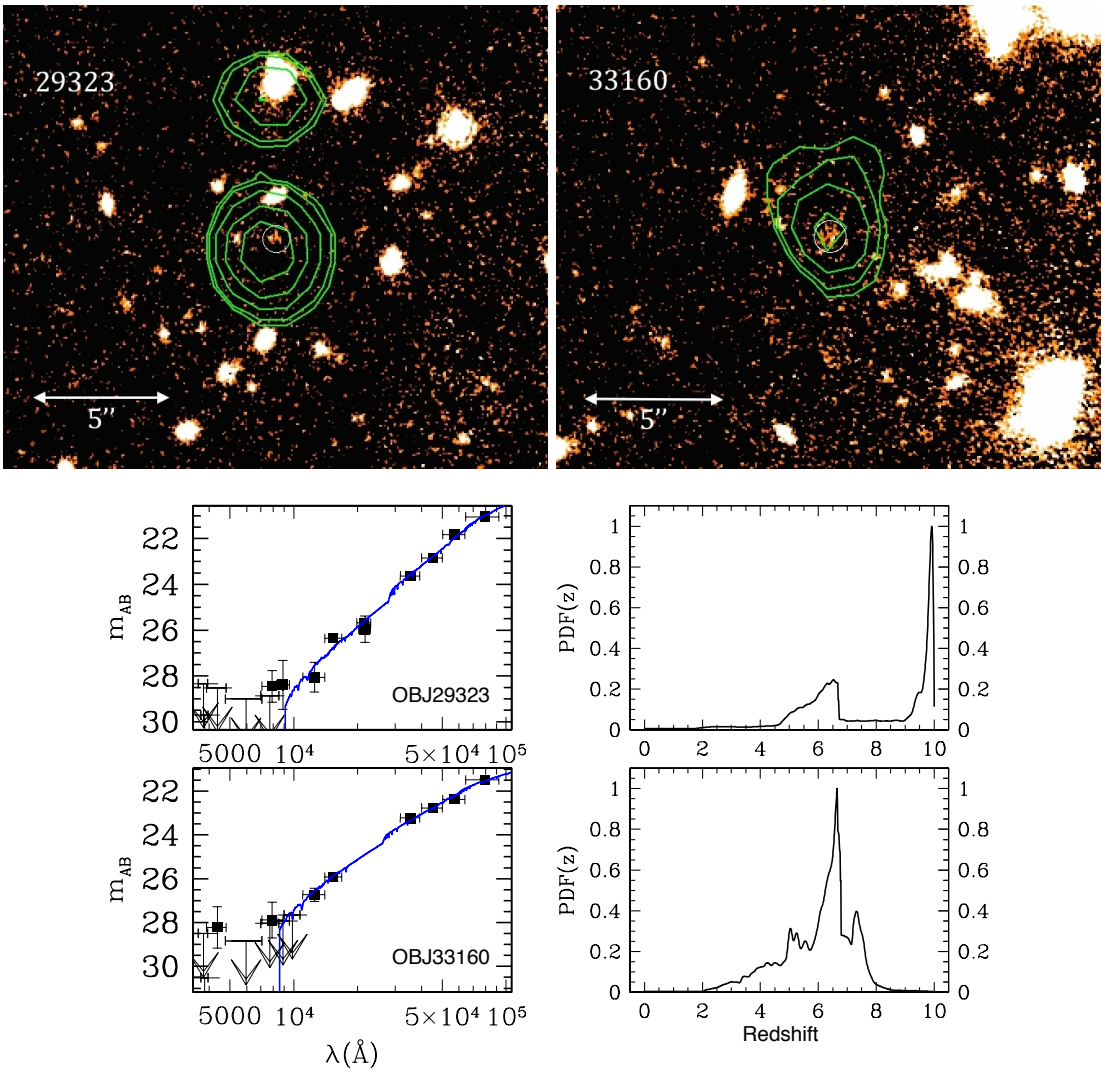

FIGURE 6.2: H band images with X-ray contours ($1-4\,\mathrm{keV}$) of the two GOODS-S sources selected as DCBH candidates. X-ray contours are from the Chandra 7 Ms field, in square root scale, from 2σ to 10σ. H band counterparts are circled. On the bottom, probability distribution functions (taken from Giallongo et al. 2015) for the photometric redshifts of the same objects, along with their optical/infrared spectra, fitted from their photometry.

6.4 Results

In this section we describe how the photometry of DCBHs changes with the column density of the host halo and with the black hole mass. Then, we present the black hole seed candidates selected in the CANDELS/GOODS-S field.

6.4.1 Column density dependence of DCBH colors

The initial black hole mass $M_\bullet(t = 0)$ is set for any given simulation in the range $10^{4-5}\,\mathrm{M}_\odot$. At some redshift z, the gas mass M_g of the host halo is also set from Eq. 6.1, which in turn translates into an initial column density N_H, with values generally in the Compton-thick range. The column density controls how photons with different frequencies are absorbed or transmitted. As long as the column density is large ($N_H \gtrsim 1.5 \times 10^{24}\,\mathrm{cm}^{-2}$), the photometry of DCBHs does not vary largely. As the black hole grows with time, its bolometric luminosity increases as well, but this effect does not modify the colors, since the increase in flux is similar in each photometric band. Once the column density falls below the Compton-thick limit, the evolution is very rapid and short-lived ($\lesssim 1 - 2\,\mathrm{Myr}$, see also Chapter 3): the DCBH performs a short photometric track in the color-color plot (see Fig. 6.1). The filled circles shown in Fig. 6.1 are computed at $z = 7$ and are averages, weighted over time, of the photometric track performed in each simulation.

6.4.2 Mass dependence of DCBH colors

The trend of DCBH colors with the black hole mass (Fig. 6.1) may be simply explained with the following argument. The column density N_H is proportional to the gas mass M_g and to the radius of the baryonic matter distribution R_g in the following way: $N_H \propto M_g/R_g^2$. Defining the concentration parameter of the gas distribution as $\mathcal{C} \equiv M_g/R_g \propto M_\bullet$ (larger black holes are more efficient and rapid in concentrating the gas around them), we derive that the column density of halos hosting more massive black holes is larger:

$$N_H \propto \frac{M_g}{R_g^2} \propto \frac{\mathcal{C}}{R_g} \propto M_\bullet\,. \tag{6.4}$$

Here we are assuming that, on sufficiently large spatial scales ($\gg R_B$), the characteristic radius of the baryonic matter distribution of the host halo is not modified by the mass of the black hole seed that forms at its center. The gas around larger black holes is more concentrated and then more efficient in reprocessing the radiation to lower energies. Consequently, the steepness of the infrared spectrum of massive black hole seeds is directly proportional to the black hole mass.

6.4.3 Identification of DCBH candidates in GOODS-S

DCBHs with larger masses are associated with steeper (i.e. redder) infrared spectra. These massive objects extend down to a region in the color-color diagram where there is a relative paucity of GOODS-S objects (see Fig. 6.1). We pick three GOODS-S objects characterized by different observational features and compare in Fig. 6.3 their SEDs with the one computed for a $\sim 5 \times 10^6\,M_\odot$ black hole, grown from a DCBH with initial mass around $\sim 10^5\,M_\odot$. The SED fitting has been executed with a standard stellar population model (Bruzual & Charlot, 2003). As described in Castellano et al. (2014) and in Grazian et al. (2015), we have included the contribution from nebular emission lines following Schaerer & de Barros (2009).

Objects 29323 (red line) and 14800 (blue line) are objects with an X-ray counterpart whose colors are very negative (29323) or close to zero (14800). Object 24021 (green line) is instead an object without an observed X-ray emission, whose colors are close to zero. The predicted infrared SED for a DCBH is redder than the ones observed for normal galaxies (e.g. 24021, in which radiation comes predominantly from stars) and AGNs (e.g. 14800, in which accretion-powered radiation co-exists with the stellar one). Current theoretical models suggest that most of the high-z black hole growth occurred into heavily-obscured hosts (see e.g. Comastri et al. 2015), providing a theoretical ground for the redness of the infrared SED of DCBHs.

Objects in the GOODS-S field may be detected up to $H \approx 28$ with a completeness $\sim 90\%$. From our simulations, we conclude that DCBH seeds with initial masses below $\sim 6 \times 10^4\,M_\odot$ cannot be detected in current surveys, assuming realistic growth rates. Then, we predict to observe DCBH candidates with initial masses $\gtrsim 6 \times 10^4\,M_\odot$, i.e. with colors $\mathrm{IRAC1} - H \lesssim -1.8$ and $\mathrm{IRAC2} - H \lesssim -1.8$ (see Fig. 6.1). The infrared SEDs of objects within this area of the color-color diagram are very red: they are promising DCBH candidates.

The two GOODS-S objects with a robust X-ray detection at $z \gtrsim 6$ (see Sec. 6.3.3) fall within our selection region for DCBH candidates, as shown in Fig. 6.4, which is the main result of this work. At $z \gtrsim 6$ the photometry of these sources is very similar to the one predicted for DCBHs, characterized by a very red infrared SED, caused by large absorbing column densities. At lower redshifts ($z \lesssim 6$) these pristine spectra are likely modified by several events, like star formation and large-scale outflows, which decrease

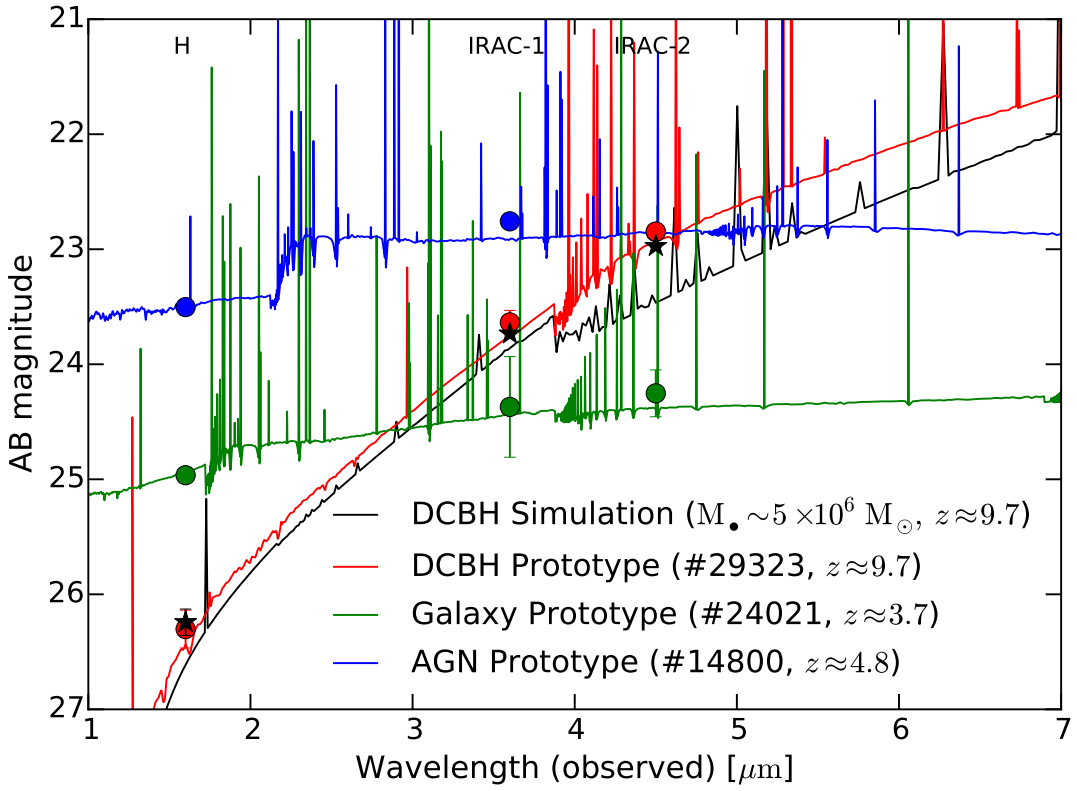

FIGURE 6.3: Comparison between the stellar SEDs of three GOODS-S objects with the computed SED of a $\sim 5 \times 10^6\,M_\odot$ black hole, born out of a DCBH with initial mass around $\sim 10^5\,M_\odot$. The three photometric bands employed in our work are shown as shaded regions. Filled circles (observations) and stars (numerical simulations) show the magnitudes in the three filters, with error bars. Objects 29323 and 14800 have X-ray counterparts (i.e. they are likely associated with a black hole), while 24021 has not (i.e. it is likely a normal galaxy). Moreover, object 29323 is characterized by very negative colors (i.e. its infrared SED is very steep, as we predict for DCBHs), while objects 14800 and 24021 are not. The steepness of the SED and the infrared magnitudes for the object 29323 are well fitted by the spectrum predicted for a $\sim 5 \times 10^6\,M_\odot$ black hole. In the computed SED for a DCBH, the He II line (0.164 μm rest-frame) is visible and it is marginally inside the H band at $z \approx 9.7$.

the column density of the host halo. Moreover, also the pollution of the gas by metals may contribute to the modification of the SED. In Sec. 6.4.4 we discuss other kind of sources possibly mimicking DCBH colors. Conservatively, we have not included in Fig. 6.4 the position of the $z \gtrsim 6$ object 28476, which also falls in our selection region, but whose X-ray detection is less robust.

In Fig. 6.4 we also show the position of other high-z objects, to compare it with the locations of our DCBH candidates. ULAS J1120+0641 (Mortlock et al., 2011, Barnett et al., 2015) is the most distant known Quasi-Stellar Object (QSO, $z \approx 7.1$), powered by a SMBH with an estimated mass $\sim 10^9\,M_\odot$. SDSS J1148+5251 (Fan et al., 2003) and SDSS J1048+4637 (Maiolino et al., 2004) are two highly-obscured and dusty QSOs

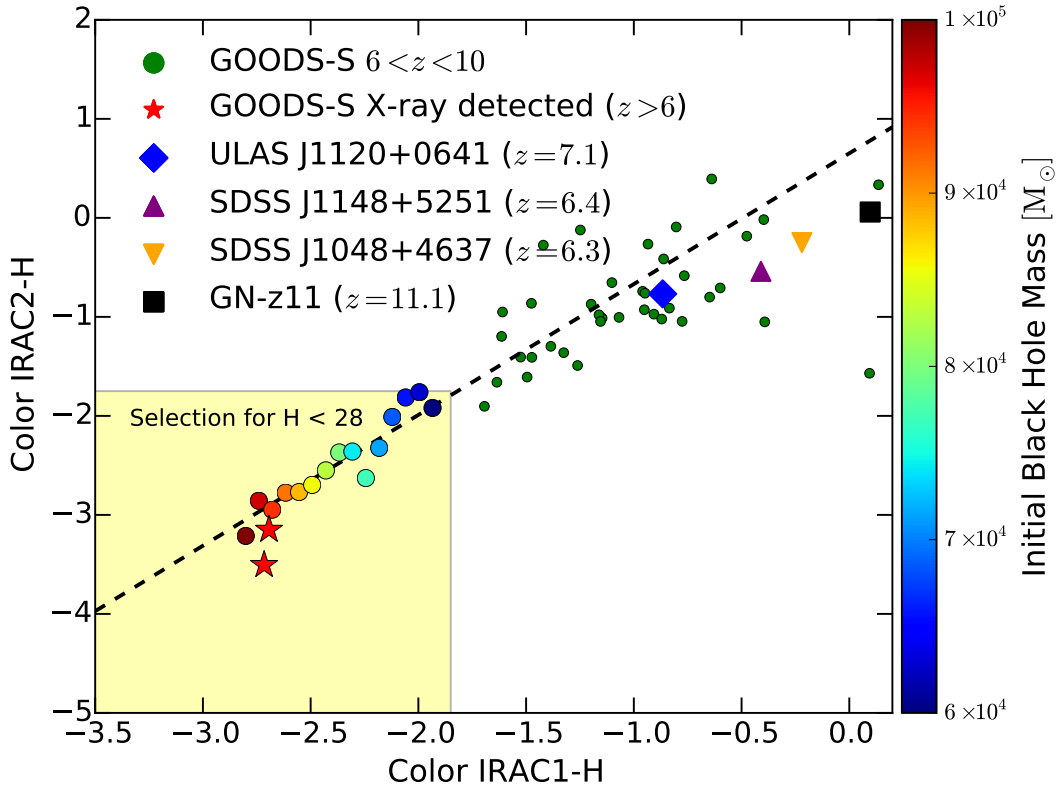

FIGURE 6.4: Color-color diagram for objects at $z \gtrsim 6$. The yellow-shaded area indicates the region in the diagram where we expect SEDs compatible with the ones predicted for DCBHs, and observable with current surveys. Green points are GOODS-S objects without an X-ray counterpart, while red stars are GOODS-S objects detected in the X-ray and likely powered by accretion onto a collapsed object. Filled circles are, as in Fig. 6.1, DCBH simulations. In addition, we report the position in the color-color plot of several $z > 6$ sources. ULAS J1120+0641 (Mortlock et al., 2011, Barnett et al., 2015) is the most distant known QSO ($z \approx 7.1$). SDSS J1148+5251 (Fan et al., 2003) and SDSS J1048+4637 (Maiolino et al., 2004) are two highly-obscured and dusty QSOs at $z \approx 6.4$ and $z \approx 6.3$, respectively. GN-z11 (Oesch et al., 2016) is the highest redshift galaxy discovered to date ($z \approx 11.1$).

at $z \approx 6.4$ and $z \approx 6.3$, respectively. GN-z11 (Oesch et al., 2016) is the highest redshift galaxy discovered to date ($z \approx 11.1$). The position of these objects in the color-color diagram is outside the region of detectability for sources powered by a DCBH: their H band magnitudes would be too faint to be currently observed. Consequently, our photometric selection method seems to separate the spectra of pristine DCBHs from those of other contaminant high-z sources.

For the couple of $z \gtrsim 6$ X-ray detected sources in the CANDELS/GOODS-S field we estimate a black hole mass in excess of $\sim 10^6\,\mathrm{M}_\odot$. For the source 33160 we are able to reproduce simultaneously with simulations both its H band magnitude, H = 25.9, and its $2-10\,\mathrm{keV}$ X-ray luminosity emerging from the host halo, $\mathrm{Log}_{10}(L_x) = 43.65$. Since

we assume the photometric redshift reported in Giallongo et al. (2015), also its X-ray flux is automatically reproduced. Source 29323 at $z \approx 9.73$ has a X-ray luminosity slightly above our predicted range (corresponding to a maximum black hole mass of $\sim 5 \times 10^6\,M_\odot$), while we successfully reproduce its H band magnitude (see Fig. 6.3). If this object is instead at redshift $z \lesssim 6$, its X-ray luminosity would be downgraded to $\mathrm{Log}_{10}(L_x) \lesssim 43.5$, well inside our predicted range. More generally, the X-ray detected objects in CANDELS/GOODS-S that are selected by our method (at any redshift) are compatible with the X-ray luminosities ($2-10\,\mathrm{keV}$) predicted for a population of DCBHs with initial masses in the range $6 \times 10^4 - 10^5\,M_\odot$. Within this ensemble of sources, more negative colors are associated with a larger X-ray luminosity (i.e. with a larger black hole mass, as in Fig. 6.1).

In the simulated DCBH spectrum of the object 29323 in Fig. 6.3, the He II line ($0.164\,\mu$m rest-frame) is visible and it is marginally inside the H band at $z \approx 9.7$. This emission line is an important indicator of DCBH activity (see e.g. Pallottini et al. 2015) and its detection, with future spectroscopic observations, may be a discriminant in the determination of the real nature of this high-z source.

6.4.4 Star formation rates in the X-ray detected sample

The photometry of all the X-ray detected objects in GOODS-S has been fitted by a stellar SED fitting model (Bruzual & Charlot, 2003). The SED fitting assumes that all the luminosity is produced by stars, without any contribution from accreting objects.

Fig. 6.5 shows the distribution of star formation rates (SFRs) of the X-ray detected objects in GOODS-S (excluding object 28476, whose X-ray detection is still debated). An increase in the SFR corresponds to a more negative value of the average (IRAC1-H) color index, as the color bar shows. As expected, a redder photometry is in general due to a larger dust extinction, which requires star formation to be active in the host galaxy. Nonetheless, fitting the photometry of extremely red spectra, as the ones of our two DCBH candidates (shown as yellow stars) requires SFRs comparable to or larger than the highest ever measured, for a massive maximum-starburst galaxy at $z = 6.34$ (Riechers et al. 2013, see also Barger et al. 2014 where the authors find a characteristic maximum SFR of $\sim 2000\,M_\odot\,\mathrm{yr}^{-1}$). The computed SFR for object 29323 is ~ 2 times larger than the maximum SFR ever measured, ~ 20 times larger than the typical SFR

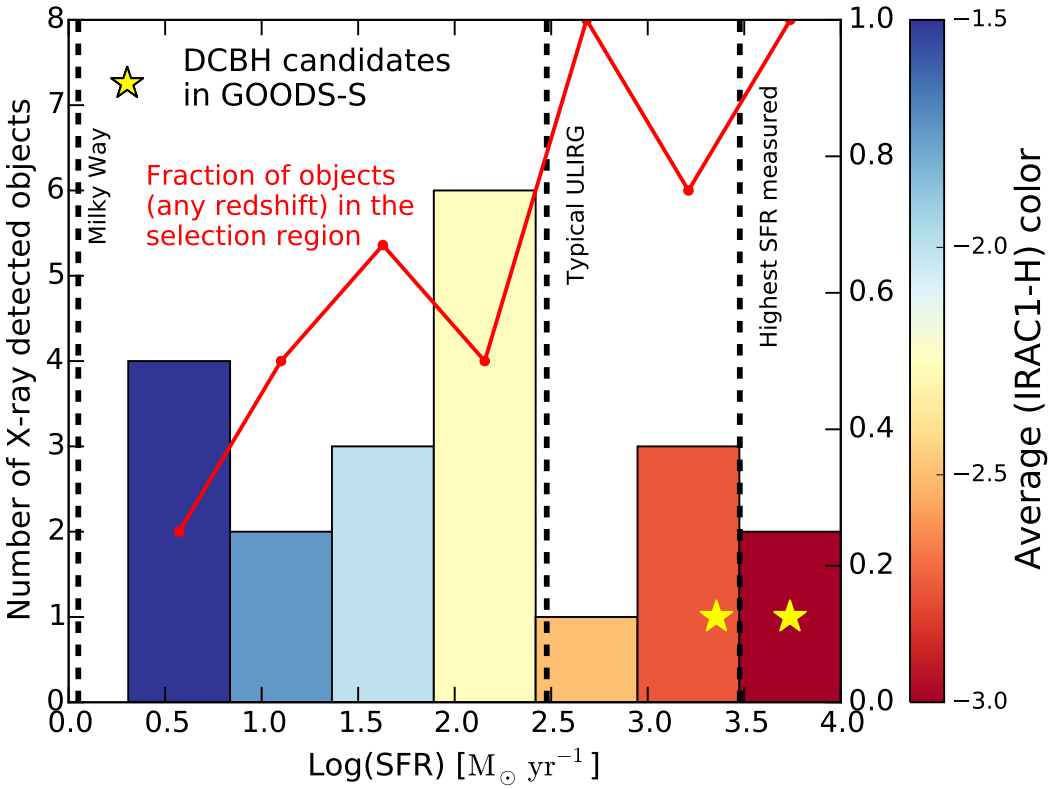

FIGURE 6.5: Distribution of star formation rates of the X-ray detected objects in GOODS-S (excluding object 28476, whose X-ray detection is still debated). Each column of the histogram is colored according to the average (IRAC1-H) color index of the objects falling within the SFR bin, as shown in the color bar. SFRs for the Milky Way (Robitaille & Whitney, 2010), a typical ULIRG (Le Floc'h et al., 2005) and for a massive maximum-starburst galaxy at $z = 6.34$ (Riechers et al., 2013) are shown for comparison. The fraction of objects in each bin, at any redshift, falling into our selection region is shown as a red line, on the right vertical axis. The two DCBH candidates selected by our method are shown with yellow stars.

of ULIRGs (Le Floc'h et al., 2005) and ~ 5000 times the SFR of our Galaxy (Robitaille & Whitney, 2010). Instead of evoking extremely large and unrealistic SFRs, we propose that these objects host a central DCBH (see Fig. 6.3 where the photometry of object 29323 is very well fitted by our DCBH model). The redness of their spectra is explained by the large, absorbing gas column densities in the host halo implicit in the DCBH evolution scenario.

A final remark: at low redshifts and for mildly negative color indexes, the colors of DCBHs may be mimicked by star forming galaxies. Fig. 6.5 shows with a red line the fraction of X-ray detected objects at any redshift that fall in our selection region. It is likely that the redness of some of these spectra may be genuinely explained by a burst of star formation underway in the host galaxy. At high redshifts and for very negative

color indexes (IRAC1-H $\lesssim -2.5$), the fraction of objects selected by our method is close or equal to unity and the required SFRs become unrealistic. We suggest that these objects are most likely high-z black hole seeds.

6.5 Caveats

In this section we revise some of the most important caveats of the current work, related to the assumptions of our radiation-hydrodynamic code and to the uncertainties in the photometric redshift estimate of the X-ray detected sources.

6.5.1 Assumptions of the radiation-hydrodynamic code

As described in Sec. 6.2, our radiation-hydrodynamic code simulates the accretion onto an already formed DCBH with some assumptions on the geometry of the flow and on the environment hosting the compact object.

On sufficiently large scales (comparable with the Bondi radius of the DCBH) the geometry is assumed to be spherical, with gas moving radially without angular momentum. As discussed in Chapter 4 and in Chapter 5, this assumption is supported by several studies (e.g. Choi et al. 2013, 2015) on the triaxiality of primordial halos, which should allow the gas to flow radially well beyond the centrifugal radius of the system.

The accretion rate is computed self-consistently from the density and velocity fields of the gas at the inner boundary of our simulation domain. While some accretion models allow for a fraction of the inflowing mass to be lost on small scales during the accretion process (see e.g. Begelman 2012, Coughlin & Begelman 2014), our simulations assume that the gas reaching the inner boundary of our spatial domain is entirely accreted onto the black hole. The bolometric luminosity emerging from the accretion disk is then computed consistently from the accretion rate (see Eq. 6.2).

Star formation is not active in our simulations. Consequently, the emerging spectrum is computed for a metal-free environment. The presence of a stellar component in the host halo (Pop II or Pop III) may modify the emerging spectrum in the optical/UV region, while we checked that the infrared part, upon which our photometric method is based, is

totally unaffected. Note, however, that, in the classical DCBH scenario, fragmentation, and hence star formation, is heavily suppressed by the external UV background.

6.5.2 Redshift estimates for DCBH candidates

The redshift estimates for sources 33160 and 29323, selected by our method as DCBH candidates (see Fig. 6.4), are photometric and subject to uncertainties (see Fig. 6.2, bottom panel).

As already mentioned, the photometric redshifts of the GOODS-S galaxies have been computed with the unconventional technique described in Dahlen et al. (2013). In summary, it is an optimal bayesian combination of six different probability distribution functions of the photometric redshift computed by six different groups within the CANDELS Team. For the object 29323, the individual probability distribution functions are centered at $z \sim 6.5$ and at $z \sim 9.7$, and only one solution out of six gives $z \approx 10$. The 68% (95%) confidence level region is between $z_{min} = 5.46$ and $z_{max} = 9.86$ ($z_{min} = 2.36$, $z_{max} = 9.97$). From the final probability distribution function for this object we can conclude that the redshift is unconstrained at $z \gtrsim 5.5$ at 1σ (or 2.4 at 2σ), due to the power law SED without significant breaks at the bluer wavelengths. Given the extreme steepness of the infrared SED of object 29323 (see Fig. 6.3), however, it would still be selected as a DCBH candidate down to $z \sim 2$.

Other photometric redshift catalogs on the same field have been published (e.g. by the 3D-HST collaboration, Brammer et al. 2012, and by Hsu et al. 2014). Nonetheless, we decided to adopt the CANDELS photometric redshifts for several reasons. Firstly, the 3D-HST photometric redshifts are very accurate for bright objects with strong emission lines. For faint galaxies such as the ones in this paper we prefer to use the CANDELS photometric redshifts, which are based on point spread function deconvolved photometry, which is quite robust also for faint and contaminated objects (e.g. object 29323). Moreover, the CANDELS photometric redshifts have the unique feature of averaging the differences between different photometric redshift codes, which could have their own biases. To conclude, the accuracy in the determination of the photometric redshift at $z \gtrsim 4$ relies mainly on the absorption of the IGM, which is an accurate feature independently of the adopted templates. The photometric redshifts of our DCBH candidates

are $z(29323) \approx 5.3$ and $z(33160) \approx 4.9$ in the 3D-HST catalog and $z(29323) \approx 4.7$ and $z(33160) \approx 3.4$ in the Hsu et al. (2014) catalog.

6.6 Discussion and Summary

Supported by radiation-hydrodynamic simulations, we have devised a novel method to identify black hole seed candidates at $z \gtrsim 6$: at high-z the infrared SED of pristine DCBHs is predicted to be significantly red. At lower redshifts, intervening processes (e.g. star formation, metal pollution, outflows) make the selection more uncertain. By applying our method to state-of-the-art photometric observations of the CANDELS/GOODS-S field, we select the only 2 sources at $z \gtrsim 6$ with a robust X-ray detection. The SFRs required to mimic their extremely red spectra are unrealistic ($\gtrsim 2000\,\mathrm{M_\odot\,yr^{-1}}$), being comparable to or larger than the highest SFR ever measured, in a maximum-starburst galaxy. *These objects represent the most stringent observational identification of black hole seed candidates, likely formed as DCBHs, so far obtained.* The possible presence of markers of DCBH activity, such as the predicted He II emission line, needs to be investigated with spectroscopic follow-up observations.

The extension of the current work to more infrared photometric bands may prove to be useful in distinguishing the different classes of objects observed, especially at lower redshifts. However, our two-dimensional color-color plot aims at conveying the simple and clear idea that, in looking for pristine DCBH candidates, observational efforts should be focused on objects with very steep infrared spectra.

This work extends previous efforts in understanding the observational features of DCBHs. Our previous studies (Pallottini et al. 2015, but see also Chapter 5) investigated the spectrum emitted from these sources, foreseeing the possibility that they could be observed by the JWST. We suggested that CR7, the brightest Ly-α emitter discovered to date, could be powered by a typical DCBH of initial mass $\sim 10^5\,\mathrm{M_\odot}$. Recently, CR7 has been the subject of great interest in the community, with a large wealth of studies investigating its nature (e.g. Agarwal et al. 2015, Hartwig et al. 2015, Visbal et al. 2016, Smith et al. 2016, Smidt et al. 2016, Dijkstra et al. 2016a), most of them confirming the possibility that this source may host a DCBH. The efforts to observe these objects have recently spread to other regions of the electromagnetic spectrum. For instance, Dijkstra

et al. (2016b) suggested that the large neutral hydrogen column densities of primordial gas at $\sim 10^4$ K with low molecular abundance (all key aspects of the DCBH scenario) give rise to stimulated fine structure emission at ~ 3 cm in the rest-frame. Detecting this signal is challenging, but would provide direct evidence for the DCBH scenario.

Our current work has, of course, some limitations. Firstly, high-z sources with a robust X-ray detection in the GOODS-S field are few: making a precise assessment on the robustness of our selection criterion is beyond current reach. Secondly, only deep high/medium-resolution spectroscopy may conclusively confirm the DCBH nature of these objects. A spectroscopic analysis of these sources is beyond the capabilities of current observatories (e.g. HST, VLT, Keck) because they are too faint. With the start of JWST operations, a large wealth of infrared spectroscopic data (extended above the $\sim 2.5\,\mu$m limit of ground telescopes) will be available, disclosing to our eyes the first glimpses of light in the Universe. Currently, we probe only the most massive and luminous black holes, the peak of their mass distribution. JWST will mark a breakthrough in this field, by detecting the light from the most distant stars and accreting black holes, probing the mass range ($10^{4-5}\,M_\odot$) of the first black hole seeds, if they were formed via the DCBH scenario. Our work establishes a solid theoretical framework to interpret these data with the aim of finding the first black holes in the Universe.

Chapter 7

Gravitational Waves from Direct Collapse Black Holes Formation

7.1 Introduction

The recent announcement of the first detection of a Gravitational Wave (GW) from the Laser Interferometer Gravitational Wave Observatory (LIGO) has marked the official birth of gravitational wave astronomy. The event GW150914 (Abbott et al., 2016b) was originated by the merging of a binary black hole, with component masses $M_1 \sim 36\,\mathrm{M}_\odot$ and $M_2 \sim 29\,\mathrm{M}_\odot$ (source frame) at $z \sim 0.1$, corresponding to a luminosity distance of $\sim 410\,\mathrm{Mpc}$. Current predictions (Abbott et al., 2016a) indicate that this kind of events will be detected regularly, with a rate of several per day up to $z \sim 1$, with the incoming operation of additional GW detectors, like VIRGO and KAGRA. Every time a new observational window is opened up, a major revolution in our capabilities to probe the Universe is expected.

The primary emitters of electromagnetic radiation are charged particles. Because of overall charge neutrality, electromagnetic radiation is typically emitted in small regions (i.e. with short wavelengths) and conveys direct information about the physical conditions of small portions of the astronomical sources. By contrast, GWs are emitted by the cumulative mass and momentum of entire systems, so they have long wavelengths and convey direct information about large-scale regions. In addition, electromagnetic waves

couple strongly to charges and so are easy to detect but are also easily scattered or absorbed by intervening material, while GWs couple extremely weakly to matter, making them very hard to detect but also allowing them to travel substantially unaffected.

First-generation GWs detectors (e.g. LIGO, Virgo) have been successfully commissioned, and the development of the next advanced sensitivity ground-based detectors (Advanced LIGO, Advanced Virgo) is well underway. However, the construction of the planned space-based detectors (DECIGO, eLISA) is still in the development phase (see e.g. Kawamura et al. 2011, Seoane et al. 2013).

The GW spectrum is conventionally divided into several regions, from extremely low ($\sim 10^{-18}$ Hz) to high ($\sim 10^{4}$ Hz) frequencies. In the low frequency range (approximately from 10^{-4} Hz to 1 Hz, see Camp & Cornish 2004 for an extensive review) the most important sources are Galactic compact binaries, massive black hole binary mergers, massive black hole capture of compact objects, the collapse of super-massive stars (SMSs) and the primordial GWs background (see Amaro-Seoane et al. 2013).

In particular, the collapse of SMSs (the first massive objects formed in unpolluted atomic cooling halos at $z \gtrsim 10$) may lead to a significant emission of GWs, depending on the collapse asymmetry. A possible mechanism for a highly asymmetrical collapse is the development of a dynamical bar-mode instability as the SMS cools (Smith et al., 1996, Saijo et al., 2002, Shapiro, 2003, Franci et al., 2013). This may be likely if viscosity and magnetic fields are insufficient to keep the star rotating uniformly during the cooling phase. Given enough energy and a long enough lifetime of the bar mode, a significant fraction of the rest energy of the star could be lost as gravitational radiation (see e.g. Schneider et al. 2000).

If this signal is actually observable by current or future GWs surveys, it would provide a highly valuable tool to prove the existence of Intermediate-Mass Black Holes (IMBHs), formed from the collapse of SMSs.

In the commonly accepted ΛCDM cosmological scenario, the formation of the first stars and black holes occurred at $z = 20-30$ (Miralda-Escudé, 2003, Bromm & Yoshida, 2011, Volonteri & Bellovary, 2012) in molecular cooling halos, i.e. dark matter structures with virial temperatures below 10^{4} K and halo masses below $M_h \sim 10^{8}\,\mathrm{M}_{\odot}$.

These structures cooled their metal-free gas through molecular hydrogen line emission. Under intense UV irradiation, particularly in the Lyman-Werner (LW) band (11.2 – 13.6 eV), the molecular hydrogen is photo-dissociated, so that the cooling is quenched (see Machacek et al. 2001, Fialkov et al. 2012). On the contrary, larger metal-free halos (with masses above $\sim 10^8\,M_\odot$ and temperatures $T_{\rm vir} > 10^4\,K$), when illuminated by LW photons with fluxes above a threshold $J_\nu^\bullet$ (Loeb & Rasio 1994, Eisenstein & Loeb 1995, Begelman et al. 2006, Lodato & Natarajan 2006, Regan & Haehnelt 2009, Shang et al. 2010, Johnson et al. 2012, Agarwal et al. 2012, Inayoshi & Omukai 2012, Latif et al. 2013a, Sugimura et al. 2014, Dijkstra et al. 2014) are the ideal environment for the formation of Direct Collapse Black Holes (DCBHs).

Several theoretical works (Bromm & Loeb 2003, Begelman et al. 2006, Volonteri et al. 2008, Shang et al. 2010, Johnson et al. 2012, Ferrara et al. 2014) have shown that the result of this collapse is the formation of a DCBH of mass $10^4 - 10^6\,M_\odot$. The collapse of SMSs is mainly driven by General Relativity (GR) instabilities, as described in Shibata & Shapiro (2002). The subsequent accretion of mass contributes to the final mass of the IMBHs.

The existence of IMBHs at high-redshifts would provide a very convenient solution to two problems still unsolved by modern Cosmology, namely: (i) What are the sources responsible for the Cosmic Infrared Background (Cappelluti et al. 2013, Yue et al. 2013)? (ii) How did the local SMBHs form (see Volonteri & Bellovary 2012 for a recent review and references therein)?

We propose here a tentative test of the IMBH hypothesis based on the detection of the GWs emitted during the collapse phase.

Several works have been focused on the theoretical determination of the GWs waveform for the most important sources in the low frequency range, starting from the seminal paper Saenz & Shapiro (1978). For example, Schneider et al. 2000, Ott et al. 2004, Sekiguchi & Shibata 2005, Ott 2009, Li & Benacquista 2010 have developed waveforms for the asymmetrical collapse of a SMS into a black hole both with simple theoretical arguments and, more recently, with numerical simulations.

Employing this modern waveform for the collapse of DCBHs at high redshifts ($z \sim 15$) we study their observability with the aid of recent estimates of their formation rates.

The outline of this chapter is as follows. In Sec. 7.2 we present an overview of the theory describing the GWs emission, specifying the waveform used. In Sec. 7.3 we describe the results and the possible observability of these gravitational signals. Finally, in Sec. 7.4 we provide further discussion and a summary. Throughout, we adopt recent Planck cosmological parameters (Planck Collaboration et al., 2015) as reported in Table 1.1.

7.2 Theoretical Background

The output of a GW detector is a time series $s(t)$ that includes the instrument noise $n(t)$ and the response to the gravitational signal $h(t)$:

$$s(t) = P_+(t)h_+(t) + P_X(t)h_X(t) + n(t)\,. \tag{7.1}$$

The instrument response is a convolution of the antenna patterns $P_+(t)$ and $P_X(t)$ with the two GW polarizations h_+ and h_X. The antenna patterns depend on the frequency and on the sky location of the source. For wavelengths that are large compared to the baseline, the antenna patterns are simple quadrupoles. The signal analysis is usually performed in the frequency domain since, in this representation, the noise is usually assumed to be uncorrelated and gaussian in each frequency bin.

The information contained in the time series is usually represented in the Fourier domain as a strain amplitude spectral density, $\tilde{h}(\nu)$. This quantity is defined in terms of the power spectral density:

$$S_s(\nu) = \tilde{s}^*(\nu)\tilde{s}(\nu)\,. \tag{7.2}$$

The tilde operator is the Fourier transform of the time series:

$$\tilde{s}(\nu) = \int_{-\infty}^{+\infty} s(t)e^{2\pi i\nu t}\,\mathrm{d}t\,, \tag{7.3}$$

and the star indicates the conjugation operation in complex numbers. The power spectral density $S_s(\nu)$ has units of time or, as usually indicated, Hz^{-1}. The strain amplitude spectral density is then defined as:

$$\tilde{h}(\nu) = \sqrt{S_s(\nu)}\,. \tag{7.4}$$

This quantity has units $\mathrm{Hz}^{-1/2}$ and is the one usually reported in plots showing gravitational signals. From the prediction of the time evolution of the gravitational signal shape $h(t)$, derived from the instrumental time series $s(t)$, it is then possible to compute the strain amplitude spectral density $\tilde{h}(\nu)$.

It is standard practice to quote the strength of a gravitational signal in terms of the energy density per logarithmic frequency interval, $d\rho_{gw}/d\ln\nu$, scaled by the energy density needed to close the Universe:

$$\Omega_{gw}(\nu) = \frac{1}{\rho_{crit}} \frac{d\rho_{gw}}{d\ln\nu} = \frac{4\pi^2}{3H_0^2}\nu^3 S_s(\nu)\,, \tag{7.5}$$

where H_0 is the Hubble constant, ρ_{crit} is the critical density and ρ_{gw} is the energy density in a GW, given by:

$$\rho_{gw} = \frac{1}{32\pi G} < h^2 >\,, \tag{7.6}$$

where G is the gravitational constant and the brackets denote a spatial average over the wavelengths.

The actual prediction of the shape $h(t)$ is far from being trivial and strongly depends on the nature of the source and on its physical properties. Only recently a number of accurate waveforms have been proposed for binary systems and for collapsing SMSs (see the works Schneider et al. 2000, Li & Benacquista 2010, Li et al. 2012, Ajith et al. 2011, Pan et al. 2014). The form of the gravitational waveform template plays a crucial role for data analysis: very often, only a detailed prediction of the signal shape allows to disentangle it from the receiver noise and/or from other sources of gravitational radiation. We will discuss this point more carefully in the following subsections.

7.2.1 Waveform for IMBH collapse and ringdown

A black hole can emit GWs during its formation through the asymmetric core collapse of its progenitor. Indeed, in order to emit gravitational radiation, a physical system needs to be non-spherical: one possibility for having a non-spherical collapse is requesting the primordial halo, hosting the to-be-formed black hole, to be in rotation. DCBHs are formed during a brief era of cosmic time ($13 \lesssim z \lesssim 20$, Yue et al. 2014) due to the collapse of the inner part of metal-free halos. The angular momentum of high-redshift halos is small (Davis & Natarajan, 2010) and is preserved during the collapse. The

newly formed DCBH is then characterized by low values of angular momentum, which is later increased by accretion and merging events.

We focus on black hole progenitors, i.e. the inner section of the collapsing halo, with mass $M_\bullet$, mean mass density ρ and dimensionless spin parameter a defined as:

$$a = \frac{Jc}{GM_\bullet^2}\,, \tag{7.7}$$

where J is the angular momentum and c is the speed of light. Note that $a = 0$ denotes a non-rotating black hole, while $a = 1$ is a maximally rotating Kerr black hole, although we note that Thorne (1974) showed that accretion-driven spin is limited to $a = 0.998$. Magnetic fields connecting material in the disk and the plunging region may further reduce the equilibrium spin: magneto-hydrodynamic simulations for a series of thick accretion disks suggest an asymptotic equilibrium spin at $a \sim 0.9$ (Gammie et al., 2004). Rotating black hole progenitors will distort to an oblate spheroid shape despite their own immense gravity. The collapse, under this non-spherical geometry, causes the emission of a huge amount of energy through GWs.

The final evolution of the collapsing halo is usually characterized by two distinct phases:

1. **Collapse:** under the influence of its overwhelming self-gravity, the black hole progenitor collapses in a time scale equal to the dynamical time $t_{dyn} \sim 1/\sqrt{G\rho}$.
2. **Ringdown:** the collapsed non-spherical object undergoes strong oscillations which progressively allow it to acquire a spherical shape.

As we shall see, the maximum of gravitational radiation is released at the end of the collapse, when the black hole bounces back and starts the subsequent ringdown phase.

In the work by Li & Benacquista (2010), the core collapse of the SMS is approximated as an axisymmetric Newtonian free-fall of a rotating relativistic degenerate iron core. In addition, the collapse waveform is reasonably well modeled by an exponential growth. Following this paper, the time-series of the waveform for the ringdown phase is expressed analytically as:

$$h_{RD}(t) = A\frac{GM_\bullet}{c^2 d_L}\exp(-\pi\nu_0 t/Q)\cos(2\pi\nu_0 t)\,, \tag{7.8}$$

where d_L is the luminosity distance between the source and the detector, $Q = 2(1-a)^{-9/20}$, $g(a) = 1 - 0.63(1-a)^{3/10}$, $\nu_0 = c^3 g(a)/(2\pi G M_\bullet)$. Note that ν_0^{-1} is the typical timescale of GWs emission. In addition:

$$A = \sqrt{\frac{5\epsilon}{2}} Q^{-1/2} \left(1 + \frac{7}{24Q^2}\right) g(a)^{-1/2}\,, \tag{7.9}$$

where ϵ is the fraction of the initial mass of the black hole that is transformed into GWs radiation. Numerical simulations have shown that approximately 1% of the final black hole mass is emitted in GWs so, throughout, we adopt the value $\epsilon = 0.01$ (see Buonanno et al. 2007, Abbott et al. 2009 for details). In Abbott et al. (2009), the authors investigate the presence of possible GWs burst signals in the high-frequency range $1 - 6\,\mathrm{kHz}$, without finding any evidence of them, but putting an indirect upper limit on the emitted energy. Although the survey was dedicated to a different frequency range, we make use of the same upper limit, in accordance with Li & Benacquista (2010).

The waveform for the collapse is found by analytically fitting a numerical relativistic simulation in Li & Benacquista (2010). The time series has the following general form:

$$h_C(t) \sim \alpha + \frac{a}{\rho} e^{\gamma M_\bullet t}\,, \tag{7.10}$$

where a is the spin parameter, $M_\bullet$ is the mass, ρ is the mean mass density of the collapsing object, and α and γ are two free parameters that we determine by imposing that $h_C(t=0) = 0$ and $h_C(t=t_c) = h_{RD}(t=t_c)$, i.e. the gravitational signal is null at the initial time and the two waveforms match at the collapse time t_c.

The collapse time is found by imposing its identity with the dynamical time of a quasi-spherical object with a mean mass density ρ:

$$t_c = t_{dyn} \sim \frac{1}{\sqrt{G\rho}}\,. \tag{7.11}$$

Calling V the value of the ringdown waveform at the collapse time t_c, our final form for the collapse waveform is the following:

$$h_C(t) = \frac{a}{\rho}\left(e^{\gamma M_\bullet t} - 1\right)\,, \tag{7.12}$$

with

$$\gamma = \frac{1}{M_\bullet t_c} \ln\left(\frac{\rho}{a} V + 1\right) . \tag{7.13}$$

The physical parameters in the model are: the mean mass density of the collapsing object ρ, the black hole mass $M_\bullet$ and the spin parameter a. The range of their values used in our calculations is detailed in Sec. 7.3. Fig. 7.1 shows an example of time series for the gravitational strain: the collapse and subsequent ringdown phases are evident and separated by the vertical line at $t_c \sim t_{dyn} \sim 0.7\,\mathrm{s}$. Fig. 7.2 shows the spectral strain for a single source with the parameters reported in the caption. The peak amplitude $\sim 10^{-22}\,\mathrm{Hz}^{-1/2}$ is reached at $\nu \sim 3 \times 10^{-3}\,\mathrm{Hz}$.

Other waveforms have been proposed for the collapse of SMSs with lower masses. For example, Suwa et al. (2007) employed GR numerical simulations and the standard quadrupole formula developed in Moenchmeyer et al. (1991) to study the collapse of $\sim 500\,\mathrm{M}_\odot$ SMSs, obtaining a peak power in the range $10 - 100\,\mathrm{Hz}$. Due to important differences in the collapse modeling, a direct comparison between the classical quadrupole formula derived in Moenchmeyer et al. (1991) and the one used in the present work is hard to obtain.

7.2.2 Other sources of gravitational signals in the low-frequency band

Most of the gravitational power emitted from the DCBH collapse falls in the low-frequency range, approximately from $10^{-4}\,\mathrm{Hz}$ to $1\,\mathrm{Hz}$ (see Camp & Cornish 2004 for an extensive review). In this range the most important sources of GWs are Galactic and extragalactic compact binaries, massive black holes binary mergers, massive black holes capture of compact objects and the primordial GW background.

The last one is too weak to be of any concern in this work (see e.g. Yagi & Seto 2011). This is not the case with the Galactic and extragalactic compact binaries.

The unresolved background generated by the GWs emission of Galactic and extragalactic compact binaries acts as a confusion noise in this frequency range (Schneider et al., 2001, Farmer & Phinney, 2003, Nelemans, 2009, Sathyaprakash & Schutz, 2009, Regimbau & Hughes, 2010, Marassi et al., 2011, Regimbau et al., 2012). This is produced by the coalescence of two neutron stars (BNS), two black holes (BBH) or a neutron star and a black hole (NS-BH) in our Galaxy or in the $z \lesssim 5$ Universe. The duty-cycle (i.e. the

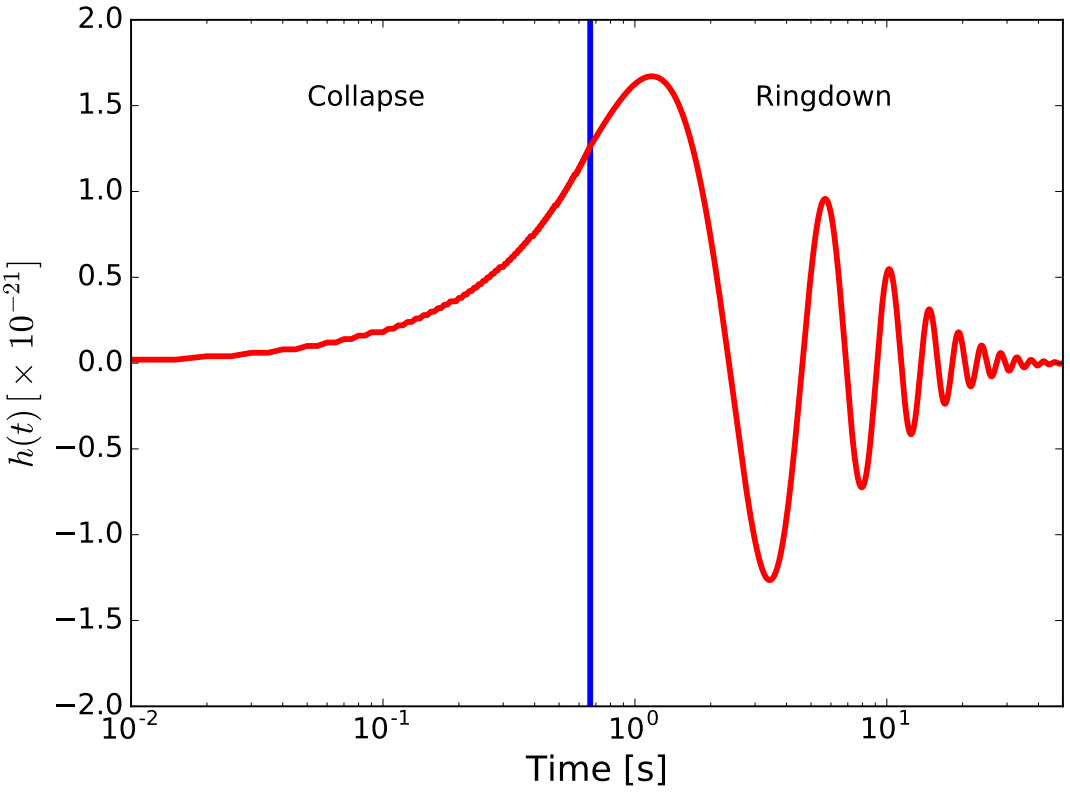

FIGURE 7.1: Gravitational strain as a function of time for the collapse of a $10^5\,M_\odot$ black hole at $z = 15$, with a mean mass density $\rho = 10^7\,\mathrm{g\,cm^{-3}}$. The separation between the collapse and the ringdown phases is marked by the vertical blue line.

percentage of one period in which a signal is active, see a more complete definition below) for these events, for future space-borne gravitational observatories like DECIGO, will be higher than unity, i.e. the signals overlap and create a confusion noise of unresolved sources.

The merging event for SMBHs also produces very energetic GWs (Kocsis & Loeb, 2008) that may represent an important foreground contribution to the detected gravitational signal. One very simple method to reproduce the gravitational signals generated by SMBHs merging events is presented in Li et al. (2012) where the interested reader is referenced to for a detailed description. However, the signal generated by these events is very different (in terms of both the duty-cycle and the characteristic energy) from the one of our interest and their separation should be quite simple.

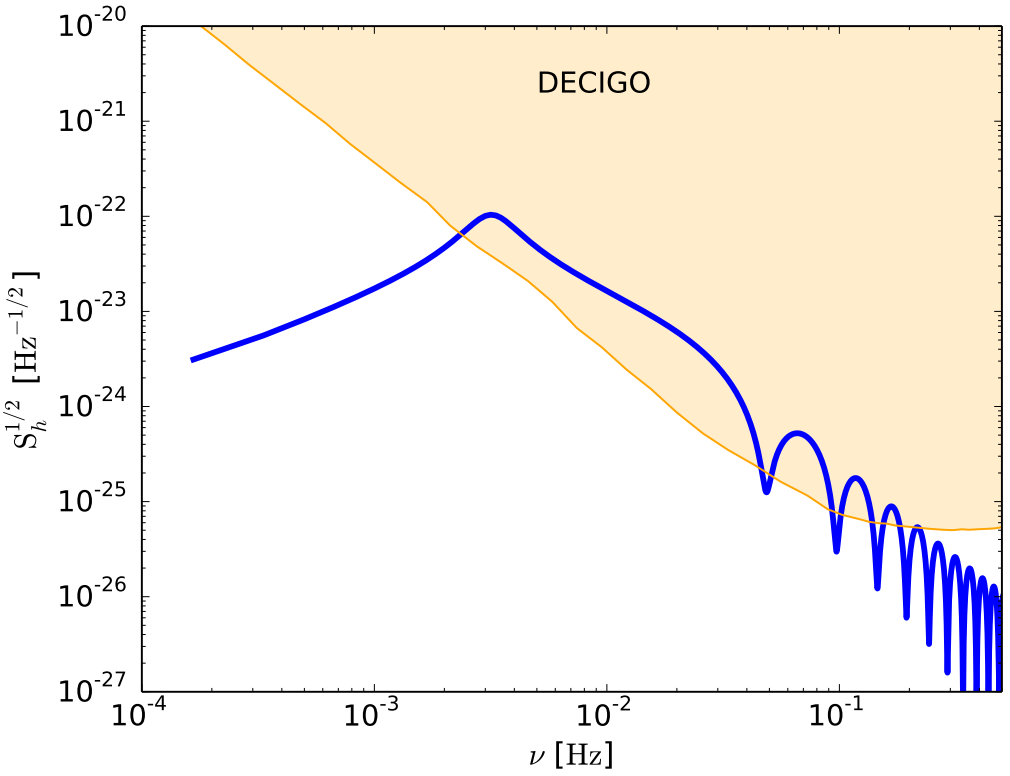

FIGURE 7.2: Spectral strain for a single source, due to the collapse of a $10^5\,M_\odot$ black hole at $z = 14$, with a mean mass density of $\rho = 10^7\,\mathrm{g\,cm^{-3}}$. The power peak is reached at $\nu \sim 3 \times 10^{-3}\,\mathrm{Hz}$. The sensitivity curve for the DECIGO observatory is reported as a shaded orange line.

7.2.3 Calculation of rates and duty-cycles

The calculation of the formation rate of DCBHs at high redshifts is based on the work Yue et al. (2013), where they present the rate of formation per unit volume of DCBHs, $\dot{\rho}(z)$, that matches the observed near infrared background.

The Universe enters the DCBHs era at $z \approx 20$ when a large fraction of atomic-cooling haloes are experiencing DCBHs formation. Their formation is suppressed after $z \approx 13$, so that the DCBHs era lasts only $\sim 150\,\mathrm{Myr}$ of the cosmic history (see Yue et al. 2014 for details).

Then, the number of GWs sources formed per unit time out to a given redshift z can be computed integrating the cosmic DCBHs formation rate density $\dot{\varphi}(z)$, see Fig. 7.3.

An important parameter to describe the signal in the time domain is the duty-cycle, $\mathcal{D}$. This is defined as the ratio between the typical duration of the signal emitted by a single source and the average time interval between two consecutive emissions. When $\mathcal{D} \gtrsim 1$,

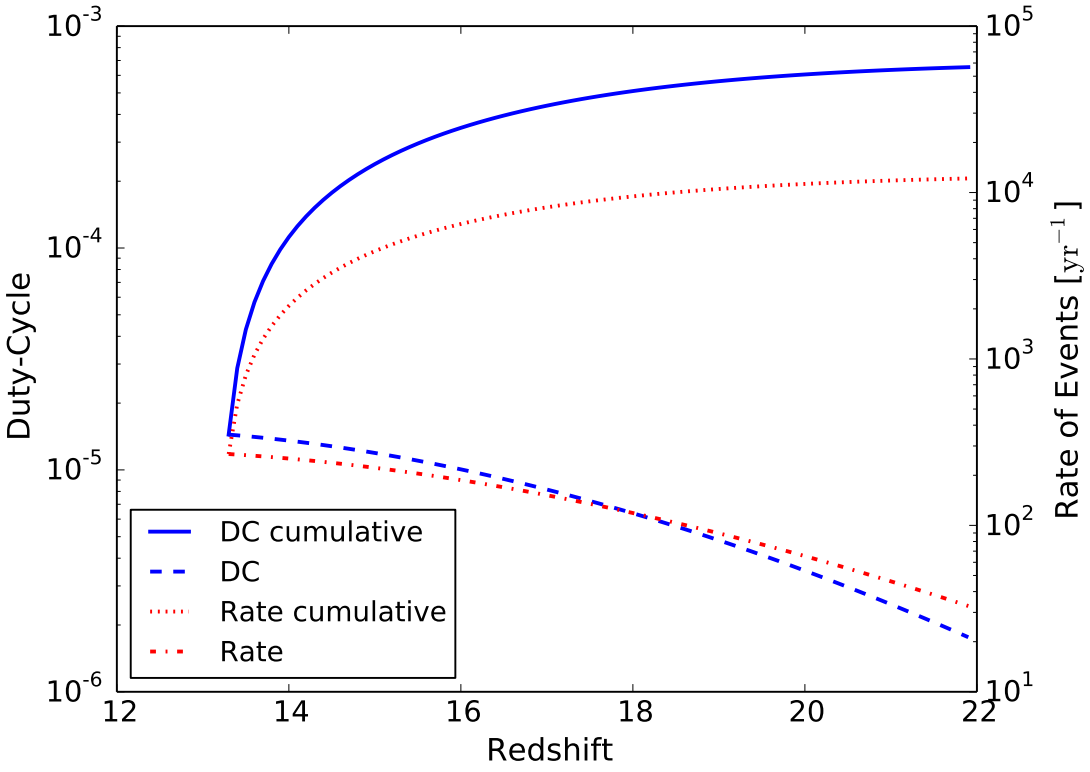

FIGURE 7.3: The event rate and the duty-cycle for the formation of DCBHs as a function of redshift. The values shown with dashed lines are cumulative, i.e., obtained summing all the values up to the given redshift.

the overall signal is continuous (i.e. the different signals overlap in time), conversely if $\mathcal{D} < 1$ the resulting background is characterized by a shot-noise structure.

From the value of $\dot{\varphi}(z)$ and from the Initial Mass Function (IMF) $\Phi(M)$ of the population, it is possible to compute the duty-cycle as:

$$\frac{d\mathcal{D}(z)}{dz} = \frac{\dot{\varphi}(z)}{(1+z)} \frac{dV}{dz} \frac{(1+z)}{\nu_0} \int \Phi(M)\, \mathrm{d}M. \tag{7.14}$$

Here, the IMF of IMBHs seeds (which is normalized by the mass) is taken from Ferrara et al. (2014) and ν_0^{-1} is the typical timescale of GWs emission (see Sec. 7.2). The double appearance of the term $(1+z)$ is to take into account the redshift dependence of both ν_0 and $\dot{\varphi}$. Both the event rate and the duty-cycle are shown in Fig. 7.3.

The event rate for all-sky observations is very high, reaching a peak of $\sim 10^4\,\mathrm{yr}^{-1}$ at $z \sim 22$. However, due to a rather short duration of the GW burst ($\sim 2 - 30\,\mathrm{s}$ depending on the DCBH mass, see Fig. 7.1) the duty-cycle is very small, of order 10^{-3}. This result suggests that the gravitational signal generated by the collapse of high-redshift DCBHs

is a shot-noise. The decrease, with increasing redshift, of both the event rate and the duty-cycle (and the corresponding leveling of their cumulative values) is ascribed to the decrease in $\dot{\rho}(z)$, as in Yue et al. (2013). Both the event rate and the duty-cycle are comparable with the results in Marassi et al. (2009) who, however, considered the contribution to the stochastic background of Pop III stars with masses in the range $(300 - 500)\,\mathrm{M}_{\odot}$ that collapse to black holes.

7.2.4 Calculation of the signal-to-noise ratio

Here we describe the method to compare the GW amplitude with the instrumental sensitivity and to assess what sort of sources will be observable against noise. The comparison is almost always made in the frequency domain, since stationary noise is most conveniently characterized by its Power Spectral Density (PSD).

In this work, we deal with short-lived signals, which have wide bandwidths and the actual observation time of the source is not relevant in the determination of the Signal-to-Noise Ratio (SNR).

It is useful to define the dimensionless noise power per logarithmic bandwidth:

$$\hat{h}_n^2(\nu) = \nu S_n(\nu)\,, \tag{7.15}$$

where $\hat{h}_n(\nu)$ is called the effective GW noise. From the signal side, we may define the characteristic signal amplitude:

$$\hat{h}_c = \nu|\tilde{h}(\nu)|\,, \tag{7.16}$$

which is dimensionless. This last quantity is to be compared with the effective GW noise $h_n(\nu)$ to obtain a rough estimate of the SNR of the signal:

$$SNR(\nu) = \frac{h_c(\nu)}{h_n(\nu)}\,. \tag{7.17}$$

The sensitivity curve for Ultimate-DECIGO has been taken from Marassi et al. (2009).

The SNR with respect to the instrumental noise is not the only parameter to take into account in order to assess the observability of a source. The signal also needs to be distinguished from all the other components received in the same frequency band, as

TABLE 7.1: Variation of the physical parameters characterizing the population of high-z DCBHs.

	MIN	MAX	Bins
z	14	22	10
Log ρ [g cm^{-3}]	6	8	10
Log $M_\bullet$ [M$_\odot$]	4.5	5.7	10

described previously in this section. The observability will be addressed more broadly in Sec. 7.3.

7.3 Results

In this section we present the results of our calculations and we discuss on the observability of the signal. In Sec. 7.2 we presented the waveform we employed for the gravitational signal generated by the collapse of a high-redshift atomic cooling halo, with the subsequent formation of a DCBH. The waveform is a function of the mean mass density ρ, the mass $M_\bullet$ and the spin parameter a (see Eq. 7.12). The amplitude of the detected gravitational signal depends also on the luminosity distance from the source, i.e. from its redshift.

In order to simulate the gravitational signal generated by a realistic ensemble of the population of high-z DCBHs, we let these parameters vary into different ranges of values, summarized in Table 7.1.

The redshift range has been chosen in accordance with the results of Yue et al. (2013), while the mass range to be compatible with the IMF values in Ferrara et al. (2014). The density interval has been taken from simulations in Li & Benacquista (2010), while the variation of the spin parameter a for high-redshift black holes from Volonteri (2010), Volonteri et al. (2013). Generally speaking, the rotational energy of early black holes is very low compared with local ones: the spin is progressively increased by the accretion of matter onto the compact object and by merging events. For this reason, our average value for the spin parameter is $a \sim 0.05$ (see also Davis & Natarajan 2010).

The variation of these physical quantities have different impacts on the gravitational signal that is generated. A study of their effect has been sketched in the following Fig. 7.4 and Fig. 7.5. In these figures, the number of bins for mass and redshift are the same

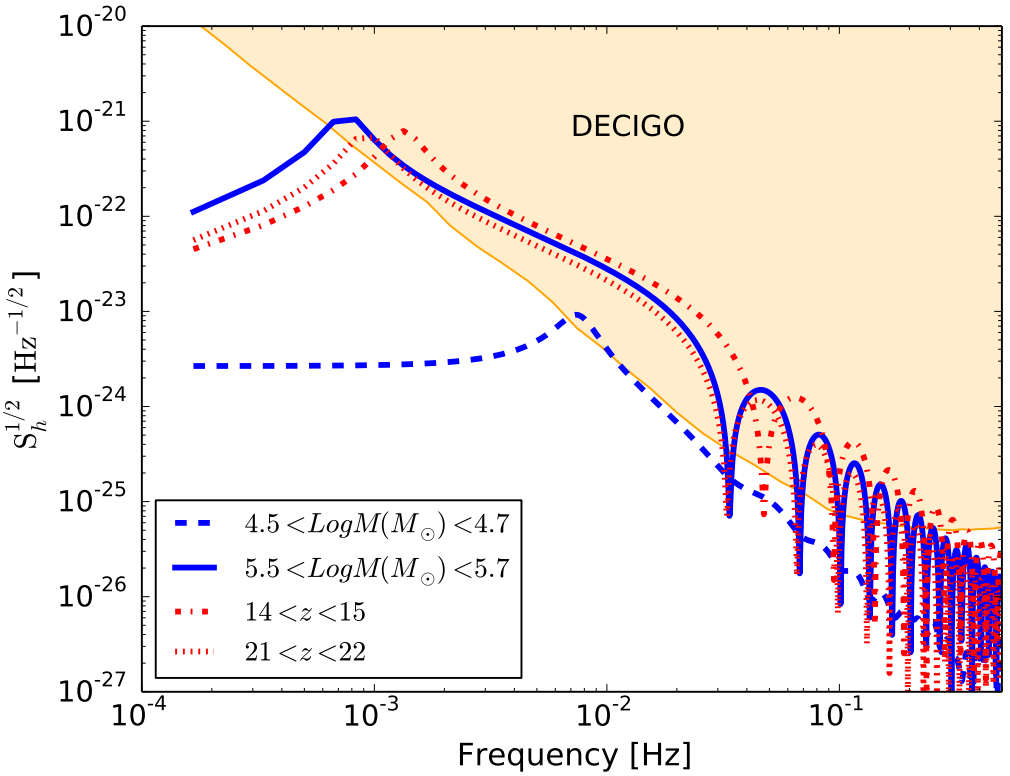

FIGURE 7.4: Effect on the strain amplitude $\tilde{h}(\nu)$ of the black hole mass and of its redshift. In this case the calculation has been performed in narrow ranges of the parameters, as indicated in the legend. The orange region is the sensitivity for the future Ultimate-DECIGO observatory.

number as reported in Table 7.1, but their ranges are restricted to the values shown in the legend.

The effect of the redshift on the gravitational signal is very small. This is due to the fact that the whole range of redshift values spans only $\sim 150\,\mathrm{Myr}$ of cosmic history. For higher redshifts, the observed gravitational signal is shifted to lower frequencies, as expected. On the contrary, the effect of the mass is greatly important: lower masses correspond to higher frequencies of the peak ($\nu_0 \propto 1/M_\bullet$, see Sec. 7.2), but also to an overall amplitude of the signals ~ 2 orders of magnitude lower, at the extreme detection limit with the DECIGO observatory. The spin parameter affects mainly the shape of the spectral strain amplitude and its peak frequency, which is shifted to higher values for larger values of a, while the amplitude is not affected. The mean mass density ρ has virtually no effect on the peak frequency and on its amplitude, but varies the shape of the spectrum at higher frequencies. This is due to the fact that the mean mass density directly controls the duration of the collapse phase, $t_c \sim t_{dyn} \sim 1/\sqrt{G\rho}$, i.e. the

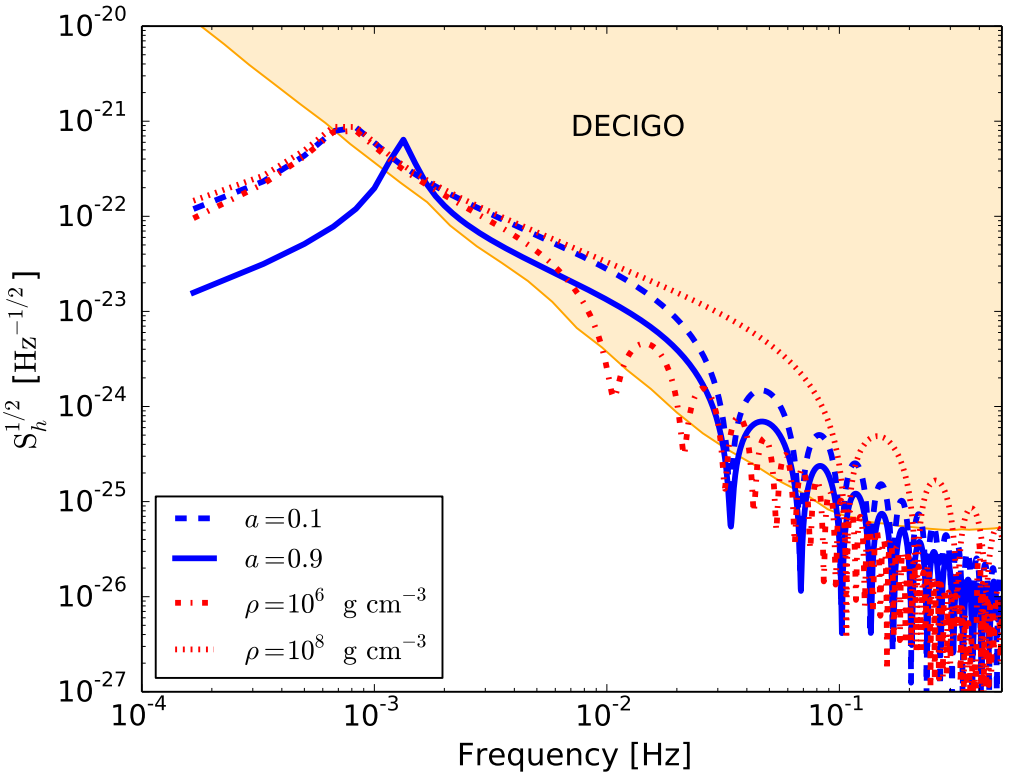

FIGURE 7.5: As in Fig. 7.4, but for the spin parameter and the mean density. In this case, the single values used for the parameters are shown in the legend.

transition from the collapse to the ringdown phases.

The gravitational strain $\tilde{h}(\nu)$ for the total ensemble is reported in Fig. 7.6. The orange region is the sensitivity curve of Ultimate-DECIGO, as obtained from Marassi et al. (2009), and it has been used to compute the SNR, reported as a solid red line in Fig. 7.6.

The estimated signal lies above the foreseen sensitivity of Ultimate-DECIGO in the frequency range 0.8 mHz and 0.3 Hz, with a peak amplitude $\Omega_{gw} = 1.1 \times 10^{-54}$ at $\nu_{max} = 0.9$ mHz. The SNR ratio is generally of order unity in most of the frequency band, and it reaches a maximum SNR ~ 22 at $\nu = 20$ mHz. A source is considered detectable if the resulting SNR exceeds some standard threshold value, typically between 5 and 10 (Plowman et al., 2010), so the signal generated by the collapse of high-redshift atomic cooling halos into DCBHs is detectable by the future Ultimate-DECIGO observatory.

However, in this frequency interval the sensitivity of Ultimate-DECIGO is limited by the unresolved background produced by the GW emission of Galactic compact binaries

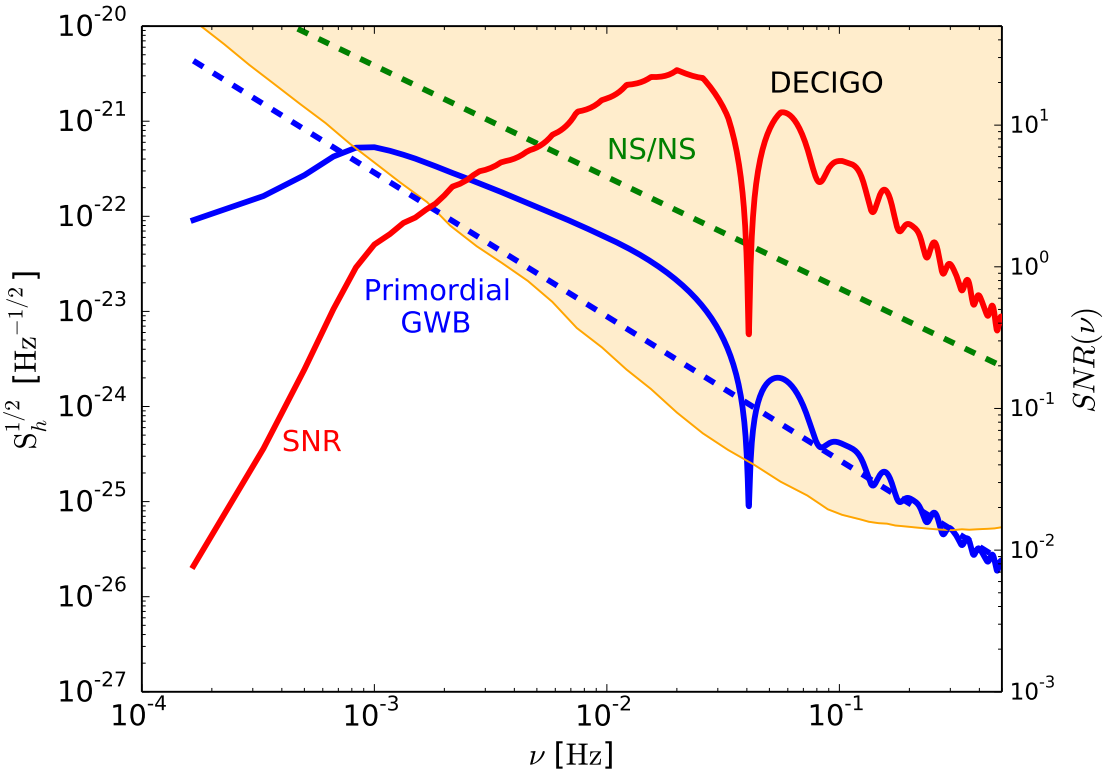

FIGURE 7.6: Gravitational strain $\tilde{h}(\nu)$ for the total ensemble. The orange region is the sensitivity for the future Ultimate-DECIGO observatory. The dashed lines indicate the Galactic Confusion Background (GCB) due to the GWs emission from double neutron stars (NS/NS), which is the dominant foreground component (see Yagi & Seto 2011).

that acts as a confusion noise (Nelemans, 2009, Regimbau & Hughes, 2010, Regimbau et al., 2012): this is shown in Fig. 7.6 with a green dashed line (Sathyaprakash & Schutz, 2009). The duty-cycle for these events, for future space-borne gravitational observatories like DECIGO, will be higher than unity, i.e. the signals overlap and create a confusion noise of unresolved sources. See Yagi & Seto (2011) for a detailed description of the binary confusion noise as observed by the future DECIGO observatory.

The gravitational signal generated by DCBHs is characterized by $\mathcal{D} \ll 1$, so there is a superposition of a discontinuous signal over a background noise: in this case, the component separation is easier to perform. Our Fig. 7.7 is a simple proof of concept of a signal processing method that allows to: (i) probe the presence of an underlying signal buried into a background noise and (ii) estimate its periodicity. The red solid line is the sum of $h_s(t)$, the signal from DCBHs collapse with $\mathcal{D} = 0.2$ (this value has been chosen for an easier visualization on the plot), and the binary confusion background $h_n(t)$, as in Regimbau & Hughes (2010) but with observations extended up to $z = 15$. The signal is

completely buried into the noise. Nonetheless, the blue points are the auto-correlation function of the signal, which shows a clear structure. It starts from a value $A_0 \sim 0.4$ and drops approximately after ~ 4 cycles of the signal to a value $\sim A_0/10$: this time separation is highlighted by the vertical orange line. In addition, the periodic behavior of the auto-correlation function resembles the intrinsic oscillations of the ringdown phase during the collapse. As a comparison, the green points represent the auto-correlation function for the noise component only: the absence of any structure is evident.

The two parameters that greatly affect the appearance of the auto-correlation function are the mass $M_\bullet$ and the mean density ρ. The total duration of the GWs emission depends on: (i) the duration of the collapse phase (proportional to $1/\sqrt{\rho}$) and (ii) the duration of the ringdown phase, which depends on $M_\bullet$ (see the expression for ν_0 in Sec. 7.2). In addition, the mass greatly affects the overall normalization (magnitude) of the signal, see Fig. 7.4. For masses $M_\bullet > 10^5\,\mathrm{M}_\odot$, the signal would not be buried into the fore/background, then its detection would be straightforward. If we allow the mass of the population to vary below $M_\bullet = 10^5\,\mathrm{M}_\odot$ and the density to vary as well, what happens is that the auto-correlation function may have several rises and falls, around the typical time separations between these signals, as clearly shown in Fig. 7.7.

This simple method proves the existence of an underlying periodic signal and provides a range of possible values for the period, i.e. the time separation needed for the auto-correlation function to drop. Anyway, a possible future detection of this signal with Ultimate-DECIGO would require the application of more sophisticated algorithms for data analysis, similar to those that have been proposed for the LISA experiment (e.g. Crowder & Cornish 2007).

7.4 Discussion and Summary

In this chapter, we have employed modern waveforms and the improved knowledge on the DCBHs formation rate to estimate the gravitational signal emitted by the formation of DCBHs at $13 \lesssim z \lesssim 20$, in the so-called "DCBHs Era" (see Yue et al. 2014).

We have investigated the effects of a wide range of masses, spin parameters and mean mass densities on the gravitational signal, in order to build up a realistic ensemble of these high-redshift sources.

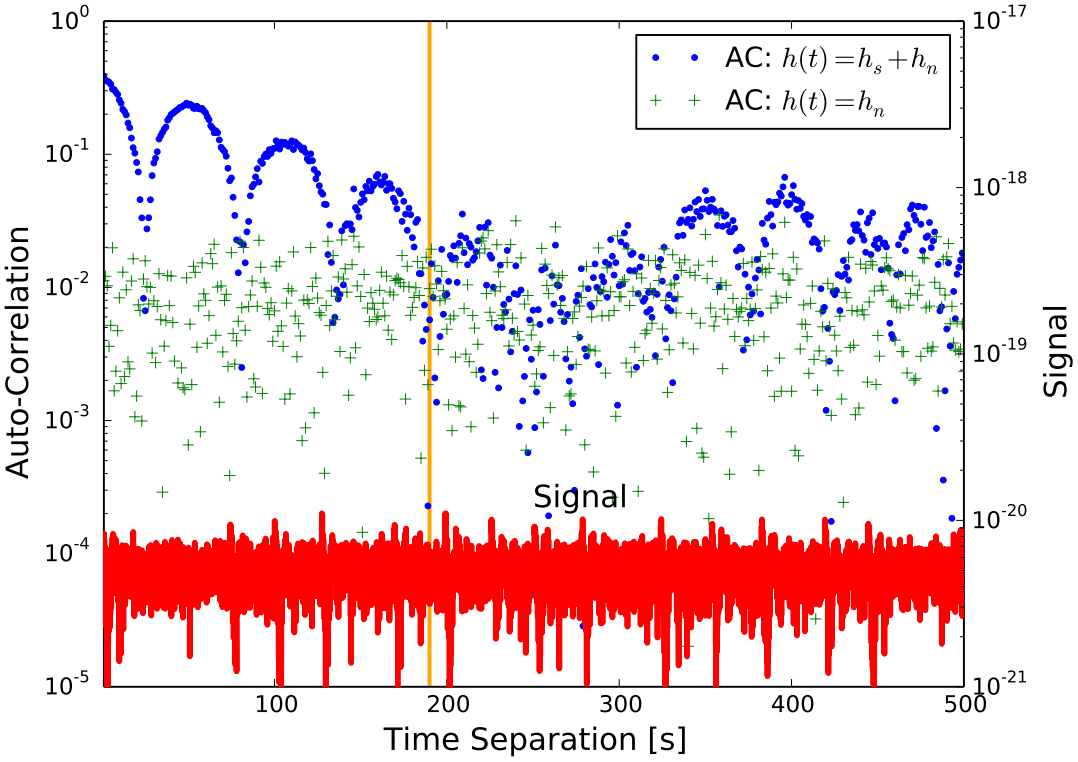

FIGURE 7.7: Simple example of a signal processing method to separate a signal with $\mathcal{D} \ll 1$ from the confusion noise. The sum $h(t) = h_s(t) + h_n(t)$, where $h_s(t)$ is the shot-noise signal and $h_n(t)$ is the background noise component, is shown on the bottom, in red. The blue and green points are the auto-correlation function for $h(t)$ and for $h_n(t)$ only, respectively. The duty-cycle of the signal is $\mathcal{D} = 0.2$ (this value has been chosen for an easier visualization on the plot), while the population of collapsing DCBHs has a realistic distribution of masses ($10^4\,\mathrm{M}_\odot < M_\bullet < 10^5\,\mathrm{M}_\odot$, spin paramenters ($0.01 < a < 0.5$) and densities ($10^6\,\mathrm{g\,cm^{-3}} < \rho < 10^8\,\mathrm{g\,cm^{-3}}$). See the main text for a complete description.

We have shown that, despite the very high rate of events for all-sky surveys ($\sim 10^4\,\mathrm{yr}^{-1}$ up to $z \sim 20$), the integrated signal from these sources is characterized by a very low duty-cycle ($\mathcal{D} \sim 10^{-3}$), i.e. it is a shot-noise. This is a consequence of the small duration of the GW emission from this kind of sources ($\Delta T_{gw} \sim 2 - 30\,\mathrm{s}$).

Our results show that the gravitational signal lies above the foreseen sensitivity of the Ultimate-DECIGO observatory in the frequency range 0.8 mHz and 0.3 Hz, with a peak amplitude $\Omega_{gw} = 1.1 \times 10^{-54}$ at $\nu_{max} = 0.9\,\mathrm{mHz}$ and a peak Signal-to-Noise Ratio of ~ 22 at $\nu = 20\,\mathrm{mHz}$. This amplitude is lower than the Galactic confusion noise in the same frequency band, generated by binary systems of compact objects.

For a gravitational signal characterized by $\mathcal{D} \ll 1$ and buried into this confusion noise, we have provided a very simple signal processing method to prove the existence of

an underlying periodic oscillation such as those we expect from DCBHs. However, more advanced techniques will be required to separate this signal from background and foreground noise components.

The signal investigated in this chapter lies in the same frequency range of the one produced by NS binaries and, in the same way, acts as a noise for the cosmological background, which is the ultimate target of the experiment DECIGO. For this reason, it is very important to model any gravitational signal that may fall into the frequency range of interest for the primordial signal.

Despite all the technical difficulties, the actual observation of DCBHs may be a keystone in modern Cosmology, providing a significant contribution to the formation theory of SMBHs and to the understanding of the Cosmic Infrared Background.

Part IV

Conclusions and Future Developments

Conclusions and Future Developments

In the standard ΛCDM cosmological model, the formation of the first stars started approximately 100 Myr after the Big Bang. The formation of the first black holes, as a final product of the runaway evolution of the first massive stars or by means of other mechanisms, represents a second key event during the same cosmic epoch. The first massive black holes formed are generally recognized as playing an important role in galaxy evolution: both the proportionality between black hole mass and host halo properties and the importance of feedback from accreting black holes indicate a profound black hole - host galaxy interconnection.

Notwithstanding the relevant progresses made in this field in recent years, both theoretically and observationally, the answers to the most important questions related to the first black holes are still missing. What is the main physical process that drove their formation? Why do we observe extremely massive objects already in the very early Universe? What is their connection with the SMBHs that are almost omnipresent at the center of local galaxies? How did they contribute to the formation process of galaxies? Answering these questions is a complicated task, since: (i) detecting objects in the early Universe is at the edge or beyond the current observational capabilities, and (ii) the physical conditions in which their formation process occurred are poorly constrained.

Currently, we probe only the most massive and luminous black holes, quite literally the tip of the iceberg of their mass distribution: the advent of new observatories will definitely mark a breakthrough in this field. Upcoming facilities such as the JWST will revolutionize our view of the ancient Universe, by detecting the light from the most distant stars and accreting black holes, including lower luminosity AGNs, hopefully powered by lower-mass black holes. In the high-energy range, a similar role will be played by deeper Chandra fields and, further in the future, by ATHENA and the X-ray Surveyor. A solid theoretical framework is more than ever needed to understand and effectively exploit the huge amount of data that will be provided in the near future by these observatories, which will disclose to our eyes the first glimpses of light in the Universe.

Building a theoretical framework to understand the growth, cosmological evolution and observational features of the first black holes is the objective of the research developed during the Ph.D. and presented in this Thesis. Much work needs to be done to tackle

the open questions mentioned before. Possible strategies to expand this work are briefly summarized in the following, divided schematically into theoretical and observational frameworks.

Theoretical Framework

From a theoretical standpoint, the final goal of this research is to devise a general framework to understand the formation, growth and cosmological evolution of the first black holes. In principle, this theory should be able to: (i) predict the physical features of the first black holes and their birth environments, (ii) predict their evolution up to the observed early ($z \sim 7$) SMBHs, explaining the observations of accreting high-z objects, and (iii) support the observations of SMBHs in the local Universe.

Currently, the most relevant tension between theory and observations is the presence of AGNs less than 800 Myr after the Big Bang, suggesting that accreting black holes with masses up to $10^{10}\,\mathrm{M}_{\odot}$ were shining very early in the Universe. For the standard theory of black hole growth, it is challenging to build up such massive objects from a low-mass black hole seed, of hundreds of solar masses. The pathway to overcome this problem is thought to be twofold: (i) the black hole seeds that gave birth to the observed early SMBHs could have been very massive, up to $10^{5}\,\mathrm{M}_{\odot}$, and (ii) in optically-thick, highly-obscured environments the accretion rate may not have been capped by the Eddington rate. A combination of massive black hole seeds and super-Eddington accretion episodes could be able to reproduce the high-z observations, but the mystery remains unsolved so far. Possible pathways to improve and expand the work presented in this Thesis include the following:

1) **Determine the main formation channel of the first black holes:** In the work presented so far, the assumed formation process was the DCBH scenario, which produces a high-mass black hole at the center of an unpolluted dark matter halo. This is not the only possible formation channel, others being for instance the direct collapse of self-gravitating pre-galactic disks and the formation of a very massive star from mergers in a dense cluster. The principal difference between these formation channels is the metallicity of the host halo gas, the crucial reason being related to fragmentation and mass losses through winds. Identifying the main formation channel is of the utmost importance to predict the subsequent cosmological evolution of the population of the first

black holes and it is certainly one of the main goals that this field of research should aim at. This task will require a mixed effort of theory, to predict the observables of each formation channel, and observations. For instance, the detection of a black hole seed without any metal emission line may favor the DCBH scenario. Moreover, the observation of a paucity of high-z AGNs may disfavor the formation channels leading to smaller-mass seeds, and also gravitational waves observations may contribute to the effort.

2) **Understand the role of super-Eddington accretion:** Several works in the literature assume that accretion rates are not capped by the Eddington limit, proposing the occurrence of short and recurring, but strongly super-Eddington, accretion episodes at high-z. Super-Eddington accretion is feasible in highly-obscured, optically-thick environments, where radiation trapping is significant. Since the black hole mass increases exponentially with the accretion rate, super-Eddington accretion would dramatically speed up the growth process, easing the constraints on the growth of early SMBHs. The relevance of highly-obscured accretion environments in the early Universe is unclear so far. Their relative significance in the growth process of the first black holes is one of the main unknown in this field. Again, this would require a mixture of theory and observations, the first being needed to predict the observables of an obscured population of high-z black holes. The first steps towards testing the role of obscured phases in the early growth of black holes have been already accomplished during my Ph.D., but many more are needed.

3) **Extend the theory in a cosmological context to explain the observation of early SMBHs:** Once the contribution of the different formation channels to the population of the first black holes is well constrained and the significance of super-Eddington accretion is determined, it will be of crucial importance to evolve in a cosmological sense the initial population of collapsed objects, in order to make predictions at lower redshifts. A merger tree approach will likely be needed to accomplish this task. Once the underlying rules of black hole formation and growth are well constrained, this approach will yield very precise information about their cosmological evolution. In principle, the merger tree approach will predict the evolution of the black hole mass function over the cosmic time, providing a wealth of precious astrophysical and cosmological information. For instance, this will definitely help in clarifying the relation between the first black

holes and the SMBHs we observe at the center of most local galaxies. Moreover, this approach will shed some light on the mystery of the early SMBHs. We analytically showed that black holes with masses above a critical value should produce a negligible feedback effect on the surrounding halo, which would lead to an extremely rapid growth. We then suggested that objects at the high-mass end of the black hole initial mass function could be the seeds which gave birth to the extremely massive objects we observe at high-z. This hypothesis needs to be tested. To conclude, the study of the very early evolution of black hole seeds will provide valuable insights to solve other relevant questions, like the strength of the infrared cosmic background and its cross-correlation with the cosmic X-ray background.

Observational Framework

The capability of observing the first black hole seeds formed in the Universe would represent a milestone in this research field. Detecting the light of these primordial sources is challenging, due to their extreme faintness, but possibly also to the current lack of clear theoretical indications about their mass, host halo properties and typical accretion rates, resulting in large uncertainties in the prediction of their observational signatures. We were the first to propose that CR7, a very bright Lyα emitter at $z = 6.6$, could be powered by a DCBH with an initial mass of $\sim 10^5\,\mathrm{M}_\odot$. This proposition needs deeper X-ray observations to be confirmed. For CR7 high-resolution spectra were available, easing the task of comparing its observational signatures with the predicted radiation of a DCBH. The next step would be to find a way to systematically locate black hole seed candidates in deep surveys.

We proved that the X-ray emission of these objects is relatively faint, especially in heavily Compton-thick environments, while their infrared emission should be sufficiently strong to be detected by current and future observatories. Supported by numerical simulations, we developed a photometric method to identify black hole seed candidates in deep multi-wavelength surveys. We predict that these highly-obscured sources are characterized by a steep spectrum in the infrared. The method selects the only 2 objects with a robust X-ray detection found in the CANDELS/GOODS-S survey with $z \gtrsim 6$. To date, the selected objects represent the most promising black hole seed candidates, possibly formed via the DCBH scenario, with predicted mass in excess of $10^5\,\mathrm{M}_\odot$. The possibility

of systematically detecting the first black holes is of the greatest importance in the synergy between theory and observations and much focus on this topic will be provided in the next years by the scientific community.

Notwithstanding the relevant questions that remain unanswered, the work developed so far establishes the first elements of a theoretical framework to support the next generation of telescopes, with the aim of finding the first black holes in the Universe.

Part V

Appendix

Summary of Additional Work

This appendix contains the abstracts of additional published papers developed during the Ph.D., but not included in the present Thesis because they are co-authored works or the subject matter is different from the main subject of this Thesis. The order of appearance is chronological.

1. **Pacucci F.**, Ferrara A., D'Onghia E., *Detectability of Free Floating Planets in Open Clusters with the James Webb Space Telescope*, 2013, ApJ Letters, Volume 778, Issue 2, article id. L42.

Abstract:

Recent observations have shown the presence of extra-solar planets in Galactic open stellar clusters, as in the Praesepe (M44). These systems provide a favorable environment for planetary formation due to the high heavy-element content exhibited by the majority of their population. The large stellar density, and corresponding high close-encounter event rate, may induce strong perturbations of planetary orbits with large semimajor axes. Here we present a set of N-body simulations implementing a novel scheme to treat the tidal effects of external stellar perturbers on planetary orbit eccentricity and inclination. By simulating five nearby open clusters we determine the rate of occurrence of bodies extracted from their parent stellar system by quasi-impulsive tidal interactions. We find that the specific free-floating planet production rate $\dot{N}_o$ (total number of free-floating planets per unit of time, normalized by the total number of stars) is proportional to the stellar density $\rho_\star$ of the cluster: $\dot{N}_o = \alpha\rho_\star$, with $\alpha = (23 \pm 5) \times 10^{-6} \mathrm{pc}^3\,\mathrm{Myr}^{-1}$. For the Pleiades (M45) we predict that $\sim 26\%$ of stars should have lost their planets. This raises the exciting possibility of directly observing these wandering planets with the James Webb Space Telescope in the NIR band. Assuming a surface temperature of the planet of ~ 500 K, a free-floating planet of Jupiter size inside the

Pleiades would have a specific flux of F_ν (4.4 μm) $\approx 4 \times 10^2$ nJy, which would lead to a very clear detection ($S/N \sim 100$) in only one hour of integration.

2. **Pacucci F.**, Mesinger A., Haiman Z., *Focusing on Warm Dark Matter with Lensed High-Redshift Galaxies*, 2013, MNRAS Letters, Volume 435, Issue 1, p. L53-L57.

Abstract:

We propose a novel use of high-redshift galaxies, discovered in deep Hubble Space Telescope (HST) fields around strong lensing clusters. These fields probe small comoving volumes ($\sim 10^3$ Mpc^3) at high magnification ($\mu \gtrsim 10$), and can detect otherwise inaccessible ultra-faint galaxies. Even a few galaxies found in such small volumes require a very high number density of collapsed dark matter (DM) halos. This implies significant primordial power on small scales, allowing these observations to rule out popular alternatives to standard cold dark matter (CDM) models, such as warm dark matter (WDM). In this work, we analytically compute WDM halo mass functions at $z = 10$, including the effects of both particle free-streaming and residual velocity dispersion. We show that the two $z \approx 10$ galaxies already detected by the Cluster Lensing And Supernova survey with Hubble (CLASH) survey are sufficient to constrain the WDM particle mass to $m_x > 1$ (0.9) keV at 68% (95%) confidence limit (for a thermal relic relativistic at decoupling). This limit depends only on the WDM halo mass function and, unlike previous constraints on m_x, is independent of any astrophysical modeling. The forthcoming HST Frontier Fields can significantly tighten these constraints.

3. Dayal P., Choudhury T., Bromm V., **Pacucci F.**, *Reionizing the Universe in Warm Dark Matter Cosmologies*, 2015, arXiv:1501.02823.

Abstract:

We compare model results from our semi-analytic merger tree based framework for high-redshift ($z \simeq 5 - 20$) galaxy formation against reionization indicators including the Planck electron scattering optical depth (τ_{es}) and the ionizing photon emissivity ($\dot{n}_{ion}$) to constrain the particle mass of Warm Dark Matter (WDM). Our framework traces the Dark Matter (DM) and baryonic assembly of galaxies in 4 DM cosmologies: Cold Dark Matter (CDM) and WDM with a particle mass of $m_x =$

2.25, 3 and 5 keV. It includes all the key processes of star formation, supernova feedback, the merger/accretion/ejection driven evolution of gas and stellar mass, and the effect of the ultra-violet background (UVB) created during reionization in photo-evaporating the gas content of galaxies in halos with $M_h \leq 10^9\,\mathrm{M}_\odot$. We show that current Planck τ_{es} values rule out $m_x \leq 2.5$ keV WDM, even in the physically unlikely scenario that all ionizing photons produced by these galaxies escape and contribute to reionization (i.e. $f_{esc} = 1$). With the largest number of UVB-suppressed galaxies, CDM faces a "stalling" of the reionization process with this effect decreasing with the disappearance of small-scale structure with decreasing m_x. Finally, we find the bulk of the reionization photons come from galaxies with a halo mass $M_h \leq 10^9\,\mathrm{M}_\odot$, stellar mass $M_* \leq 10^7\,\mathrm{M}_\odot$ and UV magnitude $-18 \leq M_{UV} \leq -13$ in CDM. The progressive suppression of low-mass halos with decreasing m_x leads to a shift in the "reionization" population to larger (halo and stellar) masses of $M_h \geq 10^9\,\mathrm{M}_\odot$ and $M_* \geq 10^7\,\mathrm{M}_\odot$ for $m_x \geq 3$ keV WDM, although the UV limits effectively remain unchanged.

4. **Pacucci F.**, Mesinger A., Mineo S., Ferrara A., *The X-ray Spectra of the First Galaxies: 21 cm Signatures*, 2014, MNRAS, Volume 443, Issue 1, p. 678-686.

Abstract:

The cosmological 21cm signal is a physics-rich probe of the early Universe, encoding information about both the ionization and the thermal history of the intergalactic medium (IGM). The latter is likely governed by X-rays from star-formation processes inside very high redshift ($z \gtrsim 15$) galaxies. Due to the strong dependence of the mean free path on the photon energy, the X-ray SED can have a significant impact on the interferometric signal from the cosmic dawn. Recent *Chandra* observations of nearby, star-forming galaxies show that their SEDs are more complicated than is usually assumed in 21cm studies. In particular, these galaxies have ubiquitous, sub-keV thermal emission from the hot interstellar medium (ISM), which generally dominates the soft X-ray luminosity (with energies $\lesssim 1$ keV, sufficiently low to significantly interact with the IGM). Using illustrative soft and hard SEDs, we show that the IGM temperature fluctuations in the early Universe would be substantially increased if the X-ray spectra of the first galaxies were dominated

by the hot ISM, compared with X-ray binaries with harder spectra. The associated large-scale power of the 21cm signal would be higher by a factor of $\sim$ three. More generally, we show that the peak in the redshift evolution of the large-scale ($k \sim 0.2$ Mpc^{-1}) 21cm power is a robust probe of the soft-band SED of the first galaxies, and importantly, is not degenerate with their bolometric luminosities. On the other hand, the redshift of the peak constrains the X-ray luminosity and halo masses which host the first galaxies.

5. Dayal P., Ferrara A., Dunlop J., **Pacucci F.**, *Essential Physics of Early Galaxy Formation*, 2014, MNRAS, Volume 445, Issue 3, p. 2545-2557.

Abstract:

We present a theoretical model embedding the essential physics of early galaxy formation ($z \simeq 5 - 12$) based on the single premise that any galaxy can form stars with a maximal *limiting efficiency that provides enough energy to expel all the remaining gas, quenching further star formation.* This simple idea is implemented into a merger-tree based semi-analytical model that utilises two mass and redshift-independent parameters to capture the key physics of supernova feedback in ejecting gas from low-mass halos, and tracks the resulting impact on the subsequent growth of more massive systems via halo mergers and gas accretion. Our model shows that: *(i)* the smallest halos (halo mass $M_h \leq 10^{10}\,\mathrm{M}_\odot$) build up their gas mass by accretion from the intergalactic medium; *(ii)* the bulk of the gas powering star formation in larger halos ($M_h \geq 10^{11.5}\,\mathrm{M}_\odot$) is brought in by merging progenitors; *(iii)* the faint-end UV luminosity function slope evolves according to $\alpha = -1.75 \log z - 0.52$. In addition, *(iv)* the stellar mass-to-light ratio is well fit by the functional form $\log M_* = -0.38 M_{UV} - 0.13\,z + 2.4$, which we use to build the evolving stellar mass function to compare to observations. We end with a census of the cosmic stellar mass density (SMD) across galaxies with UV magnitudes over the range $-23 \leq M_{UV} \leq -11$ spanning redshifts $5 < z < 12$: *(v)* while currently detected LBGs contain $\approx 50\%$ (10%) of the total SMD at $z = 5$ (8), the *JWST* will detect up to 25% of the SMD at $z \simeq 9.5$.

6. Dayal P., Mesinger A., **Pacucci F.**, *Early Galaxy Formation in Warm Dark Matter Cosmologies*, 2015, ApJ, Volume 806, Issue 1, article id. 67.

Abstract:

We present a framework for high-redshift ($z \gtrsim 7$) galaxy formation that traces their dark matter (DM) and baryonic assembly in four cosmologies: Cold Dark Matter (CDM) and Warm Dark Matter (WDM) with particle masses of $m_x = 1.5$, 3 and 5 keV. We use the same astrophysical parameters regulating star formation and feedback, chosen to match current observations of the evolving ultraviolet luminosity function (UV LF). We find that the assembly of observable (with current and upcoming instruments) galaxies in CDM and $m_x \geq 3\,\mathrm{keV}$ WDM results in similar halo mass to light ratios (M/L), stellar mass densities (SMDs) and UV LFs. However the suppression of small-scale structure leads to a notably delayed and subsequently more rapid stellar assembly in the 1.5 keV WDM model. Thus galaxy assembly in $m_x \lesssim 2\,\mathrm{keV}$ WDM cosmologies is characterized by: (i) a dearth of small-mass halos hosting faint galaxies; and (ii) a younger, more UV bright stellar population, for a given stellar mass. The higher M/L ratio (effect ii) partially compensates for the dearth of small-mass halos (effect i), making the resulting UV LFs closer to CDM than expected from simple estimates of halo abundances. We find that the redshift evolution of the SMD is a powerful probe of the nature of DM. Integrating down to a limit of $M_{UV} = -16.5$ for the James Webb Space Telescope (JWST), the SMD evolves as $\log(\mathrm{SMD}) \propto -0.63(1+z)$ in $m_x = 1.5\,\mathrm{keV}$ WDM, as compared to $\log(\mathrm{SMD}) \propto -0.44(1+z)$ in CDM. Thus high-redshift stellar assembly provides a powerful testbed for WDM models, accessible with the upcoming JWST.

7. Pallottini A., Ferrara A., **Pacucci F.**, Gallerani S., Salvadori S., Schneider R., Schaerer D., Sobral D., Matthee J., *The Brightest Lyα Emitter: Pop III or Black Hole?*, 2015, MNRAS, Volume 453, Issue 3, p. 2465-2470.

Abstract:

CR7 is the brightest $z = 6.6$ Lyα emitter (LAE) known to date, and its spectroscopic follow-up suggests that CR7 might host Population (Pop) III stars. We examine this interpretation using cosmological hydrodynamical simulations. Several simulated galaxies show the same "Pop III wave" pattern observed in CR7. However, to reproduce the extreme CR7 Lyα/HeII(1640) line luminosities ($L_{\alpha/\mathrm{HeII}}$) a

top-heavy IMF and a massive ($\gtrsim 10^7\,M_\odot$) Pop III burst with age $\lesssim 2$ Myr are required. Assuming that the observed properties of Lyα and HeII emission are typical for Pop III, we predict that in the COSMOS/UDS/SA22 fields, 14 out of the 30 LAEs at $z = 6.6$ with $L_\alpha > 10^{43.3}\,\mathrm{erg\,s^{-1}}$ should also host Pop III stars producing an observable $L_{\mathrm{HeII}} \gtrsim 10^{42.7}\,\mathrm{erg\,s^{-1}}$. As an alternate explanation, we explore the possibility that CR7 is instead powered by accretion onto a Direct Collapse Black Hole (DCBH). Our model predicts L_α, L_{HeII}, and X-ray luminosities that are in agreement with the observations. In any case, the observed properties of CR7 indicate that this galaxy is most likely powered by sources formed from pristine gas. We propose that further X-ray observations can distinguish between the two above scenarios.

8. Volonteri M., Habouzit M., **Pacucci F.**, Tremmel M., *The Evolution of High-Redshift Massive Black Holes*, 2015, Galaxies at High Redshift and Their Evolution over Cosmic Time, Proceedings IAU Symposium No. 319, 2015.

Abstract:

Massive black holes (MBHs) are nowadays recognized as integral parts of galaxy evolution. Both the approximate proportionality between MBH and galaxy mass, and the expected importance of feedback from active MBHs in regulating star formation in their host galaxies point to a strong interplay between MBHs and galaxies. MBHs must form in the first galaxies and be fed by gas in these galaxies, with continuous or intermittent inflows that, at times, can be larger than the Eddington rate. Feedback from supernovae and from the MBHs themselves modulates the growth of the first MBHs. While current observational data only probe the most massive and luminous MBHs, the tip of the iceberg, we will soon be able to test theoretical models of MBH evolution on more "normal" MBHs: the MBHs that are indeed relevant in building the population that we observe in local galaxies, including our own Milky Way.

9. Cappelluti N., Li Y., Ricarte A., Agarwal B., Ajello M., Civano F., Comastri A., Elvis M., Gilli R., Hasinger G., Marchesi S., Natarajan P., **Pacucci F.**, Tasnin Ananna T., Treister E., Urry C. M., *The X-ray background in the Chandra*

COSMOS-Legacy field I: Energy Spectrum and undetected populations in the [0.3-7] keV band, 2016, submitted to arXiv and to ApJ Letters.

Abstract:

With $\sim$ 0.5 million net counts, we present one of the most accurate measurements of the Cosmic X-ray Background (CXB) spectrum to date in the [0.3-7] keV energy band using Chandra observations in the 2.15 deg^2 COSMOS legacy field. The CXB has three distinct components: two collisional thermal plasmas at kT$\sim$0.23 and 0.06 keV; and an extragalactic power law with a photon spectral index Γ=1.41$\pm$0.02. The 1 keV normalization of the extragalactic component is 10.25$\pm$0.14 keV cm^{-2} s^{-1} sr^{-1} keV^{-1}. Removing all known X-ray detected sources, the remaining unresolved CXB is best-fit by a power-law with normalization 3.95$\pm$0.1 keV cm^{-2} s^{-1} sr^{-1} keV^{-1} and photon spectral index Γ=1.28$\pm$0.03. Removing faint galaxies down to R_{AB} $\sim$27 leaves a hard spectrum with Γ $\sim$1.3 and a 1 keV normalization of $\sim$0.39 keV cm^{-2} s^{-1} sr^{-1} keV^{-1}, which accounts for 96$\pm$0.8% of the total unresolved CXB. This suggests that unresolved sources that contribute $\sim$ 4% of the total CXB, are harder and possibly more obscured than the resolved sources. Another 1% of the CXB can be attributed to star forming galaxies and faint absorbed AGN. Accounting for coherent fluctuations between the Cosmic Infrared Background and the CXB, we argue that the remaining 3% of the total CXB can be attributed to accreting black holes at high redshifts. If a population of direct collapse black holes exists, in order to not exceed the z$\sim$6 accreted mass density, they must grow in Compton thick envelopes with N_H $>1.6\times10^{25}$ cm^{-2} and form in extremely low metallicity environments $Z_\odot \sim 10^{-3}$.

Acknowledgements

Many people contributed, directly or indirectly, to the realization of the research presented in this Thesis. All my efforts to understand what "to be a scientist" is would have been vain without their help and support.

Firstly, I would like to thank my supervisor and friend, Andrea Ferrara, for his strenuous effort to make a scientist out of me, hopefully a good one. It has been a pleasure and a privilege to work with him. I am utterly grateful to Andrei Mesinger and his wonderful family (Linda, Luka and Nikola) for his invaluable support, his fantastic friendship, his wine tastings and his attempts to learn the doubles of the Italian language.

This work would have not seen the light, despite it revolves around darkness, without the friendship and the inspiration coming from many people. I would like to thank all my "fellow-adventurers" in Pisa: Paramita Barai, Paolo Comaschi, Arpan Das, Chiara Feruglio, Simona Gallerani, Bradley Greig, Serena Manti, Maria Orofino, Andrea Pallottini, Emanuele Sobacchi, Antonio Stamerra, Graziano Ucci, Marcos Valdes, Livia Vallini, Bin Yue. In particular, thanks to Marcos for our fruitful "war meetings" and to Simona, simply for being born in Bari. Special thanks to all the people I met during my two long-term visits at the IAP (Paris) and at Yale University (USA), in particular to Marta Volonteri, Priya Natarajan, Meg Urry, Nico Cappelluti and Avi Loeb for their wonderful hospitality and for having taught me so much, not only about astronomy.

The full list of people that I met during all conferences, visiting periods, coffee breaks, cosmic soccer matches et cetera would require a chapter apart. After all, the best part of our work is to have the possibility to visit so many countries in so many continents and to meet so many interesting people. To all of them, thank you so much for having shaped the person and the scientist that I am today. I am thankful to all the people working at my institution, the SNS: it will be hard to find another working place so full of competency and inspiration. To all the people that make it such a great place, I express all my gratitude.

Finally, a special thanks to the very special people that have accompanied me, totally or partly, during this wonderful travel: Emilio Sassone Corsi, Cosimo Distratis, Mimmo Matichecchia, Emanuele Spagnulo, Donato Massimino, Marco Sciannamea, Adriana Cola, Louise Dehondt, Martina Gerbino. Thank you, Cristina, for the latest months spent together and, hopefully, for many more yet to come. And, of course, all my gratitude to my parents, Luigi and Francesca, for having always believed in me.

Bibliography

Abbott B. P., et al., 2009, PRD, 80, 062001

Abbott B. P., et al., 2016a, preprint, (arXiv:1602.03842)

Abbott B. P., et al., 2016b, Physical Review Letters, 116, 061102

Abramowicz M. A., Fragile P. C., 2013, Living Reviews in Relativity, 16, 1

Abramowicz M. A., Czerny B., Lasota J. P., Szuszkiewicz E., 1988, ApJ, 332, 646

Agarwal B., Khochfar S., Johnson J. L., Neistein E., Dalla Vecchia C., Livio M., 2012, MNRAS, 425, 2854

Agarwal B., Davis A. J., Khochfar S., Natarajan P., Dunlop J. S., 2013, MNRAS, 432, 3438

Agarwal B., Dalla Vecchia C., Johnson J. L., Khochfar S., Paardekooper J.-P., 2014, MNRAS, 443, 648

Agarwal B., Johnson J. L., Zackrisson E., Labbe I., van den Bosch F. C., Natarajan P., Khochfar S., 2015, preprint, (arXiv:1510.01733)

Ajith P., et al., 2011, Physical Review Letters, 106, 241101

Alexander T., Natarajan P., 2014, Science, 345, 1330

Alvarez M. A., Wise J. H., Abel T., 2009, ApJ, 701, L133

Amaro-Seoane P., et al., 2013, GW Notes, Vol. 6, p. 4-110, 6, 4

Antonucci R., 1993, ARAA, 31, 473

Ashby M. L. N., et al., 2013, ApJ, 769, 80

Bardeen J. M., Press W. H., Teukolsky S. A., 1972, ApJ, 178, 347

Barger A. J., et al., 2014, ApJ, 784, 9

Barkana R., Loeb A., 2001, Physics Reports, 349, 125

Barnett R., et al., 2015, A&A, 575, A31

Begelman M. C., 1978, MNRAS, 184, 53

Begelman M. C., 2012, MNRAS, 420, 2912

Begelman M. C., Meier D. L., 1982, ApJ, 253, 873

Begelman M. C., Volonteri M., Rees M. J., 2006, MNRAS, 370, 289

Begelman M. C., Rossi E. M., Armitage P. J., 2008, MNRAS, 387, 1649

Bellovary J., Volonteri M., Governato F., Shen S., Quinn T., Wadsley J., 2011, ApJ, 742, 13

Blandford R. D., Begelman M. C., 1999, MNRAS, 303, L1

Bombaci I., 1996, A&A, 305, 871

Bondi H., 1952, MNRAS, 112, 195

Brammer G. B., et al., 2012, ApJS, 200, 13

Bromm V., 2013, Reports on Progress in Physics, 76, 112901

Bromm V., Loeb A., 2003, ApJ, 596, 34

Bromm V., Yoshida N., 2011, ARAA, 49, 373

Bruzual G., Charlot S., 2003, MNRAS, 344, 1000

Bryan G. L., Norman M. L., 1998, ApJ, 495, 80

Buonanno A., Cook G. B., Pretorius F., 2007, PRD, 75, 124018

Camp J. B., Cornish N. J., 2004, Annual Review of Nuclear and Particle Science, 54, 525

Campanelli M., Lousto C. O., Zlochower Y., Merritt D., 2007, Physical Review Letters, 98, 231102

Cappelluti N., et al., 2013, ApJ, 769, 68

Cappelluti N., et al., 2015, preprint, (arXiv:1512.00510)

Cassinelli J. P., Castor J. I., 1973, ApJ, 179, 189

Castellano M., et al., 2014, A&A, 566, A19

Castor J. I., 1972, ApJ, 178, 779

Chandrasekhar S., 1960, Proceedings of the National Academy of Science, 46, 253

Choi J.-H., Shlosman I., Begelman M. C., 2013, ApJ, 774, 149

Choi J.-H., Shlosman I., Begelman M. C., 2015, MNRAS, 450, 4411

Coe D., Bradley L., Zitrin A., 2014, preprint, (arXiv:1405.0011)

Comastri A., Gilli R., Marconi A., Risaliti G., Salvati M., 2015, A&A, 574, L10

Costa T., Sijacki D., Trenti M., Haehnelt M. G., 2014, MNRAS, 439, 2146

Coughlin E. R., Begelman M. C., 2014, ApJ, 781, 82

Cowie L. L., Barger A. J., Hasinger G., 2012, ApJ, 748, 50

Crowder J., Cornish N. J., 2007, PRD, 75, 043008

Dahlen T., et al., 2013, ApJ, 775, 93

Davies M. B., Miller M. C., Bellovary J. M., 2011, ApJ, 740, L42

Davis A. J., Natarajan P., 2010, MNRAS, 407, 691

Devecchi B., Volonteri M., 2009, ApJ, 694, 302

Di Matteo T., Colberg J., Springel V., Hernquist L., Sijacki D., 2008, ApJ, 676, 33

Dijkstra M., Ferrara A., Mesinger A., 2014, MNRAS, 442, 2036

Dijkstra M., Gronke M., Sobral D., 2016a, preprint, (arXiv:1602.07695)

Dijkstra M., Sethi S., Loeb A., 2016b, ApJ, 820, 10

Draine B. T., Bertoldi F., 1996, ApJ, 468, 269

Dubois Y., Pichon C., Devriendt J., Silk J., Haehnelt M., Kimm T., Slyz A., 2013, MNRAS, 428, 2885

Dubois Y., Volonteri M., Silk J., Devriendt J., Slyz A., Teyssier R., 2015, MNRAS, 452, 1502

Eisenstein D. J., Loeb A., 1995, ApJ, 443, 11

Fan X., et al., 2001, AJ, 122, 2833

Fan X., et al., 2003, AJ, 125, 1649

Fan X., et al., 2006, AJ, 131, 1203

Farmer A. J., Phinney E. S., 2003, MNRAS, 346, 1197

Ferland G. J., et al., 2013, Revista Mexicana de Astronomia y Astrofisica, 49, 137

Ferrara A., Loeb A., 2013, MNRAS, 431, 2826

Ferrara A., Salvadori S., Yue B., Schleicher D., 2014, MNRAS, 443, 2410

Fialkov A., Barkana R., Tseliakhovich D., Hirata C. M., 2012, MNRAS, 424, 1335

Fialkov A., Barkana R., Visbal E., Tseliakhovich D., Hirata C. M., 2013, MNRAS, 432, 2909

Fiore F., et al., 2012, A&A, 537, A16

Franci L., De Pietri R., Dionysopoulou K., Rezzolla L., 2013, PRD, 88, 104028

Frank J., King A., Raine D. J., 2002, Accretion Power in Astrophysics: Third Edition. Cambridge University Press

Gammie C. F., Shapiro S. L., McKinney J. C., 2004, ApJ, 602, 312

Giallongo E., et al., 2015, A&A, 578, A83

Gnedin N. Y., 2000, ApJ, 542, 535

Grazian A., et al., 2015, A&A, 575, A96

Guo Y., et al., 2013, ApJS, 207, 24

Haiman Z., 2013, in Wiklind T., Mobasher B., Bromm V., eds, Astrophysics and Space Science Library Vol. 396, Astrophysics and Space Science Library. p. 293 (arXiv:1203.6075), doi:10.1007/978-3-642-32362-1˙6

Hartwig T., et al., 2015, preprint, (arXiv:1512.01111)

Hopkins P. F., Lidz A., Hernquist L., Coil A. L., Myers A. D., Cox T. J., Spergel D. N., 2007, ApJ, 662, 110

Hosokawa T., Yorke H. W., Inayoshi K., Omukai K., Yoshida N., 2013, ApJ, 778, 178

Hsu L.-T., et al., 2014, ApJ, 796, 60

Hummel J. A., Stacy A., Jeon M., Oliveri A., Bromm V., 2015, MNRAS, 453, 4136

Hummer D. G., Rybicki G. B., 1971, MNRAS, 152, 1

Inayoshi K., Haiman Z., 2016, preprint, (arXiv:1601.02611)

Inayoshi K., Omukai K., 2012, MNRAS, 422, 2539

Jeon M., Pawlik A. H., Greif T. H., Glover S. C. O., Bromm V., Milosavljević M., Klessen R. S., 2012, ApJ, 754, 34

Jiang Y.-F., Stone J. M., Davis S. W., 2014, ApJ, 796, 106

Johnson J. L., Bromm V., 2007, MNRAS, 374, 1557

Johnson J. L., Whalen D. J., Fryer C. L., Li H., 2012, ApJ, 750, 66

Johnson J. L., Whalen D. J., Li H., Holz D. E., 2013, ApJ, 771, 116

Kawamura S., et al., 2011, Classical and Quantum Gravity, 28, 094011

King A., 2003, ApJ, 596, L27

King A. R., 2010, MNRAS, 402, 1516

King A., 2016, MNRAS, 456, L109

Kocsis B., Loeb A., 2008, Physical Review Letters, 101, 041101

Lasota J.-P., 2015, preprint, (arXiv:1505.02172)

Latif M. A., Schleicher D. R. G., Schmidt W., Niemeyer J., 2013a, MNRAS, 433, 1607

Latif M. A., Schleicher D. R. G., Schmidt W., Niemeyer J. C., 2013b, MNRAS, 436, 2989

Latif M. A., Schleicher D. R. G., Schmidt W., 2014a, MNRAS, 440, 1551

Latif M. A., Niemeyer J. C., Schleicher D. R. G., 2014b, MNRAS, 440, 2969

Le Floc'h E., et al., 2005, ApJ, 632, 169

Li J., Benacquista M., 2010, General Relativity and Gravitation, 42, 2511

Li G., Kocsis B., Loeb A., 2012, MNRAS, 425, 2407

Linde A. D., 1982, Physics Letters B, 108, 389

Lodato G., Natarajan P., 2006, MNRAS, 371, 1813

Lodato G., Pringle J. E., 2007, MNRAS, 381, 1287

Loeb A., Furlanetto S. R., 2013, The First Galaxies in the Universe. Princeton University Press

Loeb A., Rasio F. A., 1994, ApJ, 432, 52

Machacek M. E., Bryan G. L., Abel T., 2001, ApJ, 548, 509

Madau P., Rees M. J., 2001, ApJ, 551, L27

Madau P., Haardt F., Dotti M., 2014, ApJ, 784, L38

Maiolino R., Oliva E., Ghinassi F., Pedani M., Mannucci F., Mujica R., Juarez Y., 2004, A&A, 420, 889

Maiolino R., et al., 2012, MNRAS, 425, L66

Marassi S., Schneider R., Ferrari V., 2009, MNRAS, 398, 293

Marassi S., Ciolfi R., Schneider R., Stella L., Ferrari V., 2011, MNRAS, 411, 2549

Marziani P., Sulentic J. W., 2012, New Astronomy Reviews, 56, 49

Maselli A., Ferrara A., Ciardi B., 2003, MNRAS, 345, 379

McKinney J. C., Tchekhovskoy A., Sadowski A., Narayan R., 2014, MNRAS, 441, 3177

McKinney J. C., Dai L., Avara M. J., 2015, MNRAS, 454, L6

Milosavljević M., Bromm V., Couch S. M., Oh S. P., 2009, ApJ, 698, 766

Mineshige S., Kawaguchi T., Takeuchi M., Hayashida K., 2000, PASJ, 52, 499

Miralda-Escudé J., 2003, Science, 300, 1904

Moenchmeyer R., Schaefer G., Mueller E., Kates R. E., 1991, A&A, 246, 417

Montero P. J., Janka H.-T., Müller E., 2012, ApJ, 749, 37

Mortlock D. J., et al., 2011, Nature, 474, 616

Nakauchi D., Inayoshi K., Omukai K., 2014, MNRAS, 442, 2667

Natarajan P., Treister E., 2009, MNRAS, 393, 838

Nelemans G., 2009, Classical and Quantum Gravity, 26, 094030

Novak G. S., Ostriker J. P., Ciotti L., 2011, ApJ, 737, 26

Novak G. S., Ostriker J. P., Ciotti L., 2012, MNRAS, 427, 2734

Oesch P. A., et al., 2016, ApJ, 819, 129

Ohsuga K., Mineshige S., Mori M., Umemura M., 2002, ApJ, 574, 315

Ott C. D., 2009, Classical and Quantum Gravity, 26, 204015

Ott C. D., Burrows A., Livne E., Walder R., 2004, ApJ, 600, 834

Pacucci F., Volonteri M., Ferrara A., 2015, MNRAS, 452, 1922

Paczynski B., Abramowicz M. A., 1982, ApJ, 253, 897

Pallottini A., Ferrara A., Evoli C., 2013, MNRAS, 434, 3293

Pallottini A., et al., 2015, MNRAS, 453, 2465

Pan Y., Buonanno A., Taracchini A., Kidder L. E., Mroué A. H., Pfeiffer H. P., Scheel M. A., Szilágyi B., 2014, PRD, 89, 084006

Park K., Ricotti M., 2011, ApJ, 739, 2

Park K., Ricotti M., 2012, ApJ, 747, 9

Park K., Ricotti M., 2013, ApJ, 767, 163

Petri A., Ferrara A., Salvaterra R., 2012, MNRAS, 422, 1690

Planck Collaboration et al., 2015, preprint, (arXiv:1502.01589)

Planck Collaboration et al., 2016, preprint, (arXiv:1605.03507)

Plowman J. E., Jacobs D. C., Hellings R. W., Larson S. L., Tsuruta S., 2010, MNRAS, 401, 2706

Press W. H., Schechter P., 1974, ApJ, 187, 425

Press W. H., et al., 1992, Numerical recipes in C. The art of scientific computing. Cambridge University Press

Regan J. A., Haehnelt M. G., 2009, MNRAS, 396, 343

Regimbau T., Hughes S. A., 2010, Journal of Physics Conference Series, 228, 012009

Regimbau T., et al., 2012, PRD, 86, 122001

Riechers D. A., et al., 2013, Nature, 496, 329

Robitaille T. P., Whitney B. A., 2010, ApJ, 710, L11

Roe P. L., 1981, Journal of Computational Physics, 43, 357

Sadowski A., 2009, ApJS, 183, 171

Sadowski A., 2011, preprint, (arXiv:1108.0396)

Sadowski A., Narayan R., McKinney J. C., Tchekhovskoy A., 2014, MNRAS, 439, 503

Saenz R. A., Shapiro S. L., 1978, ApJ, 221, 286

Saijo M., Baumgarte T. W., Shapiro S. L., Shibata M., 2002, ApJ, 569, 349

Sakashita S., Yokosawa M., 1974, Astrophysics and Space Science, 31, 251

Salvaterra R., Haardt F., Volonteri M., Moretti A., 2012, A&A, 545, L6

Sathyaprakash B. S., Schutz B. F., 2009, Living Reviews in Relativity, 12, 2

Sądowski A., Narayan R., Tchekhovskoy A., Abarca D., Zhu Y., McKinney J. C., 2015, MNRAS, 447, 49

Schaerer D., de Barros S., 2009, A&A, 502, 423

Schleicher D. R. G., Palla F., Ferrara A., Galli D., Latif M., 2013, A&A, 558, A59

Schneider R., Ferrara A., Ciardi B., Ferrari V., Matarrese S., 2000, MNRAS, 317, 385

Schneider R., Ferrari V., Matarrese S., Portegies Zwart S. F., 2001, MNRAS, 324, 797

Schödel R., et al., 2002, Nature, 419, 694

Sekiguchi Y.-I., Shibata M., 2005, PRD, 71, 084013

Seoane P. A., et al., 2013, ArXiv:1305.5720,

Sesana A., Volonteri M., Haardt F., 2007, MNRAS, 377, 1711

Sesana A., Gair J., Berti E., Volonteri M., 2011, PRD, 83, 044036

Shakura N. I., Sunyaev R. A., 1973, A&A, 24, 337

Shakura N. I., Sunyaev R. A., 1976, MNRAS, 175, 613

Shang C., Bryan G. L., Haiman Z., 2010, MNRAS, 402, 1249

Shapiro S. L., 2003, in Centrella J. M., ed., American Institute of Physics Conference Series Vol. 686, The Astrophysics of Gravitational Wave Sources. pp 50–60 (arXiv:astro-ph/0310070), doi:10.1063/1.1629414

Shibata M., Shapiro S. L., 2002, ApJ, 572, L39

Silk J., Rees M. J., 1998, A&A, 331, L1

Smidt J., Wiggins B. K., Johnson J. L., 2016, preprint, (arXiv:1603.00888)

Smith S. C., Houser J. L., Centrella J. M., 1996, ApJ, 458, 236

Smith A., Bromm V., Loeb A., 2016, preprint, (arXiv:1602.07639)

Smoot G. F., et al., 1992, ApJ, 396, L1

Sobral D., Matthee J., Darvish B., Schaerer D., Mobasher B., Röttgering H. J. A., Santos S., Hemmati S., 2015, ApJ, 808, 139

Spaans M., Silk J., 2006, ApJ, 652, 902

Springel V., et al., 2005, Nature, 435, 629

Stacy A., Bromm V., 2014, ApJ, 785, 73

Sugimura K., Omukai K., Inoue A. K., 2014, MNRAS, 445, 544

Suwa Y., Takiwaki T., Kotake K., Sato K., 2007, ApJ, 665, L43

Tamazawa S., Toyama K., Kaneko N., Ono Y., 1975, Astrophysics and Space Science, 32, 403

Tanaka T., Perna R., Haiman Z., 2012, MNRAS, 425, 2974

Tanvir N. R., et al., 2009, Nature, 461, 1254

Teo E., 2003, General Relativity and Gravitation, 35, 1909

Thorne K. S., 1974, ApJ, 191, 507

Treister E., Schawinski K., Volonteri M., Natarajan P., 2013, ApJ, 778, 130

Visbal E., Haiman Z., Terrazas B., Bryan G. L., Barkana R., 2014, MNRAS, 445, 107

Visbal E., Haiman Z., Bryan G. L., 2016, preprint, (arXiv:1602.04843)

Volonteri M., 2010, in Maraschi L., Ghisellini G., Della Ceca R., Tavecchio F., eds, Astronomical Society of the Pacific Conference Series Vol. 427, Accretion and Ejection in AGN: a Global View. p. 3 (arXiv:1002.3827)

Volonteri M., Bellovary J., 2012, Reports on Progress in Physics, 75, 124901

Volonteri M., Rees M. J., 2005, ApJ, 633, 624

Volonteri M., Lodato G., Natarajan P., 2008, MNRAS, 383, 1079

Volonteri M., Sikora M., Lasota J.-P., Merloni A., 2013, ApJ, 775, 94

Volonteri M., Silk J., Dubus G., 2015, ApJ, 804, 148

Wang J.-M., Netzer H., 2003, A&A, 398, 927

Weigel A. K., Schawinski K., Treister E., Urry C. M., Koss M., Trakhtenbrot B., 2015, MNRAS, 448, 3167

Willott C. J., 2011, ApJ, 742, L8

Wu K. K. S., Lahav O., Rees M. J., 1999, Nature, 397, 225

Wu X.-B., et al., 2015, Nature, 518, 512

Xue Y. Q., et al., 2011, ApJS, 195, 10

Yagi K., Seto N., 2011, PRD, 83, 044011

Yu Q., Tremaine S., 2002, MNRAS, 335, 965

Yue B., Ferrara A., Salvaterra R., Xu Y., Chen X., 2013, MNRAS, 433, 1556

Yue B., Ferrara A., Salvaterra R., Xu Y., Chen X., 2014, MNRAS, 440, 1263

Zaroubi S., 2013, in Wiklind T., Mobasher B., Bromm V., eds, Astrophysics and Space Science Library Vol. 396, Astrophysics and Space Science Library. p. 45 (arXiv:1206.0267), doi:10.1007/978-3-642-32362-1˙2

de Bernardis P., et al., 2000, Nature, 404, 955

de Souza R. S., Ciardi B., Maio U., Ferrara A., 2013, MNRAS, 428, 2109